A Mathematical Model for Photothermal Therapy of Spherical Tumors

Ahmed Mostafa Abdelhady Ismaeel

Submitted in fulfilment of the requirements for the
Degree of Doctor of Philosophy

School of Mathematics and Statistics
College of Science and Engineering
University of Glasgow

October 2019

Abstract

Photothermal ablation is a promising new technique for treatment of some cancers, where metal nanoparticles are introduced into the tumor and the system is locally heated with a laser to destroy the malignant cells. The aim is to have nanoparticles accumulate within the tumor and not in the surrounding healthy tissue, so that the heat source leads to a differential increase in temperature in the cancer and hence cell death.

We begin by examining nanoparticle delivery from a single blood vessel into surrounding tissue using asymptotic analysis to construct the extravasation flux of nanoparticles into the tissue.

We then incorporate this flux into a spatially one dimensional model which includes interstitial fluid flow to examine the distribution of nanoparticles across the tumor and the surrounding tissue. In this model we also consider nanoparticles conjugated with ligands which selectively bind to tumor cell surface receptors and eventually leads to nanoparticle internalization within the cell. We study how the mass of accumulated nanoparticles within the tumour (and the surrounding tissue) is influenced by the nanoparticle delivery time interval, ligand nanoparticle conjugation and tumor cell capacity for internalized nanoparticles.

We then mimic laser irradiation of the tumor and the surrounding tissue (which comprise nanoparticles) estimating the temperature elevation and the induced tissue damage within the tissue. Finally, we validate our predictions against two different sets of experimental data and then discuss how to optimize the outputs of the photothermal therapy. We show that conjugating binding ligands to the nanoparticles can lead to a heterogeneous spatial distribution of nanoparticles and reduce tumor damage induced by laser irradiation. We conclude by discussing strategies to optimize the treatment protocol to induce maximal tumor damage with minimal side effects in the surrounding healthy tissue.

Contents

List of Tables

List of Figures

Acknowledgements

All praise be to Allah who says in the Qura'n

> *'And God has extracted you from the wombs of your mothers not knowing a thing, and He made for you hearing and vision and hearts [i.e., intellect] that perhaps you would be grateful.'* (Qura'n 16:78)

Then my appreciation is due my parents who have been giving me support as much as they could and I owe my success to them.

> *'And lower to them the wing of humility out of mercy and say: My Lord, have mercy upon them as they brought me up [when I was] small.'* (Qura'n 17:24)

I would like to express my gratitude to my supervisors (Peter Stewart and Xiaoyu) who gave me all the support that I needed to finish my PhD over the four years. I would like to say a big thank to Peter, who spent his time and effort helping me to overcome all obstacles that I had in my PhD. He did his best to construct the essential foundations for my future research. A special thank to Xiaoyu, who was the reason I got this PhD scholarship at the University of Glasgow. She worked hard to support and guide me before I started my PhD and during my PhD. I consider her as my second mother before my supervisor. Whatever I say about Peter and Xiaoyu, my words cannot describe what I owe them because of their dedicated support.

I am also very grateful to the British Council and the Egyptian Cultural Affairs and Missions Sector which funded me through the Newton-Mosharafa program. I would like to also thank all my colleagues and all the staff at school of Mathematics and Statistics in addition to the International Family Network members who helped me enjoy my PhD.

Finally, a special thank you to my wife who strove to support and encourage me in every step I had in my life. Thank you for your support and being my happiness.

Declaration

This thesis is submitted in accordance with the regulations for the degree of Doctor of Philosophy at the University of Glasgow. With the exception of chapter 1, which contains introductory material, all work in this thesis was carried out by the author unless otherwise explicitly stated.

Nomenclature

α	The ratio of the vasculature to the interstitium hydraulic conductivities.
α_2	A constant dependent on the average pore diameter of the vessel wall.
$\breve{P}$	The effective permeability.
$\Delta\hat{T}$	The temperature rise at the tumor center due to laser.
δ	The ratio of the wall thickness to the vessel radius.
ϵ	The ratio of the vessel thickness to the vessel length.
γ_c	The ratio of disassociation and diffusion timescales.
γ_p	The vessel surface area fraction occupied by pores.
γ_u	The dimensionless hydraulic conductivity of the vascular walls.
$\hat{\eta}$	The dimensionless radial direction in the vessel wall domain.
$\hat{\gamma}_b$	The specific heat capacity of the blood.
$\hat{\gamma}_s$	The gold specific heat capacity.
$\hat{\gamma}_t$	The specific heat capacity of the tissue.
$\hat{\mu}$	The interstitial fluid viscosity.
$\hat{\mu}_a$	The light absorption coefficient.
$\hat{\mu}_b$	The blood viscosity.
$\hat{\mu}_s$	The light scattering coefficient.
$\hat{\mu}_{at}$	The medium absorbance coefficient.
$\hat{\mu}_{eff}$	The effective radiation coefficient.
$\hat{\mu}_{st}$	The medium scattering coefficient.

$\hat{\mu}_{tr}$ The transport attenuation coefficient.

$\hat{\omega}$ The fluid velocity in the axial direction.

$\hat{\omega}_b$ The blood perfusion rate.

$\hat{\phi}$ The light fluence rate.

$\hat{\pi}_i$ The interstitial osmotic pressure in the tissue.

$\hat{\pi}_v$ The vascular osmotic pressure in the tissue.

$\hat{\rho}$ The tissue density.

$\hat{\rho}_b\hat{\omega}_b$ The blood density times blood perfusion rate.

$\hat{\rho}_g$ The gold density.

$\hat{\rho}_t$ The tissue density (skin).

$\hat{\sigma}_a$ The absorption cross-section.

$\hat{\sigma}_s$ The scattering cross-section.

$\hat{\sigma}_{ext}$ The extinction cross-section.

$\hat{\tau}$ The GNR blood half life.

$\hat{\xi}$ The dimensionless radial direction in the tissue domain.

$\hat{C}$ The concentration of free GNRs.

$\hat{C}_b$ The concentration of bound GNRs.

$\hat{C}_i$ The concentration of internalized GNRs.

$\hat{C}_{av}$ The maximum average GNR concentration in the tumor.

$\hat{C}_{bs_{max}}$ The maximum cell receptor concentration.

$\hat{C}_{i_{max}}$ The maximum internalized GNR concentration.

$\hat{C}_{tot}$ The total concentration of GNRs.

$\hat{C}_v$ The vascular concentration of GNRs.

$\hat{D}$ The GNR (solute) diffusion coefficient.

$\hat{d}_n$ The GNR diameter.

$\hat{d}_p$ The laser beam diameter.

$\hat{E}$ The internal energy.

$\hat{H}$ The heaviside step function.

$\hat{h}$ The heat transfer coefficient.

$\hat{J}_r$ The solute radial flux.

$\hat{J}_z$ The solute axial flux.

$\hat{J}_{tot}$ The total solute flux.

$\hat{K}$ The interstitial hydraulic conductivity.

$\hat{k}_2$ The interstitial permeability in the vessel wall.

$\hat{k}_3$ The interstitial permeability in the tissue.

$\hat{k}_a$ The association rate coefficient.

$\hat{k}_d$ The dissociation rate coefficient.

$\hat{k}_i$ The internalization rate coefficient.

$\hat{K}_s$ The gold thermal conductivity.

$\hat{K}_t$ The tissue thermal conductivity.

$\hat{L}$ The vessel length.

$\hat{L}$ The vessel wall thickness.

$\hat{L}_n$ The GNR length.

$\hat{L}_{pl}^{(N)}\hat{S}_l^{(N)}/\hat{V}^{(N)}$ The lymphatic density.

$\hat{L}_{pv}^{(N)}$ The hydraulic conductivity of the microvascular wall in the tissue.

$\hat{M}$ The total solute mass.

$\hat{M}_g$ The gold molecular weight (molar mass).

$\hat{P}$ The fluid pressure.

$\hat{P}$ The laser density.

$\hat{P}_0$ Blood pressure at the vessel outlet.

$\hat{P}_i$ The interstitial fluid pressure.

$\hat{P}_l$ The lymphatic pressure.

$\hat{P}_v$ The vascular pressure.

$\hat{P}_{laser}$ The laser power.

$\hat{Q}_l$ The fluid flux into lymphatics.

$\hat{Q}_v$ The vascular fluid flux into tissue.

$\hat{Q}_{in}$ The inlet fluid flux.

$\hat{Q}_{out}$ The outlet fluid flux.

$\hat{Q}_{tr}$ The transmural fluid flux.

$\hat{R}$ The tumor radius.

$\hat{r}$ The radial direction.

$\hat{r}_0$ The radius of tumor core where the laser source term is independent of r.

$\hat{R}_1$ The vessel radius.

$\hat{R}_2$ The vessel radius + the vessel wall thickness.

$\hat{R}_3$ The vessel radius + the vessel wall and tissue thicknesses.

$\hat{R}_\infty$ The width of the tumor and tissue.

$\hat{r}_n$ The GNR radius.

$\hat{r}_p$ The vessel pore radius.

$\hat{r}_{eff}$ The effective GNR radius.

$\hat{S}_v^N/\hat{V}$ The vasculature density.

$\hat{S}_{laser}$ The laser Heat source term.

$\hat{T}$ The temperature.

$\hat{t}$ Time.

$\hat{T}_b$ The blood temperature.

$\hat{u}$ The fluid velocity in the radial direction.

$\hat{V}_{tiss}$ The volume of tissue.

$\hat{W}$ Blood mean velocity at the vessel inlet.

$\hat{z}$ The axial direction.

λ The ratio of the tissue thickness to the tissue length.

$\hat{\mathbf{q}}$ The heat flux.

μ_{EE} The mean of elementary effect.

ν_1 The ratio of GNR disassociation to association timescales.

ν_2 The ratio of GNR disassociation to internalization timescales.

Ω The cell death index.

ϕ_b The vascular volume fraction.

ϕ_f The interstitial volume fraction.

ϕ_n The volume fraction of GNRs.

σ The osmotic reflection coefficient for GNRs.

σ_T The average osmotic reflection coefficient for plasma protein.

ξ_l The ratio of the lymphatic volumetric flow to GNR disassociation rates.

ξ_v The ratio of the vascular volumetric flow to disassociation rates.

ξ_{b1} The ratio of GNR disassociation time scale to GNR blood half life.

ξ_{b2} The ratio of tumor volume and blood circulatory system volume.

A_2 A measure of the slip at the vessel wall/tissue interface.

E_a The cell activation energy.

EE The elementary effects.

g The anisotropy factor.

GI_{EE} The elementary effect global index.

I_0 The first kind of the modified Bessel function of zero order.

K_0 The second kind of the modified Bessel function of zero order.

m The tissue thickness scale factor.

n The GNR shape factor.

N_A The Avogadro constant.

Pe The Peclet number.

rsd The relative standard deviation.

Chapter 1

Introduction

Cancer is the major cause of death in economically developed countries and the second leading cause of death in developing countries [57]. It is expected that over $606,808$ Americans will die because of cancer in 2019 [100]. Globally, cancer spreads largely because of the aging population [57] and human lifestyle (bad habits) [15]. For example, heavy smoking, drinking alcohol, exposure to the sun and eating fatty foods (which leads to obesity) in addition to physical inactivity. Furthermore, the spread of infectious viruses such as Human papilloma viruses (HPVs), Epstein-Barr virus (EBV), Hepatitis B virus (HBV) and hepatitis C virus (HCV) may cause gene mutations which promote cancer. Therefore, in some ways cancer is easier to prevent than treat. This is because (mostly) the symptoms of cancer appear too late to be treated effectively. In particular, cancerous tumors which have already obtained direct access to the blood circulatory system (through angiogenesis) can allow some cancer cells to travel to other organs and initiate secondary tumors; this process is called metastasis. Deep-sited tumors are difficult to be removed by surgery and there are some significant challenges for treating tumors through chemotherapy (as discussed in Sec. 1.6.2). Therefore, researchers have recently proposed new localized treatment techniques involving thermal therapy (see Sec. 1.3) and photothermal therapy (see Sec. 1.4) to overcome these issues and restrict the side effects of conventional cancer therapies.

1.1 Tumor Growth

There are different stages before a cancerous tumor becomes malignant, which may take years [13]. Any tumor starts from a single cancerous cell (from a mutation) which then starts to proliferate rapidly compared to the other surrounding healthy cells, see Fig. 1.1. This process leads to the formation of a small solid tumor within the tissue. This new cancerous mass receives most of its nutrient supply by diffusion of nutrient from the surrounding tissue (provided in turn through the blood stream in the nearby vessels). As

a result, the tumor mass engulfs and replaces the surrounding healthy tissue. The solid tumor will therefore expand until it reaches the diffusion-maximal size (approximately 2 mm^3 [13]) when the nutrient supply becomes insufficient for all the tumor cells. At this stage cancerous cells at the center of the tumor start to die because the nutrients have been consumed by the outer layer of the tumor before being able to diffuse to the center. In this stage the solid tumor (approximately) maintains its volume of living cells because the increase in volume due to the proliferation in the viable rim is equal to the volume loss in the necrotic core at the center of the tumor.

During this steady state the solid tumor stimulates the surrounding blood vessels to initiate angiogenesis (forming a new blood supply) to accumulate the high demand for nutrient. Following this stage the tumor becomes a vascular malignant tumor, where the tumor has its own blood supply which supplies sufficient nutrient and enables it to expand beyond the diffusion-maximal size and possibly spread to other parts in the body.

1.1.1 Mathematical Modeling of Tumor Growth

There are a huge number of mathematical models for tumor growth in literature. Araujo and McElwain [2004] [6] provided a comprehensive theoretical modeling review of tumor growth starting with a simple diffusion model proposed in 1928 [42] and developing into more complicated models from the 1990s such as multiphase models, mechanical models, models for tumor invasion (metastasis), avascular tumor models and vascular tumor models. They discussed the interaction between these models and how these various approaches compare to the experiment results. Theoretical models for cancer typically involve consideration of either cancer cell genetics, cell motion [36], tumor growth [113], angiogenesis [3, 18], chemotherapy [48], radio therapy [64] or other treatment methods.

For example, at the intercellular level Enderling et al. [2007] [29] considered how a cancerous tumor can exist and grow in a healthy breast by sequential mutations in genes. They used a tumor growth and invasion model in which the tumor invades the surrounding tissue by releasing matrix degradative enzymes to degrade the adjacent tissue to get extra space to expand; these occur in addition to the acidosis environment created by the cancerous cells which kills the surrounding normal cells. In their mathematical model they assumed that a mutation of only two suppressor tumor genes is sufficient to initiate a tumor cell and breast cancers could be developed from breast stem cells. They simulated three different radiotherapy strategies and analyzed their effect on the breast tumor, finding that none of these strategies can prevent the development of a new local or distant tumor.

Realizing the importance of the cancer tumor heterogeneity, Ward and King [1997] [114] proposed a continuum multi-species model for the growth of an avascular tumor spheroid. In their model they considered two phases of cells, living and dead tumor cells and the

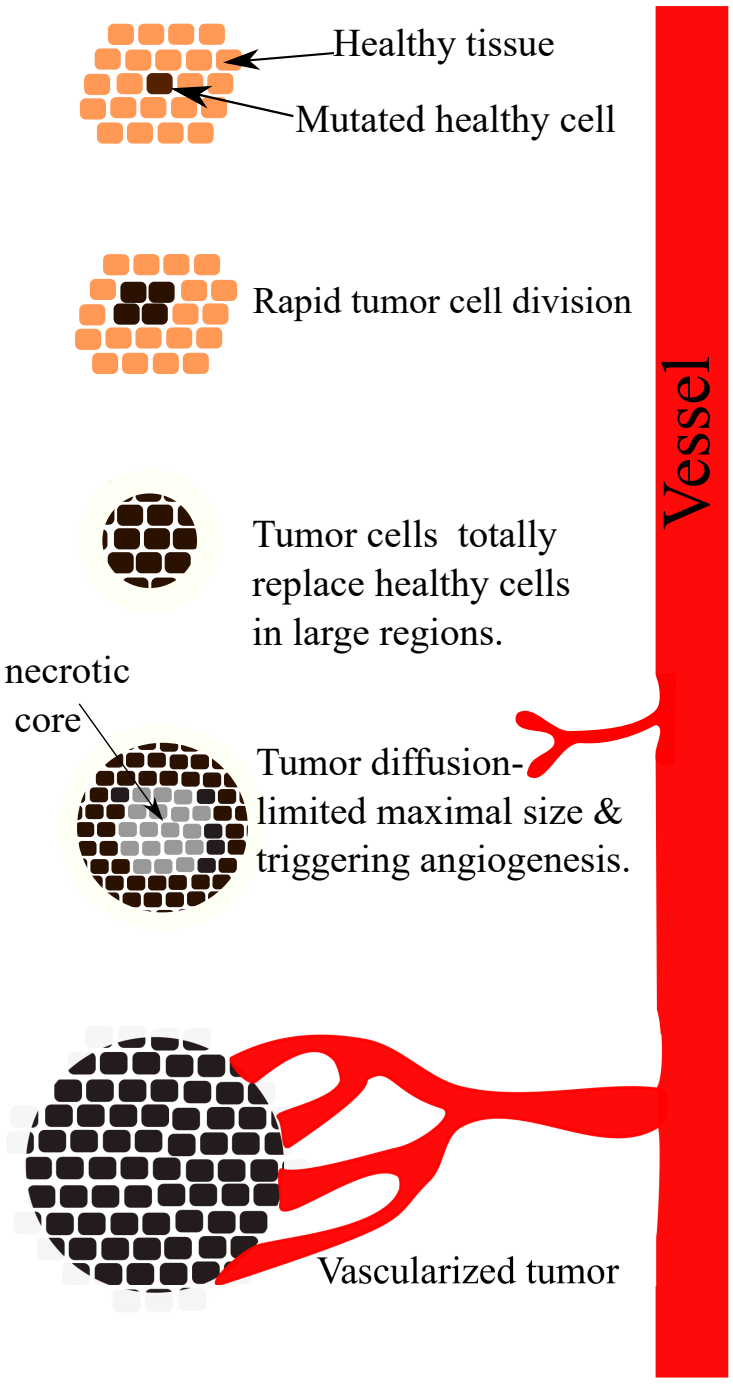

Figure 1.1: Tumor growth from an initial mutated healthy cell to a vascular tumor.

induced velocity field as a result of tumor volume change due to cell proliferation and apoptosis (programmed cell death) depending on nutrient supply. This model predicts an initial accelerated growth for the tumor for a period of time followed by a phase of uniform growth. In addition, the live cell density reaches its maximal value in a narrow region beneath the tumor surface and vanishes quickly outside this layer towards the tumor center, which represents the viable rim and the necrotic core, respectively. The concentration profiles show that the viable rim is rich in nutrient, whereas nutrient concentration in the

core is very small. Finally, the tumor expansion velocity increases rapidly in the viable rim due to cell proliferation, but decreases rapidly outside this region, to a negative value, meaning that the cell death rate is greater than the cell proliferation rate, and finally increasing to zero in the core region. An analytical traveling wave solution was obtained and asymptotic techniques (for small death rates) used to study the tumor expansion stages.

Ward and King [2003] [115] extended this model to incorporate the introduction of an anticancerous drug, assuming the drug is applied in the external environment and can diffuse into the tumor and kill cells. They studied both linear and Michaelis-Menten kinetics of drug action on cells. Their results are consistent with the experimental results and deduced that the efficiency of the drug depends on its penetration depth. Similar ideas can be used in a model of nanoparticle (NP) delivery to avascular tumors.

1.2 Hyperthermia

Hyperthermia is the process of exposing tissue to an external source of energy to elevate tissue temperature up to approximately $42 - 43°C$ [67]. This concept has been used in cancer treatment since 1800s [22] and is usually used as an additional therapy to improve the outcomes of radiotherapy or chemotherapy [67]. This is because exposing tissue to $40-41°C$ for relatively short time inhibits cell division and is cytotoxic [70]. In particular, exposing tissue to higher temperatures ($40-45°C$) for a sufficient period of time induces extensive protein denaturation which inactivates many cellular functions [70]. These cellular dysfunctionalities occur due to the increase in the vibrational, transitional and rotational motion of molecules in the cells (as a result of temperature increase) which speeds up the intracellular reaction rates and metabolism, causing an unbalanced metabolism [70].

The human body is typically exposed to electromagnetic waves or intensive ultrasound in hyperthermia [62,67], but this has severe side effects to the healthy tissue that surround the tumor, see Fig. 1.2(A). This problem restricts the maximum temperature that can be used in hyperthermia because of the expected induced damage in the healthy tissue and organs [78]. In order to overcome this issue hyperthermia can be localized through using a hot needle tip which can be placed at the tumor center, but this technique fails with deeply seated (inaccessible) tumors [62]. In addition, hyperthermia can be combined with chemotherapy and radiotherapy to improve the patient outcomes [22] where elevating tissue temperature increases blood perfusion which carry more drug to the heated tissue.

Different techniques for hyperthermia have been investigated theoretically and experimentally in the literature. Skinner et al. [1998] [101] compared theoretically the heat generated via different applicators to transmit microwaves, laser and ultrasound. They modeled the irradiation of different types of tissue: breast, brain and liver. They con-

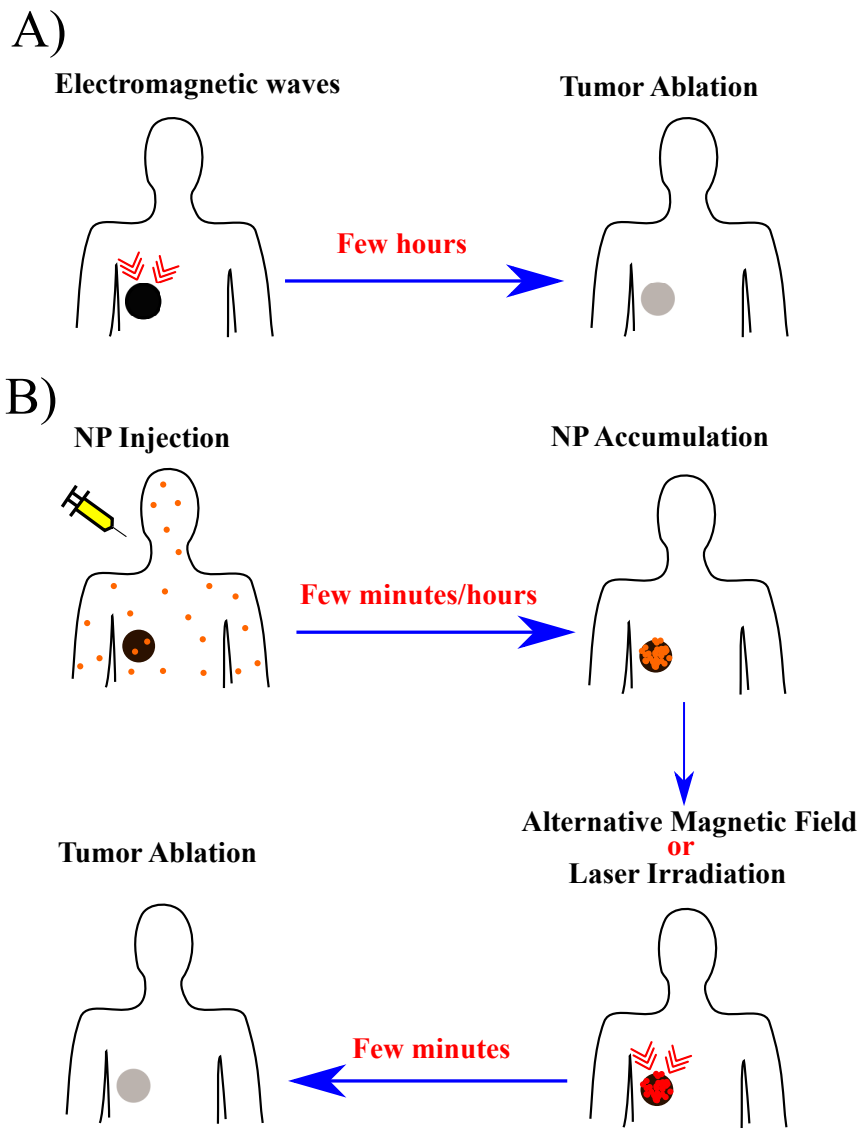

Figure 1.2: Hyperthermia (A) and thermal/photothermal therapy (B) technique diagrams.

cluded that tissue damage depends on the size of the applicator for large applicators. For small applicators, however, the tissue temperature is less dependent on the energy source.

Deep sited tumors need an alternative external source of energy because it is difficult to approach the tumor by a needle or applicator. Lang et al. [1999] [67] studied numerically a technique for hyperthermia of deep sited tumors using electromagnetic waves. In this technique they simulated the temperature induced in a patient who is surrounded by a group of antennas which transmit electromagnetic waves. These antennas were tuned in terms of their amplitudes and phases to heat a deep-seated tumor.

1.3 Thermal Therapy

Thermal therapy is a stand-alone targeted therapy in which tissue is subjected to larger temperatures than hyperthermia, $50 - 90°C$ for a few seconds or minutes [101]. Hence, the temperature of the cells can be raised sufficiently to be effectively destroyed. For example, a sustained increase in temperature to the range $41 - 47°C$ induces cell death via apoptosis, while prolonged temperatures above 50°C lead to necrosis [22]. For instance, heating a tissue sample to 44.5°C for 25 minutes kills approximately 90% of the cells [70].

The heating in thermal therapy is localized for the tumor, leaving the surrounding healthy tissue relatively safe from heat exposure [101]. The heat generated in the thermal therapy is localized within the tumor and prolonged for few seconds or minutes [78]. The effect of this therapy can be substantially enhanced by altering the thermal properties of the tissue. This can be achieved through targeting the tumor with metal nanoparticles (NPs) with large thermal conductivity prior to heating or irradiation [22]. So, these nanoscale agents are injected into the body to target either avascular (solid) or vascular tumors. NPs can be conjugated with appropriate targeting ligands in order to selectively bind to tumor cells [44,45] to help protect the surrounding tissue. The injected NPs either extravasate from nearby vasculature (intravenous administration) or are delivered directly to the tumor (intratumoral administration), advect through tumor interstitium and diffuse across the tumor [54,66,78]. The diagram in Fig. 1.2(B) shows how thermal/photothermal therapy is used for cancer treatment.

As NPs accumulate in the tumor they significantly enhance the contrast in imaging [89]. However, these NPs can also be used therapeutically to help destroy the cancer cells. In the presence of a heat source (for example a heated probe, an alternating magnetic field or a laser), these metal NPs cause the tumor tissue to increase in temperature more than the surrounding tissue. Such an increase in temperature can be beneficial for a number of cancer treatments. For example, a local increase in temperature increases the diffusivity of chemicals through the tissue [70] which improves drug delivery and so can be used to improve the effectiveness of chemotherapy [62].

These nanoscale agents are chosen according to some physical properties that can be tuned by an external source of energy [62]. This allows clinicians to safely use a stronger source of energy to maximize the damage occurs to the tumor, while protecting the surrounding healthy tissue with relatively minor side effects [79]. Furthermore, thermal therapy can be combined with chemotherapy or radiation therapy to enhance the treatment effectiveness [79].

The choice of the NP material depends on the type of the external energy used in the thermal treatment [17]. For instance, gold NPs and carbon nanotubes can be used with laser irradiation source in a technique known as photothermal therapy [62]. Iron oxide nanoparticles (IONPs) [17, 78] and ferromagnetic seeds [59] can be used in conjunction

alternating magnetic field generator.

This therapy has attracted researchers in the last two decades because thermal therapy techniques potentially ameliorate the main issues which arise in hyperthermia (the side effects and the relatively long treatment session time). Cherukuri et al. [2010] [22] and Kaur et al. [2016] [62] published reviews about enhancing hyperthermia using metal NPs. In both these review papers, the excellence of using NPs in cancer imaging was discussed in addition to generating heat within tumors using an electromagnetic field. In particular, they reviewed the characteristics of magnetic nanoparticles, gold nanoparticles and carbon nanotubes that can be exploited to induce high temperatures within the treated tissue. Kaur et al. [2016] [62] reviewed some types of magnetic NPs, such as IONPs, superparamagnetic IONPs and iron doped IONPs. Moreover, they discussed the challenges of using NPs in thermal therapy, such as NP biocompatibility (some NPs are toxic and cannot be used clinically, e.g. carbon nanotubes), whereas other NPs can only be used with restricted dose concentrations (e.g. gold NPs). Another challenge is the biodistribution of the NPs in the body after the treatment, where NPs are mostly retained in the liver, spline and kidney for several weeks/months.

Jinghua et al. [2014] [59] studied numerically and experimentally the tumor temperature in magnetic interstitial hyperthermia. In their experiment the tumor is embedded with a number of ferromagnetic seeds and then exposed to an alternating magnetic field. They used a Lattice Boltzmann method to solve the corresponding bioheat equation (known as Pennes equation [19]) to calculate the temperature profile across the tumor. They carried out *in vivo* and *in vitro* experiments to validate their mathematical model which showed high efficiency and precise results.

Cervadoro et al. [2013] [17] studied numerically three different types of superparamagnetic IONPs exposed to an alternating magnetic field to find the minimum requirements for successful hyperthermia and thermal ablation in terms of tissue temperature, NP concentration and blood perfusion. They solved the bioheat equation using the finite element method. They found that in the absence of superparamagnetic IONPs, the tissue temperature can be increased using a high frequency magnetic field ($\approx$ 30 MHZ) and this increased temperature depends on the thermal conductivity of the tissue. On the other hand, introducing NPs into tissue can increase tissue temperature using a low frequency magnetic field ($<$ 1 MHZ) and the elevated temperature becomes linearly dependent on the NP concentration.

Reflecting on the recent advances in the hyperthermia ablation experiments *in vitro* and *in vivo*, Nabil et al. [2015] [78] carried out numerical experiments using an embedded multiscale method to study how nano-based hyperthermia depends on the size of the tumor and vascularity. They modeled the fundamental mechanisms that appear in nano-based hyperthermia of a tissue sample, including realistic vasculature, coupled capillary

and interstitial flow, coupled capillary and interstitial mass transfer applied to the concentration of NPs and coupled capillary and interstitial heat transfer. Their simulations show that the concentration of nanoparticles in the tissue sample significantly decreases after injection due to a high washout rate, which is a disadvantage of using small particles. Furthermore, the distribution of nanoparticles and temperature through the tumor is affected by the blood flow in the capillaries and the capillaries network configuration. In their simulation, the host tissue is injected with IONP for 40 minutes through a blood vessel close to the tumor. The tumor is then exposed to an alternating magnetic field for the following 20 minutes. They concluded that the tumor hyperthermic treatment is greatly depends on the tumor size, where in large tumors IONP distribution is inhomogeneous causing heat heterogeneity across the tumor mass. This observation suggests that large tumors need to be treated first using anti-angiogenic drugs to get normalized tumor vasculature before applying the tumor hyperthermic treatment [53].

The model of Nabil et al. [2015] [78] was extended to study tumor vasculature targeting by Nabil and Zunino [2016] [79]. In this new model they modeled large IONPs that could not extravasate from the tumor vasculature but instead bind to receptors at the tumor vasculature inner wall. They found that bound IONPs in the tumor vasculature and the topology of the microvasculature itself influence the tumor temperature profile where tumor regions with dense vasculature allow more bound IONPs to access these tumor regions. Their model suggests that prolonging the wait time between IONP injection and heating increases the concentration of the bound IONPs at the vasculature inner wall.

1.4 Photothermal Therapy

Photothermal therapy is a promising new therapy for targeted treatment of tumors [60]. As mentioned in the preceding section (Sec. 1.3), in photothermal therapy the tumor is injected by gold nanorods (GNRs), gold nanoparticles (gold NPs) or carbon nanotubes and the tumor is then irradiated by a laser beam which heats up the introduced nano material to induce cell death in the nearby tumor cells, see Fig. 1.2(B). Hirsch et al. [2003] [43] have promising results for applying photothermal therapy to human breast carcinoma cells both *in vivo* and *in vitro*. They found that either using the laser alone or gold nanoshells (GNSs) alone was insufficient to induce cell death. This means neither laser nor GNSs are cytotoxic in their own right. However, irradiation of tumors injected with GNSs can generate localized and irreversible tissue damage around the GNSs, where the temperature can be increased by $37 \pm 6.6°C$ within 4 to 6 minutes. They used real-time magnetic resonance temperature imaging to monitor the temperature at several depths (2.5, 3.75, 5 and 7.3 mm) beneath the tissue surface showing that increasing tissue temperature by 37°C causes coagulation and tissue shrinking.

Qin and Bischof [2012] [92] provided a critical review to discuss the potential mechanisms of heat generation across biological tissue during laser irradiation in the presence of gold NPs where heat absorption in tissue depends on tissue composition. For example, haemoglobin and melanin strongly absorb light in the visible spectrum, while water absorbs more in the infrared, so NPs can be tuned to absorb laser near infrared to minimize absorption in water and haemoglobin. Hence, the amount of heat generated in the tissue depends on laser type, laser scattering and absorption in the tissue and NPs.

In addition they investigated available measurements and mathematical models for the thermal and optical response of biological tissue exposed to laser irradiation. They discussed how the radiance (laser power per unit area in a solid angle of divergence measured in steradian) at any position can be modeled mathematically using the radiative transport equations which incorporate the scattering and absorption effects and the laser power. This equation is difficult to solve, so it can be simplified using a large diffusion approximation which is valid for highly scattering media such as biological tissue. This approximation was validated experimentally for small GNP concentrations, but gave unsatisfactory results for high NP concentrations. Alternatively, laser irradiation can be mimicked using Monte Carlo ray tracing where every photon is modeled and traced in the tissue. However, this is computationally expensive. Moreover, Qin and Bischof [2012] [92] discussed the thermal therapy effects on tissue temperature, physical structure and biological processes at the nano, micro and macro scale. They discussed the important differences at every scale including macromolecular phase change, water phase change and particle heating. In addition, they reviewed the thermal injury kinetics and mathematical modeling. They showed how the photothermal therapy parameters (such as laser power, irradiation duration and gold NP dose) can be tuned to reduce toxicity and increase the outcome of the treatment. For instance, they reported that 3.5 W laser irradiation for 3 minutes was enough to treat a tumor injected by gold nanoshells, while in the absence of gold nanoshells the laser power must be over 10 W with 10 minutes of irradiation to treat the tumor. Finally, they discussed some techniques of combining photothermal therapy with other conventional therapies to enhance drug delivery, drug release and radiation therapy.

Jain et al. [2014] [56] provided a review paper to explore the potential uses of gold NPs in cancer treatment. They showed how gold NPs can be used as drug carriers, contrast agents and radiosensitizers (make tumor cells more sensitive to radiation therapy). Gold NPs surpass the standard contrast agents in tumor imaging due to the high absorption of X-rays. They also reviewed some experiments *in vivo* and *in vitro* showing that the size of gold NPs influences the rate of NP uptake by tumor cells and the sensitization of the tissue. For example, 50 nm gold NPs showed larger cell uptake rates and greater light absorbance compared to 14 nm and 74 nm NPs when tissue was irradiated by X-rays *in vitro*. Some

in vivo studies have shown that combining gold NPs with X-ray irradiation prolonged survival in tumor bearing mice, where the tumor growth was significantly reduced 1 month after treatment. The gold NP concentration peaked in the tumor vasculature within 7 minutes post injection and the NPs accumulated preferentially at the tumor rim rather than in the tumor core. Furthermore, Jain et al. [2014] [56] discussed some Monte Carlo modeling studies for using gold NPs in photothermal therapy and as an assistant to other conventional therapies. Their Monte Carlo simulations showed that a combination of gold NPs and X-ray irradiation was efficient, regardless the gold NP concentration value.

There are a number of different studies in the literature investigating the most appropriate geometric properties of GNRs to optimize heat generated by laser irradiation. Mackey et al. [2014] [72] carried out *in vitro* experiments to compare three different types of GNRs ($38 \times 11,\ 28 \times 8$ and 17×5 nm). They found that 28×8 nm GNRs were the most effective agents for phototherapy because this size showed the best balance between the total absorbed light and the converted fraction to heat. In addition, this size of GNR (28×8 nm) has an intense electromagnetic field that extends sufficiently far from the GNR surface to interact with the other particles nearby, which can lead to enhanced heating.

Some challenges appear in mathematical modeling of photothermal and thermal therapy techniques [60]. For example, the heterogeneity of the tumor structure is challenging both in terms of the modeling and computational cost. Therefore, most of the available theoretical models in the literature consider homogeneous tumors which ignore the heterogeneity of temperature distribution across the tumor. Another challenge is coupling the NP delivery to the tumor with tumor heating and tumor damage as these typically occur on vastly different timescales. Kaddi et al. [2013] [60] discussed an available commercial package software known as NanoPlan (MagForce AG, Berlin, Germany) that can be used to predict tumor temperature for a given magnetic NP distribution across the tumor. They suggested that mathematical models need to be verified by experiments and clinical trials in order to develop more realistic and sophisticated models.

Photothermal therapy has been tested in different experiments in the literature. For example, Soni et al. [2015] [102] mimicked laser irradiation of a biological tissue *in vitro* using two Agrose gel samples of cylindrical shape. They injected a specified region of gel with gold NPs (to represent the tumor tissue) with the surrounding gel to represent the surrounding healthy tissue. The whole gel was irradiated by a laser. To validate theoretically they solved (numerically) the bioheat equation incorporating blood perfusion and metabolic heat generation to mimic a real tumor tissue. Their experiments and modeling suggest that well-designed clinical technique can effectively induce cell damage within 3 mm of the surrounding healthy tissue. In this study, the effect of laser irradiation duration and intensity, gold NP concentration and laser spot size on the gel heating were investigated. They concluded that heating cylindrical tumors (treated by NPs) up to

50° C required two minutes of laser irradiation with intensity 2.5 W/cm^2. This model, however, needs to be verified by *in vivo* experiments to examine the influence of the blood perfusion rate and the metabolic heat generation with the tumor.

Mayle et al. [2017] [73] introduced novel GNSs with cores filled in block polypeptide vesicles with photothermal properties. They tested this new class of GNSs theoretically and *in vitro*, which gave a comparable temperature profile. They used their model to optimize the heat generated in the tumor via changing the parameters of the GNSs, where the GNS diameter was 150 nm. Although the GNS core is positively charged which is toxic, the golden shell removed this toxicity for all concentrations they tested. Hence, this proposed GNS structure showed low toxicity in the absence of laser exposure.

Photothermal therapy techniques need to be studied and analyzed *in vivo* in order to study the NP pharmacokinetics (drug movement and deposition within the body) and toxicity. Terentyuk et al. [2012] [110] studied the tumor growth following a photothermal treatment *in vivo* and *in vitro*, finding that 40×10 nm GNRs accumulate in the tumor within 24 h, but GNR concentration in the spleen exceeds the corresponding concentration in the tumor by $1 - 15$ times. However, the concentration of GNRs in the muscle tissue is nearly $3 - 4$ times smaller than in the tumor. This leads to more damage in the tumor compared to tissue during laser irradiation. In addition, smaller laser power ($1 - 2$ W cm^{-2}) can be used to successfully ablate the tumor.

El-Sayed et al. [2013] [28] successfully inhibited the growth of tumor bearing rats and mice by laser heating of GNRs administrated either intravenously or intratumorally. They found that the GNR blood half life in the case of intravenous injection is less than 3 hours. In addition, GNRs mostly accumulate in the spleen, but for an additive intravenous injection GNRs mostly accumulate with large concentrations in both the spleen and liver. However, these elevated GNR concentration levels in the spleen and liver were non-toxic. They concluded that the intravenous and the intratumoral administrations result in a similar GNR spatial distribution across the tumors and are equipotent for tumor ablation when coupled with laser irradiation.

Dickerson et al. [2008] [25] studied the feasibility of *in vivo* photothermal therapy for deep-seated tumors. They compared the elevated temperature at the tumor in the case of injecting GNRs directly to the tumor with the case of intravenous administration. Although the intratumoral administration provided higher temperatures during the laser irradiation, both techniques substantially inhibited tumor growth.

In the light of these *in vivo* and *in vitro* experiments various theoretical models have been used to investigate the challenges which arise in photothermal techniques. Huang et al. [2006] [45] investigated numerically and experimentally (*in vitro*) the minimum laser irradiation power required to induce tumor cell death. They conjugated gold NPs with antibodies in order to increase the concentration of gold NPs accumulated within

the tumor. They concluded from their simulations that there is a temperature threshold in the range $70 - 80°C$ required to induce cell death in the tumor and healthy tissue. Furthermore, introducing gold NPs reduced the required laser power to induce tumor damage from ≈ 104 W cm^{-2} to ≈ 19 W cm^{-2}. Moreover, the required laser irradiation time (≈ 4 min) is very small compared to the conventional hyperthermia (≈ 60 min). As a result, using gold NPs reduces the exposure time of the healthy tissue to the heat stress which leads to reduced side effects.

Another theoretical study was developed by Huang et al. [2010] [44] which they validated experimentally (*in vitro*) using human prostate cancer cells. In their mathematical model they considered GNRs that cannot diffuse through the interstitium as they bind to tissue receptors. They measured and simulated the tissue temperature and the induced cell death. They assumed that GNRs were not internalized within the cells, so all GNRs are in the extracellular matrix. Their calculated spatiotemporal temperature distribution agrees well with their experiments. They analyzed numerically the effect of cell injury activation energy on the damage induced in the tumor. They showed that conjugating the NPs with binding ligands could lead to a significant difference in tumor damage. They also showed that GNRs in the extracellular matrix are more effective than the internalized GNRs within the cells, although the reason for this difference is unclear.

Von Maltzahn et al. [2009] [112] conducted an experiment *in vivo* for photothermal therapy using GNRs with a blood half life of ≈ 17 hours. They administrated these GNRs via either intravenous or intratumoral injections. Furthermore, they computed the temperature elevation across the tumor during the irradiation using a 3D mathematical model with a temperature dependent blood perfusion rate in the bioheat equation. They showed that a single intravenous injection was enough to successfully ablate the tumor.

Feng et al. [2009] [32] simulated the heat generated a 3D spherical prostate tumor treated with GNSs. They again used the bioheat equation with a laser source term which incorporates the absorption and scattering effects of the tumor tissue and the GNSs. They used an Arrhenius damage model [70] to estimate the tumor damage induced by heating. We use a similar approach to estimate damage in chapter 4. However, their study they did not simulate the GNS delivery to the tumor. As a follow up paper, Feng et al. [2009] [32] developed an integrated mathematical model to simulate the transient temperature profile induced during laser irradiation. This model predicts changes to the optical and thermal properties of the tumor tissue (due to introducing GNSs and change in tissue temperature) using a Monte Carlo fluence model. Their (dynamical) model estimates the tissue thermal conductivity, blood perfusion rate, and tissue absorption and scattering coefficients as functions of the transient tissue temperature and wavelength of the laser light. Their model gives reliable prediction of the temperature field since it incorporates the change in thermal and optical properties of the irradiated tissue.

Barvinschi and Bunoiu [2017] [7] simulated the laser irradiation of a 3D slab of multi-layered tissue mimicking the structure of the human skin. In their model they incorporated blood vessels at different depths within the tissue. Their model suggests that the temperature profile depends on the laser power, laser spot size, blood vessel size and blood flow rate. In particular, increasing the laser power or the laser spot size can significantly magnify the maximum tissue temperature, while increasing blood flow rate in the vessel reduces the maximum temperature that can be achieved in the tissue.

Rylander et al. [2006] [95] presented a computational model for phototherapy treatment for healthy prostate and tumors [increasing heat shock proteins which are produced in moderately heated tissues in order to increase cell resistance to heat which increases cell viability]. Their model can predict two heat shock protein (HSP27 and HSP70) distributions in addition to tissue temperature and tissue damage induced via a number of laser probes. This phenomenon challenges the chemotherapy and radiation treatments combined with hyperthermia. Their model provides clinicians with the predicted regions rich in heat shock proteins which need to be treated to prevent tumor recurrence.

Xu et al. [2011] [120] numerically investigated the influence of the laser wavelength power, exposure time, concentration of NPs and the optical properties of tissue on the photothermal process. They modeled the laser beam transport in the tissue to calculate the laser source term in the bioheat equation. They concluded that the accumulated NPs prevent laser light from evolving across the tissue which means that laser cannot penetrate to the deep tissue. However, the efficiency of NP laser light absorbance balances the lack of laser light propagation across tissue. They found that for a given laser power, there is a NP concentration threshold beyond which any increase in NP concentration in the tumor does not enhance the outcome of the laser irradiation.

Zhu et al. [2002] [122] simulated the tumor temperature profile during laser irradiation of a perfused porcine liver through a spherical applicator with an optical fiber. They used a dynamic model which updates the tissue optical properties due to the transient temperature profile across the tumor and the induced tissue damage. They concluded that ignoring the dynamic effects in thermal and optical properties of the tissue leads to overestimated temperature and tissue damage.

1.5 Cell Injury

There are different intracellular pathways for cell death induced by heat [70]. For example, Lepock [2003] [70] investigated the minimum thermal dose that can induce hyperthermic cell death. Heating cells drives a transition in cellular macromolecules and structures like DNA and proteins, where increasing temperature triggers structural transformation from an ordered state to a disordered state. Moreover, heat triggers protein denaturation which

can then induce alterations in cell structure and function. Therefore, Lepock [2003] [70] concluded that cell death needs a high activation energy of $100-200$ Kcal/mole to trigger a transition in a cellular macromolecule or structure. Furthermore, hyperthermic cell death needs a high activation energy to induce protein denaturation. Finally, combining hyperthermia with other stresses such as ionizing radiation helps in breaking the activation energy threshold which leads to greater tissue damage.

The induced tissue damage as a result of heat stress can be modeled mathematically using the Arrhenius injury model [94], see Eq. 4.35. This model was correlated according to Arrhenius plots (the logarithm of dead cell number vs the inverse of the temperature) for cell growth ($30-40°$C), hypothermic killing ($0-25°$C), and hyperthermic killing ($42-45°$C). These plots showed that the logarithm of dead cell number has a linear relationship with the inverse of temperature and the slope of this linear relationship defines the injury process activation energy. This mathematical model is intensively used in the literature for simulating the tumor thermal damage. So, in this thesis we use the Arrhenius injury model to calculate the induced tumor damage following a laser irradiation session for a tumor contains GNRs, see Sec. 4.3.

1.6 Drug delivery

To be effective these thermal and photothermal techniques require significant metal GNR accumulation within the tumor. However tumor targeting is a complex and challenging process. GNRs need to be able to access the tumor and overcome clearance by the lymphatic system [35]. The immune system quickly recognizes the metal particles and starts to eliminate them from the blood stream via macrophages. The time needed for NP concentration to decrease to half its initial value is called the blood half life for NPs. The blood half life for NPs can be fitted experimentally and represented mathematically using an exponential decay function, see Eq. 3.1. The interaction between the gold NPs and the components of the immune system can be minimized through decorating the gold NP surface with a biocompatible material (such as hydrophilic polymers) [15]. This biocompatible cover hides the gold NP from the immune system which prolongs the gold NP suspension in the blood stream. As a result, gold NPs accumulate in the tumor with higher concentrations.

Arami et al. [2015] [5] provided a review which investigates the influence of IONP properties on the blood clearance pharmacokinetics, biodistribution and biodegration of IONPs. They discussed how IONPs can be optimized by tuning their size and distribution to become biocompatible. This makes IONPs suitable for cancer imaging and therapy due to their unique magnetic properties.

1.6.1 NP Blood Half Life

The NP blood half life can be prolonged by reducing uptake by macrophages. This can be achieved through choosing NP size to be < 100 nm, and high NP surface curvature and/or hydrophilic surface [14]. Another way to prolong the circulating time of NPs is by temporarily inhibiting the immune system [5]. This process requires injecting the body with some biocompatible material prior to the NP administration. This material consumes the active macrophages in the body. Then, injecting NPs intravenously guarantees a prolonged blood half life due to the lack of active immune cells [5].

Akiyama et al. [2009] [2] used decorated GNRs by various amounts of polyethylene glycol (PEG) to investigate the biodistribution of GNRs in tumor bearing mice. They found that using a PEG:Au molar ratio of 1.5 prolongs the blood half life and results in an optimal GNR distribution across the tumor. Furthermore, using a high dose of GNRs (more than 39 μg of gold) enhances the GNR accumulation in the tumor as the immune system is temporary inhibited.

Dreaden et al. [2012] [27] reported that gold NPs coated with polyethylene glycol can exhibit long circulation times in the blood (up to 51 h). They deduced that the optimal hydrodynamic diameter of NPs for successful delivery to tumors is $50 - 60$ nm. This observation is consistent with another study *in vivo* [108] where NPs of size 50 nm are delivered to tumors more effectively than 20 and 200 nm NPs.

1.6.2 Passive Targeting

It should be noted that gold NPs selectively accumulate in the tumor due to larger pores in tumor vasculature ($600-800$ nm) compared to those in the healthy vessels. Tumors also have dysfunctional lymphatics which reduce the efficiency of clearance [15], see Fig. 1.3(A). This intrinsic characteristic in tumors is known as the enhanced permeability and retention effect (EPR) which enables gold NPs to accumulate in the tumor without using binding ligands via passive targeting [13]. Passive targeting, however, leads to enhanced gold NP accumulation in the liver, spleen and kidney since the main function of these organs is to filter the bloodstream [28].

In addition, the leaky tumor vasculature increases the transvascular fluid and the osmotic pressure in the interstitial space [54]. The impaired lymphatics in tumors leave the interstitial fluid without a viable sink. As a result, the interstitial fluid pressure increases and becomes homogeneous across the tumor core and comparable to the vascular pressure [66], reducing transport across the vessel wall and across the tumor core by advection and so NP transport across the tumor core is dominated by diffusion [8].

In the light of these tumor characteristics, Lane et al. [2015] [66] mentioned in their review paper some techniques to enhance passive diffusion. They suggested preparing

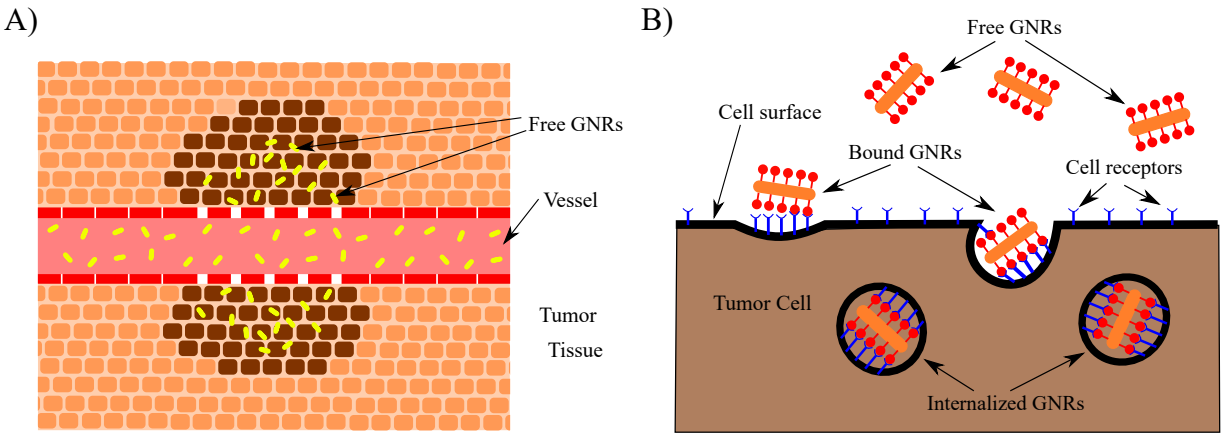

Figure 1.3: GNR Passive tumor targeting (A) and GNR active tumor targeting (B) diagrams.

tumors to have a homogeneous and high vasculature area per unit tumor volume (to increase the NP extravasation), degraded interstitium using bacterial collagenase enzymes (to enhance NP diffusion), and short distances between vasculature vessels. Furthermore, NP extravasation can be improved by temporarily increasing the vascular blood pressure in order to overcome the abnormally elevated interstitial pressure. This can be achieved by reducing the vessel wall pore size in the tumor vasculature using antiangiogenic drugs [20].

However, the temporary increase of blood pressure in the tumor vasculature can lead to retention of fluid in the tumor interstitium which elevates the interstitial pressure again, reversing flow into the tumor vasculature [66]. This will then return the NPs from the interstitium back into the vasculature. Given this delicate balance the NPs need to be prepared optimally to ensure their presence in the tumor at the required time.

1.6.3 Active Targeting

To help achieve this delicate balance gold NPs can be conjugated with binding ligands which selectively bind to receptors at the tumor cell surface, and the bound gold NPs can be engulfed by the tumor cell [34, 40]. This targeting technique is called active tumor targeting, see Fig. 1.3(B). The binding ligands used in the active tumor targeting are chosen according to the type of the targeted tumor cell receptor. These binding ligands include monoclonal antibodies, peptides/proteins, carbohydrates and DNA/RNA.

Lane et al. [2015] [66] discussed some strategies to improve the NP delivery via active targeting. They reported that cell-NP interactions (NP binding to cells or NP internalization into cells) are restricted by low cell concentrations and small NP diffusivity in the interstitium. The NP binding rates can be increased by charging the NPs or using NPs with greater hydrophobic character. In addition, binding ligand affinity and density influence the cellular uptake rate.

Kim et al. [2010] [63] studied *in vitro* and numerically the effect of NP charge on NP binding to human colon carcinoma cells and NP diffusion across the tissue. They found that positively charging the NPs improves the NP affinity to bind to tumor cell receptors, whereas negatively charging NPs improves transport across deep tissue, because negatively charged macromolecules which presence in the interstitium slows down the transport of positively charged NPs. They found that the transport of the conjugated NPs with (negative or positive) binding ligands across the tissue is dominated by the NP-cell interaction which restrict NP diffusion across the tumor. This is due to the rate of NP association and dissociation to cells is smaller than the NP diffusion rate across the interstitium. Therefore, the required NP penetration depth into the tumor can be controlled by the NP surface charge.

For successful delivery, NPs should be coated in binding ligands with high affinity to the cell receptors in order to construct strong bonds between the NP and the cell surface which can then wrap the cellular membrane to engulf the NP. Alternatively, NPs can directly penetrate the cell membrane to get internalized into the cell. Lane et al. [2015] [66] explained different techniques for preparing the NP surface to be actively or directly internalized in the cell. The bound NP on the cell surface can dissociate from the cell receptor, however, so the internalized NPs are usually trapped in the cell and cannot exit again. Murugan et al. [2015] [77] discussed the pathways of internalizing NPs in the tumor cells, and they investigated the role of NP size, shape and charge in overcoming the biological barriers for NP internalization. They concluded from other studies that the influence of NP size depends on the cell type and chemical characteristics of the NPs. Positively charged NPs can bind easily to the cell surface (which is typically negatively charged), and can then be internalized within the cells. They also concluded that spherical NPs have a larger internalization probability than cylindrical NPs, and have more drug-loading capacity than nonspherical NPs.

Guarnieri et al. [2011] [40] studied experimentally (*in vitro*) the influence of serum proteins, (present in the blood) on NP uptake. They found that the proteins physically associate to the NP surface which reduces the NP cellular uptake via reducing the rate of NP binding to the cell surface. Furthermore, they found that the concentration of the internalized NPs saturates, and the saturation point depends on the NP size. This phenomena of maximal NP capacity is introduced in our mathematical model used in this thesis, see Eq. 3.30. The fact that NP internalization saturates in the cells is very important in modeling tumor active targeting since this allows NPs to penetrate further into the tumor, see Sec. 3.4.2.

Hussain et al. [2014] [47] studied *in vivo* the effect of the number of binding ligands at the NP surface on the NP-tumor-cell interaction. They used a mathematical model to study the kinetics of the NP-tumor-cell interaction and they concluded that the number

of available receptors at the tumor cell surface restricts the NP cellular uptake. Therefore, they suggested that reducing the number of binding ligands on the NP surface may actually increase the number of NPs which bind to the tumor cells.

Huang et al. [2010b] [46] studied *in vivo* the transport of GNRs conjugated with binding ligands to tumors. They conjugated GNRs with three different types of binding ligands in order to target three different types of receptors at the tumor cell surface. They found that introducing binding ligands has a minor enhancement for drug delivery. However, binding ligands influence the intracellular and extracellular GNR distribution in the tumor. They suggested that GNR intratumoral administration gives better results compared to intravenous administration. This is consistent with other experimental studies [28]. However, in some cases intratumoral administration can be very difficult for deep-sited tumors.

Ruoslahti et al. [2010] [93] highlighted the problem of the restricted available binding sites in the tumor. They reported that a high dose of NPs (which exceeds the number of receptors in the tumor) leads to a reduction in the NP dose fraction delivered to the tumor (in the case of no NP internalization by the cells) since the unbound NPs stay in the interstitium until removal by lymphatic vessels. In order to overcome this problem they suggested using monovalent high affinity, allowing every NP to bind to one receptor, but this may reduce the NP penetration into the tumor [63]. The reduction of NP penetration due to NP-cell interaction is known as the binding site barrier, and we discuss this barrier in our mathematical model in Sec. 3.4.2. We can overcome the binding site barrier using multivalent weak affinity binding ligands which allow NPs to penetrate deeper in the tumor and the multivalent affinity strengthens the NP binding to cells.

Doiron et al. [2011] [26] found that the number of the available sites at the cell surface decreases for larger sizes of the delivered NPs. As a result, the NP binding and internalization kinetics are influenced by the NP size.

1.6.4 Toxicity of the NPs

To use NPs clinically as agents in cancer treatment for humans it is important to understand their toxicity. A NP toxicity study requires monitoring the dynamics, pathways and the fate of NPs in animal models within weeks, months and years [5]. Arami et al. [2015] [5] discussed some published results for NP toxicity studies *in vivo* and *in vitro*. Some of those studies showed that about 80% of injected IONPs remained in the blood circulatory system for 84 days as iron-protein complexes. Therefore, the NP toxicity in the body is measured according to the influence of the administrated NPs on the blood chemistry, blood cells, gene expression profiles in liver, gross of organs and body weight. Other studies showed that in the case of intravenous and intranasal administration, IONP toxicity can be reduced dramatically through coating IONPs with biocompatible polymers

and using a suitable particle size. On the other hand, Arami et al. [2015] [5] reported that according to some studies, the oral administration of lower doses of the IONPs provides a safe route with mild side effects such as vomiting, nausea or flatulence.

1.6.5 First-in-clinical Trials

Lane et al. [2015] [66] reported successful first-in-human pilot studies for image-guided surgery of tumors in humans using both active and passive targeting agents conjugated with fluorescent dyes. These clinical trials clarified that most of human tumors (such as breast, lung, ovarian and pancreatic cancers) have leaky vasculatures and can be targeted through passive delivery. For example, the irradiation of near-infrared light successfully facilitated the resection of tumors (cutting out the tumor through medical surgery) in the human body in preliminary clinical trials of passive fluorescent agents. However, this technique failed with tumors which have peritumoral inflammation. Furthermore, active targeting was successfully tested in first-in-human clinical trials for cancer imaging. These clinical trials involved patients with lung cancer and ovarian cancer. Fluorescein-conjugated agents helped to discover tumor nodules that were not located by standard techniques [66].

1.6.6 Drug Delivery Modeling

Modeling NP delivery to a tumor is challenging due to the heterogeneity of tumor tissue and vasculature. Jain [1987] [51] reviewed the key parameters for the transvascular fluid and solute transport. He discussed the measurement methods and 1D modeling techniques of these transvascular transport parameters. The transvascular fluid transport is driven by the transmural pressure (the difference between the interstitial, and the vascular and the osmotic pressures), while the transvascular solute transport is driven by both diffusion and advection. The transvascular fluid transport can be modeled by Starling's law [33,104], see Eq. (3.7). Conversely, the transvascular solute transport via diffusion and advection can be approximated by the two pore model [10,97], see Eq. (3.24). We revisit the transvascular fluid and solute transport in a single vessel model in Chapter 2.

Baxter and Jain [1989] [8] modeled the macroscopic transvascular exchange and the interstitial transport of fluid and drug macromolecules in tumors. They considered a homogenous spherical isolated tumor or tumor surrounded by a shell of normal tissue. They considered the tumor as a porous media, so they used Darcy's law for the interstitial flow (see Eq. 3.5). They modeled the tumor vasculature and lymphatics as a spatially homogenous and continuous source and sink, respectively. They used Starling's law to account the transvascular fluid (see Eq. 3.7), and considered the translymphatic fluid is driven by the pressure difference between the interstitial pressure and the lymphatic

pressure (see Eq. 3.8). For the drug transport, they used an advection diffusion equation with a source term (representing the transvascular drug flux) and a sink term (representing the translymphatic drug flux). The transvascular drug flux was calculated by the two pore model, which incorporates the transvascular exchange via diffusion and advection (see Eq. 3.24). Whereas the translymphatic flux was assumed to be proportional to the drug concentration in the interstitium (see Eq. 3.19).

The model described in the preceding paragraph was extended to the case of heterogenous tumor vasculature [8]. In particular, the tumor vasculature was considered to be present only in the tumor viable rim and in the surrounding healthy tissue. Baxter and Jain [1991] [10] extended these two models to study metabolism and drug-cell interaction using a reaction term in the drug transport equation to model drug binding to the tumor cells, but they did not model the drug internalization in the cells. They concluded from their framework that in the absence of the binding ligands, the interstitial pressure profile had the most significant influence on drug distribution. They found that introducing binding ligands slowed down the diffusion and reduce drug accumulation in the tumor core, which result in heterogeneous drug concentration profile across the tumor (this conclusion is similar to what we found in our model, see Sec. 3.4.2). The framework introduced in these three papers is used in this thesis to model the GNR delivery to a vascularised spherical tumor.

Goodman et al. [2008] [34] studied NP delivery to tumors both mathematically and *in vitro*. They conjugated the NPs with binding ligands so they included the NP-cell interaction within the mathematical model. This mathematical model accounts for NP diffusion across the tumor interstitium, NP binding to the tumor cell surface and NP internalization into the tumor cells. They used mixture theory to model three types of NPs in the tumor: free NPs, bound NPs and internalized NPs, and they assumed that free NPs can diffuse across the interstitium and not across the tumor cells. So, there is a restricted tumor volume fraction for free NPs in the tumor. They determined the model parameters experimentally and validated their numerical results against the experimental data. They concluded that the key parameters that influence the drug profile in the tissue are particle size, particle binding affinity and tissue porosity. They found that spherical NPs with diameters 20 and 40 nm accumulated in the tumor spheroid, while NPs with diameter of 200 nm showed no penetration into the spheroids. They also found the amount of NPs that penetrate into tissue can be enhanced by increasing tissue porosity using extracellular matrix degrading enzymes (collagenase). However, this model does not consider a local maximal concentration for internalized NPs in the tumor cells (tumor cell capacity for NPs) which means tumor cells can engulf very large number of NPs which is not consistent with experimental results in the literature [40]. We use a variant of the model of Goodman et al. [2008] [34] in this thesis to investigate the GNR-cell interaction,

but including a maximal capacity for GNRs.

Hussain et al. [2014] [47] investigated theoretically and *in vivo* the influence of the availability of the tumor cell receptors on the drug delivery to tumors. They used the model of Goodman et al. [2008] [34] to discuss the drug binding to the tumor cells, but did not consider drug internalization and modeled the drug clearance in the blood using a biexponential decay function (sum of two exponential decay functions). They assumed that the drug extravasation is proportional to the drug gradient across the blood vessel wall which means that they ignored the drug extravasation by advection. They concluded that the limitation of drug transport into the tumor decreases the number of cell receptors available for binding, but this can be enhanced using tumor penetrating peptides which enhance drug delivery to deep tissue or using drugs with long blood half life. Kim et al. [2010] [63] used a similar mathematical model to discuss their *in vitro* results for delivering NPs to human colon carcinoma. However, they assumed that NP binding rate coefficient is heterogeneous in the tumor (we showed the results of this paper in Sec. 1.6.3).

Chou et al. [2013] [23] mimicked mathematically (in the microscale) the problem of delivering NPs to a tumor *in vivo*. They modeled the NP clearance from the blood stream using an exponential decay model, see the first two terms of Eq. 3.1. They considered no lymphatics in the system as they modeled the tumor with no surrounding healthy tissue. They modeled the transvascular fluid and the interstitial fluid using the model of Goodman et al. [2008] [34]. However, they used Kedem-Katchalsky equation for the transvascular NP transport which is an alternative to the two pore model used by Goodman et al. [2008] [34]. In the interstitium they considered NPs that can diffuse and get internalized (absorbed) directly to the tumor cells. They found that drugs with small radius penetrate more deeply into the tumor interstitium compared to larger drugs; this means that small drugs produce a more uniform concentration profile across the tumor. They also found that enhancing vascular permeability increased the mass of drug in the tumor but did not enhance drug penetration, while increasing drug diffusivity enhanced both the drug mass in the tissue and drug penetration depth.

Stylianopoulos et al. [2015] [105] employed the model of Goodman et al. [2008] [34] to investigate the optimal setup for delivering NPs charged by therapeutic drug and binding ligands. They solved for blood flow in the tumor vasculature and used the two pore model to calculate the NP extravasation flux. They modeled the interstitial flow using Darcy's law. They studied the dynamics of NP interaction with tumor cells and the effect of the therapeutic drug release. Furthermore, they introduced a novel multistage drug delivery system. In this proposed technique they simulated delivery of 20 nm NPs which release 5 nm NPs charged by the therapeutic drug and binding ligands. They concluded that the multistage technique enhances the drug delivery provided the NPs are sufficiently small with high affinity and high drug release rate.

Tang et al. [2014] [108] extended the model of Goodman et al. [2008] [34] by assuming that NP internalization into tumor cells is reversible. They studied *in vivo* the influence of NP size on the NP biodistribution and penetration depth into the tumor. They concluded from the mathematical model and from experimental data that 50 nm NPs give the optimal NP accumulation in the tumor and NP internalization rate, compared to 20 and 200 nm NPs.

Groh et al. [2014] [38] introduced three mathematical models for tumor cord geometry using different length scales and compared their results to investigate the influence of NP binding affinity on the NP penetration depth into the tumor. In the first model (multidimensional cell-center 2D model) they considered every cell center in the tumor as a computational node. In particular, every cell in the model is represented by a position, a cell radius, a NP binding rate and available cell receptor concentration. In the second model (radially symmetric compartment model) they partitioned the tumor into a group of spherical shells surrounding the cylindrical vessel at the tumor center. They assumed that the drug transport is proportional to the interface area and the concentration gradient across the interface area. So, the NP concentration can be modeled via a system of ODEs which represent conversation of mass. In the third model (radially symmetric model) they modeled the tumor as a continuous and homogeneous spherical medium. They ignored NP transport via advection across the tumor tissue. Furthermore, they considered that the NP extravasation from the blood vessel is proportional to the drug concentration gradient across the vessel wall. They used a common NP binding model with all three NP transport models with three types of NPs: extracellular NPs, intracellular free NPs and intracellular bound NPs. So, they considered that the NP binding happens within the cell (this is in contrast with our model in Chapter 3 where we assumed that NPs bind to the cell surface). They concluded from their study that the continuum and the compartment models give approximately the same concentration profiles, while the cell-center model gives slightly higher concentration predictions across the tumor.

Ying et al. [2013] [121] reviewed different mathematical models to mimic the NP-cell interaction and the NP transport across the tumor interstitium. They also investigated different models for determining NP diffusion coefficient in the tissue and for evaluating the concentration of the available binding sites. They also discussed some mathematical compartment (lumped parameter) models that can predict and analyze the kinetics of NP accumulation in the tumor and the NP biodistribution in the body. For instance, the blood circulatory system can be considered as a compartment and the tumor can be represented by another compartment. Then, the NP delivery to the tumor can be modeled by a system of two ODEs. Another example, a more complicated (three) compartment model, incorporates NP concentration in the blood stream (the first compartment) using the exponential decay model (Eq. 2.141), the NP concentration in the interstitium (the

second compartment) and NP internalization by tumor cells (the third compartment). This three compartment model consists of three ODEs which represent the change in NP concentration in each compartment. We use this idea in chapter 3 to model three different states GNRs: free GNRs in the interstitium, bound GNRs to tumor cells and internalized GNRs within tumor cells. More complicated compartment models can incorporate simulating the pharmacokinetics for delivering NPs to tumors *in vivo*. These compartment models can help in finding the optimal design of NPs to maximize the efficiency of the NP delivery process and minimize their toxicity to the healthy tissue.

1.6.7 Thesis Outline

In this thesis we investigate photothermal therapy which comprises two steps: firstly delivering GNRs to a tumor (drug delivery problem) and secondly irradiating the tumor by laser (heat transport problem) which result in tumor damage (cell injury problem). Herein we model the whole process in one spatial dimension at the macroscale. From this we explore the optimal modeling setup for the maximal damage in the tumor and minimal damage in the surrounding tissue.

First of all, in chapter 2 we investigate fluid and solute transport in a blood vessel segment surrounded by tissue. In this chapter we model blood flow (in the vessel), interstitial fluid flow and GNR transport (in the vessel, across the vessel wall and across the tissue) using the principles of fluid mechanics. We apply asymptotic analysis to find analytical solutions for blood velocity in the vessel and the interstitial fluid velocity across the vessel wall and the tissue. The GNR concentration in the vessel and tissue are solved numerically. We then validate the two pore model approximation (see Sec. 2.7) to estimate the GNR extravasation into tissue instead of solving the full GNR transport equation in the vessel.

In chapter 3 we study the problem of GNR delivery to spherical tumors surrounded by healthy tissue at the macroscale. We use the two pore model approximation to estimate the GNR flux into tissue and investigate the GNR profile across the tumor and the surrounding tissue in the presence or absence of binding ligands. Furthermore, we consider GNR administration by either intravenous or intratumoral injection. We investigate the optimal setup which can result in a maximal homogeneous GNR concentration across the tumor and a minimal concentration in the surrounding tissue.

In chapter 4 we model the laser irradiation of a spherical tumor surrounded by healthy tissue which have both been targeted with GNRs (modeled in chapter 3) using a modified energy equation (Pennes' bioheat equation). The GNR distribution across the tumor and the healthy tissue (which was estimated in chapter 3) is dependent on time and the radial direction. We investigate the temperature elevation due to laser irradiation, and estimate the tumor and tissue damage using the Arrhenius model (Sec. 4.3).

Chapter 2

GNR Extravasation From a Single Blood Vessel

Delivering large dose fraction of anticancer (or NPs) to tumors *in vivo* is challenging [52]. This is because drug molecules encounter barriers before interacting with the tumor cells, for example: molecule distribution in the vasculature, extravasation across the vessel wall, transport through the interstitium and interacting with cell surface [51]. Therefore, estimating the solute extravasation from tumor vasculature is a key step in drug delivery modeling.

There are different mathematical expressions for solute extravasation flux [51] which were used extensively in drug delivery studies at the macroscale in the literature [10, 97]. These mathematical expressions need to be tested at the microscale.

Shipley and Chapman [2010] [99] developed a model at the microscale for fluid and solute transport through tumor vasculature and the interstitial space. They used the multiple scales method to derive the fluid and solute transport equation at the macroscale. Although they did not solve the equations, their model can be used to simulate blood perfusion and drug transport in wide range of tissue.

Shipley et. al. [2010] [98] simulated biodegradable hollow fiber membrane bioreactors. They applied lubrication theory to develop analytical solutions of the fluid transport problem. Griffiths et al. [2013] [37] developed a mathematical model for fluid and solute transport through a tube surrounded by thin porous walls. They applied Taylor dispersion to find mathematical solutions for both the fluid and solute transport equations. In the light of Griffiths et al. [2013] [37] and Shipley et. al. [2010] [98] models we develop a mathematical model for fluid and solute transport through a single vessel with a thin wall surrounded by tissue.

We consider the problem of GNRs extravasated from blood flow within a single blood vessel of length $\hat{L}$. We assume that GNRs extravasate across the vessel wall into the surrounding tissue via diffusion and advection. The extravasation of the solute depends on

the osmotic pressure which depends on the transmural concentration, however, we neglect the effect of osmosis to decouple the fluid transport problem and the solute transport problem in order to find an analytical solution for the fluid velocity in the vessel, wall and surrounding tissue. We assume that the vessel wall is an annulus with inner and outer radii $\hat{R}_1$ and $\hat{R}_2$, respectively. Similarly, we assume the surrounding tissue is also an annulus with inner and outer radii $\hat{R}_2$ and $\hat{R}_3$, respectively, as shown in Fig. 2.1.

2.1 The Model

In this model we assume that the thickness of the vessel wall is very small compared to the vessel radius. Furthermore, we assume that the radius of the vessel (and hence the vessel wall thickness) is small compared to the vessel length. Hence, we introduce the following small parameters

$$\frac{\hat{R}_1}{\hat{L}} = \epsilon \ll 1, \quad \frac{\hat{R}_2 - \hat{R}_1}{\hat{R}_1} = \delta \ll 1 \left[\Leftrightarrow \frac{\hat{R}_2 - \hat{R}_1}{\hat{L}} = \epsilon\delta \right] \text{ and } \frac{\hat{R}_3 - \hat{R}_2}{\hat{L}} = \lambda \equiv m\epsilon$$

In the analysis below we exploit the smallness of ϵ and δ to approximate the mathematical model using asymptotic analysis. Furthermore, we assume that the outer region of tissue has a thickness comparable to the radius of the vessel to study the variation in the solute concentration within a small boundary layer in the tissue next to the vessel, so we define m as an integer of $O(1)$. This approximation is valid in tumors with dense vasculatures which comprise abnormal chaotic disorganised blood vessels [80]. However, the heterogeneity of tumor vasculature makes some regions in the tumor without blood vessels or with few blood vessels with relatively large interstitium between the vessels ($m \gg 1$). The scales of the vessel and the vessel wall were chosen to be similar to the scales introduced by Griffiths et al. [2013] [37] and the scale of tissue region is chosen to construct a dominant balance. Griffiths et al. [2013] [37] studied a problem of a hollow-fiber membrane bioreactor (mimicking a segment of vessel surrounded by tissue), where nutrient was delivered to sustain an annulus of cultured cells surrounding the tube. In this chapter we extend the problem of Griffiths et al. [2013] [37] to incorporate a vessel wall to investigate the solute flux across the wall. The values of these parameters in the capillaries are $\hat{R}_1 = 3$ μm, $\hat{R}_2 - \hat{R}_1 = 1$ μm, $\hat{L} = 600$ μm [16]. Thus, we have $\epsilon = 5 \times 10^{-3}$, $\delta = 0.333$ and $\epsilon\delta = 1.7 \times 10^{-3}$.

2.1.1 The Fluid Transport Model at the Micro-scale

The blood velocity is typically very slow in the micro vasculature, so we model the blood flow in the vessel using the axisymmetric Stokes equations for a Newtonian fluid [1,84]. We

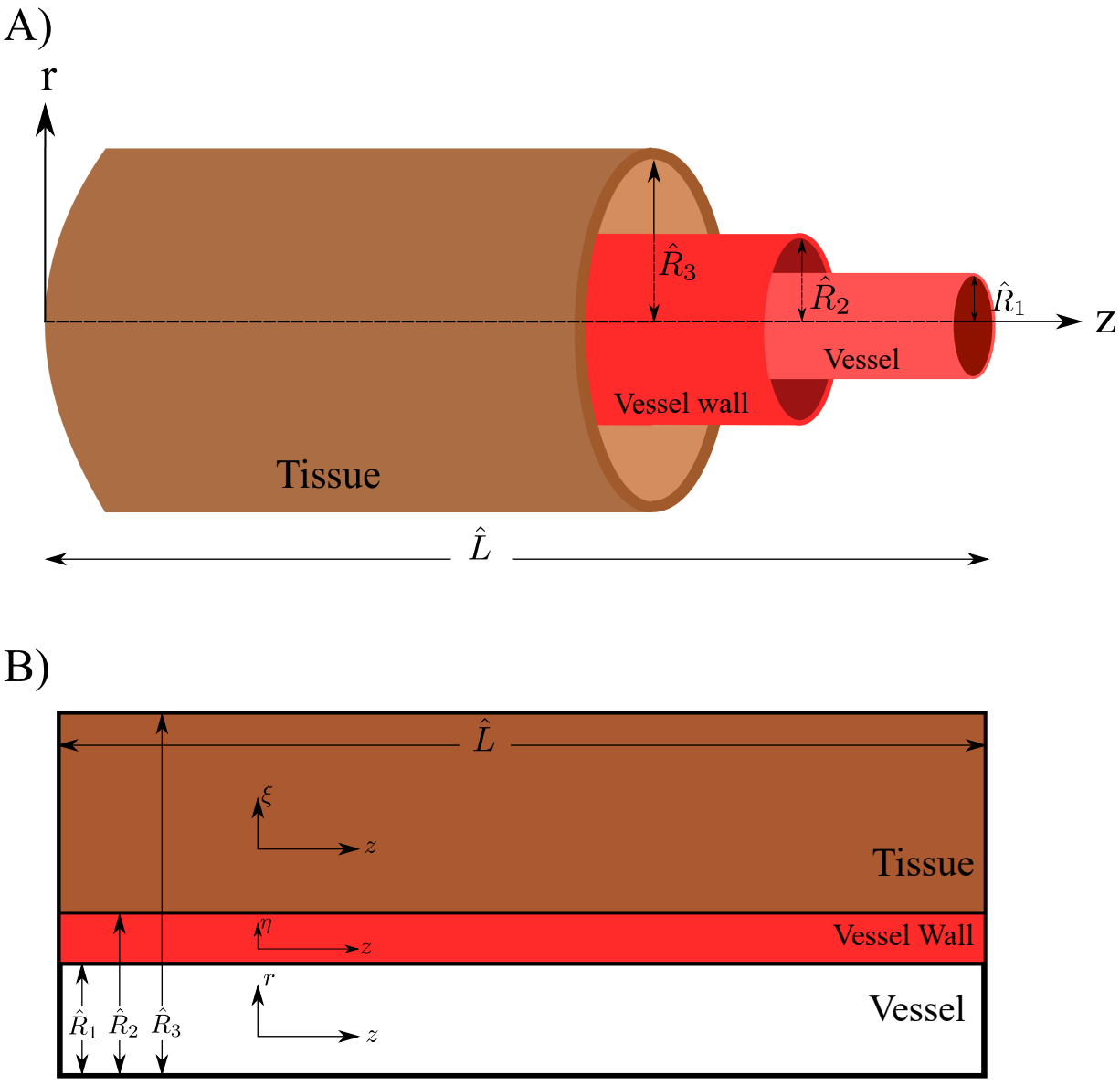

Figure 2.1: Microscale domain of a single vessel and the surrounding tissue. A)Three dimensional structure of the domain . B)Radial cross-section of the domain.

note that in reality the blood flow in the microvasculature is a highly discrete process, with relatively large red blood cells squeezing along the vessels. For simplicity we assume in this study that the blood is incompressible and Newtonian fluid with a constant viscosity $\hat{\mu}_b$.

In the vessel we consider the radial coordinate $\hat{r}$ with origin along the vessel axis and equal to $\hat{R}_1$ at the vessel/wall interface. The axial coordinate in this problem is denoted $\hat{z}$ which is zero at the vessel inlet and equal to $\hat{L}$ at the vessel outlet (see Fig. 2.1). We use the symbol $\hat{u}_i$ for the radial velocity, the symbol $\hat{w}_i$ for the axial velocity and the symbol $\hat{P}_i$ for fluid pressure, where $i = 1, 2, 3$. Note that all variables are assumed axisymmetric throughout. We use the subscript 1 to refer to the variables in the blood vessel itself, the

subscript 2 for the variables in the vessel wall and the subscript 3 for the variables in the tissue.

Region 1: Within the Vessel

Across the capillary itself and the capillary wall there is neither a source nor sink of blood. Assuming the blood is incompressible we write the blood continuity equation in the vessel in the form ($0 \leq \hat{r} \leq \hat{R}_1$, $0 \leq \hat{z} \leq \hat{L}$),

$$\frac{1}{\hat{r}}\frac{\partial}{\partial \hat{r}}(\hat{r}\hat{u}_1) + \frac{\partial \hat{w}_1}{\partial \hat{z}} = 0. \tag{2.1}$$

Furthermore, we ignore the effect of body forces and assume that inertial effects are insignificant. Therefore, the $\hat{r}$-momentum equation in the vessel is given by ($0 \leq \hat{r} \leq \hat{R}_1$, $0 \leq \hat{z} \leq \hat{L}$),

$$\frac{\partial \hat{P}_1}{\partial \hat{r}} = \hat{\mu}_b \left(\frac{1}{\hat{r}}\frac{\partial}{\partial \hat{r}}\left(\hat{r}\frac{\partial \hat{u}_1}{\partial \hat{r}} \right) + \frac{\partial^2 \hat{u}_1}{\partial \hat{z}^2} - \frac{\hat{u}_1}{\hat{r}^2} \right). \tag{2.2}$$

The corresponding $\hat{z}$-momentum equation in the vessel is given by ($0 \leq \hat{r} \leq \hat{R}_1$, $0 \leq \hat{z} \leq \hat{L}$),

$$\frac{\partial \hat{P}_1}{\partial \hat{z}} = \hat{\mu}_b \left(\frac{1}{\hat{r}}\frac{\partial}{\partial \hat{r}}\left(\hat{r}\frac{\partial \hat{w}_1}{\partial \hat{r}} \right) + \frac{\partial^2 \hat{w}_1}{\partial \hat{z}^2} \right). \tag{2.3}$$

Region 2: Within the Vessel Wall

We consider the vessel wall as a thin porous medium with uniform permeability $\hat{k}_2$ and assume the flow in the vessel wall can be described using Darcy's law (a similar idea was used by Griffiths et al. [2013] [37]).

The continuity equation for water/plasma crossing the vessel wall is ($\hat{R}_1 \leq \hat{r} \leq \hat{R}_2$, $0 \leq \hat{z} \leq \hat{L}$)

$$\frac{1}{\hat{r}}\frac{\partial}{\partial \hat{r}}(\hat{r}\hat{u}_2) + \frac{\partial \hat{w}_2}{\partial \hat{z}} = 0. \tag{2.4}$$

According to Darcy's law, the fluid radial velocity across the vessel wall is driven by the pressure gradient in the radial direction. Hence, we write the $\hat{r}$-momentum equation in the vessel wall in the form ($\hat{R}_1 \leq \hat{r} \leq \hat{R}_2$),

$$\hat{u}_2 = -\frac{\hat{k}_2}{\hat{\mu}}\frac{\partial \hat{P}_2}{\partial \hat{r}}, \tag{2.5}$$

where $\hat{\mu}$ is the viscosity of the transvascular fluid in the vessel wall. Similarly, the fluid

axial velocity along the vessel wall is driven by the pressure gradient in the axial direction $\hat{z}$ and so the $\hat{z}$-momentum equation in the vessel wall is given by ($0 \leq \hat{z} \leq \hat{L}$),

$$\hat{w}_2 = -\frac{\hat{k}_2}{\hat{\mu}} \frac{\partial \hat{P}_2}{\partial \hat{z}}. \tag{2.6}$$

Region 3: Within the Tissue

In the same way, we consider Darcy's model for the fluid flow across the outer tissue annulus which is considered as a porous medium with a constant permeability $\hat{k}_3$. In the tissue, however, there are lymphatic vessels at pressure $\hat{P}_l$ which are modeled as a continuous sink across the tissue. Hence, the continuity equation in the tissue is different to the other regions and takes the form ($\hat{R}_2 \leq \hat{r} \leq \hat{R}_3$, $0 \leq \hat{z} \leq \hat{L}$),

$$\frac{1}{\hat{r}} \frac{\partial}{\partial \hat{r}} (\hat{r} \hat{u}_3) + \frac{\partial \hat{w}_3}{\partial \hat{z}} = -\frac{\hat{Q}_l}{\hat{V}_{tiss}}, \tag{2.7}$$

where $\hat{Q}_l$ is the (constant) fluid flux into the lymphatics normalized by the volume of the tissue $\hat{V}_{tiss}$. The lymphatic flux $\hat{Q}_l$ is assumed to be proportional to the pressure difference between the tissue ($\hat{P}_3$) and the lymph vessels ($\hat{P}_l$) [8]

$$\frac{\hat{Q}_l}{\hat{V}_{tiss}} = \frac{\hat{L}_{pl} \hat{S}_l}{\hat{V}_{tiss}} (\hat{P}_3 - \hat{P}_l) \equiv \hat{B}(\hat{P}_3 - \hat{P}_l), \tag{2.8}$$

where $\hat{B}$ is a dimensional constant, $\hat{S}_l$ is the lymphatic surface area, $\hat{L}_{pl}$ is the hydraulic conductivity of the lymphatic wall and $\hat{V}_{tiss}$ is the volume of the tissue surrounding the vessel. Thus, we can write equation (2.7) in the form ($\hat{R}_2 \leq \hat{r} \leq \hat{R}_3$, $0 \leq \hat{z} \leq \hat{L}$)

$$\frac{1}{\hat{r}} \frac{\partial}{\partial \hat{r}} (\hat{r} \hat{u}_3) + \frac{\partial \hat{w}_3}{\partial \hat{z}} = -\hat{B}(\hat{P}_3 - \hat{P}_l). \tag{2.9}$$

According to Darcy's law the $\hat{r}$-momentum equation in the tissue is ($\hat{R}_2 \leq \hat{r} \leq \hat{R}_3$)

$$\hat{u}_3 = -\frac{\hat{k}_3}{\hat{\mu}} \frac{\partial \hat{P}_3}{\partial \hat{r}}. \tag{2.10}$$

Note that we assume the viscosity of the interstitial fluid in the tissue equals the viscosity of the transvascular fluid in the vessel wall (denoted $\hat{\mu}$). The $\hat{z}$-momentum equation in the tissue ($0 \leq \hat{z} \leq \hat{L}$) takes the form

$$\hat{w}_3 = -\frac{\hat{k}_3}{\hat{\mu}} \frac{\partial \hat{P}_3}{\partial \hat{z}}. \tag{2.11}$$

Boundary Conditions

We apply the continuity of fluid flux and pressure at the vessel/vessel wall interface and at the tissue/wall interface. In addition, we use the boundary condition developed by Beavers and Joseph [1967] [11] for the tangential velocity of a free Newtonian fluid flowing past a porous membrane. Beavers and Joseph [1967] [11] concluded from their experiments that there is a boundary layer developed across the porous membrane which must prevent the tangential velocity reaching zero at the membrane surface (as would be expected from the no-slip condition). They showed experimentally that this can be modeled at the membrane surface as a slip velocity proportional to the tangential velocity gradient in the normal direction. So, we write the following boundary conditions in the form

$$\hat{u}_1 = \hat{u}_2, \quad \hat{P}_1 = \hat{P}_2 \quad \text{and} \quad \frac{\partial \hat{w}_1}{\partial \hat{r}} = -\frac{\alpha_2}{\sqrt{\hat{k}_2}}(\hat{w}_1 - \hat{w}_2), \quad (\hat{r} = \hat{R}_1), \tag{2.12}$$

where α_2 is a constant dependent on the average pore diameter of the vessel wall. The Beavers-Joseph boundary condition approaches the no-slip condition ($\hat{w}_1 = \hat{w}_2$) when $\alpha_2 \to \infty$. However, $\alpha_2 = 0$ is simply a no tangential stress condition.

Similarly, at the vessel wall/tissue interface the boundary conditions take the form

$$\hat{u}_2 = \hat{u}_3, \quad \hat{P}_2 = \hat{P}_3 \quad \text{and } \hat{w}_2 = \hat{w}_3, \quad (\hat{r} = \hat{R}_2), \tag{2.13}$$

These conditions are coupled to boundary conditions on the outer edge of the domain in the form

$$\frac{\partial \hat{P}_3}{\partial \hat{r}} = 0, \quad (\hat{r} = \hat{R}_3), \tag{2.14}$$

here we considered no radial fluid flux at the tissue edge which is relatively far away from the vessel wall. At the vessel inlet we prescribe the mean velocity $\hat{W}$ (which is the typical velocity scale in the vessel chosen based on the inlet flux of the vessel) in the form

$$\hat{Q}_{in} \equiv \hat{W}\pi\hat{R}_1^2 = 2\pi \int_0^{\hat{R}_1} \hat{r}\hat{w}_1(\hat{r}, 0)d\hat{r}, \quad (\hat{z} = 0). \tag{2.15}$$

At the vessel outlet we prescribe the blood pressure in the form

$$\hat{P}_1(\hat{r}, \hat{L}) = \hat{P}_0, \qquad (\hat{z} = \hat{L}). \tag{2.16}$$

Note that in principle the outlet pressure $\hat{P}_0$ and the lymphatic pressure $\hat{P}_l$ could be different from zero, but we choose $\hat{P}_0 = \hat{P}_l = 0$ without loose of generality.

2.2 The Solute Transport Model at the Micro-scale

In the vessel, across the vessel wall and in the surrounding tissue we assume that GNRs in the vasculature can transport via diffusion and advection in the both of radial and axial directions. Therefore, we model the GNR concentration in the vessel (denoted C_1, $0 \leq \hat{r} \leq \hat{R}_1$), in the vessel wall (denoted C_2, $\hat{R}_1 \leq \hat{r} \leq \hat{R}_2$) and in the surrounding tissue (denoted C_3, $\hat{R}_2 \leq \hat{r} \leq \hat{R}_3$) using the transport equations [68] in the form ($0 \leq \hat{z} \leq \hat{L}$),

$$\frac{\partial \hat{C}_1}{\partial \hat{t}} + \frac{1}{\hat{r}}\frac{\partial}{\partial \hat{r}}(\hat{r}\hat{u}_1\hat{C}_1) + \frac{\partial}{\partial \hat{z}}(\hat{w}_1\hat{C}_1) = \frac{\hat{D}_1}{\hat{r}}\frac{\partial}{\partial \hat{r}}\left(\hat{r}\frac{\partial \hat{C}_1}{\partial \hat{r}}\right) + \hat{D}_1\frac{\partial^2 \hat{C}_1}{\partial \hat{z}^2}, \tag{2.17}$$

$$\frac{\partial \hat{C}_2}{\partial \hat{t}} + \frac{1}{\hat{r}}\frac{\partial}{\partial \hat{r}}(\hat{r}\hat{u}_2\hat{C}_2) + \frac{\partial}{\partial \hat{z}}(\hat{w}_2\hat{C}_2) = \frac{\hat{D}_2}{\hat{r}}\frac{\partial}{\partial \hat{r}}\left(\hat{r}\frac{\partial \hat{C}_2}{\partial \hat{r}}\right) + \hat{D}_2\frac{\partial^2 \hat{C}_2}{\partial \hat{z}^2}, \tag{2.18}$$

$$\frac{\partial \hat{C}_3}{\partial \hat{t}} + \frac{1}{\hat{r}}\frac{\partial}{\partial \hat{r}}(\hat{r}\hat{u}_3\hat{C}_3) + \frac{\partial}{\partial \hat{z}}(\hat{w}_3\hat{C}_3) = \frac{\hat{D}_3}{\hat{r}}\frac{\partial}{\partial \hat{r}}\left(\hat{r}\frac{\partial \hat{C}_3}{\partial \hat{r}}\right) + \hat{D}_3\frac{\partial^2 \hat{C}_3}{\partial \hat{z}^2}, \tag{2.19}$$

we substitute from the continuity equations (2.1, 2.4 and 2.9) into the transport equations (2.17, 2.18 and 2.19) we get

$$\frac{\partial \hat{C}_1}{\partial \hat{t}} + \hat{u}_1\frac{\partial \hat{C}_1}{\partial \hat{r}} + \hat{w}_1\frac{\partial \hat{C}_1}{\partial \hat{z}} = \frac{\hat{D}_1}{\hat{r}}\frac{\partial}{\partial \hat{r}}\left(\hat{r}\frac{\partial \hat{C}_1}{\partial \hat{r}}\right) + \hat{D}_1\frac{\partial^2 \hat{C}_1}{\partial \hat{z}^2}, \tag{2.20}$$

$$\frac{\partial \hat{C}_2}{\partial \hat{t}} + \hat{u}_2\frac{\partial \hat{C}_2}{\partial \hat{r}} + \hat{w}_2\frac{\partial \hat{C}_2}{\partial \hat{z}} = \frac{\hat{D}_2}{\hat{r}}\frac{\partial}{\partial \hat{r}}\left(\hat{r}\frac{\partial \hat{C}_2}{\partial \hat{r}}\right) + \hat{D}_2\frac{\partial^2 \hat{C}_2}{\partial \hat{z}^2}, \tag{2.21}$$

$$\frac{\partial \hat{C}_3}{\partial \hat{t}} + \hat{u}_3\frac{\partial \hat{C}_3}{\partial \hat{r}} + \hat{w}_3\frac{\partial \hat{C}_3}{\partial \hat{z}} = \frac{\hat{D}_3}{\hat{r}}\frac{\partial}{\partial \hat{r}}\left(\hat{r}\frac{\partial \hat{C}_3}{\partial \hat{r}}\right) + \hat{D}_3\frac{\partial^2 \hat{C}_3}{\partial \hat{z}^2} - \hat{B}(\hat{P}_3 - \hat{P}_0)\hat{C}_3, \tag{2.22}$$

where $\hat{D}_1$, $\hat{D}_2$ and $\hat{D}_3$ are the diffusion coefficients in the vessel, in the vessel wall and in the tissue, respectively. Note the final term in (2.22) arises due to the logs of GNRs into the lymphatic system.

Note that these advection-diffusion equations are defined from the principle of mass balance, assuming the flux has both diffusion and advection components in the form

$$\frac{\partial \hat{C}_j}{\partial \hat{t}} = -\hat{\nabla} \cdot \hat{\mathbf{J}}_j, \qquad (j = 1, 2, 3) \tag{2.23}$$

where

$$\hat{\mathbf{J}}_j = \hat{J}_{jr}\mathbf{e_r} + \hat{J}_{jz}\mathbf{e_z}, \qquad (j = 1, 2, 3) \tag{2.24}$$

where

$$\hat{J}_{jr} = \hat{u}_j \hat{C}_j - \hat{D}_j \frac{\partial \hat{C}_j}{\partial \hat{r}}, \qquad (j = 1, 2, 3), \tag{2.25}$$

$$\hat{J}_{jz} = \hat{w}_j \hat{C}_j - \hat{D}_j \frac{\partial \hat{C}_j}{\partial \hat{z}} \qquad (j = 1, 2, 3). \tag{2.26}$$

where $\hat{J}_r$ and $\hat{J}_z$ are the radial and axial flux components, respectively.

Boundary Conditions

We impose continuity of total solute flux and concentration at the vessel/vessel-wall interface ($\hat{r} = \hat{R}_1$) and at the vessel-wall/tissue interface ($\hat{r} = \hat{R}_2$). We do not prescribe this flux because we include the vessel wall in the model, so the flux will be computed from the model. Furthermore, we assume zero solute flux at the tissue edge (at $\hat{r} = \hat{R}_3$). So, we write the following boundary conditions

$$\hat{C}_1 = \hat{C}_2 \text{ and } \hat{J}_{1r} \equiv \hat{u}_1 \hat{C}_1 - \hat{D}_1 \frac{\partial \hat{C}_1}{\partial \hat{r}} = \hat{u}_2 \hat{C}_2 - \hat{D}_2 \frac{\partial \hat{C}_2}{\partial \hat{r}} \equiv \hat{J}_{2r}, \qquad (\hat{r} = \hat{R}_1), \tag{2.27}$$

$$\hat{C}_2 = \hat{C}_3 \text{ and } \hat{J}_{2r} \equiv \hat{u}_2 \hat{C}_2 - \hat{D}_2 \frac{\partial \hat{C}_2}{\partial \hat{r}} = \hat{u}_3 \hat{C}_3 - \hat{D}_3 \frac{\partial \hat{C}_3}{\partial \hat{r}} \equiv \hat{J}_{3r}, \qquad (\hat{r} = \hat{R}_2), \tag{2.28}$$

$$\hat{J}_{3r} \equiv \hat{u}_3 \hat{C}_3 - \hat{D}_3 \frac{\partial \hat{C}_3}{\partial \hat{r}} = 0, \qquad (\hat{r} = \hat{R}_3). \tag{2.29}$$

2.3 Dimensionless Transformations

We take advantage of the small aspect ratio between the vessel radius and the vessel length to apply the lubrication approximation to reduce the fluid flow and the solute transport equations. Thus, we apply the following dimensionless transformations to the properties of the vessel

$$\begin{aligned} &\hat{t} = \frac{\hat{L}}{\hat{W}} t, \quad \hat{w}_1 = \hat{W} w_1, \quad \hat{u}_1 = \epsilon \hat{W} u_1, \quad \hat{r} = \epsilon \hat{L} r, \quad \hat{z} = \hat{L} z, \quad \hat{P}_1 = \hat{P}_0 + \hat{P} P_1, \\ &\hat{C}_1 = \hat{C}_0 C_1, \quad \hat{J}_{1r} = \hat{W} \hat{C}_0 J_{1r}, \quad \hat{J}_{1z} = \hat{W} \hat{C}_0 J_{1z}. \end{aligned} \tag{2.30}$$

where $\hat{C}_0$ is the initial vascular GNR concentration. Similar to Griffiths et al. [2013] [37], in the vessel wall we define a dimensionless coordinate η (scaled so that $0 \leq \eta \leq 1$ across the wall) in the radial direction, in addition to the following variable transformations

$$\begin{aligned} &\hat{w}_2 = \epsilon \hat{W} w_2, \quad \hat{u}_2 = \epsilon \hat{W} u_2, \quad \hat{r} = \hat{R}_1 + \delta \hat{R}_1 \eta, \quad \hat{P}_2 = \hat{P}_0 + \hat{P} P_2, \\ &\hat{C}_2 = \hat{C}_0 C_2, \quad \hat{J}_{2r} = \hat{W} \hat{C}_0 J_{2r}, \quad \hat{J}_{2z} = \hat{W} \hat{C}_0 J_{2z}, \quad \hat{D}_2 = \hat{D}_1 D_2, \quad \hat{\mu} = \hat{\mu}_b \mu. \end{aligned} \tag{2.31}$$

Similarly, in the tissue domain we define a new dimensionless coordinate ξ (scaled so that $0 \leq \xi \leq 1$ across the tissue domain) in the radial direction, in addition to the following variable transformations

$$\hat{w}_3 = \epsilon \hat{W} w_3, \quad \hat{u}_3 = \epsilon \hat{W} u_3, \quad \hat{r} = \hat{R}_2 + \lambda \hat{L} \xi, \quad \hat{P}_3 = \hat{P}_0 + \hat{P} P_3,$$
$$\hat{C}_3 = \hat{C}_0 C_3, \quad \hat{B} = \frac{\epsilon^2}{\hat{\mu}} B, \quad \hat{D}_3 = \hat{D}_1 D_3. \tag{2.32}$$

Note that we scale both $\hat{u}_3$ and $\hat{w}_3$ to be $O(\epsilon)$ to satisfy the continuity of fluid velocity at the tissue/vessel-wall interface. Furthermore, the constant $\hat{B}$ must be $O(\epsilon^2)$ to balance the gradient of $\hat{u}_3$ in the continuity equation (2.9). Finally, we select the viscus pressure scale based on flow along the vessel $\hat{P} = \hat{\mu}_b \hat{W}/(\epsilon^2 \hat{L})$.

Applying the transformations (2.30)-(2.32) into the equations (2.1)-(2.6), (2.9)-(2.11) and (2.20)-(2.22); and the boundary conditions (C.1)-(2.16) and (2.27)-(2.29) we get the following dimensionless equations:

The dimensionless governing equations in the vessel are ($0 \leq r \leq 1$, $0 \leq z \leq 1$)

$$\frac{\partial w_1}{\partial z} + \frac{1}{r}\frac{\partial}{\partial r}(r u_1) = 0, \tag{2.33}$$
$$\epsilon^2 \left(\epsilon^2 \frac{\partial^2 u_1}{\partial z^2} + \frac{1}{r}\frac{\partial}{\partial r}\left(r \frac{\partial u_1}{\partial r} \right) - \frac{u_1}{r^2} \right) = \frac{\partial P_1}{\partial r}, \tag{2.34}$$
$$\epsilon^2 \frac{\partial^2 w_1}{\partial z^2} + \frac{1}{r}\frac{\partial}{\partial r}\left(r \frac{\partial w_1}{\partial r} \right) = \frac{\partial P_1}{\partial z}, \tag{2.35}$$
$$\epsilon^2 \left(\frac{\partial C_1}{\partial t} + u_1 \frac{\partial C_1}{\partial r} + w_1 \frac{\partial C_1}{\partial z} \right) = \frac{1}{Pe} \left(\frac{1}{r}\frac{\partial}{\partial r}\left(r \frac{\partial C_1}{\partial r} \right) + \epsilon^2 \frac{\partial^2 C_1}{\partial z^2} \right), \tag{2.36}$$

where $Pe = \hat{L}\hat{W}/\hat{D}_1$ is the dimensionless Péclet number (the ratio of advection rate to diffusion rate of GNRs) in the vessel. The dimensionless governing equations in the vessel wall are ($0 \leq \eta \leq 1$, $0 \leq z \leq 1$)

$$\delta u_2 + \epsilon\delta(1 + \delta\eta)\frac{\partial w_2}{\partial z} + (1 + \delta\eta)\frac{\partial u_2}{\partial \eta} = 0, \tag{2.37}$$

$$u_2 = -\frac{K_2}{\mu}\frac{\partial P_2}{\partial \eta}, \tag{2.38}$$

$$w_2 = -\delta\epsilon\frac{K_2}{\mu}\frac{\partial P_2}{\partial z}, \tag{2.39}$$

$$\epsilon^2\delta(1 + \delta\eta)\left(\delta\frac{\partial C_2}{\partial t} + u_2\frac{\partial C_2}{\partial \eta} + \epsilon\delta w_2\frac{\partial C_2}{\partial z} \right) = \frac{D_2}{Pe}\left((\epsilon\delta)^2(1 + \delta\eta)\frac{\partial^2 C_2}{\partial z^2} + \frac{\partial^2 C_2}{\partial \eta^2} + \delta\frac{\partial}{\partial \eta}\left(\eta\frac{\partial C_2}{\partial \eta} \right) \right), \tag{2.40}$$

In Eq. (2.38) we chose $\hat{K_2} = \delta\epsilon^4\hat{L}^2K_2$ so that we balance the radial velocity $\hat{u}$ with the pressure gradient. The dimensionless governing equations in the tissue are ($0 \leq \xi \leq 1$, $0 \leq z \leq 1$)

$$mu_3 + (1+\delta+m\xi)\left(\frac{\partial u_3}{\partial \xi} + m\left(\epsilon\frac{\partial w_3}{\partial z} + BP_3\right)\right) = 0, \tag{2.41}$$

$$u_3 = -\frac{K_3}{\mu}\frac{\partial P_3}{\partial \xi}, \tag{2.42}$$

$$w_3 = -m\epsilon\frac{K_3}{\mu}\frac{\partial P_3}{\partial z}, \tag{2.43}$$

$$\begin{aligned}&\epsilon^2(1+\delta+m\xi)\left(mBC_3P_3 + m\frac{\partial C_3}{\partial t} + u_3\frac{\partial C_3}{\partial \xi} + m\epsilon w_3\frac{\partial C_3}{\partial z}\right)\\ &= \frac{D_3}{mPe}\left(m^2\epsilon^2(1+\delta+m\xi)\frac{\partial^2 C_3}{\partial z^2} + (1+\delta)\frac{\partial^2 C_3}{\partial \xi^2} + m\frac{\partial}{\partial \xi}\left(\xi\frac{\partial C_3}{\partial \xi}\right)\right),\end{aligned} \tag{2.44}$$

In Eq. (2.42) we chose $\hat{K_3} = m\epsilon^4\hat{L}^2K_3$ so that we balance the radial velocity u_3 with the pressure gradient.

The dimensionless boundary conditions take the form

$$\begin{aligned}&u_1 = u_2, \quad P_1 = P_2, \ \frac{\partial w_1}{\partial r} = A_2(\epsilon w_2 - w_1), \ C_1 = C_2,\\ &\delta\epsilon^2(u_1C_1 - u_2C_2) = \frac{1}{Pe}\left(\delta\frac{\partial C_1}{\partial r} - D_2\frac{\partial C_2}{\partial \eta}\right), \qquad (r=1, \ \eta = 0)\end{aligned} \tag{2.45}$$

$$\begin{aligned}&u_2 = u_3, \quad P_2 = P_3, w_2 = w_3, \ C_2 = C_3,\\ &\delta\epsilon^2(u_2C_2 - u_3C_3) = \frac{1}{Pe}\left(\frac{\hat{D}_2}{\hat{D}_1}\frac{\partial C_2}{\partial \eta} - \frac{\delta D_3}{m}\frac{\partial C_3}{\partial \xi}\right), \qquad (\eta = 1, \ \xi = 0)\end{aligned} \tag{2.46}$$

$$\frac{\partial P_3}{\partial \xi} = 0, \ \epsilon^2 u_3C_3 = \frac{\hat{D}_3}{mPe\hat{D}_1}\frac{\partial C_3}{\partial \xi}, \qquad (\xi = 1), \tag{2.47}$$

where $A_2 = \epsilon\alpha_2\hat{L}/\sqrt{\hat{K_2}}$ is a measure for the slip at the vessel wall interface with the vessel. The dimensionless boundary conditions for the vessel at the inlet and outlet take the form

$$\int_0^1 rw_1 dr = \tfrac{1}{2}, \quad (z=0), \qquad\qquad P_1 = 0, \quad (z=1). \tag{2.48}$$

We need the transmural solute radial flux in Sec. 2.7, so we apply the transformations (2.31) at the Eqns. (2.25) and (2.26) we get the dimensionless radial and axial transmural

flux, respectively, in the form

$$J_{2r} = \epsilon u_2 C_2 - \frac{D}{\delta \epsilon Pe} \frac{\partial C_2}{\partial \eta}, \tag{2.49}$$

$$J_{2z} = \epsilon w_2 C_2 - \frac{D}{Pe} \frac{\partial C_2}{\partial z}. \tag{2.50}$$

Note that, for simplicity we assumed in this study that $\hat{\mu} = \hat{\mu}_b = 3 \times 10^{-5}$ mmHg-sec [20].

2.4 The Analytical Solutions for the Fluid Flow Problem

The governing equations for fluid and solute transport (2.33-2.44) subject to the boundary conditions (2.45-2.48) are nonlinear, coupled partial differential equations (PDEs) which are difficult to solve analytically. However, this system of equations can be simplified using asymptotic analysis.

In the vessel we write the system of PDEs (2.33-2.35) to leading order (neglecting terms of $O(\epsilon^2)$ and higher) as follows ($0 \leq r \leq 1$, $0 \leq z \leq 1$)

$$\frac{\partial w_1}{\partial z} + \frac{1}{r} \frac{\partial}{\partial r}(r u_1) = 0, \tag{2.51}$$

$$\frac{\partial P_1}{\partial r} = 0, \tag{2.52}$$

$$\frac{\partial P_1}{\partial z} = \frac{1}{r} \frac{\partial}{\partial r} \left(r \frac{\partial w_1}{\partial r} \right). \tag{2.53}$$

Similarly, in the vessel wall we write the leading order version of the PDEs (2.37-2.39) in the form ($0 \leq \eta \leq 1$, $0 \leq z \leq 1$)

$$\frac{\partial u_2}{\partial \eta} = 0, \tag{2.54}$$

$$u_2 = -\frac{K_2}{\mu} \frac{\partial P_2}{\partial \eta}, \tag{2.55}$$

$$w_2 = 0. \tag{2.56}$$

Note that in this system the flow is predominately through the wall i.e. flow along the wall is negligible at leading order.

In the same way, in the tissue we write the leading order equations of the PDEs (2.41-

2.43) in the form ($0 \leq \xi \leq 1$, $0 \leq z \leq 1$)

$$mu_3 + (1 + m\xi)\left(\frac{\partial u_3}{\partial \xi} + mBP_3\right) = 0, \tag{2.57}$$

$$u_3 = -\frac{K_3}{\mu}\frac{\partial P_3}{\partial \xi}, \tag{2.58}$$

$$w_3 = 0. \tag{2.59}$$

Finally, we write the boundary conditions (2.45-2.48) in the leading order in the form

$$u_1 = u_2, \quad P_1 = P_2, \ \frac{\partial w_1}{\partial r} = -A_2 w_1, \qquad (r = 1 \text{ and } \eta = 0). \tag{2.60}$$

$$u_2 = u_3, \quad P_2 = P_3, \quad \frac{\partial w_3}{\partial \xi} = A_3(w_2 - w_3), \qquad (\eta = 1 \text{ and } \xi = 0). \tag{2.61}$$

$$\frac{\partial P_3}{\partial \xi} = 0, \qquad (\xi = 1). \tag{2.62}$$

$$\int_0^1 r w_1 dr = \tfrac{1}{2}, \qquad (z = 0). \tag{2.63}$$

$$\frac{\partial P_1}{\partial z} = 0, \qquad (z = 1). \tag{2.64}$$

From Eqns. (2.51)-(2.53) we conclude that the blood pressure (in the leading order asymptotic approximation) is homogeneous in the radial direction and is a function of the axial coordinate z alone. Hence, Eqns. (2.51) and (2.53) along with the boundary conditions (2.60) can be solved analytically in the form

$$u_1 = \frac{r}{16A_2}(4 - (r^2 - 2)A_2)\frac{d^2 P_1}{d\eta^2}, \tag{2.65}$$

$$w_1 = \frac{1}{4A_2}((r^2 - 1)A_2 - 2)\frac{dP_1}{d\eta}, \tag{2.66}$$

where $P_1 = P_1(z)$ will be determined after solving the pressure in the vessel wall and the tissue and applying the internal boundary conditions between these three domains.

In the vessel wall the leading order equations (2.54) and (2.56) can be easily integrated with respect to η and by applying the boundary conditions (2.60) we get the following

closed form solutions

$$u_2 = \frac{4 + A_2}{16A_2}\frac{d^2P_1}{d\eta^2}, \tag{2.67}$$

$$w_2 = 0, \tag{2.68}$$

$$P_2 = P_1 - \frac{\eta(4 + A_2)\mu}{16A_2K_2}\frac{d^2P_1}{d\eta^2}. \tag{2.69}$$

In order to find an analytical solution for the pressure and velocity in the tissue (region 3) we substitute u_3 from Eqn. (2.58) into Eqn. (2.57) to obtain the following ODE (in two dimensions) for P_3 alone

$$(1 + m\xi)\frac{\partial^2 P_3}{\partial \xi^2} + m\frac{\partial P_3}{\partial \xi} - \frac{Bm\mu}{K_3}(1 + m\xi)P_3 = 0, \qquad (0 \le \xi \le 1). \tag{2.70}$$

This equation is a rescaled version of the modified Bessel differential equation. In order to find the general solution, we make a change of variable ($x = 1+m\xi$) to write this equation in the standard form of the zero order modified Bessel differential equation as follows

$$x^2\frac{\partial^2 \check{P}_3}{\partial x^2} + x\frac{\partial \check{P}_3}{\partial x} - \left(\sqrt{\frac{B\mu}{mK_3}}x\right)^2 \check{P}_3 = 0, \qquad (0 \le x \le 1). \tag{2.71}$$

The general solution to the zero order modified Bessel equation is given by [12]

$$\check{P}_3 = E_1(z,t)I_0\left(\sqrt{\frac{B\mu}{mK_3}}x\right) + E_2(z,t)K_0\left(\sqrt{\frac{B\mu}{mK_3}}x\right), \tag{2.72}$$

where E_1 and E_2 are arbitrary functions of z and t and I_0 and K_0 are the modified Bessel functions of zero order. So, we write the general solution for the pressure in the tissue in terms of P_3 and ξ as follows

$$P_3 = E_1(z,t)I_0\left(\sqrt{\frac{B\mu}{mK_3}}(1 + m\xi)\right) + E_2(z,t)K_0\left(\sqrt{\frac{B\mu}{mK_3}}(1 + m\xi)\right). \tag{2.73}$$

We determine the arbitrary functions $E_1(z,t)$ and $E_2(z,t)$ through the boundary conditions (2.61) and (2.62). Hence, we obtain the analytical solution for the pressure in the tissue in the form

$$P_3 = G_1(z)(I_0((1 + m\xi)\varphi)K_1(\varphi_m) + I_1(\varphi_m)K_0((1 + m\xi)\varphi)), \tag{2.74}$$

where

$$G_1(z) = \frac{A_2(16K_2P_1 - \mu\frac{d^2P_1}{d\eta^2}) - 4\mu\frac{d^2P_1}{d\eta^2}}{16A_2K_2(I_1(\varphi_m)K_0(\varphi) + I_0(\varphi)K_1(\varphi_m))}, \quad \varphi = \sqrt{\frac{B\mu}{mK_3}}, \quad \varphi_m = (1 + m)\varphi. \tag{2.75}$$

Hence the closed form solution for the interstitial fluid velocity in the tissue (u_3) can be found by substituting (2.74) into (2.58). This implies that the two components of the fluid velocity in the tissue at leading order are given by ($0 \leq \xi \leq 1$)

$$u_3 = G_1(z)\sqrt{m\mu BK_3}(I_1(\varphi_m)K_1((1+m\xi)\varphi) - I_1((1+m\xi)\varphi)K_1(\varphi_m)), \quad w_3 = 0. \tag{2.76}$$

Finally, we use the continuity of velocity conditions at the vessel/vessel wall and the vessel wall/tissue interfaces (Eqns. 2.60 and 2.61) to find an ODE for the blood pressure in the vessel ($P_1(z)$) in the form ($u_1\Big|_{r=1} = u_3\Big|_{\xi=0}$)

$$(4+A_2)\frac{d^2P_1}{dz^2} - G_2\sqrt{m\mu BK_3}\left(A_2\left(16\frac{K_2}{\mu}P_1 - \frac{d^2P_1}{dz^2}\right) - 4\frac{d^2P_1}{dz^2}\right) = 0, \tag{2.77}$$

where

$$G_2 = \frac{I_1(\varphi_m)K_1(\varphi) - I_1(\varphi)K_1(\varphi_m)}{K_2(I_1(\varphi_m)K_0(\varphi) + I_0(\varphi)K_1(\varphi_m))}. \tag{2.78}$$

Eqn. (2.77) can be integrated twice with respect to z and the integration constants can be determined from the boundary conditions (2.63) and (2.64). Hence, the closed form expression for the blood pressure in the vasculature is given by

$$P_1 = \frac{2A_2e^{-4G_3z}\left(e^{8G_3} - e^{8G_3z}\right)}{G_3(4+A_2)(1+e^{8G_3})}, \tag{2.79}$$

where

$$G_3 = \sqrt{\frac{A_2K_2\sqrt{m\mu BK_3}(I_1(\varphi_m)K_1(\varphi) - I_1(\varphi)K_1(\varphi_m)}{\mu(4+A_2)(K_2(I_1(\varphi_m)K_0(\varphi) + I_0(\varphi)K_1(\varphi_m)) + \sqrt{m\mu BK_3}(I_1(\varphi_m)K_1(\varphi) - I_1(\varphi)K_1(\varphi_m)))}} \tag{2.80}$$

We can check the analytical solution for the vascular fluid flow velocity by verifying conservation of fluid mass in the vessel. The fluid flux across the vessel inlet at $z = 0$ (Q_{in}), the fluid flux across the vessel outlet at $z = 1$ (Q_{out}) and the transmural fluid flux at $r = 1$ (Q_{tr}) are each defined as

$$Q_{in} = 2\pi\int_0^1 w_1(r,0)rdr, \qquad \text{at } z = 0 \tag{2.81}$$

$$Q_{out} = 2\pi\int_0^1 w_1(r,1)rdr, \qquad \text{at } z = 1 \tag{2.82}$$

$$Q_{tr} = 2\pi\int_0^1 u_1(1,z)dz, \qquad \text{at } r = 1 \tag{2.83}$$

These flux expressions can be calculated analytically using Eqns. (2.65) and (2.66). Conservation of total mass of blood can then be expressed in the form

$$Q_{in} = Q_{out} + Q_{tr}, \tag{2.84}$$

which is used to validate our predictions.

2.5 The Analytical Solutions for the Solute Transport Problem

In order to apply the asymptotic analysis for the GNR transport along the vessel and across the surrounding tissue, we need to define the order of magnitude of the parameters: $\tilde{D}_{2,3} = \epsilon^2 D$, $Pe = O(1)$ and $\delta = \epsilon^2$. Notice that the diffusion coefficients of the solute in the vessel wall ($\tilde{D}_2$) and in the tissue ($\tilde{D}_3$) are in the same order, so we assumed that they have the same value. We found these scales are the most appropriate for the transport problem as they lead to a dominant balance and are consistent with values we found in the literature [99].

We expand the GNR concentrations in each region, denoted C_i, according to the regular perturbation expansion $C_i = C_{i0} + \epsilon^2 C_{i1} + O(\epsilon^4)$ $(i = 1, 2, 3)$. Hence, the solute transport equation in the vessel (2.36) becomes

$$\begin{aligned}\epsilon^2 \left(\frac{\partial C_{10}}{\partial t} + \epsilon^2 \frac{\partial C_{11}}{\partial t} + u_1 \frac{\partial C_{10}}{\partial r} + \epsilon^2 u_1 \frac{\partial C_{11}}{\partial r} + w_1 \frac{\partial C_{10}}{\partial z} + \epsilon^2 w_1 \frac{\partial C_{11}}{\partial z} + O(\epsilon^4) \right) \\ = \frac{1}{Pe} \left(\frac{1}{r} \frac{\partial}{\partial r} \left(r \frac{\partial C_{10}}{\partial r} \right) + \epsilon^2 \frac{1}{r} \frac{\partial}{\partial r} \left(r \frac{\partial C_{11}}{\partial r} \right) + \epsilon^2 \frac{\partial^2 C_{10}}{\partial z^2} + \epsilon^4 \frac{\partial^2 C_{11}}{\partial z^2} + O(\epsilon^6) \right),\end{aligned} \tag{2.85}$$

Similarly, the solute transport equation in the vessel wall (2.40) can be written in the form

$$\begin{aligned}\epsilon^2 \left(\epsilon^2 \frac{\partial C_{20}}{\partial t} + \epsilon^4 \frac{\partial C_{21}}{\partial t} + \epsilon^3 w_2 \frac{\partial C_{20}}{\partial z} + \epsilon^5 w_2 \frac{\partial C_{21}}{\partial z} + u_2 \frac{\partial C_{20}}{\partial \eta} + \epsilon^2 u_2 \frac{\partial C_{21}}{\partial \eta} + O(\epsilon^7) \right) \\ = \frac{D}{Pe} \left(\epsilon^6 \frac{\partial^2 C_{20}}{\partial z^2} + \epsilon^8 \frac{\partial^2 C_{21}}{\partial z^2} + \frac{\epsilon^2 \frac{\partial C_{20}}{\partial \eta} + \epsilon^4 \frac{\partial C_{21}}{\partial \eta}}{1 + \epsilon^2 \eta} + \frac{\partial^2 C_{20}}{\partial \eta^2} + \epsilon^2 \frac{\partial^2 C_{21}}{\partial \eta^2} + O(\epsilon^{10}) \right),\end{aligned} \tag{2.86}$$

Likewise, the solute transport equation in the tissue $(i = 3)$ (2.44) can be written as

$$\begin{aligned}\Bigg(BmP_3(C_{30} + \epsilon^2 C_{31} + O(\epsilon^4)) + m\epsilon w_3 \frac{\partial}{\partial z}(C_{30} + \epsilon^2 C_{31} + O(\epsilon^4)) + u_3 \frac{\partial}{\partial \xi}(C_{30} + \epsilon^2 C_{31} + O(\epsilon^4)) \\ + m \left(\frac{\partial C_{30}}{\partial t} + \epsilon^2 \frac{\partial C_{31}}{\partial t} + O(\epsilon^4) \right) \Bigg) = \frac{D}{mPe} \left(m^2 \epsilon^2 \left(\frac{\partial^2 C_{30}}{\partial z^2} + \epsilon^2 \frac{\partial^2 C_{31}}{\partial z^2} + O(\epsilon^4) \right) \right. \\ \left. + \frac{1}{1 + \epsilon^2 + m\xi} \left(\frac{\partial C_{30}}{\partial \xi} + \epsilon^2 \frac{\partial C_{31}}{\partial \xi} + O(\epsilon^4) \right) + \frac{\partial^2 C_{30}}{\partial \xi^2} + \epsilon^2 \frac{\partial^2 C_{31}}{\partial \xi^2} + O(\epsilon^4) \right).\end{aligned} \tag{2.87}$$

The expanded boundary conditions become

$$\epsilon^2(u_1C_{10}+\epsilon^2u_1C_{11}+O(\epsilon^4))-\frac{1}{Pe}\left(\frac{\partial C_{10}}{\partial r}+\epsilon^2\frac{\partial C_{11}}{\partial r}+O(\epsilon^4)\right)=$$
$$\epsilon^2(u_2C_{20}+\epsilon^2u_2C_{21}+O(\epsilon^4))-\frac{D}{Pe}\left(\frac{\partial C_{20}}{\partial \eta}+\epsilon^2\frac{\partial C_{21}}{\partial \eta}+O(\epsilon^4)\right),$$
$$C_{10}+\epsilon^2C_{11}=C_{20}+\epsilon^2C_{21},\qquad (r=1 \text{ and } \eta=0), \tag{2.88}$$
$$\epsilon^2m(u_2C_{20}+\epsilon^2u_2C_{21}+O(\epsilon^4))-\frac{mD}{Pe}\left(\frac{\partial C_{20}}{\partial \eta}+\epsilon^2\frac{\partial C_{21}}{\partial \eta}+O(\epsilon^4)\right)=$$
$$\epsilon^2\left(m(u_3C_{30}+\epsilon^2u_3C_{31}+O(\epsilon^4))-\frac{D}{Pe}\left(\frac{\partial C_{30}}{\partial \xi}+\epsilon^2\frac{\partial C_{31}}{\partial \xi}+O(\epsilon^4)\right)\right),$$
$$C_{20}+\epsilon^2C_{21}=C_{30}+\epsilon^2C_{31}+O(\epsilon^4),\qquad (\eta=1 \text{ and} \xi=0), \tag{2.89}$$
$$(u_3C_{30}+\epsilon^2u_3C_{31}+O(\epsilon^4))-\frac{D}{mPe}\left(\frac{\partial C_{30}}{\partial \xi}+\epsilon^2\frac{\partial C_{31}}{\partial \xi}+O(\epsilon^4)\right)=0,\qquad (\xi=1). \tag{2.90}$$

2.5.1 The Leading Order Equations

To extract the leading order GNR transport equations we ignore all terms of order $O(\epsilon)$ and higher in (2.85-2.90). So, we get the following system of solute transport equations at leading order

$$\frac{\partial}{\partial r}\left(r\frac{\partial C_{10}}{\partial r}\right)=0, \qquad (0\le r\le 1) \tag{2.91}$$
$$\frac{\partial^2 C_{20}}{\partial \eta^2}=0, \qquad (0\le \eta\le 1) \tag{2.92}$$
$$(1+m\xi)\left(mBP_3C_{30}+u_3\frac{\partial C_{30}}{\partial \xi}+m\frac{\partial C_{30}}{\partial t}\right)=$$
$$\frac{D}{mPe}\left(\frac{\partial^2 C_{30}}{\partial \xi^2}+m\frac{\partial}{\partial \xi}\left(\xi\frac{\partial C_{30}}{\partial \xi}\right)\right),\qquad (0\le \xi\le 1). \tag{2.93}$$

These are coupled to the leading order boundary conditions

$$C_{10}=C_{20} \text{ and } \frac{\partial C_{10}}{\partial r}=D\frac{\partial C_{20}}{\partial \eta},\qquad (r=1 \text{ and } \eta=0), \tag{2.94}$$
$$C_{20}=C_{30} \text{ and } \frac{\partial C_{20}}{\partial \eta}=0,\qquad (\eta=1 \text{ and } \xi=0), \tag{2.95}$$
$$Peu_3C_{30}-\frac{D}{m}\frac{\partial C_{30}}{\partial \xi}=0,\qquad (\xi=1). \tag{2.96}$$

Note that conservation of flux condition across the wall/tissue boundary does not involve the GNR concentration in the tissue at leading order (i.e. Eq. (2.95) is independent of C_{30}). It emerges below that we must go to the next order in the expansion to close this system.

Equations (2.91) and (2.92) can be integrated twice with respect to r (or η) and the constants determined using the boundary conditions (2.94) and (2.95). Thus, we get the following solution

$$C_{10}(r,z) = C_{20}(\eta,z) = E_3(z,t) \tag{2.97}$$

where $E_3(z,t)$ is an arbitrary function which we determine by matching into the tissue region at the next order. On the other hand, (2.93) is a linear second order ODE with variable coefficients which is not possible to solve analytically (to the best of our knowledge). In order to solve this equation numerically we need to determine the arbitrary function $E_3(z,t)$ by writing the system of equations (2.85-2.90) to the $O(\epsilon^2)$ asymptotic order.

2.5.2 The GNR Transport Equations at $O(\epsilon^2)$

In order to solve the leading order GNR transport problem in the tissue we must consider the asymptotic equations of $O(\epsilon^2)$ in the vessel and in the vessel wall. This solution at $O(\epsilon^2)$ provides us with the boundary condition at the vessel wall/tissue interface which is essential to determine $E_3(z,t)$ and solve the leading order transport problem in the tissue. The solute transport equations in the vessel and the vessel wall of $O(\epsilon^2)$ are

$$\frac{\partial C_{10}}{\partial t} + w_1 \frac{\partial C_{10}}{\partial z} = \frac{1}{Pe}\left(\frac{1}{r}\frac{\partial}{\partial r}\left(r\frac{\partial C_{11}}{\partial r}\right) + \frac{\partial^2 C_{10}}{\partial z^2}\right), \qquad (0 \le r \le 1) \tag{2.98}$$

$$\frac{\partial^2 C_{21}}{\partial \eta^2} = 0, \qquad (0 \le \eta \le 1). \tag{2.99}$$

Eq. (2.98) indicates that at this order the diffusion of the perturbation concentration across the vessel is balanced by unsteady effects, advective effects and diffusion along the vessel of the leading order concentration. Conversely, Eq. (2.99) indicates that the perturbation concentration is constant across the vessel wall at this order.

These equations are coupled to boundary conditions at $O(\epsilon^2)$ in the form

$$C_{11} = C_{21}, \quad u_1 C_{10} - \frac{1}{Pe}\frac{\partial C_{11}}{\partial r} = u_2 C_{20} - \frac{D}{Pe}\frac{\partial C_{21}}{\partial \eta}, \qquad (r = 1 \text{ and } \eta = 0). \tag{2.100}$$

$$C_{21} = C_{31}, \quad u_2 C_{20} - \frac{D}{Pe}\frac{\partial C_{21}}{\partial \eta} = u_3 C_{30} - \frac{D}{mPe}\frac{\partial C_{30}}{\partial \xi}, \qquad (\eta = 1 \text{ and } \xi = 0). \tag{2.101}$$

The general analytical solution for this system of equations (2.98) and (2.99) (determined

by Mathematica) is given by

$$C_{11} = f_2(z,t) - \frac{Pe}{8A_2} r^2 \frac{dP_1}{d\eta}\frac{\partial C_{10}}{\partial z} + \frac{r^2}{64}\left(16Pe\frac{\partial C_{10}}{\partial t} + Pe(r^2-4)\frac{dP_1}{d\eta}\frac{\partial C_{10}}{\partial z} - 16\frac{\partial^2 C_{10}}{\partial z^2}\right), \tag{2.102}$$

$$\begin{aligned} C_{21} = {} & f_2(z,t) \\ & + \frac{1}{64DA_2}\left(-8Pe\left(2\eta C_{10}\frac{d^2P_1}{d\eta^2} + (D+2\eta)\frac{dP_1}{d\eta}\frac{\partial C_{10}}{\partial z}\right) + A_2\left(4Pe\eta C_{10}(16u_2 - \frac{d^2P_1}{d\eta^2})\right.\right. \\ & \left.\left. + 16Pe(D+2\eta)\frac{\partial C_{10}}{\partial t} - Pe(3D+4\eta)\frac{dP_1}{d\eta}\frac{\partial C_{10}}{\partial z} - 16(D+2\eta)\frac{\partial^2 C_{10}}{\partial z^2}\right)\right), \end{aligned} \tag{2.103}$$

where $f_2(z,t)$ is an arbitrary function. Note that we have not yet applied boundary conditions (2.101) which will determine f_2.

The solute flux at vessel/vessel-wall interface can be written using (2.102) in (2.100) in the form

$$J_{1r} = u_1 C_{10} - \left[\frac{r}{2}\frac{\partial C_{10}}{\partial t} + \frac{1}{64}(4r^3 - 8r)\frac{dP_1}{d\eta}\frac{dC_{10}}{d\eta} - \frac{1}{4A_2} r \frac{dP_1}{d\eta}\frac{dC_{10}}{d\eta} - \frac{1}{2Pe} r \frac{\partial^2 C_{10}}{\partial z^2}\right]_{r=1}. \tag{2.104}$$

2.5.3 The Transmural Radial Solute Flux

We can calculate the radial solute flux across the vessel wall (J_{1r}) at $r = 1$ from the left hand side of (2.100) and using the Eq. (2.102) we get

$$J_{1r} = u_1 C_{10} - \frac{1}{Pe}\frac{\partial C_{11}}{\partial r} + O(\epsilon^2) = u_1 C_{10} + \frac{4+A_2}{16A_2}\frac{dP_1}{d\eta}\frac{\partial C_{10}}{\partial z} - \frac{1}{2}\frac{\partial C_{10}}{\partial t} + \frac{1}{2Pe}\frac{\partial^2 C_{10}}{\partial z^2} + O(\epsilon^2). \tag{2.105}$$

This flux can be written in terms of the vascular pressure P_1 rather than the radial vascular velocity u_1 by substituting the analytical solution for u_1 (2.65) where we obtain

$$J_{1r} = \frac{4+A_2}{16A_2}\frac{\partial}{\partial z}\left(\frac{dP_1}{d\eta}C_{10}\right) - \frac{1}{2}\frac{\partial C_{10}}{\partial t} + \frac{1}{2Pe}\frac{\partial^2 C_{10}}{\partial z^2}, \qquad (0 \le z \le 1) + O(\epsilon^2). \tag{2.106}$$

Similarly, we can calculate the radial solute flux across the vessel wall (J_{3r}) at $\xi = 1$ in the form

$$J_{3r} = u_3 C_{30} - \frac{D}{mPe}\frac{\partial C_{30}}{\partial \xi} + O(\epsilon^2). \tag{2.107}$$

Note that both of the flux expressions J_{1r} and J_{3r} are equal up to the order evaluated as the radial solute flux across the vessel wall is uniform to this asymptotic order.

2.6 Numerical Solution for GNR Transport Equation in the Tissue

To form a closed system of equations we must impose boundary conditions between the vessel wall and the tissue (2.101). This condition, substituting (2.103), becomes a constraint on the system including C_{10} and C_{30} alone. The resulting leading order transport equations in the tissue (in terms of C_{30}) takes the form ($0 \leq \xi \leq 1$, $0 \leq z \leq 1$)

$$(1+m\xi)\left(mBP_3C_{30} + u_3\frac{\partial C_{30}}{\partial \xi} + m\frac{\partial C_{30}}{\partial t}\right) = \frac{D}{mPe}\left(\frac{\partial^2 C_{30}}{\partial \xi^2} + m\frac{\partial}{\partial \xi}\left(\xi\frac{\partial C_{30}}{\partial \xi}\right)\right), \quad (2.108)$$

while the leading order transport equation in the vessel (in terms of C_{10}) takes the form ($0 \leq z \leq 1$)

$$Pe(4+A_2)\frac{\partial}{\partial z}(\frac{dP_1}{d\eta}C_{10}) + 8A_2\left(\frac{\partial^2 C_{10}}{\partial z^2} + \frac{2D}{m}\frac{\partial C_{30}}{\partial \xi}\bigg|_{\xi=0}\right) = 8PeA_2\left(2u_3C_{30}\bigg|_{\xi=0} + \frac{\partial C_{10}}{\partial t}\right). \quad (2.109)$$

Note that $A_2 = \epsilon\alpha_2\hat{L}/\sqrt{\hat{K}_2}$ and B is constant determined by (2.32). Also (2.109) does not depend on ξ and so is a 1D PDE in z, t. These coupled 1D advection diffusion equations (in z and t) represent a model for studying drug (GNR) delivery to tissue in the presence of flow. These two equations are solved subject to leading order boundary conditions of continuity of GNR concentration

$$C_{10} = C_{30}, \qquad (\eta = 1 \text{ and } \xi = 0). \quad (2.110)$$

and net GNR flux out of the tissue region,

$$Peu_3C_{30} - \frac{D}{m}\frac{\partial C_{30}}{\partial \xi} = 0, \qquad (\xi = 1). \quad (2.111)$$

In order to close this system we need to prescribe boundary conditions for C_{10} at $z = 0$ and $z = 1$. Previous work has assumed that the GNR concentration in the blood decreases due to clearance by the liver and spleen at fixed rate τ [76] according to

$$C_v = C_{v_0}e^{-t/\tau}, \quad (2.112)$$

where C_v is the instantaneous GNR concentration in the blood and C_{v_0} is the initial GNR concentration. Hence, in our problem we impose the GNR concentration at the capillary inlet to be equal to the exponential decay model (2.112) and we impose zero GNR diffusive

Table of dimensional parameters				
parameter	value	units	description	Ref.
$\hat{R}_1$	3×10^{-4}	cm	The vessel radius	[16]
$\hat{R}_2$	4×10^{-4}	cm	The outer wall radius	[16]
$\hat{R}_3$	7×10^{-4}	cm	The tissue outer radius	[16]
$\hat{L}$	0.06	cm	The vessel length	[16]
m	1	–	the ratio of width of the tissue to the radius of vessel	Assumed
$\hat{\mu}_b$	3×10^{-5}	mm Hg s	The blood viscosity	[20]
$\hat{\mu}$	3×10^{-5}	mm Hg s	The interstitial fluid viscosity	[20]
$\hat{k}_2$	1.33×10^{-12}	cm^2	The interstitial permeability ($\hat{k}_2 = \delta \hat{k}_3$)	Assumed
$\hat{k}_3$	4×10^{-12}	cm^2	The interstitial permeability	[99]
$\hat{L}_{pl}^{(N)} \hat{S}_l^{(N)} / \hat{V}^{(N)}$	1.33×10^{-5}	1/mm Hg s^{-1}	The lymphatic density	[91, 97]
α_2	0.01	-	a constant	[11]
$\hat{W}$	0.07	cm/s	blood mean velocity at the vessel inlet	[16]
$\hat{P}_0$	0	mm Hg	blood pressure at the vessel outlet	Chosen
$\hat{P}_l$	0	mm Hg	lymphatic pressure	[97]
$\hat{\tau}$	12.5	h	The GNR blood half life	[2]

Table 2.1: Dimensional parameters used in the GNR and fluid transport models.

flux at the capillary outlet as follows

$$C_{10} = C_{v_0} e^{-t/\tau}, \qquad (z = 0), \tag{2.113}$$

$$\frac{\partial C_{10}}{\partial z} = 0, \qquad (z = 1). \tag{2.114}$$

2.7 The Two Pore Model

The transmural radial flux defined in the Eqn. (2.106) can be approximated using an alternative approach known as the two pore model [87]. In this approximation it is assumed that the radial solute flux (J_{2r}) is uniform across the vessel wall. In addition, the wall between the vessel and the tissue is very thin. According to (2.49), the full equation for the radial flux across the wall can be written implicitly as

$$\frac{\partial C_2}{\partial \eta} - \frac{\epsilon^2 \delta Pe}{D} u_2 C_2 = -\frac{\epsilon \delta Pe}{D} J_{2r}. \tag{2.115}$$

Assuming u_2 and J_{2r} are constant (i.e. independent of η), the previous equation is a nonhomogeneous ODE in C_2 which can be solved using an integration factor $\breve{\mu}$ defined as

$$\breve{\mu} = e^{-\omega \eta}, \quad \omega = \frac{\epsilon^2 \delta Pe u_2}{D}. \tag{2.116}$$

Hence, multiplying Eqn.(2.115) by the integrating factor $\breve{\mu}$ and integrating across the vessel wall we obtain

$$C_2(1) e^{-\omega} - C_2(0) = \frac{1}{u_2 \epsilon} J_{2r} \left(e^{-\omega} - 1 \right). \tag{2.117}$$

We can rearrange the previous equation to get the radial transmural flux in terms of the concentrations on either side in the form

$$J_{2r} = \frac{\epsilon u_2 \left(C_2(\eta = 0, z) - C_2(\eta = 1, z)e^{-\omega}\right)}{1 - e^{-\omega}} \equiv \frac{\epsilon u_1(r = 1, z) \left(C_1(r = 1, z) - C_3(\xi = 0, z)e^{-\omega}\right)}{1 - e^{-\omega}}. \tag{2.118}$$

We will use this approximation for the solute flux J_{2r} across the wall (2.118) to replace the continuity of concentration boundary condition at the vessel/wall interface (2.110) in Sec. 2.8.2. Note that the solute transmural flux J_{2r} (2.118) is purely advective if $Pe \to \infty$ where $J_{2r} = \epsilon u_1 C_1\Big|_{r=1}$. We also consider the limit $Pe = 0$ which is corresponding to the totally diffusive flux. However, this is problematic as we have scaled the transmural flux (J_{2r}) based on the advective component (see Eq. 2.31). So, we rescale J_{2r} in the form

$$J_{2r} = \frac{1}{Pe}\tilde{J}_{2r}, \tag{2.119}$$

where $\tilde{J}_{2r}$ is the transmural flux nondimensionalized using the diffusive component of the flux. In this case we can write Eq. (2.115) in the form

$$\frac{\partial C_2}{\partial \eta} - \frac{\epsilon^2 \delta Pe}{D} u_2 C_2 = -\frac{\epsilon \delta}{D}\tilde{J}_{2r}. \tag{2.120}$$

Assuming $\tilde{J}_{2r}$ is independent on η and solving for C_2 when $Pe = 0$ we obtain

$$\tilde{J}_{2r} = \frac{D}{\epsilon\delta}(C_2(\eta = 0, z) - C_2(\eta = 1, z)) \equiv \frac{D}{\epsilon\delta}(C_1(r = 1, z) - C_3(\xi = 0, z)). \tag{2.121}$$

This flux expression (2.121) has been investigated by Shipley and Chapman [2010] [99]. Note that we cannot have $C_1(r = 1, z) = C_3(\xi = 0, z)$ and still maintain a transmural flux. Hence, we ignore this case in this thesis since we estimated Pe which is greater than zero.

2.7.1 The Numerical Method

The system of PDEs. (2.108) and (2.109) are linear with non-constant coefficients which are difficult to solve analytically. Therefore, we solve these two equations with the boundary conditions (2.110), (2.111), (2.113) and (2.114) numerically using method of lines. We discretize the ξ and z-domains onto a uniformly spaced mesh ($\xi_j = j\Delta\xi,\ \Delta\xi = 1/N_2$ in the tissue and $z_i = i\Delta z,\ \Delta z = 1/N_1$ in the tissue or the vessel, see Fig. 2.2) using central finite difference and solve the resulting system of ODEs using a built-in function in MATLAB (ode15s) which solves systems of algebraic differential equations. We test the MATLAB code by studying the mesh convergence, then we choose the number of mesh

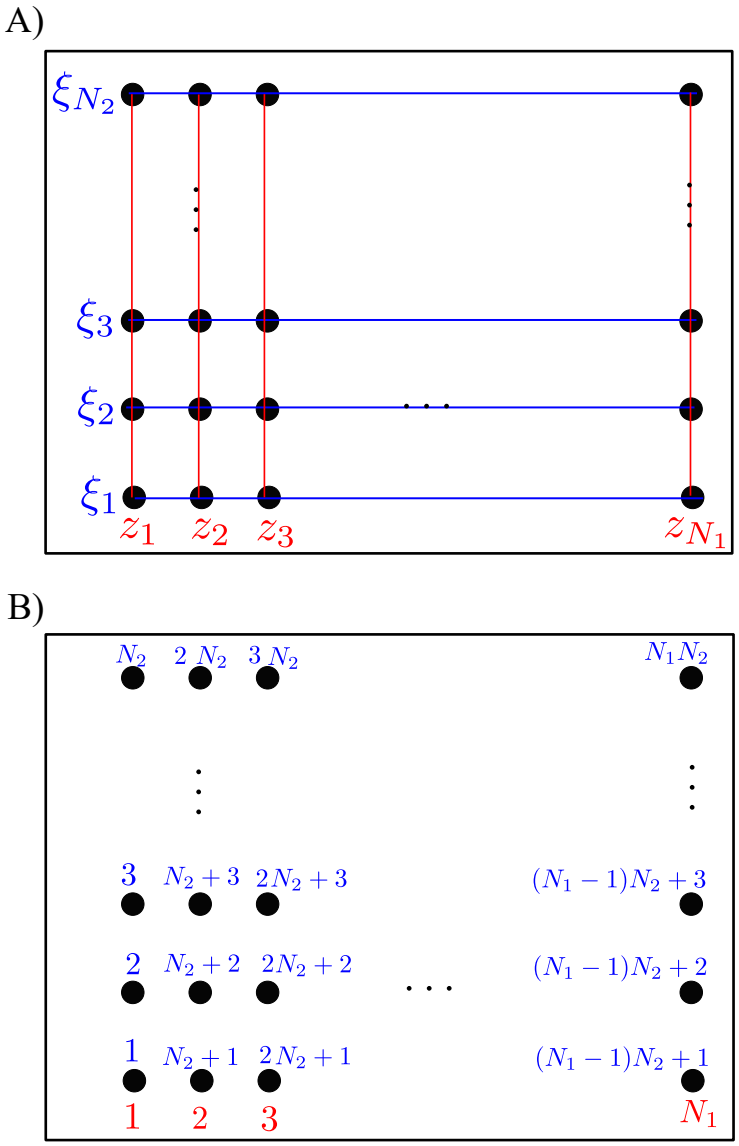

Figure 2.2: The computational domain for the healthy tissue. A)The grid of ξ_j ($j = 1, 2, \cdots, N_2$) and z_i ($i = 1, 2, \cdots, N_1$) lines. B) The grid point numbers used in the MATLAB code.

points which is corresponding to a relative error of $O(10^{-4})$, see Appendix C.

It should be noted that Eqn. (2.108) has only derivative terms with respect to ξ, but the coefficients are functions of z. On the other hand, Eqn. (2.109) is defined at $\xi = 0$ and only has derivatives with respect to z. Across the bulk of either the ξ or z domains we use second order central finite difference approximations. At the boundaries we use staggered (off centered) grids to maintain the second order approximation. The time derivatives are left to be integrated using the built-in MATLAB solver. This gives us a system of algebraic differential equations, where at every spatial mesh point we get an ODE (method of lines) that can be solved by the MATLAB subroutine (ode15s) according to appropriate initial conditions for solute concentration at every mesh point at the computational domain.

The finite difference approximations at $\xi = \xi_1 = 0$ are given by

$$\frac{\partial C_{30}}{\partial \xi}(\xi_1, z_i) = \frac{-3C_{30}(\xi_1, z_i) + 4C_{30}(\xi_2, z_i) - C_{30}(\xi_3, z_i)}{2\Delta\xi}, \quad (i = 1, 2, \cdots, N_1), \tag{2.122}$$

while at $\xi = \xi_{N_2} = 1$ are approximated in the form

$$\frac{\partial C_{30}}{\partial \xi}(\xi_{N_2}, z_i) = \frac{C_{30}(\xi_{N_2-2}, z_i) - 4C_{30}(\xi_{N_2-1}, z_i) + 3C_{30}(\xi_{N_2}, z_i)}{2\Delta\xi}, \quad (i = 1, 2, \cdots, N_1). \tag{2.123}$$

At the mesh points at $0 < \xi < 1$ we use central difference formulas for the first and second derivatives with ξ in the form $(j = 2, 3, \cdots, N_2 - 1)$

$$\frac{\partial C_{30}}{\partial \xi}(\xi_j, z_i) = \frac{C_{30}(\xi_{j+1}, z_i) - C_{30}(\xi_{j-1}, z_i)}{2\Delta\xi}, \quad (i = 1, 2, \cdots, N_1), \tag{2.124}$$

$$\frac{\partial^2 C_{30}}{\partial \xi^2}(\xi_j, z_i) = \frac{C_{30}(\xi_{j+1}, z_i) - 2C_{30}(\xi_j, z_i) + C_{30}(\xi_{j-1}, z_i)}{(\Delta\xi)^2}, \quad (i = 1, 2, \cdots, N_1). \tag{2.125}$$

The derivatives with z at $z = z_1 = 1$ are approximated in the form

$$\frac{\partial C_{10}}{\partial z}(z_{N1}) = \frac{C_{10}(z_{N_1-2}) - 4C_{10}(z_{N_1-1}) + 3C_{10}(z_{N_1})}{2\Delta z}. \tag{2.126}$$

and at $0 < z < 1$ the first derivative is given by

$$\frac{\partial C_{10}}{\partial z}(z_i) = \frac{C_{10}(z_{i+1}) - C_{10}(z_{i-1})}{2\Delta z}, \quad (i = 1, 2, \cdots, N_1), \tag{2.127}$$

$$\frac{\partial^2 C_{10}}{\partial z^2}(z_i) = \frac{C_{10}(z_{i+1}) - 2C_{10}(z_i) + C_{10}(z_{i-1})}{(\Delta z)^2}, \quad (i = 1, 2, \cdots, N_1). \tag{2.128}$$

2.7.2 GNR Conservation of Mass

We validate our numerical method by verifying conservation of GNR (solute) mass. The total mass of GNRs in the vessel is calculated as

$$\hat{M}_1 = 2\pi \int_0^{\hat{R}_1} \hat{r} d\hat{r} \int_0^{\hat{L}} \hat{C}_{10} d\hat{z}. \tag{2.129}$$

The change in mass in the vessel is then calculated from

$$\frac{d\hat{M}_1}{d\hat{t}} = 2\pi \int_0^{\hat{R}_1} \hat{r} d\hat{r} \int_0^{\hat{L}} \frac{\partial \hat{C}_{10}}{\partial \hat{t}} d\hat{z}. \tag{2.130}$$

Applying the dimensionless transformations (2.30) on (2.130) we get

$$\frac{dM_1}{dt} = 2\pi\epsilon^2 \int_0^1 rdr \int_0^1 \frac{\partial C_{10}}{\partial t} dz, \quad M_1(t) = \frac{\hat{M}_1(t)}{\hat{L}^3 \hat{C}_0}. \tag{2.131}$$

This change in mass is balanced by fluxes into and out of the vessel. Applying the nondimensional transformations (2.30) on (2.26) we get the axial flux in the vessel at any arbitrary z coordinate ($z = z_0$) in the from

$$J_{1z}\Big|_{z=z_0} = 2\pi \left[\int_0^1 (w_1 C_{10} - \frac{1}{Pe} \frac{\partial C_{10}}{\partial z}) r dr \right]_{z=z_0}, \quad (z_0 = 0,\ 1). \tag{2.132}$$

The radial flux (2.107) is calculated from

$$J_{3r}\Big|_{\xi=0} = 2\pi \left[\int_0^1 (u_3 C_{30} - \frac{D}{mPe} \frac{\partial C_{30}}{\partial \xi}) dz \right]_{\xi=0}. \tag{2.133}$$

Thus the conservation of mass at any arbitrary time $t_0 \geq 0$ is given by

$$\int_0^{t_0} \left(\frac{dM_1}{dt} - J_{1z}\Big|_{z=0} + J_{1z}\Big|_{z=1} + J_{3r}\Big|_{\xi=0} \right) dt = 0, \tag{2.134}$$

which can be written in the form

$$M_1(t_0) = M_1(0) + \int_0^{t_0} (J_{1z}\Big|_{z=0} - J_{1z}\Big|_{z=1} - J_{3r}\Big|_{\xi=0}) dt. \tag{2.135}$$

2.7.3 The Solute Total Mass in the Tissue

We can calculate the total mass of solute ($\hat{M}_3$) accumulated in the tissue using the following equation

$$\hat{M}_3 = \int_0^{\hat{L}} \hat{C}_3 d\hat{V}, \tag{2.136}$$

where $d\hat{V}$ is the control volume in the tissue in cylindrical coordinates which is defined as

$$d\hat{V} = \hat{r} d\hat{r} d\hat{\theta} d\hat{z}. \tag{2.137}$$

The control volume defined in the preceding equation can be written in terms of the dimensionless variables ($d\xi$ and dz) using the transformations (2.32) we get

$$d\hat{V} = 2\pi m \epsilon^2 \hat{L}^3 (\delta + m\xi + 1) d\xi dz. \tag{2.138}$$

Hence, the dimensionless total mass (M_3) in the tissue is calculated as

$$M_3(t) = 2\pi m\epsilon^2 \int_0^{z_{max}} \int_0^{\xi_{max}} (\delta + m\xi + 1) C_3(\xi, z, t) d\xi dz, \quad M_3(t) = \frac{\hat{M}_3(t)}{\hat{L}^3 \hat{C}_0}. \tag{2.139}$$

2.8 Reduced Problems

In this section we introduce two reduced models which replace the vessel domain (Eqn. 2.108) with an appropriate boundary condition. We show that these reductions remove the constraint ODE (2.109) from the system and so the final reduced system is a two-dimensional PDE for solute transport in the tissue. This approach is then used when we study GNR delivery to vascularised tumors at the macroscale, see Chap. 3.

2.8.1 Problem 1

In the first problem we prescribe the concentration of the solute in the vessel everywhere using the exponential decay model defined in Eqn. (2.112), hence, the vascular concentration is independent of z. In addition, we assume continuity of concentration at the tissue/vessel-wall interface ($\xi = 0$). Thus, the system reduces to the following one-dimensional PDE

$$(1 + m\xi) \left(mBP_3 C_{30} + u_3 \frac{\partial C_{30}}{\partial \xi} + m \frac{\partial C_{30}}{\partial t} \right) = \frac{D}{mPe} \left(\frac{\partial^2 C_{30}}{\partial \xi^2} + m \frac{\partial}{\partial \xi} \left(\xi \frac{\partial C_{30}}{\partial \xi} \right) \right), \tag{2.140}$$

subject to the following boundary conditions

$$C_{30} = C_{v_0} e^{-t/\tau}, \qquad (\xi = 0), \tag{2.141}$$

$$Peu_3 C_{30} - \frac{D}{m} \frac{\partial C_{30}}{\partial \xi} = 0, \qquad (\xi = 1). \tag{2.142}$$

2.8.2 Problem 2: The Two Pore Model

In the second reduced problem we construct a more ad-hoc boundary condition using the approach of the two pore model to define the solute flux across the vessel wall, see Sec. 2.7. So, in this model we prescribe the vascular concentration using the decay model (2.112) and specify the flux at the tissue/vessel-wall using the pore model that we derived in Sec. 2.7. Hence, we write the following system of equations

$$(1 + m\xi) \left(mBP_3 C_{30} + u_3 \frac{\partial C_{30}}{\partial \xi} + m \frac{\partial C_{30}}{\partial t} \right) = \frac{D}{mPe} \left(\frac{\partial^2 C_{30}}{\partial \xi^2} + m \frac{\partial}{\partial \xi} \left(\xi \frac{\partial C_{30}}{\partial \xi} \right) \right), \tag{2.143}$$

$$C_{10} = C_{v_0} e^{-t/\tau}. \tag{2.144}$$

The system is solved according to the following boundary conditions

$$u_3 C_{30} - \frac{D}{mPe}\frac{\partial C_{30}}{\partial \xi} = \frac{\epsilon u_1(r=1,z)\left(C_{10}(r=1,z) - C_{30}(\xi=0,z)e^{-\omega}\right)}{1-e^{-\omega}}, \quad (\xi = 0), \quad (2.145)$$

$$Pe u_3 C_{30} - \frac{D}{m}\frac{\partial C_{30}}{\partial \xi} = 0, \quad (\xi = 1), \quad (2.146)$$

where ω is determined by (2.116). In this reduced problem we balance the flux (at the tissue/wall interface) calculated by the two pore model (2.118) with the radial flux defined in (2.107).

2.9 Results

The Fluid Flow Predictions

To begin we examine the fluid flow in the domain, where in Fig. 2.3 we plot the analytical solutions for the vascular pressure ($\hat{P}_1$), the components of the blood velocity ($\hat{u}_1$ and $\hat{w}_1$), the interstitial pressure ($\hat{P}_3$) and the interstitial fluid velocity ($\hat{u}_3$), which are defined in Eqns. (2.65-2.69), (2.74), (2.76) and (2.79), respectively.

The radial blood velocity is typically very small (see Figs. 2.3(A), (B)) compared to the axial velocity (see Fig. 2.3(C), (D)) and is approximately linearly decreasing along the vessel (see Fig. 2.3(A)), due to the approximately linear vascular pressure drop as revealed in Fig. 2.3(E). However, the radial velocity has a parabolic profile akin to Hagen-Poiseuille flow, as shown in Fig. 2.3(B). The velocity of the blood in the axial direction has also a parabolic profile across the vessel, but is approximately uniform along the vessel as shown in the Figs. 2.3(C), (D).

Fig. 2.3(E) shows how the vascular pressure ($\hat{P}_1$) and the interstitial pressure ($\hat{P}_3$) in the tissue decrease approximately linearly in $\hat{z}$ and both pressures are very close in value ($\hat{P}_1$ is slightly bigger than $\hat{P}_3$, and so the transmural pressure $\hat{P}_1 - \hat{P}_3 > 0$). This suggests a very small transmural pressure and as a result a very small transvascular fluid flux across the wall. Although the interstitial pressure ($\hat{P}_3$) is a function of $\hat{\xi}$ and $\hat{z}$ (see Eq. (2.74)), Fig. 2.3(F) shows that the interstitial pressure profile is approximately uniform across the tissue and depends on $\hat{z}$ only. However, the interstitial fluid velocity is very small ($\sim 10^{-8}$) decreases approximately exponentially in the radial direction $\hat{r}$ and decreases linearly in the $\hat{z}$ direction as shown in Fig. 2.3(G), (H). As expected from the continuous velocity boundary conditions at the tissue/vessel interface, the interstitial fluid velocity is typically very small (see Fig. 2.3(G), (H)) and of the same order as the radial blood velocity (see Fig. 2.3(A), (B)).

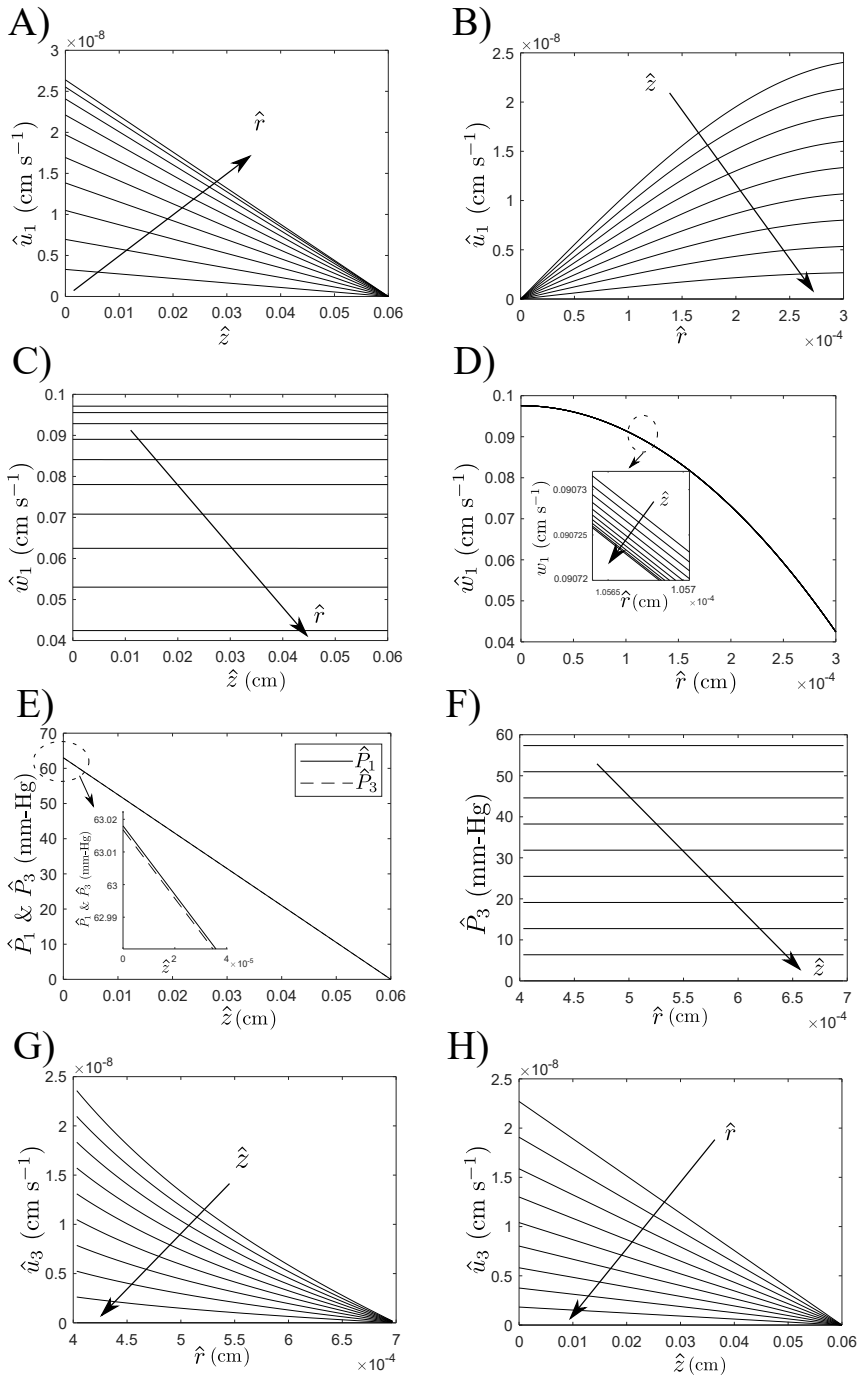

Figure 2.3: Pressure and velocity profiles in the vessel and tissue using the parameter values in Table 2.1. A) The interstitial pressure P_3 across tissue. B) The vascular pressure P_1 along the vessel and the interstitial pressure P_3. C)The interstitial velocity across the tissue. D)The interstitial velocity along the tissue. E)The vascular axial velocity along the vessel. F)The vascular axial velocity across the vessel. G)The vascular radial velocity along the vessel. H)The vascular radial velocity across the vessel.

The Solute Concentration Predictions

The Fig. 2.4 shows the predictions of solute concentrations in the vessel ($\hat{C}_{10}$) and the tissue ($\hat{C}_{30}$) which are results of solving Eqns. (2.108-2.111) numerically (the numerical

technique is described in Sec. 2.7.1). The solute vascular concentration is approximately spatially uniform as revealed in Fig. 2.4(A). As a result, the vascular concentration is exponentially decreasing over time (see Fig. 2.4(B)) since the concentration is uniform (in the vessel) and we impose the exponential decay model (2.112) at the vessel inlet.

The radial profile of the solute concentration across the tissue for different values of $\hat{z}$ are shown in Figs. 2.4(C)-(F). These four figures show that the solute concentration initially increases as an approximate traveling wave advances away from the vessel, then saturates, then decreases homogeneously following the exponential decay of the solute vascular concentration, see Eqn. (2.112).

We plot the spatial concentration profiles along the tissue for different time points in Fig. 2.4(G) and the temporal concentration profiles for different $\hat{z}$ mesh points in Fig. 2.4(H). In these two figures we compared the concentration profiles at two radial mesh points: at $\hat{r} = 4.9 \times 10^{-4}$ cm ($\xi = 0.3$) using solid line plot and at $\hat{r} = 6.7 \times 10^{-4}$ cm ($\xi = 1$) using dashed line plot. We will use these two radial mesh points to assess the two reduced models introduced in Sec. 2.8. Fig. 2.4(G) demonstrates a homogeneous increase of GNR concentration until saturation; the GNR concentration decreases faster closer to the vessel inlet than the concentration near the vessel outlet, resulting in an inhomogeneous concentration decay along the tissue. Furthermore, the GNR concentration rapidly increases in the tissue within the first four hours post injection, and then gradually decreases until the end of the simulation (within the last eight hours of the simulation) as depicted in Fig. 2.4(H), where the concentration increases to its maximum within $2 - 3$ hours, but needs 10 hours to decrease to half of its maximum value.

We conclude from Fig. 2.4 that GNRs accumulate at the tissue edge ($\hat{r} = 6.7 \times 10^{-4}$) achieving 60% of the dose concentration within four hours post injection (Fig. 2.4(H)) which is a result of uniform GNR concentration in vessel (Fig. 2.4(A)), according to the parameter values considered in this case study. The decay of GNR concentration in the tissue (Fig. 2.4(C)-(F)) is due to the GNR removal by lymph vessels in the tissue (2.8) in addition to the GNR clearance from the blood stream via the liver and spleen (mimicked by the exponential decay model (2.112)) which is the only source of GNRs in the tissue (Fig. 2.4(B)).

Predictions from the Reduced Problems

In to the Fig. 2.5 we compare the predictions of the reduced problems considered in Sec. 2.8 against the predictions of the full model discussed in Sec. 2.9 and Figs. 2.5(A), (B) depict the predictions of the reduced problem 1 (defined in Sec. 2.8.1) alongside the predictions of the full model at the radial mesh points $r = 6.7 \times 10^{-4}$ cm (Fig. 2.5(A)) and $r = 4.9 \times 10^{-4}$ cm (Fig. 2.5(B)). The predictions of the reduced problem 2 (defined in Sec. 2.8.2) at $r = 6.7 \times 10^{-4}$ cm and $r = 4.9 \times 10^{-4}$ cm are plotted alongside the predictions

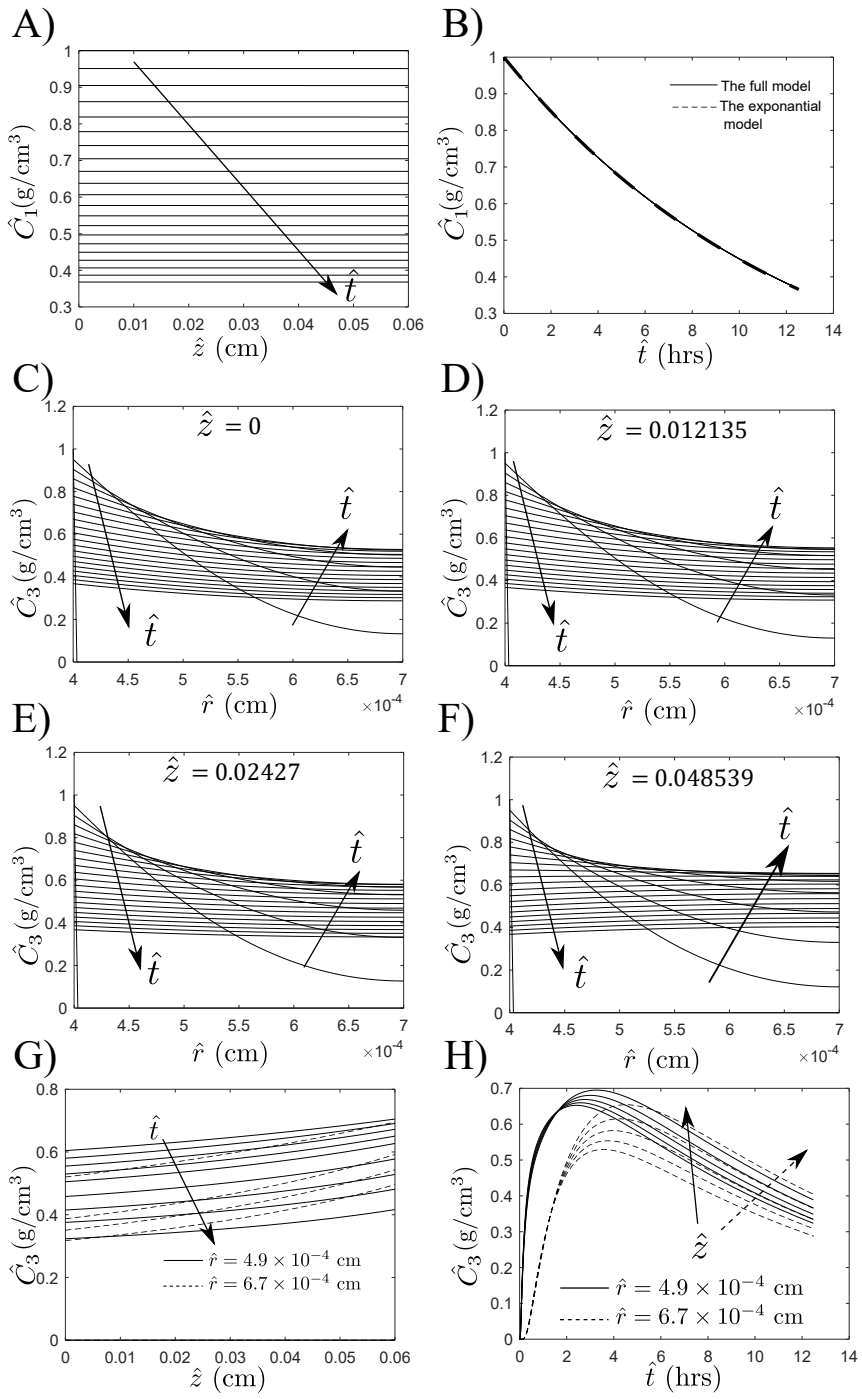

Figure 2.4: Predictions for the solute transport problem at the microscale using the parameter values in Table 2.1. A) Vascular concentration along the vessel axis for different time steps. B) A comparison for the temporal profiles of the vascular concentration calculated through the model described in Sec. 2.6 and exponential decay model (see Eq. (2.112)). The radial spatial profiles for the solute concentration in the tissue at C) $\hat{z} = 0$, D) $\hat{z} = 0.012$, E) $\hat{z} = 0.02$ and F) $\hat{z} = 0.049$ for different values of time steps. G)The axial spatial profiles for the solute concentration in the tissue at $\hat{r} = 4.9 \times 10^{-4}$ and at $\hat{r} = 6.7 \times 10^{-4}$ (tissue outer edge) for different values of time steps. H)The temporal profiles for the solute concentration in the tissue at $\hat{r} = 4.9 \times 10^{-4}$ and at $\hat{r} = 6.7 \times 10^{-4}$ (tissue outer edge) for different values of axial positions.

of the full model in Figs. 2.5(C), (D), respectively. We conclude from these four figures that the reduced models give a reasonable agreement with the full model near the vessel-wall/tissue interface as shown in Figs. 2.5(B), (D). However, both reduced models slightly overestimate the solute concentration in the deep tissue as shown in Figs. 2.5(A), (C), which means the GNR flux at the wall computed by either the pore model (problem 2) or the reduced problem 1 is larger than the GNR flux computed by the full model.

We conclude from these results that the reduced models successfully predict the solute concentration near the vessel/tissue interface for the chosen values of parameters in this study with a slightly overestimation of the concentration at the first 6 hours of simulation. However, this overestimation vanishes as the temporal concentration profiles decay (see Figs. 2.5(B), (D)).

In the reduced model 2 we impose the GNR flux according to the two pore model and this model slightly overestimates the concentration near the vessel/tissue interface (Fig. 2.5(E)). The overestimation of the GNR concentration in the deep tissue away from the vessel is because the flux defined in the full model (2.106) is different from the flux computed via the two pore model (which is defined in Eq. 2.118).

In the reduced model 1 we impose the GNR concentration at the tissue/wall interface using the exponential model (Eq. 2.141) which means in this reduced problem we solve for the GNR flux at the tissue/wall boundary. Interestingly, for a fixed axial position both reduced models give approximately the same solute concentration temporal profile which is very close to the full model predictions as revealed in Fig. 2.5(E).

In Fig. 2.5(F) we compare the transient total mass of solute accumulated in the tissue (defined according to Eq. 2.139) which is calculated via the full model and the two reduced models. This figure shows that both reduced problems predict exactly the same total mass transient profile which almost exactly agree with the full model predictions during the first six hours of the simulation and slightly deviate for larger times which is a result of the difference in the concentration predictions of the three models.

In Figs. 2.6 (A), (B) we compare the radial profiles at $\hat{z} = 0.022$ cm for solute concentration in tissue computed via the three models at various times. This figure shows that the predictions of the three models agree very well across approx 17% of the tissue adjacent to the vessel, then the reduced problems predictions overestimate the concentration across the remainder of the tissue. Overall, for the chosen parameter values in this study, the two reduced problems give close predictions for the solute concentration in the tissue and agree very well with the full model near the vasculature (within 0.5 μm of tissue). This means the two reduced models successfully predict the solute concentration in the tumor regions with dense capillaries. Furthermore, we compare the GNR radial flux at the tissue/wall interface computed by the three models in the Figs. 2.6 (C), (D). Fig. 2.6 (C) shows that the solute radial flux predictions at the tissue/wall interface computed by the

three models are approximately the same within the first two hours post GNR injection and within the last four hours of the simulation time considered in this study, however, within the time in between the reduced models predict lower flux values compared to the full model. Moreover, the three models predict an exponential decay for the radial flux at the tissue/wall interface. The axial profiles for the radial flux for different times are shown in Fig. 2.6 (D). This figure shows that the flux decays approximately linearly, but reverses its direction to be from tissue into the vessel near the vessel outlet at large times post injection which indicate that the local GNR concentration saturates in the tissue and eventually becomes larger than the concentration in the vessel. Overall, the flux predicted by either of the reduced models is a reasonable approximation to the full model, according to the parameter values chosen in this study. Hence, we use the two pore model to define the GNR flux at the macroscale model provided in chapter 3. At the macroscale study we prefer to use the flux boundary condition calculated from the two pore model (reduced model 2) over imposing the continuity of concentration at the vessel/tissue interface as the two pore model can more easily incorporate the tumor vasculature density (which is a key parameter in the drug delivery models as discussed in Secs. 3.5 and 3.5.3).

2.10 Conclusion

In this chapter we investigated the solute transport in a single vessel surrounded by tissue at the microscale. We used the asymptotic analysis to develop analytical solutions for the fluid transport equations and numerical solutions for the solute transport equations. We investigated the solute concentration in the tissue and the solute extravasation flux using our model. In our model we imposed the continuity of solute concentration and flux at the two interfaces of the vessel wall. We compared our model results with the solution of the transport problem in the tissue using the two pore model boundary condition at the vessel wall which showed a reasonable agreement very close to the vessel, but not in the deep tissue. We also investigated the solute concentration in the tissue using the continuity concentration boundary condition at the vessel wall which agreed very well with the two pore model, for the chosen values of parameters in this study.

However, in this model we applied some simplifying assumptions to find analytical solutions for the fluid transport equations. In particular, we assumed that the tissue is very thin at the same length scale of the vessel thickness. This assumption is valid only in the presence of high dense vasculature where vessels are very close to each other.

We also neglected the osmotic pressure (which depends on the solute transvascular flux) to decouple the fluid transport and solute transport models.

This model is a preliminary model to examine the mathematical expressions for the solute flux boundary conditions used vastly in the literature, such as the two pore model.

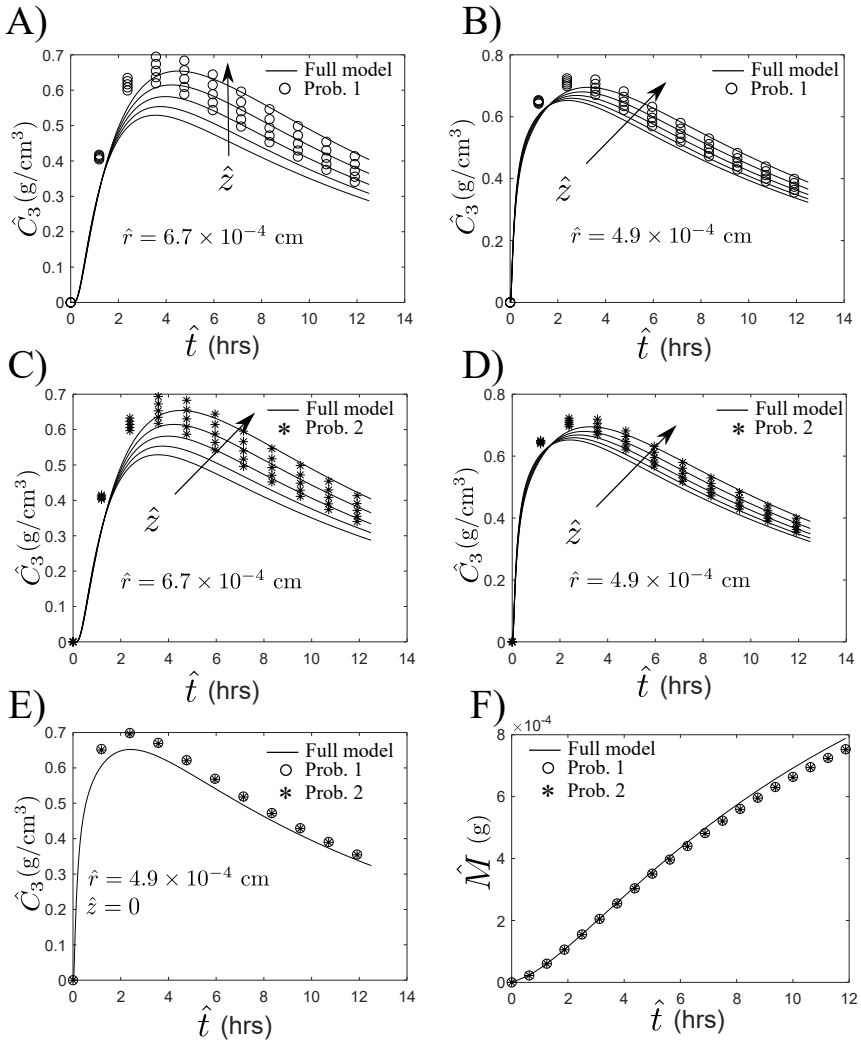

Figure 2.5: Prediction comparison of the solute transport problem at the microscale to the two reduced problems using the parameter values in Table 2.1. A comparison of the concentration predictions in the tissue calculated through the full model (see Sec. 2.6) and the reduced problem 1 (see Sec. 2.8.1) at: A) $\hat{r} = 6.7 \times 10^{-4}$ and B) $\hat{r} = 4.9 \times 10^{-4}$ for different axial mesh points. A comparison of the concentration predictions in the tissue calculated through the full model and the reduced problem 2 (see Sec. 2.8.2) at: C) $\hat{r} = 6.7 \times 10^{-4}$ and D) $\hat{r} = 4.9 \times 10^{-4}$ for different axial mesh points. E) A comparison of the concentration predictions in the tissue calculated through the full model and the reduced problem 2 at $\hat{r} = 6.7 \times 10^{-4}$ for different axial mesh points. F) A comparison of the temporal total mass accumulated in the tissue calculated through the full model and the reduced problem 2.

The next step will be investigating the case of thick tissue and including the osmotic pressure as a function of solute transvascular concentration.

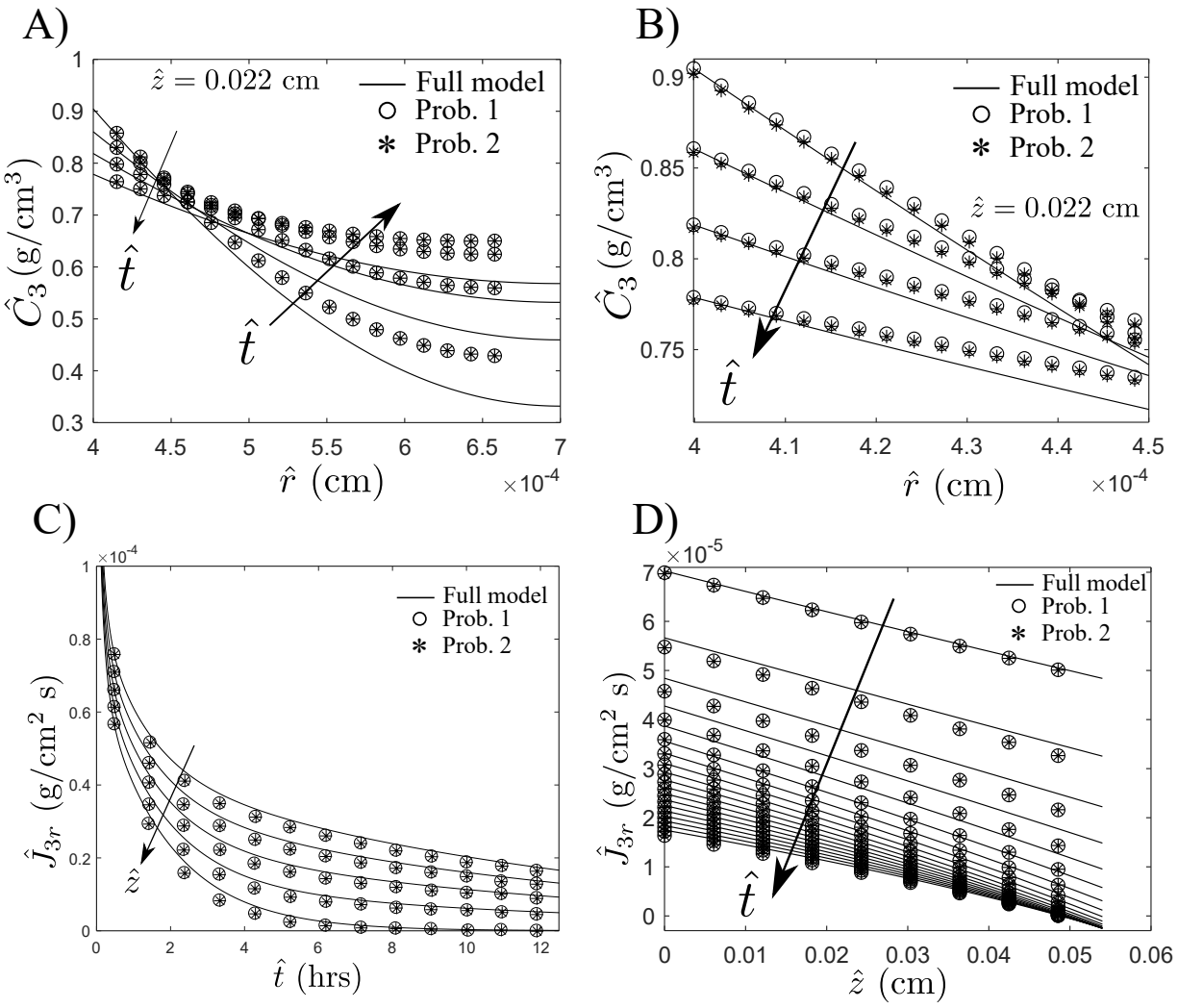

Figure 2.6: Prediction comparison of the GNR concentration and flux at the tissue/wall computed by the full model and the two reduced models using the parameter values in Table 2.1. A) The concentration profiles across the tissue for different time steps. B) The concentration profiles very close to the wall (a zoom in for (A)). C) The temporal radial flux at the tissue/wall for different axial positions. D)The axial profiles for the solute flux for different time steps.

Chapter 3

Mathematical Model for GNR Delivery to Tumors

3.1 Introduction

Delivering gold nanorods (GNRs) to tumors is an essential process in the photothermal therapy [92]. However, GNRs have to overcome some biological barriers such as: GNR clearance from the blood by the immune system [2], elevated interstitial pressure in tumors which restricts GNR extravasation in the tumors [66] and the maximal tumor capacity for internalizing GNRs [40]. So, this needs comprehensive theoretical and experimental studies to optimize the GNR delivery to tumors.

The GNR blood half life can be controlled by decorating GNRs with hydrophilic polymers [15]. So, the influence of GNR blood half life on GNR delivery to tumors needs to be investigated theoretically and experimentally. In addition, the tumor vasculature density and the vessel pore size play a vital role in breaking the interstitial pressure barrier [20]. Moreover, the efficacy of passive targeting needs to be investigated and compared to active targeting which is restricted by the available tumor receptors.

Baxter and Jain [8,10] provided a framework for modeling macroscopic fluid and solute transport across tumors. They modeled the solute interaction with tumor cells, but they neglected solute internalization by tumor cells. They found that the interstitial pressure has a significant impact on the solute concentration in the absence of the binding ligands. In addition, introducing the binding ligands reduced the solute accumulation in the tumor. A more sophisticated model for drug interaction with tumor cells was provided by Goodman et al. [2008] [34]. They modeled NP delivery to spheroids mathematically and validated their results *in vitro*. However, they assumed in their model that tumor cells can internalize an unlimited number of NPs. Chou et al. [2013] [23] modeled mathematically NP delivery to tumors *in vivo* (at the microscale). They assumed that NPs in the interstitium can be directly internalized into the tumor cells (without binding to cell receptors).

They found that increasing tumor vascular permeability enhances the NP accumulation in the vascularised regions in the tumor, while increasing NP diffusivity increases the both NP accumulation and NP homogeneity across the tumor.

In this chapter we introduce a mathematical model (at the macroscale) to investigate GNR delivery to tumors prior to laser irradiation. In this model we mimic both methods used for GNR administration to patients which consist of either intravenous and intra-tumoral injections. We focus on the intravenous injection since it is convenient for deep sited tumors which cannot be treated by tumor resection (cutting out a tumor through surgery). Modeling GNR transport in the bloodstream is complicated, so we approximate the transient GNR concentration in the bloodstream using an exponential decay model which is validated by our asymptotic analysis in Sec. 2.8. In addition, we use the two pore approximation to calculate the GNR extravasation flux from tumor vasculature, which we validated against the predictions of the asymptotic model derived from the basic fluid mechanical equations at the microscale (see Sec. 2.9). We then model the GNR transport across the tumor and the surrounding tissue, where we consider active and passive tumor targeting techniques (Sec. 3.2). We then investigate the model parameter space to discover how GNR delivery to tumors can be optimized (Sec. 3.5).

3.2 The Model

We consider a spherical (partially vascularised) tumor of fixed radius $\hat{R}$ surrounded by an annulus of healthy vascularized tissue of thickness $\hat{R}_\infty - \hat{R}$, see Fig. 3.1. We model the presence of vasculature in the tumor and tissue as a continuous and uniformly distributed source of both interstitial fluid and GNRs. We choose GNRs rather than other types of nanoparticles (NPs) due to their optical thermal properties [72]. We assume that these GNRs can access the tumor and the normal tissue from the vasculature by advection with the flow into the tumor from the bloodstream and also by diffusion across the capillary walls. In this model we assume that the system is spherically symmetric and denote $\hat{r}$ as the radial coordinate, so the tumor domain is $0 \leq \hat{r} \leq \hat{R}$ and the domain of healthy tissue is $\hat{R} \leq \hat{r} \leq \hat{R}_\infty$. Furthermore, we consider that the radius of the avascular tumor core is $\hat{r}_n \leq \hat{R}$ (i.e. the width of the tumor vascular rim is $\hat{R} - \hat{r}_n$). We denote $\hat{t}$ as time.

We study the problem of targeting a tumor with GNRs treated with antibodies which can only bind to malignant cells. Therefore, in the tumor zone ($0 \leq \hat{r} \leq \hat{R}$) GNRs can diffuse through the extracellular matrix, bind to tumor cell receptors and get engulfed by these cells, as detailed in Fig 3.1. On the other hand, in the healthy tissue region ($\hat{R} \leq \hat{r} \leq \hat{R}_\infty$) GNRs can only diffuse through the interstitial compartment and cannot react with the healthy cells as they do not have compatible receptors.

We now describe the constituents of the model in detail. We first describe the blood

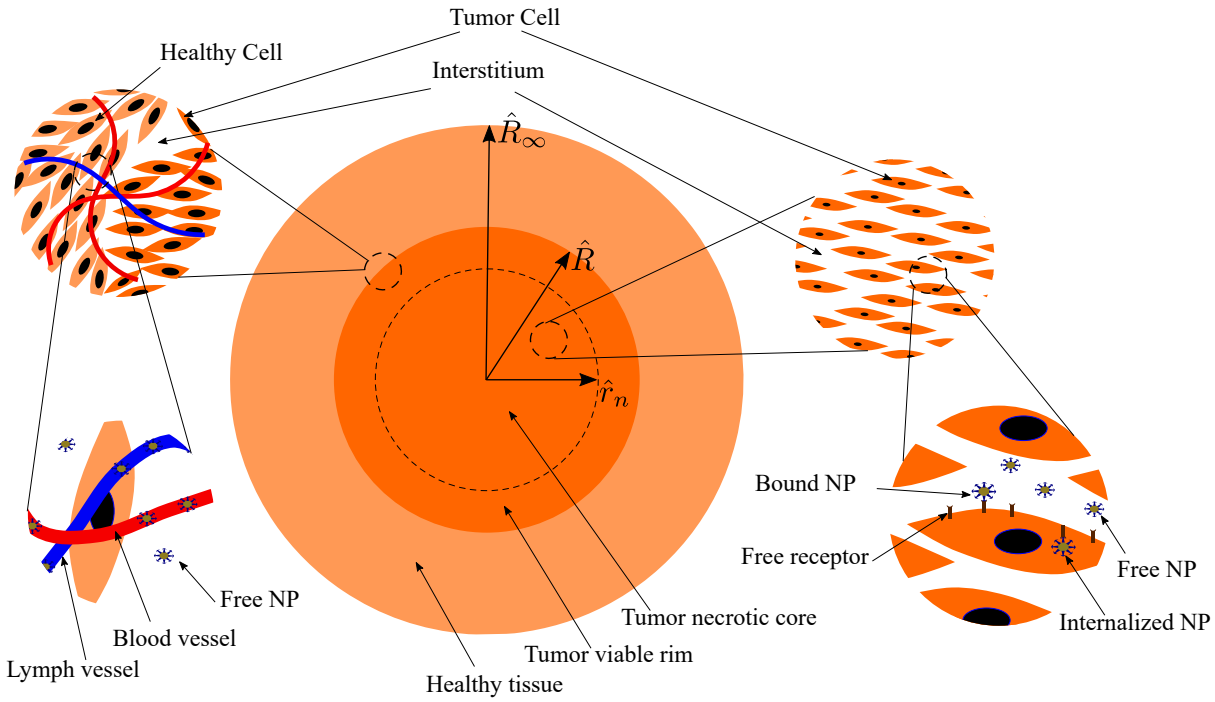

Figure 3.1: The domain of a tumor surrounded by normal tissue.

and lymphatic phases (Sec. 3.2.1). We then describe the interstitial flow in both the healthy and tumor tissue (Sec. 3.2.2). After that we model the GNR transport in the both healthy tissue (Sec. 3.2.4) and the tumor tissue (Sec. 3.2.6). Then, we introduce the numerical method used to solve our model (Sec. 3.2.10) and describe our parameter estimation (Sec. 3.3). We discuss the results of this model in Sec. 3.4.

In the model we denote quantities specific to the tumor with the index (T), and specific to the normal tissue with the index (N). In both regions we assume the tissue is formed by four phases, cells (volume fraction $\phi_c^{(j)}$), fluid (volume fraction $\phi_f^{(j)}$), blood vessels (volume fraction $\phi_b^{(j)}$) and lymph vessels (volume fraction $\phi_l^{(j)}$), such that $\phi_c^{(j)}+\phi_f^{(j)}+\phi_b^{(j)}+\phi_l^{(j)}=1$, i.e. there are no voids. Furthermore, the timescales considered in this study are very short compared to the timescale of the tumor growth and vasculature density change. Therefore, the cell, fluid, blood and lymph volume fractions are constants in our study as well as the tumor radius.

In the following all variables are functions of the radial coordinate $\hat{r}$ and time $\hat{t}$, unless specified otherwise. All variables and their units are listed in Table 3.1.

3.2.1 Blood and Lymph systems

Blood flows through the capillaries due to the pressure difference between the supplying arteries $(\hat{P}_{in})$ and the draining veins $(\hat{P}_{out})$, see Fig. 3.2. In this chapter we consider a zero dimensional problem for blood flow in capillaries, where for simplicity, we consider that the blood pressure is constant and the blood velocity is zero.

Therefore, we assume that the pressure in the blood (denoted $\hat{P}_v$) and lymph (denoted $\hat{P}_l$) have constant values in both tumor and tissue. That means there is no flow in either the vasculature or the lymphatic systems in the radial direction $\hat{r}$. However, we still build in features driven by the flow based on our analysis in chapter 2 (such as GNR extravasation flux out of the vasculature into the surrounding tissue).

In addition, we assume that the GNR vascular concentration is spatially uniform (i.e. $\hat{C}_v = \hat{C}_v(t)$), but a decreasing function of time due to GNR clearance from the bloodstream. We consider a bolus injection of GNRs into the vasculature at initial concentration $\hat{C}_{v0}^{(j)}$ at time $\hat{t} = 0$ (without loss of generality). The GNR concentration in the vasculature decreases due to clearance by the liver and spleen at fixed rate $\hat{\tau}$ (consistent with the assumptions of Mpekris et al. [2015] [76]).

Furthermore, the GNR mass in the vasculature decreases due to extravasation into the tumor (with mass flux $\breve{J}_{tot}^{(T)}$) and tissue (with mass flux $\breve{J}_{tot}^{(N)}$), hence we can write the following ODE for the vascular GNR concentration,

$$\frac{d\hat{C}_v^{(j)}}{d\hat{t}} = -\frac{1}{\hat{\tau}}\hat{C}_v^{(j)} - (\breve{J}_{tot}^{(T)} + \breve{J}_{tot}^{(N)}), \qquad (j = N, T). \tag{3.1}$$

In previous models $\hat{\tau}$ is chosen so that clearance takes place on a timescale of hours [20]. We examine the influence of this decay rate on our predictions in the Secs. 3.4.1 and 3.4.2 below. The transient GNR total vascular flux in the tumor ($\breve{J}_{tot}^{(T)}$) and in healthy tissue ($\breve{J}_{tot}^{(N)}$) are calculated from

$$\breve{J}_{tot}^{(T)} = 4\pi \int_0^{\hat{R}} H^{(T)}(\hat{r} - \hat{r}_n) \frac{\breve{J}_1^{(T)}}{\hat{V}^{(T)}} \hat{r}^2 \mathrm{d}\hat{r}, \tag{3.2}$$

$$\breve{J}_{tot}^{(N)} = 4\pi \int_{\hat{R}}^{\hat{R}_\infty} \frac{\breve{J}_1^{(N)}}{\hat{V}^{(N)}} \hat{r}^2 \mathrm{d}\hat{r}, \tag{3.3}$$

where $\breve{J}_1^{(j)}$ is the GNR partial perfusion mass flux out of the vasculature normalized by total volume $\hat{V}^{(j)}$ $(j = T, N)$, $\hat{r}_n$ is the radius of the avascular region in the tumor and $H(r - r_n)^{(T)}$ is the Heaviside step function which is defined as

$$H(\hat{r} - \hat{r}_n)^{(T)} = \begin{cases} 0, & 0 \le \hat{r} \le \hat{r}_n, \\ 1, & \hat{r} \ge \hat{r}_n. \end{cases} \tag{3.4}$$

We use the Heaviside step function (defined in the preceding equation) to define the GNR extravasation flux in the tumor rim only (at $\hat{r} \ge \hat{r}_n$) since we considered the tumor core as an avascular tissue (at $0 \le \hat{r} \le \hat{r}_n$).

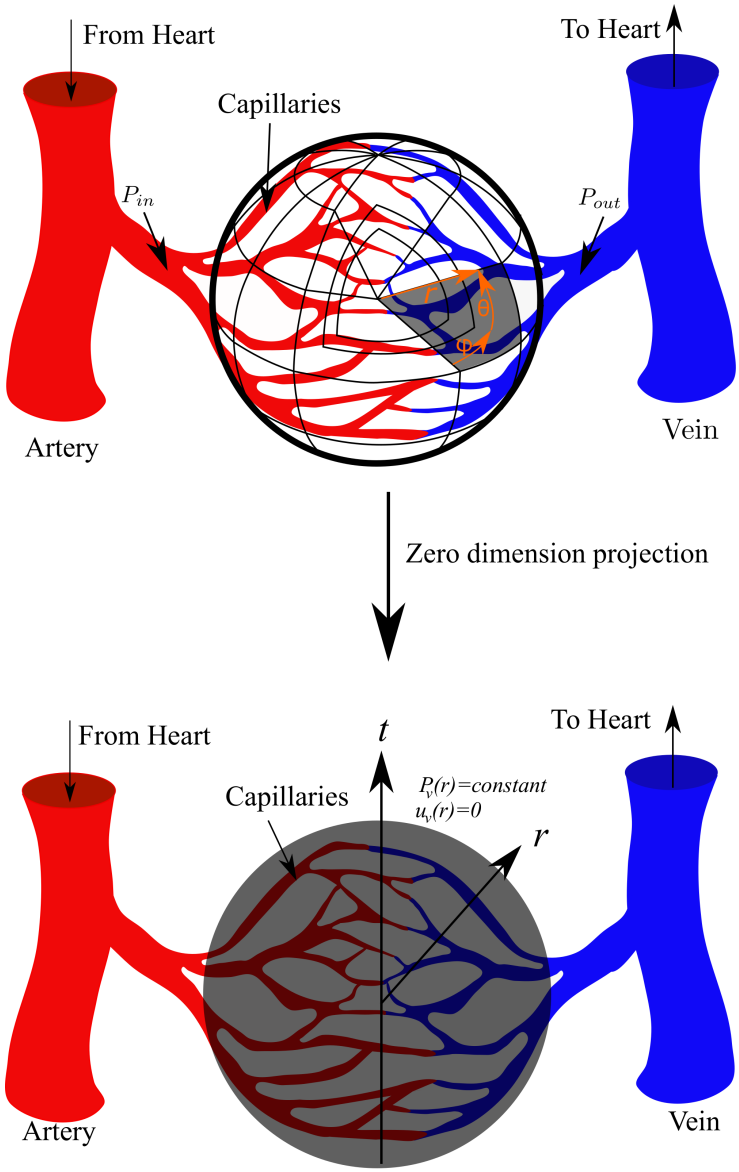

Figure 3.2: The vasculature projection in the spherically symmetric model.

3.2.2 Macroscopic Fluid Transport

To form a macro-scale continuum model for the fluid transport in vascular tissues we average out the variations which occur over the microscopic length scale (the intercapillary distance, $O(100\ \mu\text{m})$ as considered in Chapter 2) which is very small compared to the tumor radius length scale, $O(1\ \text{cm})$, see Baxter and Jain [1989] [8]. At the macro-scale we apply Darcy's law for the interstitial fluid flow in the tumor and normal tissue [105]. The interstitial flow velocity in the radial direction (denoted $\hat{u}^{(j)},\ j = N,\ T$) in the tumor and the normal tissue as a function of the interstitial pressure ($\hat{P}_i^{(j)},\ j = N,\ T$) can be

written as [76],

$$\phi_f^{(j)}\hat{u}^{(j)} = -\hat{K}^{(j)}\frac{\partial \hat{P}_i^{(j)}}{\partial \hat{r}}, \qquad (j = N, T), \tag{3.5}$$

where $\hat{K}^{(j)}$ is the hydraulic conductivity of the interstitium.

The volume of interstitial fluid increases due to flow in from the blood phase and decreases due to flux out into the lymph phase. Thus, conservation of mass for the interstitial fluid is given by [8],

$$\frac{1}{\hat{r}^2}\frac{\partial}{\partial \hat{r}}(\hat{r}^2\phi_f^{(j)}\hat{u}^{(j)}) = H^{(j)}(\hat{r} - \hat{r}_n)\left(\frac{\hat{Q}_v^{(j)}}{\hat{V}^{(j)}} - \frac{\hat{Q}_l^{(j)}}{\hat{V}^{(j)}}\right), \qquad (j = N, T), \tag{3.6}$$

where $\hat{Q}_v$ is the transvascular volumetric flow rate out of the vasculature into the interstitium (driven by the pressure difference across the capillary walls) normalized using total volume $\hat{V}^{(j)}$ $(j = T, N)$ [8] and $\hat{Q}_l$ is the volumetric flow rate out of the interstitium into the lymphatic system, which is also normalized by $\hat{V}^{(j)}$. To capture the transvascular flux $(\hat{Q}_v)$ we use Starling's law [33, 104], dependent on both the local pressure drop between the interstitium $(\hat{P}_i)$ and the vasculature $(\hat{P}_v)$, and also the difference between the osmotic pressure in the plasma (π_v) and in the tissue (π_i) which takes the form

$$\hat{Q}_v^{(j)} = \hat{L}_{pv}^{(j)}\hat{S}_v^{(j)}(\hat{P}_v - \hat{P}_i^{(j)} - \sigma_T^{(j)}(\hat{\pi}_v - \hat{\pi}_i^{(j)})) \equiv \hat{L}_{pv}^{(j)}\hat{S}_v^{(j)}(\hat{P}_e - \hat{P}_i^{(j)}), \quad (j = N, T), \tag{3.7}$$

$$\hat{P}_e^{(j)} = \hat{P}_v - \sigma_T^{(j)}(\hat{\pi}_v - \hat{\pi}_i^{(j)}), \qquad (j = N, T), \tag{3.8}$$

where $\hat{S}_v$ is the vasculature surface area, $\hat{L}_{pv}$ is the hydraulic conductivity of the microvascular wall, σ_T is the average osmotic reflection coefficient for plasma proteins and $\hat{P}_e$ is the net filtration pressure. In this study we ignore the variation of the osmotic pressure due to the change in the GNR transvascular concentration, so we consider constant osmotic pressures in both the tumor and surrounding tissue. This approximation decouples the fluid transport and GNR transport models.

Similarly, the flux from the tissue into the lymphatic system is assumed to be proportional to the pressure difference between the interstitium and the hydrostatic pressure of the lymphatics $(\hat{P}_l)$ [8] in the form

$$\hat{Q}_l^{(j)} = \hat{L}_{pl}^{(j)}\hat{S}_l^{(j)}(\hat{P}_i^{(j)} - \hat{P}_l^{(j)}), \qquad (j = N, T), \tag{3.9}$$

where $\hat{S}_l$ is the lymphatic surface area and $\hat{L}_{pl}$ is the hydraulic conductivity of the lymphatic wall.

For constant vascular and lymphatic pressures, substituting Eqs. (3.5), (3.7) and (3.9) into Eq. (3.6) we obtain one-dimensional PDEs for the interstitial pressure in both the

healthy and tumor regions, in the form

$$\frac{1}{\hat{r}^2}\frac{\partial}{\partial \hat{r}}\left(\hat{r}^2\frac{\partial \hat{P}_i^{(j)}}{\partial \hat{r}}\right) = \\ -\frac{H^{(j)}(\hat{r}-\hat{r}_n)}{\hat{K}^{(j)}}\left(\hat{L}_{pv}^{(j)}\frac{\hat{S}_v^{(j)}}{\hat{V}^{(j)}}(\hat{P}_e-\hat{P}_i^{(j)}) - \hat{L}_{pl}^{(j)}\frac{\hat{S}_l^{(j)}}{\hat{V}^{(j)}}(\hat{P}_i^{(j)}-\hat{P}_l^{(j)})\right), \quad (j=N,T). \tag{3.10}$$

On the right hand side of the preceding equation we group $\hat{P}_i^{(j)}$ as a common factor, so we get

$$\frac{1}{\hat{r}^2}\frac{\partial}{\partial \hat{r}}\left(\hat{r}^2\frac{\partial \hat{P}_i^{(j)}}{\partial \hat{r}}\right) = \\ \frac{H^{(j)}(\hat{r}-\hat{r}_n)}{\hat{K}^{(j)}\hat{V}^{(j)}}\left((\hat{L}_{pv}^{(j)}\hat{S}_v^{(j)}+\hat{L}_{pl}^{(j)}\hat{S}_l^{(j)})\hat{P}_i^{(j)} - (\hat{L}_{pv}^{(j)}\hat{S}_v^{(j)}\hat{P}_e+\hat{L}_{pl}^{(j)}\hat{S}_l^{(j)}\hat{P}_l^{(j)})\right), \quad (j=N,T). \tag{3.11}$$

Hence, we can write the preceding equation in the form

$$\frac{1}{\hat{r}^2}\frac{\partial}{\partial \hat{r}}\left(\hat{r}^2\frac{\partial \hat{P}_i^{(j)}}{\partial \hat{r}}\right) = \frac{\alpha^{(j)}}{\hat{R}^2}(\hat{P}_i^{(j)}-\hat{P}_{ss}^{(j)}), \qquad (j=N,T), \tag{3.12}$$

where

$$\alpha^{(j)} = \hat{R}^2 H^{(j)}(\hat{r}-\hat{r}_n)\frac{\hat{L}_{pv}^{(j)}\hat{S}_v^{(j)}+\hat{L}_{pl}^{(j)}\hat{S}_l^{(j)}}{\hat{K}^{(j)}\hat{V}^{(j)}}, \qquad (j=N,T), \tag{3.13}$$

$$\hat{P}_{ss}^{(j)} = \frac{\hat{L}_{pv}^{(j)}\hat{S}_v^{(j)}\hat{P}_e^{(j)}+\hat{L}_{pl}^{(j)}\hat{S}_l^{(j)}\hat{P}_l^{(j)}}{\hat{L}_{pv}^{(j)}\hat{S}_v^{(j)}+\hat{L}_{pl}^{(j)}\hat{S}_l^{(j)}}, \qquad (j=N,T), \tag{3.14}$$

here $\alpha^{(j)}$ is the ratio of the vasculature to the interstitium hydraulic conductivities; and $\hat{P}_{ss}$ is the interstitial pressure required for the transvascular flux to identically balance the translymphatic flux.

For spatially uniform vascular pressure ($\hat{P}_v$) and lymphatic pressure ($\hat{P}_l$), this PDE can be solved analytically [8], but we consider only a numerical approach here.

3.2.3 Boundary Conditions for Macroscopic Fluid Transport

Following Baxter and Jain [1990] [9], we apply symmetry boundary conditions at the center of the tumor, continuity of pressure and velocity, and a constant interstitial pressure ($\hat{P}_{ss}^{(N)}$, the interstitial pressure which results in equilibrium between vascular and lymphatic

fluxes) at the outer edge of the healthy tissue. These boundary conditions take the form

$$\frac{\partial \hat{P}_i^{(T)}}{\partial \hat{r}} = 0, \qquad (\hat{r} = 0), \tag{3.15}$$

$$-\hat{K}^{(T)}\frac{\partial \hat{P}_i^{(T)}}{\partial \hat{r}} = -\hat{K}^{(N)}\frac{\partial \hat{P}_i^{(N)}}{\partial \hat{r}}, \quad \hat{P}_i^{(T)} = \hat{P}_i^{(N)}, \qquad (\hat{r} = \hat{R}), \tag{3.16}$$

$$\hat{P}_i^{(N)} = \hat{P}_{ss}^{(N)}, \qquad (\hat{r} = \hat{R}_\infty). \tag{3.17}$$

3.2.4 GNR Transport in the Healthy Tissue

To form a macro-scale continuum model for the GNR transport in the healthy tissue we average the variations of intercapillary distances over some region that is small compared to the tumor radius. Following Baxter and Jain [1989] [8], we model GNR concentration (in the total healthy tissue volume, $\hat{C}^{(N)}$) equation in the healthy tissue using an advection-diffusion equation with a source term for GNRs from the uniformly distributed vasculature and a sink term into the lymphatic system across the whole normal tissue, in the form ($\hat{R} \leq \hat{r} \leq \hat{R}_\infty$)

$$\frac{\partial \hat{C}^{(N)}}{\partial \hat{t}} + \frac{1}{\hat{r}^2}\frac{\partial}{\partial \hat{r}}(\hat{r}^2 \hat{u}^{(N)} \hat{C}^{(N)}) = \frac{1}{\hat{r}^2}\frac{\partial}{\partial \hat{r}}\left(\hat{r}^2 \hat{D}^{(N)}\frac{\partial \hat{C}^{(N)}}{\partial \hat{r}}\right) + \frac{\breve{J}_1^{(N)}}{\hat{V}^{(N)}} - \frac{\breve{J}_2^{(N)}}{\hat{V}^{(N)}}, \tag{3.18}$$

where $\hat{D}^{(N)}$ is the diffusion coefficient of GNRs in the healthy interstitial space, $\breve{J}_1$ is the GNR mass flux out of the vasculature into the tissue and $\breve{J}_2$ is the GNR mass flux out of the tissue into the lymph system. The GNR mass flux into the lymphatic system is assumed to be proportional to GNR concentration in the interstitium [9] in the form

$$\breve{J}_2^{(j)} = \hat{Q}_l^{(j)} \hat{C}^{(j)}, \qquad (j = N, T). \tag{3.19}$$

In this study we define the GNR transvascular flux ($\breve{J}_1^{(N)}/V^{(N)}$) according to the two pore model which has been validated (at the microscale) against the full asymptotic model introduced in chapter 2. We derive the corresponding GNR transvascular flux at the macroscale [51, 83] following the same technique we used in Sec. 2.7 (at the microscale).

3.2.5 The Two Pore Model at the Macroscale

We assume that the GNR transvascular flux ($\breve{J}_1$) across the vessel wall is approximately steady and homogeneous, where we assume that the vessel wall thickness ($\Delta\hat{\eta}$) is very thin. Therefore, according to Fick's law the GNR flux across the vessel wall can be written in

terms of diffusion and advection in the form

$$\breve{J}_1^{(j)} = -\hat{D}_w^{(j)}\hat{S}_v^{(j)}\frac{d\hat{C}_w^{(j)}}{d\hat{\eta}} + \hat{Q}_v^{(j)}(1-\breve{\sigma}^{(j)})\hat{C}_w^{(j)}, \qquad (j=N,T), \tag{3.20}$$

where $\hat{D}_w^{(j)}$ is the GNR diffusion coefficient in the vessel wall, $\breve{\sigma}^{(j)}$ is the osmotic reflection coefficient of GNRs (in either the tumor ($j=T$) or the healthy tissue ($j=N$)) and $\hat{C}_w^{(j)}$ is the GNR concentration across the vessel wall which is a function of the local spatial coordinate $\hat{\eta}$. Rearranging the preceding equation into the form of a nonhomogeneous first order ODE we get

$$\frac{d\hat{C}_w^{(j)}}{d\hat{\eta}} - \frac{\hat{Q}_v^{(j)}}{\hat{D}_w^{(j)}\hat{S}_v^{(j)}}(1-\breve{\sigma}^{(j)})\hat{C}_w^{(j)} = -\frac{\breve{J}_1^{(j)}}{\hat{D}_w^{(j)}\hat{S}_v^{(j)}}, \qquad (j=N,T). \tag{3.21}$$

This equation can be integrated using the integrating factor $\exp(-\hat{Q}_v^{(j)}(1-\breve{\sigma}^{(j)})\hat{\eta}/(\hat{D}_w^{(j)}\hat{S}_v^{(j)}))$, so we obtain

$$\hat{C}_w^{(j)}\exp\left(-\frac{\hat{Q}_v^{(j)}}{\hat{D}_w^{(j)}\hat{S}_v^{(j)}}(1-\breve{\sigma}^{(j)})\hat{\eta}\right)\Bigg|_0^{\Delta\hat{\eta}} = \int_0^{\Delta\hat{\eta}}\frac{\breve{J}_1^{(j)}}{\hat{D}_w^{(j)}\hat{S}_v^{(j)}}\exp\left(-\frac{\hat{Q}_v^{(j)}}{\hat{D}_w^{(j)}\hat{S}_v^{(j)}}(1-\breve{\sigma}^{(j)})\hat{\eta}\right)\mathrm{d}\hat{\eta}, \quad (j=N,T), \tag{3.22}$$

which can be written in the form

$$\hat{C}^{(j)}\exp\left(-\frac{\hat{Q}_v^{(j)}}{\hat{D}_w^{(j)}\hat{S}_v^{(j)}}(1-\breve{\sigma}^{(j)})\Delta\hat{\eta}\right) - \hat{C}_v^{(j)} = \frac{\breve{J}_1^{(j)}}{\hat{Q}_v^{(j)}(1-\breve{\sigma}^{(j)})}\left(\exp\left(-\frac{\hat{Q}_v^{(j)}}{\hat{D}_w^{(j)}\hat{S}_v^{(j)}}(1-\breve{\sigma}^{(j)})\Delta\hat{\eta}\right)-1\right), \quad (j=N,T). \tag{3.23}$$

Thus we can write the GNR transvascular flux across the vessel wall in the form

$$\breve{J}_1^{(j)} = \hat{Q}_v^{(j)}(1-\breve{\sigma}^{(j)})\frac{\hat{C}_v^{(j)} - \hat{C}^{(j)}e^{-\breve{P}e^{(j)}}}{1-e^{-\breve{P}e^{(j)}}}, \qquad (j=N,T), \tag{3.24}$$

where $\hat{C}_v^{(j)}$ is the GNR vascular concentration, $\hat{C}^{(j)}$ is the free GNR concentration in the interstitium and $\breve{P}e$ is the effective local transmural Péclet number across the vascular wall, representing the ratio of advection to diffusion and is defined as [10],

$$\breve{P}e^{(j)} = \frac{\hat{Q}_v^{(j)}(1-\breve{\sigma}^{(j)})\Delta\hat{\eta}}{\hat{D}_w^{(j)}\hat{S}_v^{(j)}} \equiv \frac{\hat{Q}_v^{(j)}(1-\breve{\sigma}^{(j)})}{\breve{P}^{(j)}\hat{S}_v^{(j)}}, \quad \breve{P} = \frac{\hat{D}_w^{(j)}}{\Delta\hat{\eta}}, \qquad (j=N,T), \tag{3.25}$$

where $\breve{P}$ is the vascular permeability coefficient. The experimentally estimated mathematical correlation between $\breve{P}$ and $\breve{\sigma}$ is defined in the Appendix A.

In this study we assume the GNRs are typically larger than vasculature pore size in the healthy tissue. Therefore, there is no GNR transvascular flux in healthy tissue (i.e. $\breve{J}_1^{(N)} = 0$).

3.2.6 GNR Transport in the Tumor

In a similar manner to Sec. (3.2.4), inside the tumor we assume that free GNRs ($\hat{C}^{(T)}$) can diffuse through the extracellular matrix, but can also bind to cell surface receptors and become engulfed by these cells. We denote the concentration of bound GNRs by $\hat{C}_b^{(T)}$, cell receptors by $\hat{C}_{bs}^{(T)}$ and the internalized GNRs by $\hat{C}_i^{(T)}$. The transport equation for $\hat{C}^{(T)}$ in the tumor will be very similar to that in the normal tissue ($\hat{C}^{(N)}$) with additional binding and disassociation terms [105], in the form ($0 \leq \hat{r} \leq \hat{R}$)

$$\frac{\partial \hat{C}^{(T)}}{\partial \hat{t}} + \frac{1}{\hat{r}^2}\frac{\partial}{\partial \hat{r}}(\hat{r}^2 \hat{u}^{(T)} \hat{C}^{(T)}) = \frac{1}{\hat{r}^2}\frac{\partial}{\partial \hat{r}}(\hat{r}^2 \hat{D}^{(T)} \frac{\partial \hat{C}^{(T)}}{\partial \hat{r}}) + H(\hat{r} - \hat{r}_n)(\frac{\breve{J}_1^{(T)}}{\hat{V}^{(T)}} - \frac{\breve{J}_2^{(T)}}{\hat{V}^{(T)}}) - \frac{\hat{k}_a \hat{C}_{bs}^{(T)} \hat{C}^{(T)}}{\phi_f^{(T)}} + \hat{k}_d \hat{C}_b^{(T)}, \quad (3.26)$$

where $\hat{k}_a$ is binding coefficient of GNRs to available receptors and $\hat{k}_d$ is the corresponding dissociation rate. A similar model was previously proposed by Goodman et al. [2008] [34] for nanodrug delivery to tumors with radially dependent tumor volume fraction $\phi_f^{(T)}$ which is accessible to GNRs. This macro-scale equation can be derived from the micro-scale using the method of volume averaging, where $\hat{C}^{(T)}$ would be a superficial average and the source terms normalized appropriately by the tumor volume fraction accessible to GNRs [8].

The concentration of GNRs bound to the surface of the tumor cells ($\hat{C}_b^{(T)}$) can be calculated from the following equation

$$\frac{\partial \hat{C}_b^{(T)}}{\partial \hat{t}} = \frac{\hat{k}_a \hat{C}_{bs}^{(T)} \hat{C}^{(T)}}{\phi_f^{(T)}} - \hat{k}_d \hat{C}_b^{(T)} - \hat{k}_i f(\hat{C}_i^{(T)}) \hat{C}_b^{(T)}, \qquad (0 \leq \hat{r} \leq \hat{R}), \quad (3.27)$$

where $\hat{C}_i^{(T)}$ is the concentration of the internalized GNRs, $\hat{k}_i$ is the internalization rate and $f(\hat{C}_i^{(T)})$ is a dimensionless function of internalized GNR concentration that saturates as $\hat{C}_i^{(T)}$ approaches $\hat{C}_{i_{max}}$ (a constant). In this case we choose the simple saturating function

$$f(\hat{C}_i^{(T)}) = \frac{\hat{C}_{i_{max}} - \hat{C}_i^{(T)}}{\hat{C}_{i_{max}}}. \quad (3.28)$$

Hence, for small $\hat{C}_i^{(T)}$ ($\hat{C}_i^{(T)} \leq \hat{C}_{i_{max}}$), the loss of bound GNRs due to internalization

is a constant ($\hat{k}_i$) proportion of $\hat{C}_b^{(T)}$, while as $\hat{C}_i^{(T)} \to \hat{C}_{i_{max}}$ the rate of internalization approaches zero i.e. the tissue is saturated and cannot internalize any more GNRs. We introduced the maximal GNR capacity in this study since this phenomenon has been demonstrated experimentally [40]. The role of the parameter $\hat{C}_{i_{max}}$ is examined below.

To solve for the concentration of free receptors (to which the GNRs can bind), $\hat{C}_{bs}^{(T)}$, we write the following equation, where the rate of change of the concentration of binding sites is the negative of the R.H.S. of Eq. (3.27),

$$\frac{\partial \hat{C}_{bs}^{(T)}}{\partial \hat{t}} = -\frac{\hat{k}_a \hat{C}_{bs}^{(T)} \hat{C}^{(T)}}{\phi_f^{(T)}} + \hat{k}_d \hat{C}_b^{(T)} + \hat{k}_i f(\hat{C}_i^{(T)}) \hat{C}_b^{(T)}, \qquad (0 \le \hat{r} \le \hat{R}). \tag{3.29}$$

By conservation of mass, the concentration of internalized GNRs ($\hat{C}_i^{(T)}$) must then satisfy

$$\frac{\partial \hat{C}_i^{(T)}}{\partial \hat{t}} = \hat{k}_i f(\hat{C}_i^{(T)}) \hat{C}_b^{(T)}, \qquad (0 \le \hat{r} \le \hat{R}). \tag{3.30}$$

The total concentration of GNRs in the tumor ($\hat{C}_{tot}^{(T)}$) and healthy tissue ($\hat{C}_{tot}^{(N)}$) take the form

$$\hat{C}_{tot}^{(T)} = \phi_f^{(T)} \hat{C}^{(T)} + \phi_b^{(T)} \hat{C}_b^{(T)} + \phi_c^{(T)} \hat{C}_i^{(T)}, \tag{3.31}$$

$$\hat{C}_{tot}^{(N)} = \phi_f^{(N)} \hat{C}^{(N)}. \tag{3.32}$$

3.2.7 Boundary Conditions for Macroscopic GNR transport

We consider no-flux boundary conditions across both the outer boundary of the domain ($\hat{r} = \hat{R}_\infty$) of the normal tissue and also at the center of the tumor ($\hat{r} = 0$), with continuity of GNR concentration and flux across the interface between the tumor and normal tissue ($\hat{r} = \hat{R}$), in the form

$$-\hat{D}^{(T)} \frac{\partial \hat{C}^{(T)}}{\partial \hat{r}} + \hat{u}^{(T)} \hat{C}^{(T)} = 0, \qquad (\hat{r} = 0), \tag{3.33}$$

$$-\hat{D}^{(T)} \frac{\partial \hat{C}^{(T)}}{\partial \hat{r}} + \hat{u}^{(T)} \hat{C}^{(T)} = -\hat{D}^{(N)} \frac{\partial \hat{C}^{(N)}}{\partial \hat{r}} + \hat{u}^{(N)} \hat{C}^{(N)}, \quad \hat{C}^{(T)} = \hat{C}^{(N)}, \qquad (\hat{r} = \hat{R}), \tag{3.34}$$

$$-\hat{D}^{(N)} \frac{\partial \hat{C}^{(N)}}{\partial \hat{r}} + \hat{u}^{(N)} \hat{C}^{(N)} = 0, \qquad (\hat{r} = \hat{R}_\infty). \tag{3.35}$$

The volume fraction of the fluid phase does not appear in the equations (3.18) and the boundary conditions (3.33)-(3.35) because we have used superficially averaged concentrations in this model. Note that these would appear if we were instead to use the intrinsically averaged concentrations. We used a zero GNR total flux boundary condition at the tissue edge ($\hat{r} = \hat{R}_\infty$) since we use a sufficiently large computational domain to

ensure that the interstitial pressure gradient is zero at the tissue edge (corresponding to zero interstitial velocity).

3.2.8 Initial Conditions

We assume that at the beginning of the simulations there are no GNRs inside the tumor or the healthy tissue and there is a finite number of available binding sites, which is uniform across the tumor ($\hat{C}_{bs} = \hat{C}_{bs_{max}}$). Thus, we write the following initial conditions

$$\begin{aligned}
&\hat{C}_v^{(j)}(\hat{r},0) = \hat{C}_{v0}^{(j)}, \quad \hat{C}^{(j)}(\hat{r},0) = \hat{C}_b^{(T)}(\hat{r},0) = \hat{C}_i^{(T)}(\hat{r},0) = 0, \quad (j = N,T)\\
&\hat{C}_{bs}^{(T)}(\hat{r},0) = \hat{C}_{bs_{max}}.
\end{aligned} \tag{3.36}$$

3.2.9 Dimensionless Transformation

The full model has seven dependent variables. For computational efficiency it is appropriate to nondimensionalize the system of the dimensional Eqs. (3.12), (3.18), (3.26), (3.27) and (3.29)-(3.30) along with the boundary conditions (3.15)-(3.17) and (3.33)-(3.35) and the initial conditions (3.36) into dimensionless equations using the following transformations,

$$\begin{aligned}
&\hat{t} = \frac{1}{\hat{k}_d}t, \quad \hat{r} = \hat{R}r, \quad \hat{C}_b^{(T)} = \hat{C}_{bs_{max}}C_b^{(T)}, \quad \hat{C}_{bs}^{(T)} = \hat{C}_{bs_{max}}C_{bs}^{(T)}, \quad \hat{u}^{(j)} = \hat{R}\hat{k}_d u^{(j)}\\
&\hat{C}_i^{(T)} = \hat{C}_{bs_{max}}C_i^{(T)}, \quad \hat{C}^{(j)} = \hat{C}_{bs_{max}}C^{(j)}, \quad \hat{C}_v^{(j)} = \hat{C}_{bs_{max}}C_v^{(j)}, \quad \hat{P}_i^{(j)} = \hat{P}_{ss}^{(N)} + \hat{P}_e^{(N)}P_i^{(j)},\\
&\hat{P}_{ss}^{(j)} = \hat{P}_{ss}^{(N)} + \hat{P}_e^{(N)}P_{ss}^{(j)}, \quad \hat{P}_e^{(j)} = \hat{P}_{ss}^{(N)} + \hat{P}_e^{(N)}P_e^{(j)},\\
&\hat{P}_l^{(j)} = \hat{P}_{ss}^{(N)} + \hat{P}_e^{(N)}P_l^{(j)}, \quad (j = N,T),
\end{aligned} \tag{3.37}$$

where we scale time using the GNR disassociation rate ($\hat{k}_d$), GNR concentration using initial cell-receptor concentration ($\hat{C}_{bs_{max}}$), lengths using the tumor radius ($\hat{R}$), velocities using the corresponding velocity scale ($\hat{R}\hat{k}_d$) in the tumor and pressure using the net vascular pressure in healthy tissue ($\hat{P}_e^{(N)}$).

Thus, we obtain the following system of seven dimensionless differential equations

$$\frac{dC_v^{(j)}}{dt} = -\xi_{b_1}C_v^{(j)} - \xi_{b_2}\int_0^1 H(r-r_n)\xi_v^{(T)}(P_e^{(T)} - P_i^{(T)})(C_v^{(T)} - C^{(T)}e^{-\check{P}e^{(T)}})r^2 dr, \tag{3.38}$$

$$\frac{1}{r^2}\frac{\partial}{\partial r}\left(r^2\frac{\partial P_i^{(N)}}{\partial r}\right) = \alpha^{(N)}P_i^{(N)}, \tag{3.39}$$

$$\frac{\partial C^{(N)}}{\partial t} + \frac{1}{r^2}\frac{\partial}{\partial r}\left(r^2 u^{(N)}C^{(N)}\right) = \gamma_c\frac{1}{r^2}\frac{\partial}{\partial r}\left(r^2 D\frac{\partial C^{(N)}}{\partial r}\right) - \xi_l^{(N)}(P_i^{(N)} - P_l^{(N)})C^{(N)}, \tag{3.40}$$

$$\frac{\partial C^{(T)}}{\partial t}+\frac{1}{r^2}\frac{\partial}{\partial r}\left(r^2u^{(T)}C^{(T)}\right)=\gamma_c\frac{1}{r^2}\frac{\partial}{\partial r}\left(r^2\frac{\partial C^{(T)}}{\partial r}\right)+H(r-r_n)\Bigg(\xi_v^{(T)}(P_e^{(T)}-P_i^{(T)})(C_v^{(T)}-C^{(T)}e^{-\breve{P}e^{(T)}})-\xi_l^{(T)}(P_i^{(T)}-P_l^{(T)})C^{(T)}\Bigg)-\nu_1C_{bs}^{(T)}C^{(T)}+C_b^{(T)}, \tag{3.41}$$

$$\frac{\partial C_b^{(T)}}{\partial t}=\nu_1C_{bs}^{(T)}C^{(T)}-C_b^{(T)}-\nu_2f(C_i^{(T)})C_b^{(T)}, \tag{3.42}$$

$$\frac{\partial C_{bs}^{(T)}}{\partial t}=-\nu_1C_{bs}^{(T)}C^{(T)}+C_b^{(T)}+\nu_2f(C_i^{(T)})C_b^{(T)}, \tag{3.43}$$

$$\frac{\partial C_i^{(T)}}{\partial t}=\nu_2f(C_i^{(T)})C_b^{(T)}, \tag{3.44}$$

$$\frac{1}{r^2}\frac{\partial}{\partial r}\left(r^2\frac{\partial P_i^{(T)}}{\partial r}\right)=\alpha^{(T)}(P_i^{(T)}-P_{ss}^{(T)}). \tag{3.45}$$

Note that the dimensionless interstitial flow is related to the interstitial pressure in the form

$$u^{(N)}=-\gamma_u^{(N)}\frac{\partial P_i^{(N)}}{\partial r},\qquad\qquad u^{(T)}=-\gamma_u^{(T)}\frac{\partial P_i^{(T)}}{\partial r}. \tag{3.46}$$

The dimensionless parameters which appear in the dimensionless equations are defined as

$$\gamma_u^{(j)}=\frac{\hat{P}_e^{(N)}\hat{K}^{(j)}}{\phi_f^{(j)}\hat{R}^2\hat{k}_d},\quad \gamma_c=\frac{\hat{D}^{(T)}}{\hat{k}_d\hat{R}^2},\quad \xi_v^{(T)}=\frac{\hat{L}_{pv}^{(T)}\hat{S}_v^{(T)}\hat{P}_e^{(N)}(1-\breve{\sigma}^{(T)})}{\hat{k}_d\hat{V}^{(T)}(1-e^{-\breve{P}e^{(T)}})},\quad \xi_l^{(j)}=\frac{\hat{L}_{pl}^{(j)}\hat{S}_l^{(j)}\hat{P}_e^{(N)}}{\hat{k}_d\hat{V}^{(j)}},$$
$$\xi_{b_1}=\frac{1}{\hat{k}_d\hat{\tau}},\quad \xi_{b_2}=\frac{4\pi\hat{R}^3}{3\hat{V}_b},\quad \nu_1=\frac{\hat{k}_a\hat{C}_{bs_{max}}}{\hat{k}_d\phi_f^{(T)}},\quad \nu_2=\frac{\hat{k}_i}{\hat{k}_d},$$
$$C_{i_{max}}=\frac{\hat{C}_{i_{max}}}{\hat{C}_{bs_{max}}},\quad C_{v0}^{(j)}=\frac{\hat{C}_{v0}^{(j)}}{\hat{C}_{bs_{max}}}$$
$$D=\frac{\hat{D}^{(N)}}{\hat{D}^{(T)}},\quad \bar{K}=\frac{\hat{K}^{(N)}}{\hat{K}^{(T)}},\quad R_\infty=\frac{\hat{R}_\infty}{\hat{R}},\quad (j=N,T), \tag{3.47}$$

where $\gamma_u^{(j)}$ is the dimensionless hydraulic conductivity of the vascular wall, γ_c is the ratio of disassociation and diffusion timescales, ξ_{b1} is the ratio of GNR disassociation time scale to GNR blood half life, ξ_{b2} is the ratio of tumor volume and blood circulatory system volume, R_∞ is the dimensionless healthy tissue radius, D is the ratio of GNR diffusion coefficient in the healthy tissue to GNR diffusion coefficient in the tumor, $\bar{K}$ is the ratio of the interstitium hydraulic conductivity in the healthy tissue to its corresponding value in the tumor, $\xi_v^{(T)}$ is the ratio of the vascular volumetric flow to disassociation rates,

$\xi_l^{(j)}$ is the ratio of the lymphatic volumetric flow to disassociation rates, ν_1 is the ratio of disassociation to association timescales and finally ν_2 is the ratio of disassociation to internalization timescales, see Table 3.2.

The corresponding dimensionless boundary and initial conditions are

$$\frac{\partial P_i^{(T)}}{\partial r} = 0, \quad -\gamma_c \frac{\partial C^{(T)}}{\partial r} + u^{(T)} C^{(T)} = 0, \qquad (r = 0), \quad (3.48)$$

$$\frac{\partial P_i^{(T)}}{\partial r} = \bar{K} \frac{\partial P_i^{(N)}}{\partial r}, \quad P_i^{(T)} = P_i^{(N)}, \qquad (r = 1), \quad (3.49)$$

$$-\gamma_c \frac{\partial C^{(T)}}{\partial r} + u^{(T)} C^{(T)} = -\gamma_c D \frac{\partial C^{(N)}}{\partial r} + u^{(N)} C^{(N)}, \quad C^{(T)} = C^{(N)}, \qquad (r = 1), \quad (3.50)$$

$$P_i^{(N)} = 0, \quad -\gamma_c D \frac{\partial C^{(N)}}{\partial r} + u^{(N)} C^{(N)} = 0, \qquad (r = R_\infty). \quad (3.51)$$

Finally, the dimensionless initial conditions are

$$C_v^{(j)}(r,0) = C_{v0}^{(j)}, \quad C_{bs}^{(T)}(r,0) = 1,$$
$$C^{(j)}(r,0) = C_b^{(T)}(r,0) = C_i^{(T)}(r,0) = 0, \quad (j = N, T). \qquad (3.52)$$

3.2.10 Numerical Approach

We solve the system of PDEs, ODEs and algebraic constraints described in Sec. 3.2.9 using a semi-discretisation method. We choose R_∞ as an integer (i.e. the outer annulus is an integer multiple of the radius of the tumor). In this method, we convert the PDEs into ODEs by discretising the radial coordinate on a uniformly spaced grid ($r_j^{(T)} = j\Delta r^{(T)}$, $\Delta r^{(T)} = 1/N$ in the tumor and $r_j^{(N)} = j\Delta r^{(N)}$, $\Delta r^{(N)} = (R_\infty - 1)/N$ in the healthy tissue where $j = 1, 2, \ldots, N$) using a finite difference method. This results in a system of differential algebraic equations (DAEs) which we solve using MATLAB DAE solver ode15s. We studied the mesh convergence by testing different mesh sizes (C), so we choose 400 spatial mesh points which is corresponding to relative error of $O(10^{-3})$.

3.3 Model Parameter Estimation

Tumor radius and GNR dose. In order to simulate GNR delivery to a tumor bearing rat, we used results from a published *in vivo* experiment [28] to choose the parameter values for our mathematical model. In particular, to compare the GNR concentration profile calculated by our model to the results provided by that study, we use the same tumor radius ($\hat{R} = 0.42$ cm) and GNR dose ($\hat{C}_{v0} = 2.34 \times 10^{-5}$ g/cm^3) administrated either intravenously or intratumorally. Furthermore, the surrounding healthy tissue thickness is considered such that GNR concentration is zero at the tissue edge within the time scale of

Table of dimensional parameters				
parameter	value	units	description	Ref.
$\hat{P}_v^{(N)}$	15.6	mm Hg	vascular pressure	[97]
$\hat{P}_v^{(T)}$	15.6	mm Hg	vascular pressure	[55]
$\hat{P}_l^{(N)}$	0	mm Hg	lymphatic pressure	[97]
$\hat{P}_l^{(T)}$	0	mm Hg	lymphatic pressure	[97]
$\sigma_T^{(N)}$	0.91	-	Average osmotic reflection coefficient for plasma protein	[97]
$\sigma_T^{(T)}$	$(1-(1-\lambda)^2)^2$	-	Average osmotic reflection coefficient for plasma protein	[55]
$\sigma^{(T)}$	$1-W$	-	Osmotic reflection coefficient for GNRs	[20]
$\hat{\pi}_v^{(N)}$	20	mm Hg	vascular osmotic pressure in the tissue	[9]
$\hat{\pi}_v^{(T)}$	19.8	mm Hg	vascular osmotic pressure in the tumor	[55]
$\hat{\pi}_i^{(N)}$	10	mm Hg	interstitial osmotic pressure in the tissue	[9]
$\hat{\pi}_i^{(T)}$	15	mm Hg	interstitial osmotic pressure in the tumor	[9]
$\hat{K}^{(N)}$	8.53×10^{-9}	cm^2/mm Hg s^{-1}	interstitial hydraulic conductivity in the tissue	[9]
$\hat{K}^{(T)}$	4.13×10^{-8}	cm^2/mm Hg s^{-1}	interstitial hydraulic conductivity in the tumor	[9]
ϕ_f^T	0.2	-	interstitial volume fraction	[106]
ϕ_f^N	0.4	-	interstitial volume fraction	[106]
$\phi_b^{(T)}$	$(0.2(R^3-r_n^3)/R^3)$	-	vascular volume fraction	[8]
$\hat{R}$	0.42	cm	tumor radius	[28]
$\hat{r}_p^{(T)}$	10^{-5}	cm	vessel pore radius	[85]
$\hat{r}_p^{(N)}$	$5(3-6)\times10^{-7}$	cm	healthy tissue vessel pore radius	[96]
$\hat{r}_n$	6×10^{-7}	cm	GNR radius	[20]
$\hat{L}$	5×10^{-4}	cm	vessel wall thickness	[20]
$\hat{k}_d$	3.58×10^{-4}	s^{-1}	dissociation rate coefficient	[109]
$\hat{k}_a$	1.21×10^{5}	$M^{-1}s^{-1}$	the association rate coefficient	[109]
$\hat{k}_i$	0.69×10^{-4}	s^{-1}	the internalization rate coefficient	[34]
$\hat{D}^{(T)}$	estimated function	cm^2/s	GNR diffusion coefficient in the tumor	[111]
$\hat{D}^{(N)}$	estimated function	cm^2/s	GNR diffusion coefficient in the healthy tissue	[111]
$\hat{L}_{pv}^{(N)}$	0.36×10^{-7}	cm/mm Hg s^{-1}	the hydraulic conductivity of the microvascular wall in the tissue	[8]
$\hat{L}_{pv}^{(T)}$	estimated function	cm/mm Hg s^{-1}	the hydraulic conductivity of the microvascular wall in the tumor	[20]
$\hat{S}_v^N/\hat{V}^{(N)}$	70	cm^{-1}	the tissue vasculature density	[97]
$\hat{S}_v^T/\hat{V}^{(T)}$	200	cm^{-1}	the tumor vasculature density	[97]
$\hat{R}_\infty$	see the text	cm	Tissue edge	Chosen
γ	10^{-4}		vessel surface area fraction occupied by pores	[85]
$\hat{\mu}_b$	3×10^{-5}	mm Hg s	blood viscosity	[85]
$\hat{\tau}$	16.883	hr	GNR half life	[2]
$\hat{C}_{bs_{max}}$	3.66×10^{-6}	M	maximum cell receptor concentration	[74]
$\hat{L}_{pl}^{(N)}\hat{S}_l^{(N)}/\hat{V}^{(N)}$	1.33×10^{-5}	1/mm Hg s	the tissue lymphatic density	[91, 97]
$\hat{L}_{pl}^{(T)}S_l^{(T)}/V^{(T)}$	0	1/mm Hg s	the tumor lymphatic density	[55]
$\hat{C}_{i_{max}}^{(T)}$	8×10^{-8}	M	constant concentration	Chosen
$\hat{C}_{v0}$	1.6×10^{-5}	g/cm^3	vascular concentration of GNRs	[28]
$\hat{P}^{(N)}$	estimated function	cm/s	effective permeability	[20]
$\hat{P}^{(T)}$	estimated function	cm/s	effective permeability	[20]
$\hat{L}_n$	55×10^{-7}	cm	GNR length	[2]
$\hat{d}_n$	9×10^{-7}	cm	GNR diameter	[2]
$\hat{M}_g$	196.9665	g molˆ-1	gold molecular weight (molar mass)	

Table 3.1: Dimensional parameters used in the GNR and fluid transport models.

Table of dimensionless parameters		
parameter	value	description
ξ_{b1}	0.0621	the ratio of GNR disassociation time scale to GNR blood half life.
ξ_{b2}	0.0321	the ratio of tumor volume and blood circulatory system volume.
$\xi_v^{(T)}$	$0.04 - 0.15$	the ratio of the vascular volumetric flow to disassociation rates.
$\alpha^{(N)}$	35.12	the ratio of the vasculature to the interstitium hydraulic conductivities in the healthy tissue.
$\alpha^{(T)}$	1.3	the ratio of the vasculature to the interstitium hydraulic conductivities in the tumor.
γ_c	0.0323	the ratio of disassociation and diffusion timescales.
$\xi_l^{(N)}$	0.2415	the ratio of the lymphatic volumetric flow in the healthy tissue to GNR disassociation rates.
$\xi_l^{(T)}$	0	the ratio of the lymphatic volumetric flow in the tumor to GNR disassociation rates.
ν_1	6.2×10^3	the ratio of GNR disassociation to association timescales.
ν_2	0.1927	the ratio of GNR disassociation to internalization timescales.
$\gamma_u^{(N)}$	0.0172	the dimensionless hydraulic conductivity of the vascular walls in the healthy tissue.
$\gamma_u^{(T)}$	0.1666	the dimensionless hydraulic conductivity of the vascular walls in the tumor.
$\bar{K}$	0.2065	the ratio of the interstitium hydraulic conductivity in the healthy tissue to its corresponding value in the tumor.
D	1	the ratio of GNR diffusion coefficient in the healthy tissue to GNR diffusion coefficient in the tumor.

Table 3.2: Dimensionless parameters used in the GNR and fluid transport models.

the experiment i.e. we choose $\hat{R}_\infty$ sufficiently large so that the outer boundary condition has no influence on the behavior of the model.

GNR blood half-life. GNR blood half-life (denoted $\hat{\tau}$) is the time that GNRs spend in the circulatory system to decrease to half their initial concentration. The GNR half-life must be as long as possible to increase GNR extravasation time into the tumor. Arami et al. [2015] [5] reviewed different strategies to maximize $\hat{\tau}$ which strongly depends on the dose level and GNR dimensions. In this study we use $\hat{\tau} = 16.88$ hrs which corresponds GNRs of length 55 nm and of diameter 9 nm [2].

GNR extravasation and diffusion. In addition to GNR dimensions, the vascular wall pore size and the fraction of wall surface area occupied by these pores determine how many GNRs can extravasate into interstitium [20]. Most of studies in nanomedicine consider spherical nanoparticles which makes it difficult to find data for GNR parameters in biological tissues. We address this issue by assuming that the physical properties of GNRs are similar to the corresponding physical properties of spherical NPs which have the same volume. Therefore, we approximate the effective permeability ($\breve{P}^{(j)}$) and reflection coefficient ($\breve{\sigma}^{(j)}$) of GNRs (of length 55 nm and of diameter 9 nm) to be similar to spherical nanoparticles of radius 9.4 nm which are functions of the nanoparticle size ratio to vessel wall pore size [20, 24]. The GNRs diffusion coefficient depends on their length and width which can be calculated according to the approach introduced by Tirado et al. [1984] [111], see the Appendix A.

Fluid transport parameters. The fluid transport model used in this study has been developed by Baxter and Jain [1989] [8]. In a follow up paper [55] they summarized the model parameters which have been measured experimentally or estimated, see Table 3.1.

Since vascular pore size in the tumor and normal tissue blood capillaries are different, we use an empirical function for the hydraulic conductivity as a function of pore size determined from experimental data [20], see the Appendix A.

3.4 Results in the Absence of Heating

In this section we consider the temporal and spatial distribution of GNRs following a bolus injection. We consider baseline cases pertinent to photothermal ablation, which we discuss in turn. Firstly, we consider intravenous injection of GNRs which have not been conjugated with binding ligands (Sec. 3.4.1). Secondly, we examine the importance of binding (Sec. 3.4.2). Thirdly, we examine the intratumoral GNR administration both with and without binding ligands (Sec. 3.4.3). We then explore the parameter space of the model and particularly discuss the role of the tumor vascularity in Sec. 3.5.1 and the internalized GNR saturation threshold (i.e. how many GNRs the tissue can absorb) in Sec. 3.5.2. We further study the sensitivity of the model to changes in the most pertinent parameters in Sec. 3.5.3.

3.4.1 Baseline Case 1: Intravenous Administration of GNRs Without Binding Ligands

In Fig. 3.3 we consider a baseline case where we plot the predictions of the model in the case of GNRs without binding ligands, which means that GNRs cannot bind to tumor cell receptors or become internalized into the tumor. In the spatial distribution figures (Fig. 3.3(A), (C), the tumor center is at $\hat{r} = 0$ and the shaded region represents the tumor vascularized region (the outer 10% of the tumor in this case) with an external domain of healthy tissue. In this example the interstitial fluid pressure distribution across the tumor (Fig. 3.3(A)) is uniformly elevated compared to the healthy tissue; outside the tumor, a distance of approximately half a tumor radius the pressure drops to its equilibrium value. At the interstitial fluid pressure equilibrium value in the tissue, the net vascular and lymphatic volume flux is zero, i.e. there is no net fluid transport into the tissue. This pressure profile is expected since in this study we assume there are no functional lymphatics in the tumor and so fluid cannot escape and must accumulate [8]. This is similar to that predicted in previous spherical tumor models [9]. It should be noted that the interstitial fluid pressure in the avascular region of the tumor is flat (no pressure gradient). However, in the tumor rim there is a negative pressure gradient which drives fluid (and hence GNRs by advection) out of the tumor and towards the surrounding healthy tissue. The assumption of constant transvascular concentration of GNRs approximates the profile of the interstitial pressure within the tumor rim because

the change in the transvascular concentration changes the osmotic pressure (post GNR injection). We will address this issue in the future work by coupling the fluid transport model with the solute transport model. In this baseline case (GNR dose $= 2.025 \times 10^{-4}$ g) the average concentration (GNR mass normalized by the tumor volume) of GNRs in the tumor increases over the first 16 hrs post intravenous administration to a peak and then decreases monotonically due to GNR diffusion towards the surrounding healthy tissue (Fig. 3.3(B)). Conversely, in the healthy tissue the GNR average concentration (GNR mass normalized by tissue volume) increases gradually from zero to almost one tenth of the corresponding concentration value in the tumor at 34 hrs post injection. Fig. 3.3(C) shows the corresponding spatial GNR concentration distributions in the tumor and healthy tissue at different time points. This figure reveals that GNRs can penetrate into the tumor center within less than 8 hrs post injection and then GNR concentration increases to its maximal within one day post injection. Although the GNRs diffuse towards the surrounding tissue, GNR concentration in the healthy tissue is decaying quickly to zero at a distance equivalent to three tumor radii. This can be explained as tissue volume is relatively large compared to the tumor, so that GNR concentration cannot build up like in the tumor. In addition, in the healthy tissue GNRs are removed by lymphatic vessels, while in tumors the lymphatics are dysfunctional. In Fig. 3.3(D) we compare the temporal GNR concentration profiles at the tumor center (dashed blue line), tumor rim (solid black line), midway between the tumor center and tumor rim (dashed red line), healthy tissue edge (solid blue line) and a chosen position in the healthy tissue (solid red line). The line styles used in this figure match the vertical lines in Fig. 3.3(C) to visualize the corresponding spatial positions in the computational domain. In this figure we can see that GNR concentrations in the tumor are larger than in the healthy tissue. Furthermore, the GNR concentration temporal profiles at the three considered positions in the tumor show a relatively homogenous GNR distribution at the time between 21 and 28 hours post injection. After one day the concentration decreases in the tumor and loses its homogeneity, see Figs. 3.3(C), (D). We can determine the optimal time for GNR distribution in the tumor by determining the time when GNRs are most homogenous across the tumor. In order to measure the GNR homogeneity across the tumor we calculate the coefficient of variation (CV) (the ratio of the standard deviation to the mean) of the GNR concentration at ten equally spaced positions across the tumor at each time, see Fig. 3.3(E). The CV is maximal at $\hat{t} = 0$ as GNRs are initially in the vasculature only. Over time CV decreases as GNRs spread across the whole tumor until GNR concentration becomes approximately homogeneous (CV$\approx$ 0). Eventually, the CV elevates again as GNRs diffuse towards the surrounding healthy tissue. We conclude from this figure that GNRs become homogenous (CV ≤ 0.01) in the range $22.9 - 25.5$ hrs post injection. Of course since the tumor is only partially vascularized, it may not be necessary to force

GNRs to the center of the tumor if it is already undergoing apoptosis. If we assume a necrotic core for $\hat{r} \leq 0.5\hat{R}$ and compute the coefficient of variation for 10 equally spaced intervals across $\hat{r}_c \leq \hat{r} \leq \hat{R}$, we find instead that GNRs become homogeneous from 21 hours post GNR administration (Fig. 3.3(F)). The spatio-temporal carpet plot shown in Fig. 3.4 visualizes the temporal and spatial GNR profiles in the tumor and the surrounding tissue. It is clear that GNRs accumulate within the tumor in preference to the healthy tissue.

3.4.2 Baseline Case 2 and 3: Intravenous Administration of GNRs With Binding Ligands

We now investigate the case of intravenously administrated GNRs loaded with binding ligands (GNR dose = 2.025×10^{-4} g), as shown in Fig. 3.5. Again, we assume only the outer 10% of the tumor radius is vascularized. In this case, according to our assumptions free GNRs extravasate from the tumor vasculature and diffuse through the interstitium of the tumor and healthy tissue. In addition, the free GNRs can bind to tumor cell receptors (due to the conjugated binding ligands) and then become internalized by tumor cells similar to Goodman et al. [2008] [34]. Introducing binding leads to a much more heterogeneous spatial distribution of GNRs within the tumor (Fig. 3.5(A)). As the GNRs enter the tissue they rapidly bind to the tumor cells across the vascular region and become internalized within these cells. This then leads to a much more dilute concentration of free GNRs in the avascular region compared to case 1. As a result, the penetration depth of GNRs into the tumor depends on the timescales of the GNR clearance from the blood, GNR diffusion, binding and internalization processes. In this case, we assumed there is no maximal tumor capacity for internalized GNRs [34], which leads to almost no GNR penetration into the tumor beyond the vascular region. However, the GNR concentration in this narrow shell increases monotonically as long as there are available GNRs in the vasculature (Fig. 3.5(B)). The spatial profiles of bound GNRs shown in Fig. 3.5(C) exhibit traveling waves propagating from the tumor boundary towards the tumor center, but confined within the outer 20% of the tumor volume. That means free GNRs which diffuse through the interstitium quickly bind to the available free receptors, which elevates bound GNR concentration to its maximal value (the maximum concentration of available binding sites). However, tumor cells internalize the bound GNRs which frees up the receptors and retains the free GNRs rather than allowing them to diffuse towards the tumor center. Since there is no maximal tumor capacity for internalized GNRs, the internalized GNR concentration increases monotonically generating an unlimited sink for GNRs in the system (see Fig. 3.5(C)). For this reason the spatial profiles of bound GNRs decay over time within the tumor rim (see Fig. 3.5(D)) which means the internalized GNRs dominate the total GNR distribution across the tumor (Fig. 3.5(A), (D)). Fig. 3.5(E) shows the corresponding

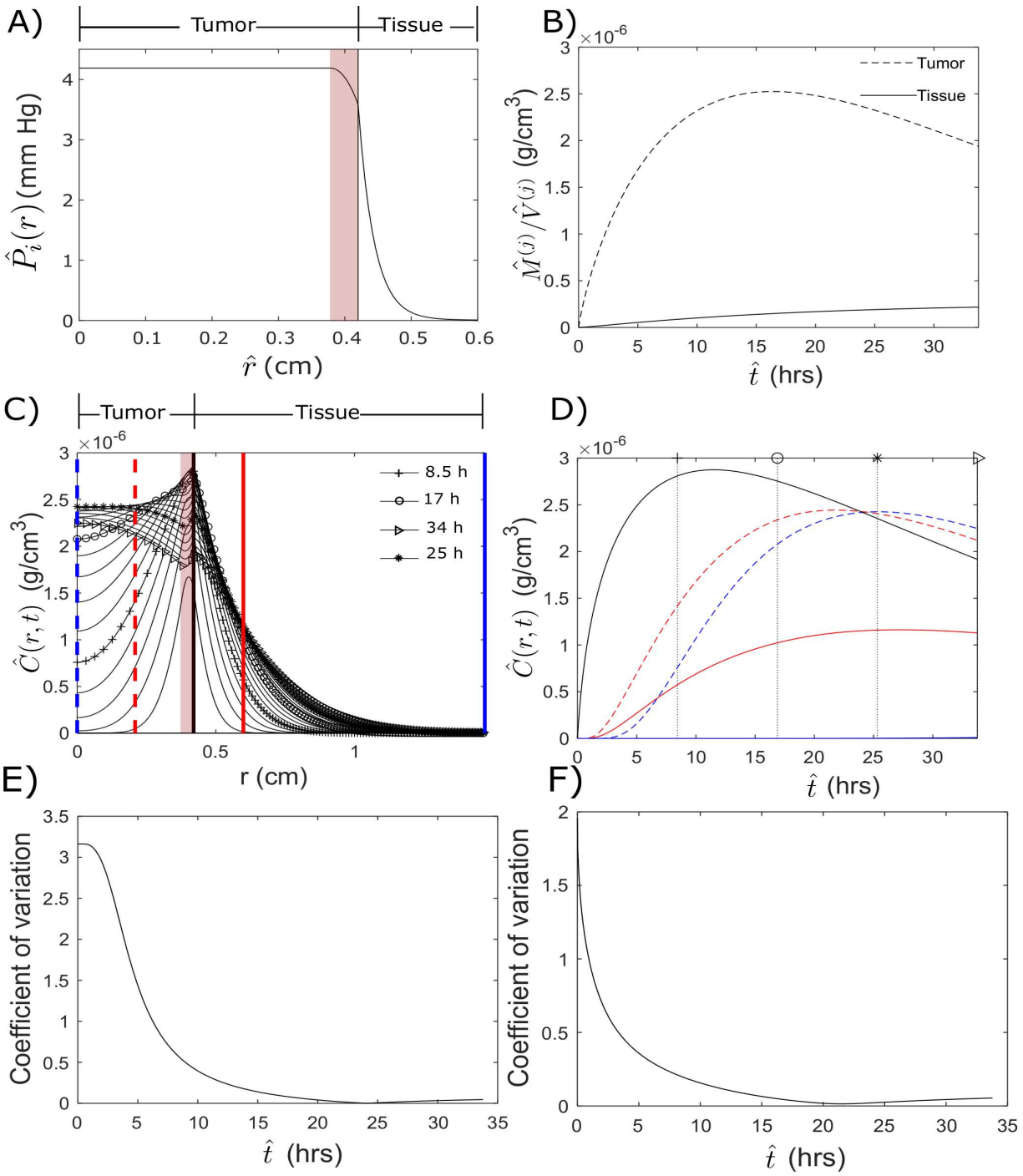

Figure 3.3: The interstitial fluid pressure and GNR concentration profiles in the tumor and tissue in the absence of binding ligands. A) The interstitial fluid pressure profile, where $\hat{P}_v^{(T)} = \hat{P}_v^{(N)} = 5.6$ mm Hg. B) GNR temporal average concentration. C) GNR spatial concentration, where $\hat{C}_v(0,r) = 2.34 \times 10^{-5}$ g. D) GNR temporal concentrations for different spatial positions in the tumor and tissue. The line styles used in (D) match the vertical lines in (C) to visualize the corresponding spatial positions in the tumor and tissue. E) The coefficient of variation of temporal GNR concentration at equally spaced 10 positions in the tumor domain. F) The coefficient of variation of temporal GNR concentration at equally spaced 10 positions in the tumor half domain ($0.5\hat{R} \leq \hat{r} \leq \hat{R}$).

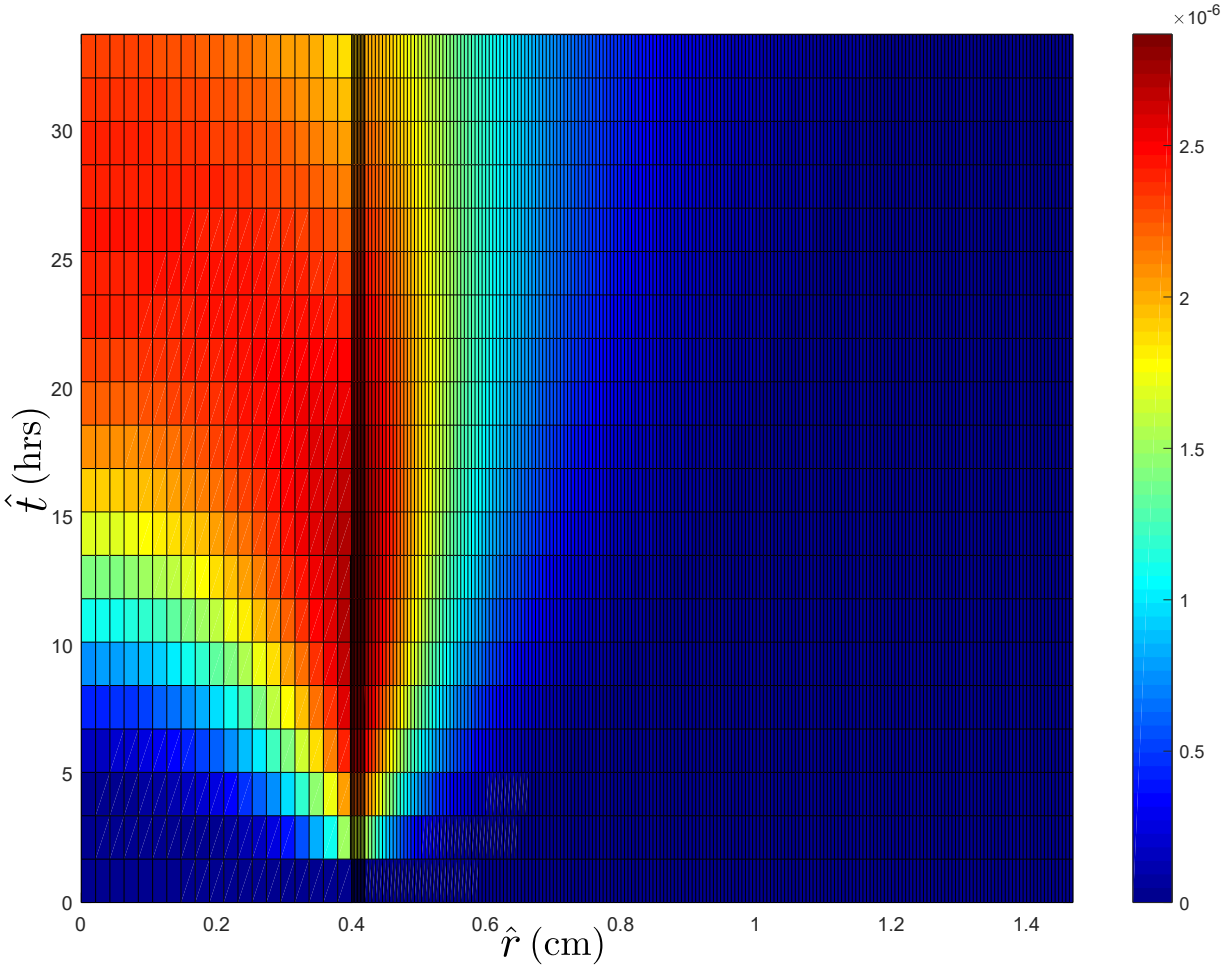

Figure 3.4: GNR concentration spatio-temporal carpet plot for the case of no binding ligands conjugated to the GNRs using the parameter values in Table 3.1.

penetration depth of the bound and internalized GNRs into the tumor. These changes occur at approximately the same rate until the threshold at 0.33 cm measured from the tumor center. Beyond this threshold the bound GNR penetration depth decreases due to internalization and eventually we expect all free and bound GNRs in the tumor to be removed and only the internalized ones will remain within the system. However, in this case the average GNR concentration across the tumor is about 5 times the corresponding average concentration in the case of no binding ligands conjugated to the GNRs (compare Figs. 3.5(F) and 3.3(B)). Despite the GNR average concentration being relatively high, the GNR distribution is strongly heterogeneous across the tumor as revealed in the carpet plot in Fig. 3.6. This heterogeneous GNR distribution suggests that the efficiency of using binding ligands is restricted to tumors with a narrow viable rim. The optimal time to achieve maximal concentration of GNRs distribution is when GNRs disappear from the blood stream (see Fig. 3.5(F)), since the concentration of internalized GNRs saturate where GNR internalization is irreversible [34].

On the other hand, in our model we introduce a tumor capacity for internalized GNRs,

where tumor cells cannot internalize GNRs when the concentration inside the tumor cell reaches a threshold ($\hat{C}_{i_{max}}$). Therefore, we choose a parameter value for $\hat{C}_{i_{max}}$ in the baseline case to study the influence of this parameter on the spatial GNR distribution within the tumor, see Fig. 3.7, but then consider a larger range in Sec. 3.5.2. Plotting the total GNR concentration across the tumor and the surrounding tissue in Fig. 3.7(A) we see that the GNRs cover almost half of the tumor, but with smaller concentrations compared to the case in Fig. 3.7(B). This distribution is mainly driven by the saturation of the bound and internalized GNRs (Fig. 3.7(C) and (D)), where the internalized GNR concentration saturates due to the maximal tumor capacity for internalized GNRs, and the bound GNR concentration saturates due to the restricted number of receptors at the tumor cell surface. As a result free GNRs can diffuse further towards the tumor center (compared to Fig. 3.5) which start to bind and become internalized. This effectively means that GNRs can invade the whole tumor but on a much longer timescale compared to the case of GNRs without binding ligands (see Fig. 3.3). In the time scale considered in this study GNRs invade 21% of the tumor (see Fig. 3.7(E)) with a threefold increase in the GNR mass compared to the case without binding ligands, see Fig. 3.7(F). The spatio-temporal plot for the GNR concentration shows a monotonic increase of the GNR concentration and penetration which suggests that the optimal time for GNR profile is beyond the time of simulation considered in this study (Fig. 3.8).

3.4.3 Baseline Case 4: Intratumoral Adminstration of GNRs

In some cases GNRs can be injected directly into the tumor (intratumoral adminstration). El-Sayed et al. [2013] [28] have carried out intratumoral injection for rats and mice *in vivo* and compared it to intravenous adminstration. We can also use our model to simulate the intratumoral administration mimicking the injection profile as an initial condition in the free GNR concentration. To accommodate spherical symmetry this injection (2.025×10^{-4} g) must be centered at the center of the tumor and spread over a radius $\hat{r}_i \leq 1$. We consider an initial concentration of GNRs (in the absence of binding ligands) at the tumor center occupying about 25% of the tumor volume, so there is no GNR extravasation from the blood stream into the tumor. We run the simulation using our model with the same boundary conditions and plot the results in the Fig. 3.9. The GNR concentration starts initially high (0.16 g/cm^3) at the tumor center as the whole dose is injected over a small volume (25% of the tumor volume, $\hat{r}_i \simeq 0.105$ cm) which then takes about 6 hrs to spread across the whole tumor (Fig. 3.9(A)). In Fig. 3.9(B) we show the corresponding temporal profile of the GNR concentration at four different spatial points which are the tumor center, half way between the tumor center and the tumor boundary, the tumor/tissue interface and 17 mm away from the tumor/tissue interface. This figure shows that the concentration at the tumor center drops by 1.7% within 6 hrs. Whereas,

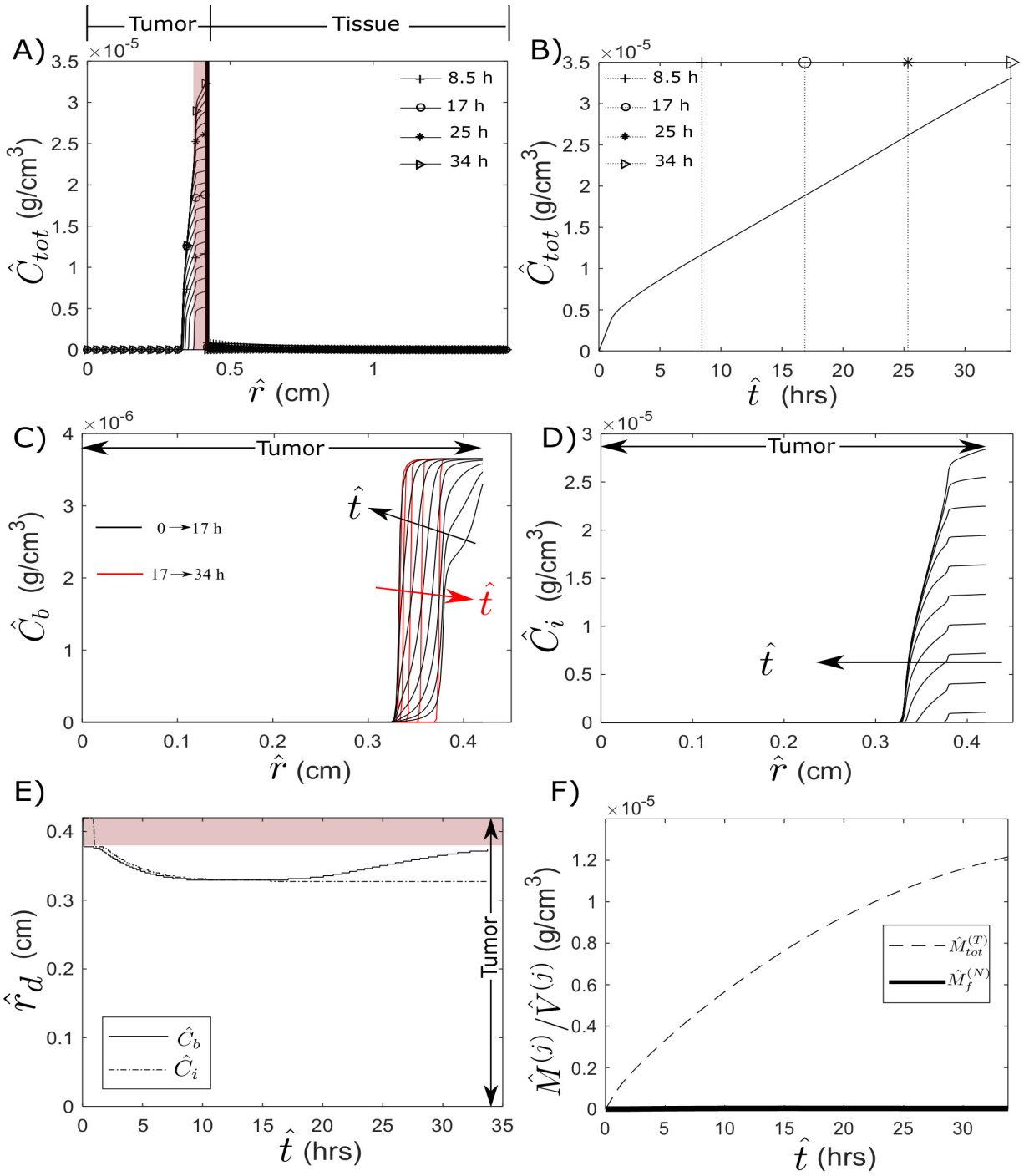

Figure 3.5: GNR concentration profiles in the tumor and healthy tissue for the case of binding ligands conjugated to the GNRs using the parameter values in Table 3.1. A) Total GNR spatial concentration, where $\hat{C}_v(0,\hat{r}) = 2.34\times10^{-5}$ g. B) Total GNR temporal concentration at the tumor/tissue interface. C) Bound GNR spatial concentration. D) Internalized GNR spatial concentration. E) Bound and internalized GNR wave front penetration depth. F) GNR temporal average concentration.

midway between the tumor center and the tumor surface the GNR concentration increases from zero concentration to 0.0016 g/cm^3 within 3 hrs and then decreases monotonically to

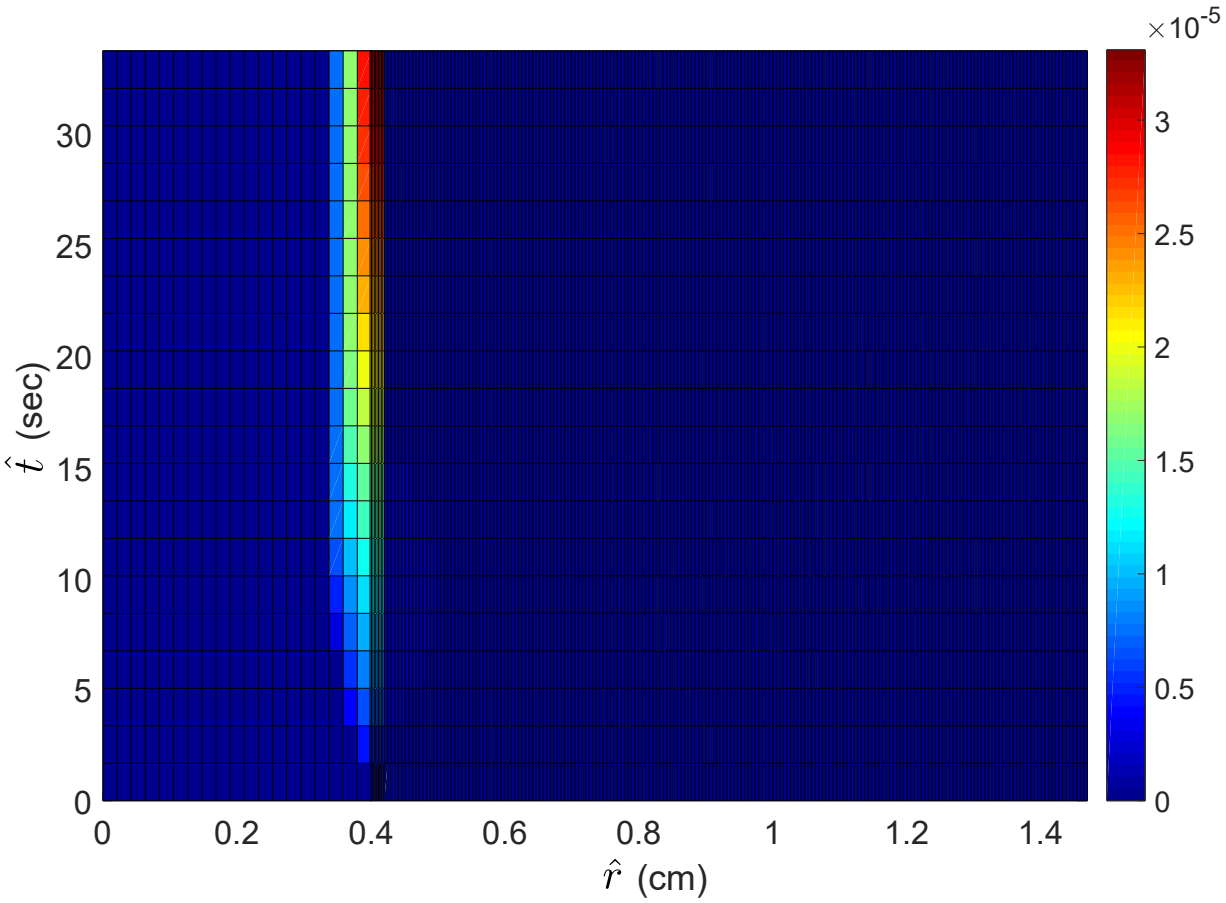

Figure 3.6: GNR concentration spatio-temporal carpet plot for the case of binding ligands conjugated to the GNRs and no maximal tumor capacity for internalizing GNRs using the parameter values in Table 3.1.

13.56×10^{-5} gm/cm^3 by the end of the simulation (33.8 hrs). Similarly, at the tumor/tissue interface the concentration elevates from zero to a maximum value of 0.0002 g/cm^3 at 11.8 hrs post injection, then decreases monotonically to very small values by the end of the simulation. The average concentration of GNRs in the tumor is significantly larger than the corresponding average concentration in the healthy tissue (Fig. 3.9(C)). This figure reveals that the system attains an approximately constant GNR average concentration across the tumor until approximately 3.7 hrs post administration, then the average concentration decreases monotonically. This decrease in the average concentration is due to the spread of GNRs over the tumor and the surrounding tissue. We deduce from these figures that the GNRs are initially concentrated at the tumor center and the concentration decreases rapidly over time with a slow diffusion towards the tumor rim and the surrounding tissue. In addition, when the GNRs reach the surface of the tumor, they accumulate in a relatively thick annulus of the healthy tissue (of width about half of the tumor radius), where GNR concentration builds up and becomes comparable to the concentration in the tumor.

On the other hand, in Fig. 3.9(E) we examine the case of GNRs conjugated with

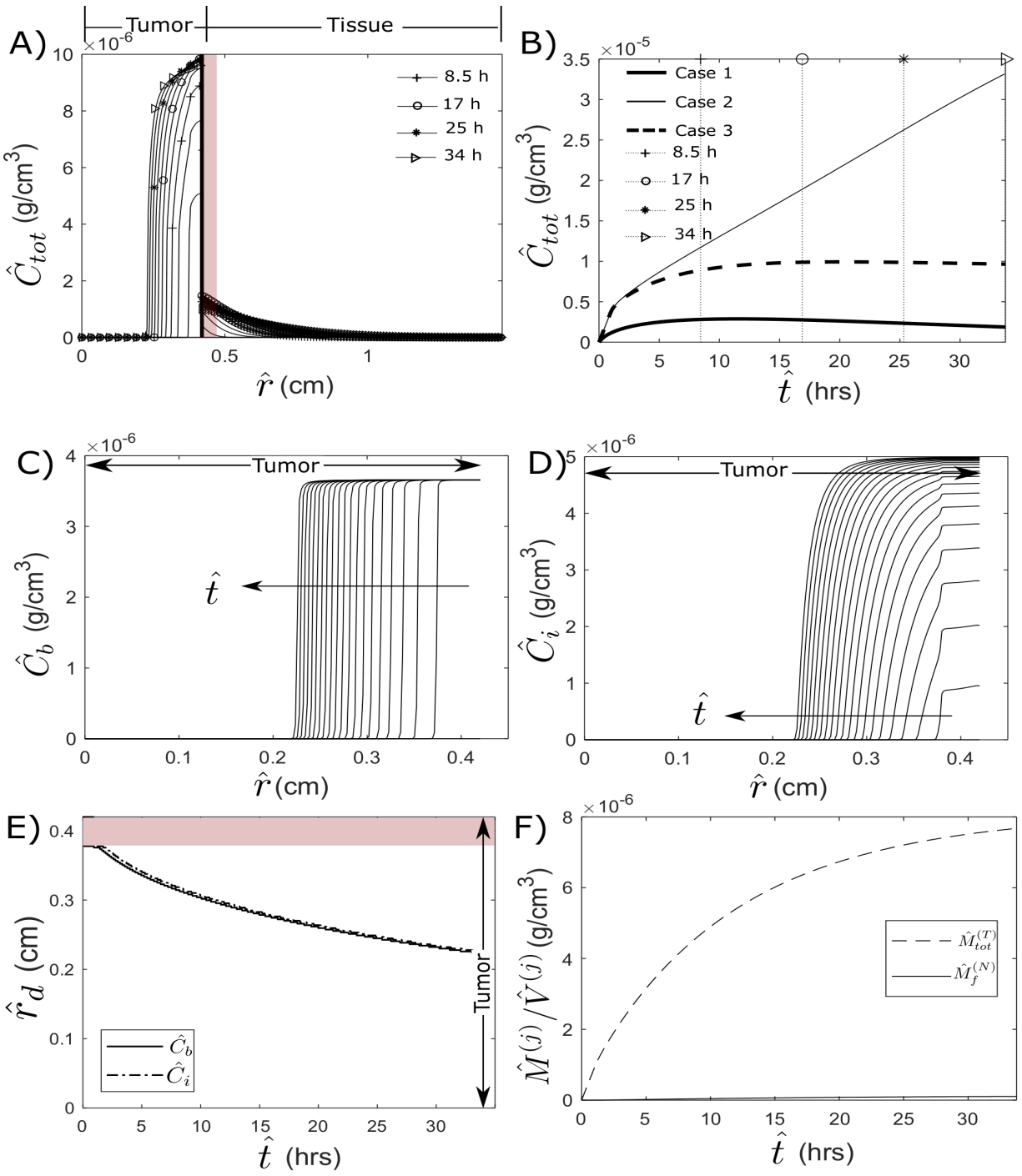

Figure 3.7: GNR concentration profiles in the tumor and healthy tissue for the case of binding ligands conjugated to the GNRs using the parameter values in Table 3.1. A) Total GNR spatial concentration, where $\hat{C}_v(0,\hat{r}) = 2.34 \times 10^{-5}$ g. B) A comparison for GNR temporal concentrations at the tumor/tissue interface in the case of no binding ligands (case 1), with binding ligands (case 2) and with binding ligands in the case of limited GNR internalization (case 3). C) Bound GNR spatial concentration. D) Internalized GNR spatial concentration. E) Bound and internalized GNR wave front penetration depth. F) GNR temporal average concentration.

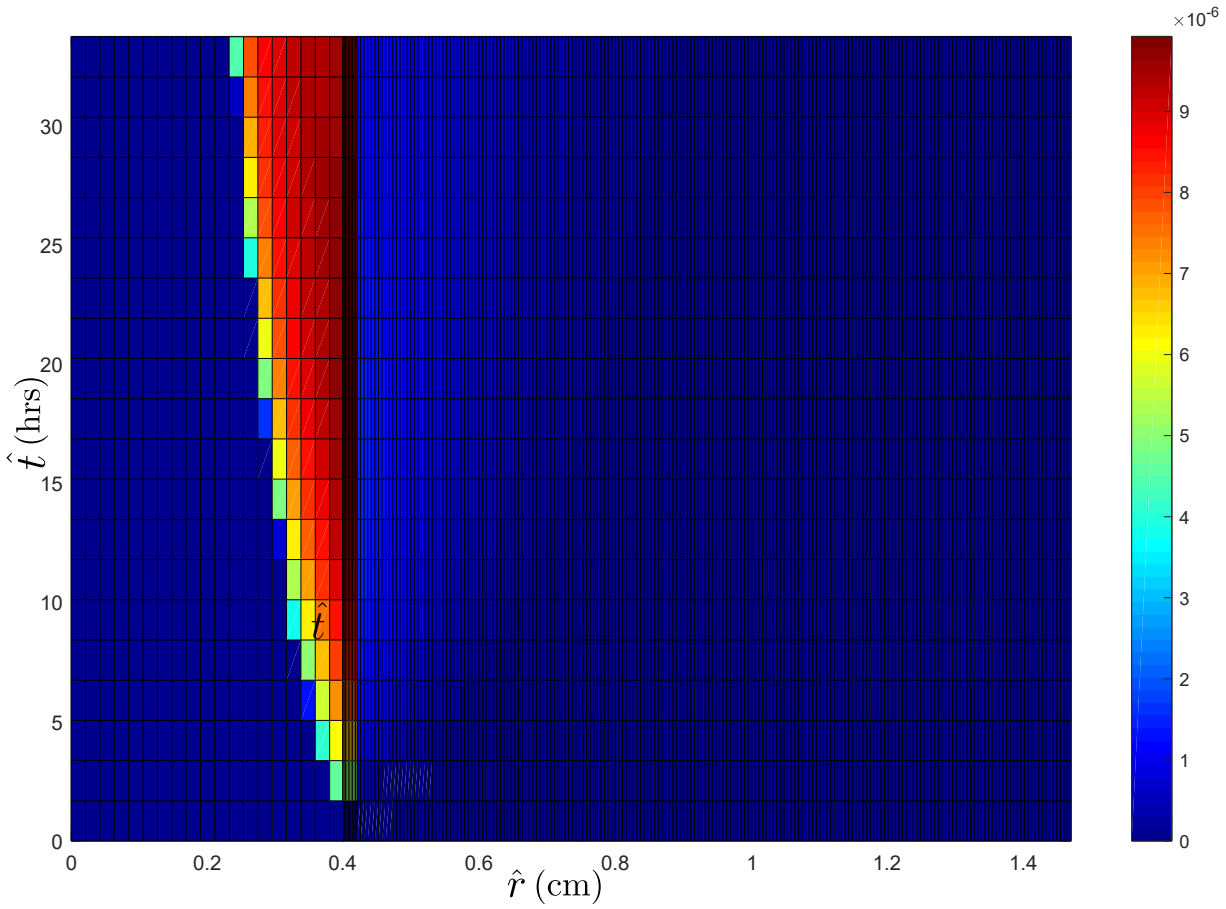

Figure 3.8: GNR concentration spatio-temporal carpet plot for the case of binding ligands conjugated to the GNRs and the tumor has a maximal capacity for internalizing GNRs using the parameter values in Table 3.1.

binding ligands for intratumoral administration. Considering a limited tumor capacity for internalized GNRs, the maximal concentrations of the internalized and bound GNR concentrations are initially very small compared to the free GNRs, since the maximum concentration of internalized GNRs is restricted by the tumor capacity (Fig. 3.9(D)), and the maximum concentration of bound GNRs is restricted by the maximum concentration of the cell receptors (not shown). Therefore the GNR spatial and temporal concentrations in this case are almost identical to the corresponding distributions shown in Figs. 3.9(A) and (B). In the case of no tumor capacity limit for internalizing GNRs the concentration of GNRs in the tumor (Fig. 3.9(E)) is slightly larger than the previous two cases due to the monotonic increase of the concentration of the internalized GNRs (Fig. 3.9(F)). We conclude from this study that intratumoral administration for GNRs is preferable in the case of tumors which have no necrotic core since the largest GNR concentrations will be at the tumor center. Note that, in our simulations we used the same amount of dose for both the intratumoral and intravenous administrations.

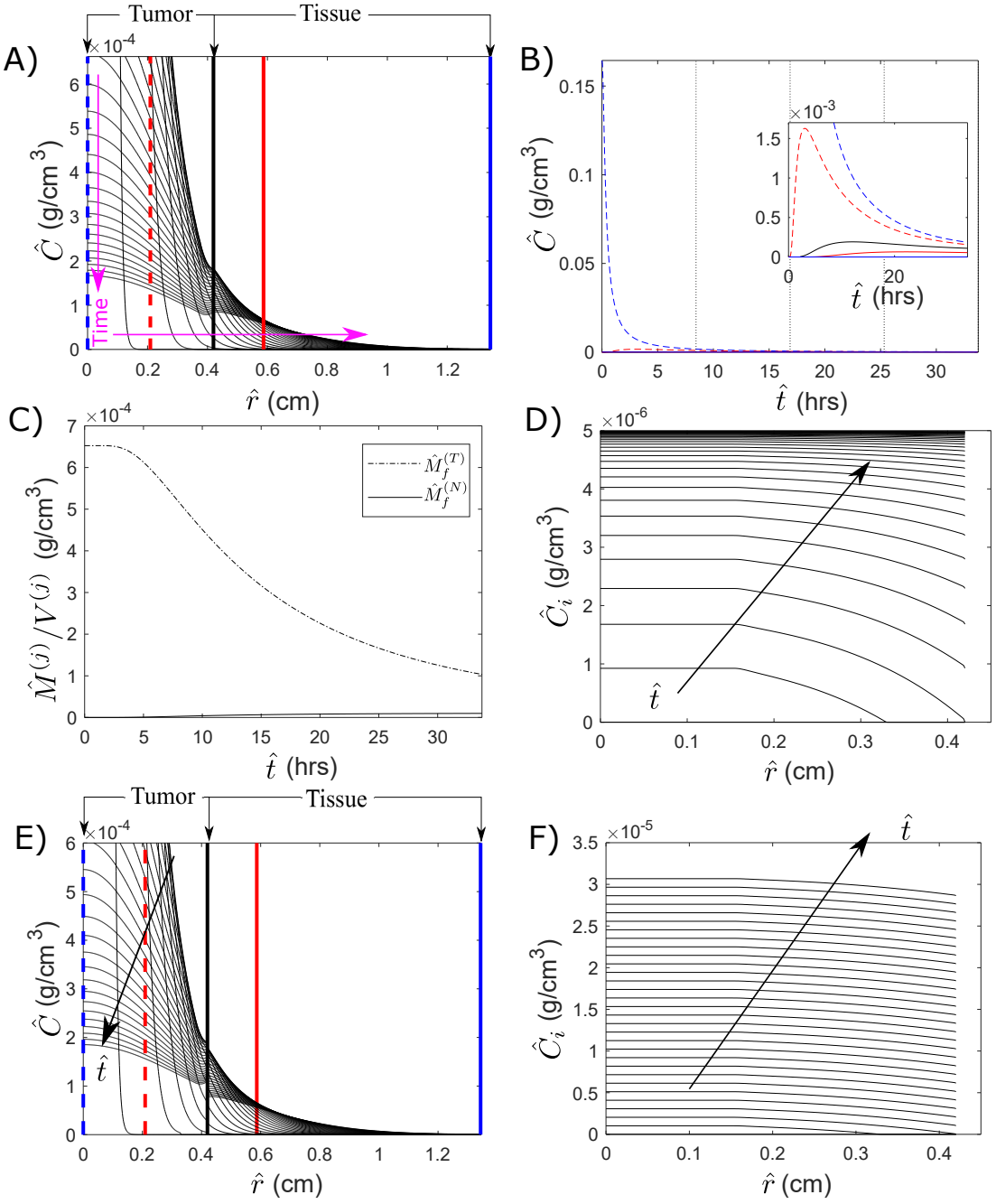

Figure 3.9: GNR concentration profile (intratumoral administration) in the tumor and healthy tissue in the presence of binding ligands using the parameter values in Table 3.1. A) GNR spatial concentration in the absence of binding ligands. B) GNR temporal concentrations for different spatial positions in the tumor and healthy tissue. The line styles used in (B) match the vertical lines in (A) to visualize the corresponding spatial positions in the tumor and tissue. C) GNR temporal average concentration. D) Internalized GNR spatial concentration with a restricted tumor capacity of GNRs. E) GNR spatial concentration in the case of presence of binding ligands with an unlimited tumor capacity for GNRs. F) Internalized GNR spatial concentration with an unlimited tumor capacity of GNRs.

3.5 Exploring the Parameter Space

3.5.1 The Influence of The Degree of Vascularisation

The tumor degree of vascularization ($\hat{r}_n$) has a nonlinear influence on the interstitial fluid pressure and average total GNR concentration across the tumor (Figs. 3.10(A), (B)). Totally vascularized tumors ($\hat{r}_n = 0$) have almost the same interstitial fluid pressures as tumors which are nonuniformly vascularized provided the vasculature rim width exceeds 15% of the tumor radius. In tumors with $0.85 \leq \hat{r}_n/\hat{R} \leq 0.99$, the interstitial fluid pressure is substantially influenced by the vasculature width. The interstitial fluid pressure significantly decreases in tumors with narrow vasculature layers (corresponding to large $\hat{r}_n$), see Fig. 3.10(A). Furthermore, the parameter $\hat{r}_n$ plays a vital role in determining the maximum GNR concentration which can be achieved in the tumor (Fig. 3.10(B)). Fig. 3.10(B) shows that the value of $\hat{C}_{av}^{(T)}$ in tumors with uniform vasculature ($\hat{r}_n = 0$) is two times as large as tumors of $\hat{r}_n/\hat{R} = 0.99$. This large difference in total GNR concentration is because the tumor vasculature is the source of GNRs.

3.5.2 The Influence of The GNR Internalization Saturation Threshold

In the presence of binding ligands (discussed in Sec. 3.4.2), the maximal tumor capacity for internalizing GNRs (administrated intravenously) controls the GNR accumulation within the tumor and the GNR penetration depth (Figs. 3.5(A), (B), 3.7(A), (B)). Here we study the bound GNR penetration depth for different tumor capacities ($\hat{C}_{i_{max}}$). In Fig. 3.10(C) we monitor the bound GNR penetration depth $\hat{r}_d$ across the tumor against time, where the tumor center is at $\hat{r} = 0$ and the tumor rim is at $\hat{r} = 1$. For small values of $\hat{C}_{i_{max}}$ the bound GNRs can access the tumor center, because the internalized GNR concentration saturates allowing free GNRs to diffuse more deeply into the tumor and then bind to cell receptors. For large capacities GNRs are internalized faster than the GNR diffusion towards the tumor center (Fig. 3.10(C)). Fig. 3.10(D) shows that value of $\hat{C}_{i_{max}}$ does not influence the mass of GNRs accumulate within the tumor, so it only determines the GNR distribution across the tumor.

3.5.3 Parameter Sensitivity Analysis

The parameters used in our model vary according to the type of the targeted tumor and the properties of the GNRs used in this therapy. For instance, the microvascular pressure ($\hat{P}_v^{(T)}$) in tumors varies between $15 - 25$ mm Hg and the vessel wall surface area per unit volume of the tumor ($\hat{S}_v^T/V^{(T)}$) has the range of $50 - 250$ cm^{-1} [55]. Furthermore, the GNR aspect ratio influences parameters in the model such as the GNR diffusion coefficient

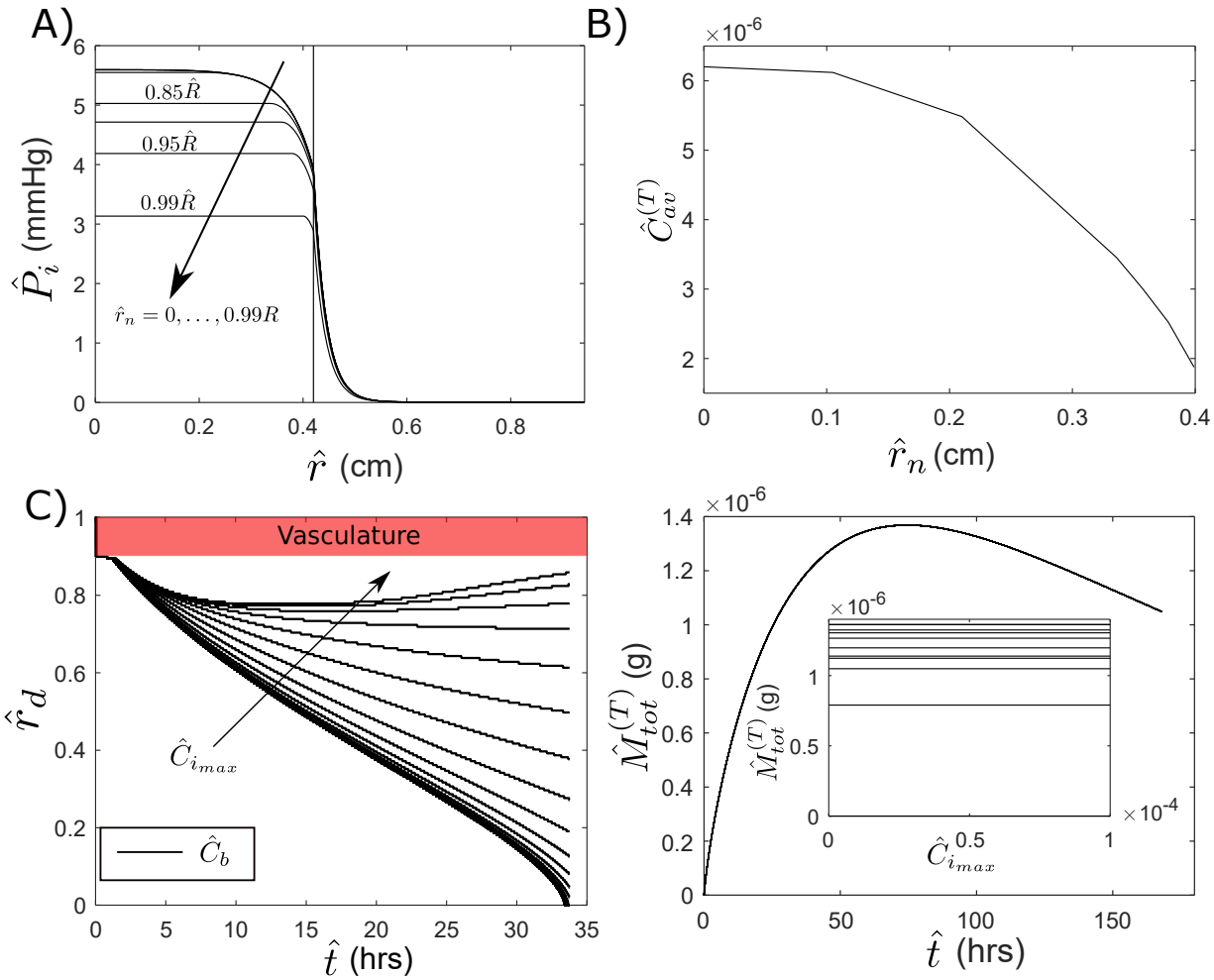

Figure 3.10: The influence of the degree of vascularization and the saturation threshold for a tumor of radius $\hat{R} = 0.42$ cm using the parameter values in Table 3.1. A) The interstitial fluid pressure for different $\hat{r}_n$ values ($\hat{r}_n = (0, \ldots, 0.99)\hat{R}$). B) The maximum average concentration in the tumor for different $\hat{r}_n$ values. C) The wave front for bound GNRs in the case of different tumor capacities for GNRs. D) The transient GNR mass in the tumor for different tumor capacities for GNRs, and the subplot shows the GNR mass against tumor capacity for GNRs for different time steps.

and the interstitium volume fraction accessible for GNRs in the tumor [34]. In addition, some parameters have significant uncertainty, such as the tumor vessel wall pore size [20]. Therefore, we study the sensitivity of the model to the following parameters: the vessel wall surface area per unit tumor volume ($\hat{S}_v^{(T)}/\hat{V}^{(T)}$), the tumor vessel wall pore size ($\hat{r}_p^{(T)}$), the GNR diffusion coefficient in the tumor ($\hat{D}^{(T)}$), tumor interstitium volume fraction ($\phi_f^{(T)}$), the hydraulic conductivity of the lymphatic wall times lymphatic density in the healthy tissue ($\hat{L}_{pl}^{(N)}\hat{S}_l^{(N)}/\hat{V}^{(N)}$) and the hydraulic conductivity of the tumor interstitium ($\hat{K}^{(T)}$). In practice, modifying the volume of the GNR diffusion coefficient requires modifying the GNR physical properties or degrading the tumor interstitium using extracellular matrix degrading enzymes (collagenase). However, changing GNR physical properties changes

the GNR blood half life. Therefore, in order to study the influence of the GNR diffusion coefficient on our model we vary its value through degrading the tumor interstitium so that the GNR blood half life remains constant. We consider the temporal maximum of the spatially averaged concentration of GNRs in the tumor ($\hat{C}^{(T)}_{max_i},\ i = 1,\dots,8$) (i.e. $M_{max} = \max(\int_0^{\hat{R}} \hat{C}^{(T)}_{tot}\hat{r}d\hat{r})$) as the objective function for this sensitivity analysis. In order to study the effect of these parameters on the considered objective function we choose eight values for one of the parameters in the range of $\pm 50\%$ deviated from the baseline value of this parameter, and we run the model for nine equally spaced values across this range (indexed by $i = 1,\dots,9$) and calculate the corresponding maximum GNR concentrations in the tumor for all time ($\hat{C}^{(T)}_{max_i},\ i = 1,\dots,8$), see Table 3.3. For simplicity we measure the sensitivity of every parameter using the relative standard deviation (rsd) from the base line case ($\hat{C}^{(T)}_{max_b}$, the maximum averaged concentration in the tumor corresponding to the parameters in Table 3.1), which is calculated as [30]

$$rsd = \sqrt{\frac{1}{8}\sum_{i=1}^{9}\left(\frac{C^{(T)}_{max_i} - C^{(T)}_{max_b}}{C^{(T)}_{max_b}}\right)^2} \times 100. \tag{3.53}$$

We calculate the relative standard deviation for each of the parameters in the same way and list the results in Table 3.3. The value of the rsd which is corresponding to some parameter gives a measure of the importance of this parameter compared to the other parameters under investigation. Hence, the relative standard deviation values show that the tumor vasculature density ($\hat{S}^{(T)}_v/\hat{V}^{(T)}$, $rsd = 14.6$) and the vessel wall pore size ($\hat{r}^{(T)}_p$, $rsd = 13.1$) are the most sensitive parameter choices (which correspond to the highest two values of rsd) compared to the other four parameters. Therefore, these two parameters control the GNR extravasation into the tumor more than the other parameters. Beyond these the next most sensitive parameters are the diffusion coefficient and the tumor interstitium volume fraction which determine the GNR diffusivity and volume accessible by GNRs in the tumor, respectively. Conversely, the sink for GNRs in the model ($\hat{L}^{(N)}_{pl}\hat{S}^{(N)}_l/\hat{V}^{(N)}$) has only a minor influence on $\hat{C}^{(T)}_{max}$ compared to the rest of parameters investigated in this section. The hydraulic conductivity of the tumor interstitium ($\hat{K}^T$) has the lowest influence on the model compared to the parameters considered in these analysis. The negligible influence of $\hat{K}^T$ on the GNR concentration in the tumor means that GNR transport across the tumor is dominated by diffusion which is a result of the flat pressure profile across the tumor core (see Fig. 3.3(A) i.e. pressure gradient across the tumor core is zero). In addition, impaired lymphatics in the tumor reduces the influence of the parameter $\hat{L}^{(N)}_{pl}\hat{S}^{(N)}_l/\hat{V}^{(N)}$ on the GNR concentration in the tumor. Furthermore, we repeat this parameter sensitivity test for larger parameter values deviated from the baseline case (this means some parameters will exceed their experimentally measured value range in the

literature) to explore the influence of these parameters on the model predictions (Table 3.4). The values of the relative standard deviation confirms that $\hat{S}_v^{(T)}/\hat{V}^{(T)}$ and $\hat{r}_p^{(T)}$ are the most important parameters compared to the other chosen parameters for this sensitivity analysis. However, the model showed more sensitivity to volume accessible by GNRs in the tumor compared to the GNR diffusivity, which is different from what we found with smaller deviation values from the baseline. Overall, the GNR diffusion coefficient showed the highest change in the relative standard deviation value which increased by 3.9 times, followed by the tumor hydraulic conductivity which increased by 3.5, and then comes the volume accessible by GNRs in the tumor which increased by 3.1 times. The remaining parameters increased by ≈ 2.6 as depicted in Table 3.4.

In the preceding paragraph we studied the local sensitivity, where each parameter is changed individually. We now study the effect of changing all of these parameters simultaneously on $\hat{C}_{max}^{(T)}$, known as a global sensitivity analysis (GSA) [90]. There are several different GSA techniques in the literature (such as Elementary Effects Test, Regional Sensitivity Analysis and Variance-Based Sensitivity Analysis [90]). Hence we use the elementary effect method (EEs) introduced by Morris [1991] [75]. In this technique, samples of parameter values are generated by randomly changing one parameter value to get the first sample, then another sample of parameter values is generated from the preceding sample by changing another parameter value at random. In other words, the first sample comprises one changed parameter value, while the second sample comprises two changed parameter values compared to the baseline parameter values etc. In effect, only one parameter is changed in every newly generated sample starting from the preceding sample. In this way we get a set of samples in which the parameters are changed randomly and simultaneously. Then we solve the model at all of these input samples and calculate the objective function ($\hat{C}_{max}^{(T)}$ in our case). We calculate the elementary effects of each parameter by computing the derivatives of the objective function with respect to each parameter under investigation. This can be calculated since every sample of the model input is generated from the preceding sample with a single parameter change, thus the elementary effect (EE) of this parameter is the change in the output between these two samples divided by the change in this parameter value [75]. Finally, we calculate the elementary effect indices (using 20 samples for each parameter, i.e. 140 samples for all parameters) which are the elementary effect mean (μ_{EE}), the elementary effect standard deviation (σ_{EE}) and the elementary effect global index (GI_{EE}) to measure the model

sensitivity to these parameters [49] and these parameters are defined in the form

$$\sigma_{EE} = \sqrt{\frac{1}{19}\sum_{i=1}^{20}(EE_i - \mu_{EE})^2}, \tag{3.54}$$

$$\mu_{EE} = \frac{1}{20}\sum_{i=1}^{20} EE_i, \tag{3.55}$$

$$GI_{EE} = \sqrt{\mu_{EE}^2 + \sigma_{EE}^2}. \tag{3.56}$$

We implement this technique using a MATLAB toolbox developed by Pianosi et al. [2015] [90] and present the results in the Figs. 3.11(A) and (B) for the same six parameters as previously investigated locally. This MATLAB toolbox generated 140 samples to compute μ_{EE} and σ_{EE} (the results are shown in the Table 3.5), then another 140 samples were generated to test the convergence of the results. In the Fig. 3.11(C) we plot the values of μ_{EE} (for the parameters under investigation) against the number of samples which shows that the results are converging. Parameters which have relatively large μ_{EE} values compared to the corresponding value of σ_{EE} ($\mu_{EE}/\sigma_{EE} >> 1$) are considered to be important to the model output. Parameters which have relatively large σ_{EE} values compared to the corresponding μ_{EE} value ($\mu_{EE}/\sigma_{EE} << 1$ are considered to be important with nonlinear effects and interaction with other parameters [75]. In Fig. 3.11(B) we show the global index graphically as a relative quantitative measure of parameter sensitivity. This index confirms the results of the local sensitivity analysis, see Tables 3.5, 3.3, where the tumor vasculature density ($GI_{EE} = 1.089 \times 10^{-6}$) and the vessel wall pore size ($GI_{EE} = 1.02 \times 10^{-6}$) have the largest figures for the elementary effect global indices calculated for the chosen parameters in these analysis. Therefore, we conclude from these analysis that the tumor vasculature density and the tumor cell density (the interstitium volume fraction) are among the key parameters in our model which control the GNR concentration profile across the tumor in the case of GNR intravenous administration.

3.6 Conclusion

In this chapter we mimicked the GNR delivery to a partially vascularized tumor and the GNR tumor-tissue interaction. The main target of this study is to explore the potential GNR delivery that can result in the optimal GNR distribution across the tumor (for the chosen model parameter values). We require the GNRs to be homogeneous and in large concentration across the tumor compared to the surrounding healthy tissue.

Using GNRs without binding ligands administrated intravenously result in a homogeneous GNR distribution across the tumor within 24 hours post injection (Fig. 3.3(D), (E)). Hence, the optimal GNR delivery timescale in this case is 24 hours which should

parameter	min.	max.	Change at min.	Change at max.	rsd_1
$\frac{\hat{S}_v^{(T)}}{\hat{V}^{(T)}}$	-50%	$+50\%$	26.5%	20.4%	14.6
$\hat{r}_p^{(T)}$	-50%	$+50\%$	29.8%	11.1%	13.1
$\hat{D}^{(T)}$	-50%	$+50\%$	10.2%	8.2%	5.7
$\phi_f^{(T)}$	-50%	$+50\%$	11.7%	4.3%	5
$\hat{L}p_l\frac{\hat{S}_l^{(N)}}{\hat{V}^{(N)}}$	-50%	$+50\%$	6.6%	4%	3.3
$\hat{K}^{(T)}$	-50%	$+50\%$	1.6%	0.6%	0.7

Table 3.3: Local sensitivity analysis results (rsd_1) for six parameters. Every parameter is varied 50% and the objective function is calculated at the minimum and the maximum of the parameter value.

parameter	min.	max.	Change at min.	Change at max.	rsd_2	rsd_2/rsd_1
$\frac{\hat{S}_v^{(T)}}{\hat{V}^{(T)}}$	-90%	$+200\%$	71.4%	69.2%	40	2.74
$\hat{r}_p^{(T)}$	-90%	$+200\%$	97.8%	25%	34.4	2.63
$\phi_f^{(T)}$	-90%	$+200\%$	62%	8.7%	19.3	3.1
$\hat{D}^{(T)}$	-90%	$+200\%$	39.7%	26.7%	17.6	3.9
$\hat{L}p_l\frac{\hat{S}_l^{(N)}}{\hat{V}^{(N)}}$	-90%	$+200\%$	18.7%	10.8%	8.3	2.5
$\hat{K}^{(T)}$	-90%	$+200\%$	8.1%	1.3%	2.5	3.5

Table 3.4: Local sensitivity analysis results (rsd_2) for six parameters. Every parameter is varied between -90% to $+200\%$ and the objective function is calculated at the minimum and the maximum of the parameter value.

parameter	min.	max.	mean (EE)	standard deviation (EE)	global index (EE)
$\frac{\hat{S}_v^{(T)}}{\hat{V}^{(T)}}$	-50%	$+50\%$	1.046×10^{-6}	3.037×10^{-7}	1.089×10^{-6}
$\hat{r}_p^{(T)}$	-50%	$+50\%$	9.506×10^{-7}	3.697×10^{-7}	1.02×10^{-6}
$\hat{D}^{(T)}$	-50%	$+50\%$	4.394×10^{-7}	2.758×10^{-7}	5.188×10^{-7}
$\phi_f^{(T)}$	-50%	$+50\%$	3.543×10^{-7}	2.142×10^{-7}	4.14×10^{-7}
$\hat{L}p_l\frac{\hat{S}_l^{(N)}}{\hat{V}^{(N)}}$	-50%	$+50\%$	2.393×10^{-7}	1.08×10^{-7}	2.626×10^{-7}
$\hat{K}^{(T)}$	-50%	$+50\%$	4.407×10^{-8}	2.792×10^{-8}	5.217×10^{-8}

Table 3.5: Global sensitivity analysis results for six parameters. Every parameter is varied 50% and the objective function is calculated at 140 samples of parameter values.

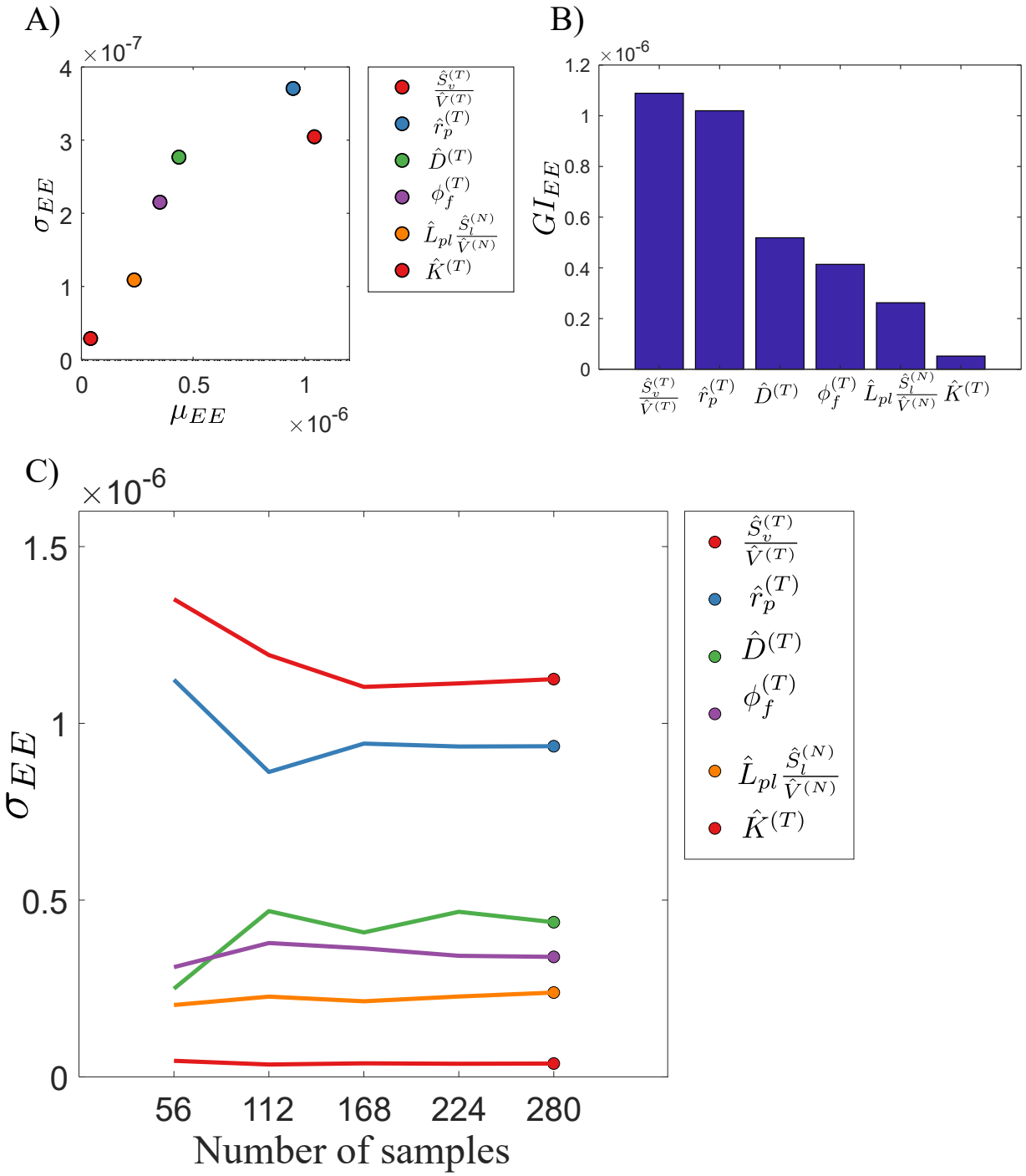

Figure 3.11: Sensitivity analysis results. A) The standard deviation and the mean for the elementary effects. B) The global index. C)The standard deviation of the elementary effect against number of samples.

be immediately followed by laser irradiation. However, in large tumors the tumor core is already dead tissue, so we measured the GNR homogeneity across the outer half of the tumor and we found that 21 hours post administration is the optimal time for laser irradiation.

On the other hand, using GNRs conjugated with binding ligands results in a hetero-

geneous GNR distribution, where GNRs accumulate in large concentration (ten times of the corresponding GNR concentration in the absence of binding ligands) within the tumor rim only (Fig. 3.5(A)). The width of this rim depends on the maximal tumor capacity for internalizing GNRs (Fig. 3.7(A) and Fig. 3.10(C)).

In the case of GNR intratumoral administration (at the tumor center) leads to a heterogeneous distribution of GNRs across the tumor, with a maximal GNR concentration at the tumor center (Fig. 3.9(A)). In this technique the GNR concentration at the tumor rim is comparable to the GNR concentration in the surrounding tissue, which means ablating the tumor rim will cause severe damage to the surrounding tissue.

In the absence of the binding ligands, we conclude from the parameter sensitivity analysis (Sec. 3.5.3) that the GNR delivery to tumors is dominated by tumor vascularity, tumor vasculature pore size and the GNR diffusivity across the tumor. That means the intravenous administration is suitable for vascularized tumors with large vasculature density.

In this study we introduced the maximal tumor cell capacity to internalize GNRs which was observed experimentally [40], but this phenomena was not included in the theoretical models in the literature, to the best of our knowledge. Therefore, our model is a generalization of those models which neglected NP internalization such as Baxter and Jain [1989] [10] (i.e. zero tumor capacity to internalize GNRs, $C_{i_{max}} = 0$) in addition to the other models which assumed unlimited NP internalization, for example Goodman et al. [2008] [34] (i.e. $C_{i_{max}} \longrightarrow \infty$). Therefore, we suggest testing this phenomena *in vivo*, *in vitro* and theoretically for different NP types and experimental setups.

However, we used some simplifying approximations (assumptions) in this study which we will address in future work. For example we assumed that the osmotic pressure is constant [55] which is typically influenced by the transvascular GNR concentration [21]. So, we plan to couple the macroscopic fluid transport model with the GNR transport model to estimate the osmotic pressure more accurately.

In addition, we considered homogeneous tumor and homogeneous continuous tumor vasculature at the tumor rim. This approximation is essential to maintain the spherical symmetry of the problem. Typically tumors have heterogeneous structures, and the tumor vasculature is discrete and heterogeneous. This tumor characteristic requires a 2D or 3D mathematical model at the microscale to mimic a realistic tumor. The extension to either a 2D or 3D requires estimation to heterogeneous GNR transvascular flux and GNR diffusion coefficient.

Finally, we proceed to study the laser irradiation theoretically using the output of this chapter to evaluate the impact of the GNR distribution across the tumor in either the absence or the presence of binding ligands.

Chapter 4

Mathematical Model for Laser Irradiation

4.1 Introduction

Laser irradiation is used in photothermal therapy to elevate tumor temperature in the presence of GNRs [43]. The impact of laser irradiation depends on the tumor size, tumor depth in the body and the GNR distribution across the tumor [43, 92]. So, theoretical modeling of laser irradiation needs to be coupled with a GNR delivery and a cell injury model to investigate the key parameters and the optimal GNR distribution which generates the maximal damage in the tumor (in the presence of laser irradiation) and minimal damage in the surrounding tissue.

Soni et al. [2015] [102] studied theoretically and experimentally the problem of delivering gold NPs to a cylindrical Agrose gel surrounded by another cylindrical Agrose gel to mimic a cylindrical tumor surrounded by healthy tissue. They investigated the influence of laser spot size, irradiation duration and laser intensity. They found that increasing tumor temperature up to 50° C requires two minutes of laser irradiation with intensity 2.5 W/cm^2. Huang et al. [2006] [45] investigated theoretically the laser power and temperature thresholds required for inducing tissue damage. In addition, they studied the significance of conjugating NPs with binding ligands. They found that tumors needed to be heated up to $70-80°$ C to induce cell death. This tumor temperature can be generated (in the presence of NPs) using laser irradiation of power 19 W cm^{-2} with 4 min of irradiation time. They also found introducing binding ligands increases the NP concentration in the tumor. They validated their results *in vitro*.

Huang et al. [2010] [44] simulated GNR delivery to human prostate cancer cells and validated their model *in vitro*. They assumed that GNRs were not internalized by the tumor cells. They studied the significance of activation energy (the minimum cell energy required to induce cell death). Von Maltzahn et al. [2009] [112] used a 3D mathematical

model to simulate laser irradiation of tumors and they validated their model *in vivo*. They used GNRs with blood half life of 17 hours which were administrated intravenously or intratumorally. They reported that their experiment setup successfully ablated the tumor.

In the preceding chapter we mimicked the GNR delivery to tumors to predict the GNR distribution profile across the tumor and the surrounding healthy tissue. We investigated the cases of administrating GNRs either intravenously or intratumorally, in addition to the influence of the presence of the binding ligands. In this chapter we extend this model to irradiation by an external laser beam (Fig. 4.1), from which we estimate the overall tissue damage. The tumor temperature can be modeled using conservation of energy through the Pennes' bioheat equation (a modified heat equation) which is commonly used in the hyperthermia therapy modelling literature and described by Welch and Van Gemert [2011] [118] in their text book. We use this thermal model to examine laser irradiation efficacy in the presence or absence of binding ligands and investigate the optimal time interval for GNR delivery and laser irradiation in order to maximize tumor damage and reduce side effects in the surrounding healthy tissue.

4.2 The Model

4.2.1 The Bioheat Equation

We return to the model discussed in chapter 3 and extend it to include a heat source (laser irradiation) and thermal effects. We study the temperature across the tumor ($\hat{T}^{(T)}$, K) and the surrounding tissue ($\hat{T}^{(N)}$, K) (both loaded with GNRs) in the presence of an external laser irradiation (Fig. 4.1) using Pennes' equation. Rylander et al. [2006] [95] reported that Pennes' equation predictions demonstrated a good agreement with the measured temperature across a prostate tumor surrounded by healthy tissue irradiated by laser *in vitro*. Pennes' bioheat equation assumes that the heat exchange between the blood available in the capillaries and the surrounding tissue is proportional to the blood perfusion rate ($\hat{\omega}_b$, s^{-1}) (the rate of blood volume flow delivered to a unit volume of tissue) times the temperature difference between the blood ($\hat{T}_b$, K) and tissue ($\hat{T}^{(j)}$, $j = T,\ N$; K) [19]. This is an empirically constructed term which encompasses the effects of both conduction and convection, similar to the concept of a heat transfer coefficient used mainly in the thermal literature. This model assumes that blood enters the tumor vasculature at temperature $\hat{T}_b$ with a very slow velocity, which results in thermal equilibrium between the tissue and the blood in the capillaries. This thermal exchange is typically thought to be dominated by conduction across vessel wall [19]. We estimated the contribution of heat transfer by convection across the vessel wall using the fluid flow driven by the Starling law (3.7) and found the heat exchange rate is $\approx 1.2 \times 10^{-5}$ s^{-1} which is much smaller than the

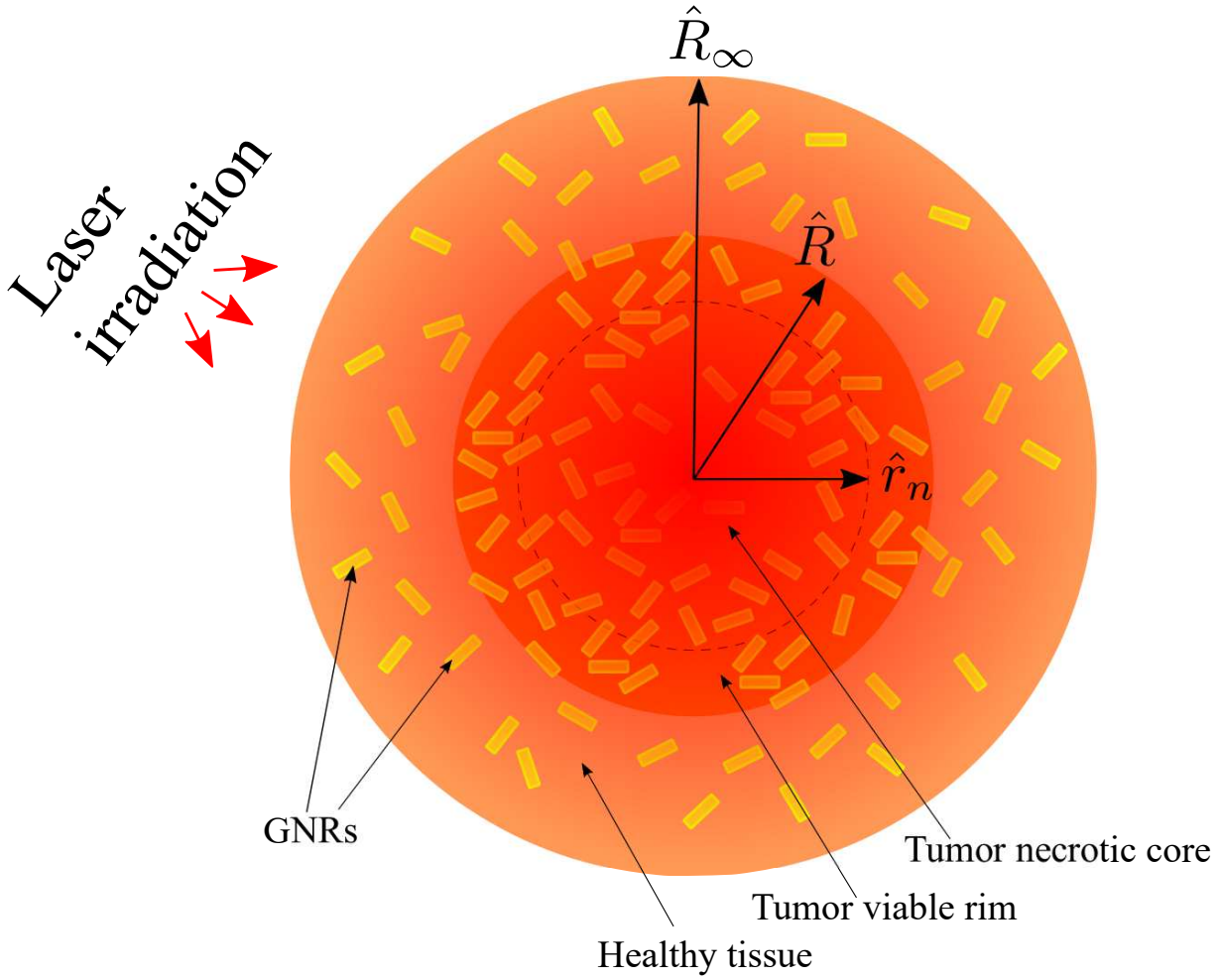

Figure 4.1: The domain of a tumor surrounded by normal tissue both loaded with GNRs.

estimated value for $\hat{\omega}_b$ in the literature, for example, Jiang et al. [2002] [58] considered $\hat{\omega}_b = 1.25 \times 10^{-3}$ (s^{-1}) in skin. Hence, in this study we treat $\hat{\omega}_b$ as an unknown parameter which we use to fit our model predictions to the experimental data, see Sec. 4.4, i.e. we ignore the thermal boundary layer adjacent the vasculature wall and replace it by a heat transfer coefficient times the transmural temperature ($\hat{\omega}_b(\hat{T}^{(j)} - \hat{T}_b), \quad (j = T,\ N)$) . We will address this approximation in the future work using asymptotic analysis for the energy equation at the microscale similar to our study in chapter 2.

We assume that the laser source is relatively far from the tumor, so we ignore the direct effect of the laser beam in favor of the light scattered across the tumor and the surrounding tissue. To maintain spherical symmetry, we assume that the laser beam generates a spherical heat source at the tumor center. The contribution of energy released by GNRs due to laser irradiation is represented by a source term ($\hat{S}_{laser}$, J s^{-1} cm^{-3}) in the energy (Pennes') equation. For simplicity, we assume that the temperature in the blood is a prescribed function. We also assume that heat exchange occurs with the capillaries (in the healthy tissue and the vascularized region of the tumor), with the lymphatic vessels

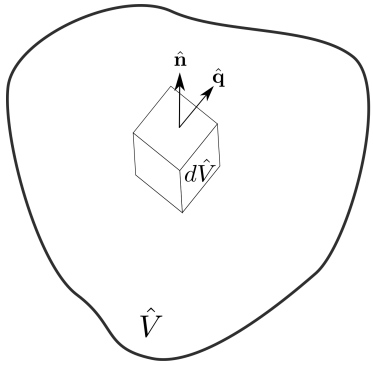

Figure 4.2: Control of volume $d\hat{V}$ of an arbitrary tissue of volume $\hat{V}$, where $\mathbf{n}$ is the unit and $\mathbf{q}$ is the heat flux across the surface area of $d\hat{V}$.

(in the healthy tissue) and across the healthy tissue outer boundary. Furthermore, we incorporate heat transfer by convection with the interstitial fluid flow (since we have shown in Sec. 3.4.1 that the interstitial fluid pressure gradient across the tumor periphery generates an interstitial fluid velocity out of tumor). Using these assumptions we can derive the energy equation for an arbitrary volume of tissue of volume $\hat{V}$ and with surface area $\hat{S}$ (see Fig. 4.2).

4.2.2 Pennes' Equation

We consider an arbitrary tissue of volume $\hat{V}$ containing a control volume $d\hat{V}$ with surface area $d\hat{S}$. We denote $\mathbf{n}$ as the unit vector perpendicular to the surface and $\mathbf{q}$ as the heat flux across $d\hat{S}$. We use Fourier's law to write the heat flux $\mathbf{q}$ in terms of the temperature gradient in the form [71]

$$\hat{\mathbf{q}} = -\hat{K}\nabla\hat{T}, \tag{4.1}$$

where $\hat{K}$ is the tissue thermal conductivity which is a function of space, tissue temperature and time which is difficult to be determined experimentally, so herein we consider $\hat{K}$ is constant across the tumor and the surrounding tissue. According to the first law of thermodynamics, the heat transfer rate $\hat{Q}$ equals the change in the internal energy $\hat{E}$, so we write [71]

$$\hat{Q} = \frac{d\hat{E}}{d\hat{t}} \equiv \int_{\hat{V}} \hat{\rho}_t \hat{\gamma}_t \frac{\partial \hat{T}}{\partial \hat{t}} d\hat{V}, \tag{4.2}$$

where $\hat{t}$ is the time variable, $\hat{\rho}_t$ is the tissue density and $\hat{\gamma}_t$ is the specific heat capacity (the heat required to raise the temperature of a unit mass of tissue by one degree). Now,

we can write the change of energy in the control volume in the form

$$d\hat{Q} = -(\hat{\mathbf{u}}\hat{T} - \hat{K}\nabla\hat{T}).\mathbf{n}d\hat{S} + (\hat{S}_{blood} + \hat{S}_{lymph} + \hat{S}_{laser})d\hat{V}, \tag{4.3}$$

where $\hat{\mathbf{u}}$ is the interstitial flow velocity, $\hat{\mathbf{u}}\hat{T}.\mathbf{n}d\hat{S}$ represents heat transfer across the control volume surface by convection, $\hat{K}\nabla\hat{T}.\mathbf{n}d\hat{S}$ represent heat flux across the control volume surface by conduction, $\hat{S}_{blood}$ represents the heat exchange with blood vessels in the control volume, $\hat{S}_{lymph}$ represent the heat exchange with lymphatics in the control volume, and $\hat{S}_{laser}$ is the heat generated within the control volume due to laser irradiation. We integrate Eq. (4.3) over the whole tissue to get the net heat rate.

$$\hat{Q} = -\int_{\hat{S}} (\hat{\mathbf{u}}\hat{T} - \hat{K}\nabla\hat{T}).\mathbf{n}d\hat{S} + \int_{\hat{V}} (\hat{S}_{blood} + \hat{S}_{lymph} + \hat{S}_{laser})d\hat{V}. \tag{4.4}$$

Substituting Eq. (4.2) into Eq. (4.4) we get

$$\int_{\hat{V}} \hat{\rho}_t\hat{\gamma}_t \frac{\partial\hat{T}}{\partial\hat{t}} d\hat{V} = -\int_{\hat{S}} (\hat{\mathbf{u}}\hat{T} - \hat{K}\nabla\hat{T}).\mathbf{n}d\hat{S} + \int_{\hat{V}} (\hat{S}_{blood} + \hat{S}_{lymph} + \hat{S}_{laser})d\hat{V}. \tag{4.5}$$

Using Gauss's theorem we can write the preceding equation in the form

$$\int_{\hat{V}} \hat{\rho}_t\hat{\gamma}_t \frac{\partial\hat{T}}{\partial\hat{t}} d\hat{V} = -\int_{\hat{V}} \nabla\cdot(\hat{\mathbf{u}}\hat{T} - \hat{K}\nabla\hat{T})d\hat{V} + \int_{\hat{V}} (\hat{S}_{blood} + \hat{S}_{lymph} + \hat{S}_{laser})d\hat{V}. \tag{4.6}$$

Hence, from the preceding equation we can write the energy equation in the form

$$\int_{\hat{V}} (\hat{\rho}_t\hat{\gamma}_t \frac{\partial\hat{T}}{\partial\hat{t}} d\hat{V} + \nabla\cdot(\hat{\mathbf{u}}\hat{T} - \hat{K}\nabla\hat{T}) - \hat{S}_{blood} - \hat{S}_{lymph} - \hat{S}_{laser})d\hat{V} = 0, \tag{4.7}$$

Since the volume $\hat{V}$ is arbitrary, we write the energy equation in the tissue in the form

$$\hat{\rho}_t\hat{\gamma}_t \frac{\partial\hat{T}}{\partial\hat{t}} d\hat{V} + \nabla\cdot(\hat{\mathbf{u}}\hat{T} - \hat{K}\nabla\hat{T}) - \hat{S}_{blood} - \hat{S}_{lymph} - \hat{S}_{laser} = 0, \tag{4.8}$$

Equation (4.8) is the bioheat equation [95] that we use to mimic laser irradiation of a spherical tumor surrounded by a shell of healthy tissue and both loaded with GNRs (Fig. 4.1). We assume that both tumor and the surrounding tissue have the same thermal properties which are independent of time, space and temperature. So, we write the source and sink terms in Eq. (4.8) as follows

$$\hat{S}_{blood} = -\hat{\rho}_b\hat{\gamma}_b\hat{\omega}_b(\hat{T} - \hat{T}_b), \tag{4.9}$$

$$\hat{S}_{lymph} = -\hat{\rho}_t\hat{\gamma}_t\hat{L}_{pl}\frac{\hat{S}_l}{\hat{V}}(\hat{P}_i - \hat{P}_l)(\hat{T} - \hat{T}_l), \tag{4.10}$$

where $\hat{\rho}_t$ (g cm^{-3}) denotes the tissue density, $\hat{\rho}_b$ (g cm^{-3}) is the density of blood, $\hat{\gamma}_t$ (J g^{-1} K^{-1}) is the specific heat capacity of the tissue, $\hat{K}_t^{(T)}$ and $\hat{K}_t^{(N)}$ (J s^{-1} cm^{-1} K^{-1}) are the thermal conductivities of the tumor and healthy tissue, respectively, $\hat{T}_l$ (K) is the temperature of the lymphatic fluid and $\hat{\gamma}_b$ (J g^{-1} K^{-1}) is the specific heat capacity of the blood. We assume that the blood density and the blood specific heat capacity of the blood are constants.

Similar to chapter 3 we use the superscript (T) to denote variables in the tumor, and (N) to denote variables in the healthy tissue. Furthermore, we assume that the tumor is partially vascularized and tumor lymphatics are dysfunctional. On the other hand, we assume that the healthy tissue is fully vascularized and contains lymphatics. Hence, using Eqs. (4.8-4.10) we write the energy equations in the tumor and the surrounding tissue in the form

$$\hat{\rho}_t\hat{\gamma}_t\left(\frac{\partial\hat{T}^{(T)}}{\partial\hat{t}} + \frac{1}{\hat{r}^2}\frac{\partial}{\partial\hat{r}}(\hat{r}^2\hat{u}^{(T)}\hat{T}^{(T)})\right) = \frac{1}{\hat{r}^2}\frac{\partial}{\partial\hat{r}}\left(\hat{r}^2\hat{K}_t^{(T)}\frac{\partial\hat{T}^{(T)}}{\partial\hat{r}}\right)$$
$$- H(\hat{r} - \hat{r}_n)\hat{\rho}_b\hat{\gamma}_b\hat{\omega}_b(\hat{T}^{(T)} - \hat{T}_b) + \hat{S}_{laser}, \qquad (0 \le \hat{r} \le \hat{R}) \tag{4.11}$$

$$\hat{\rho}_t\hat{\gamma}_t\left(\frac{\partial\hat{T}^{(N)}}{\partial\hat{t}} + \frac{1}{\hat{r}^2}\frac{\partial}{\partial\hat{r}}(\hat{r}^2\hat{u}^{(N)}\hat{T}^{(N)})\right) = \frac{1}{\hat{r}^2}\frac{\partial}{\partial\hat{r}}\left(\hat{r}^2\hat{K}_t^{(N)}\frac{\partial\hat{T}^{(N)}}{\partial\hat{r}}\right)$$
$$- \hat{\rho}_b\hat{\gamma}_b\hat{\omega}_b(\hat{T}^{(N)} - \hat{T}_b) - \hat{\rho}_t\hat{\gamma}_t\hat{L}_{pl}\frac{\hat{S}_l^{(N)}}{\hat{V}^{(N)}}(\hat{P}_i^{(N)} - \hat{P}_l^{(N)})(\hat{T}^{(N)} - \hat{T}_l) + \hat{S}_{laser}, \quad (\hat{R} \le \hat{r} \le \hat{R}_\infty) \tag{4.12}$$

where $\hat{\omega}_b$ is the blood perfusion rate parameter, $H(\hat{r} - \hat{r}_n)$ is the Heaviside function and $\hat{r}_n$ is the radius of the avascular region in the tumor. $\hat{\omega}_b$ is an empirical parameter which is used to fit the Pennes' model (4.11 and 4.12) to the measured temperature gradients and heat flows [19]. So, this parameter controls the heat exchange between blood and tissue in the Pennes' equation. For simplicity, in this study we consider the blood perfusion rates in both the tumor and the healthy tissue to be constant (since the change of blood perfusion rate is accompanied by a change of vasculature, interstitium and cell volumes which are considered constants in this study).

Laser transport in a biological tissue is attenuated due to light absorption and scat-

tering which occurs simultaneously across the tissue [118]. It is difficult to find an exact assessment of the laser distribution in tissue as this requires a model describing the spatial configuration of the tissue, the optical properties of the tissue and trace all photons scattering and absorbing within the tissue [118]. Therefore, in this chapter we assume the tissue (tumor or healthy tissue) is optically isotropic, homogeneous and absorbs the laser as a bulk material, and all the scattered photons are distributed over the whole tissue. The absorption probability for an individual photon propagating over a unit distance is known as the absorption coefficient ($\hat{\mu}_a$, cm^{-1}). The scattering probability for a single photon propagating over a unit distance is known as the scattering coefficient ($\hat{\mu}_s$, cm^{-1}).

When the scattering and absorption coefficients for a medium are comparable, it is necessary to solve the full laser transport problem using Monte Carlo simulation [7] where the light is considered as discrete particles (photons) absorbing and scattering over the medium. If light absorption dominates the light scattering process, the Beer-Lambert law which is an empirical expression for the light fluence rate ($\hat{\phi}_{laser}$, J s^{-1} cm^{-2}) is a valid approximation to the light transport equation [7]. Beer-Lambert law states that $\hat{\phi}_{laser}$ decreases exponentially with the light path depth in the medium, where $\hat{\phi}_{laser}$ is defined as the number of photons crossing per unit time per unit area. When biological tissue is irradiated by a laser beam with wave length in the infrared region of the spectrum (which is the case in this study), scattering dominates absorption [94]. In this case, the optical diffusion approximation can provide an accurate approximate solution to the laser transport problem [61] where light propagation over the tissue is treated as a diffusion process. This approximation reduces the laser transport equation across the tissue to a diffusion equation in the light fluence rate which can be solved analytically and used to estimate the heat source ($\hat{S}_{laser} = \hat{\mu}_a \hat{\phi}_{laser}$) generated by the laser inside a spherical tumor, but this solution is invalid at the tumor center within a sphere of radius $\hat{r}_0 = 0.1$ cm [118]. Hence, the rate of laser energy generated in the tumor and the surrounding tissue for a point laser source located at the tumor center can be written as a function of laser power ($\hat{P}_{laser}$, J s^{-1}), transport attenuation coefficient ($\hat{\mu}_{tr}$, cm^{-1}), the effective radiation coefficient ($\hat{\mu}_{eff}$, cm^{-1}) and the radial position in the form [118]

$$\hat{S}_{laser} = \begin{cases} \dfrac{3\hat{P}_{laser}\hat{\mu}_{tr}\hat{\mu}_a}{4\pi\hat{r}_0} e^{-\hat{\mu}_{eff}\hat{r}_0}, & (0 \le \hat{r} \le \hat{r}_0), \\ \\ \dfrac{3\hat{P}_{laser}\hat{\mu}_{tr}\hat{\mu}_a}{4\pi\hat{r}} e^{-\hat{\mu}_{eff}\hat{r}}, & (\hat{r}_0 \le \hat{r} \le \hat{R}_\infty), \end{cases} \tag{4.13}$$

where

$$\hat{\mu}_{eff} = \sqrt{3\hat{\mu}_a\hat{\mu}_{tr}}, \qquad \hat{\mu}_{tr} = (\hat{\mu}_a + \hat{\mu}_s(1-g)), \tag{4.14}$$

where $\hat{\mu}_s$ (cm^{-1}) is the total scattering coefficient and g is the anisotropy factor.

The total absorption and scattering coefficients are magnified because of the presence of GNRs, which can be written as

$$\hat{\mu}_a = \hat{\mu}_{at} + \hat{\mu}_{an}, \quad \hat{\mu}_s = \hat{\mu}_{st} + \hat{\mu}_{sn}, \tag{4.15}$$

where $\hat{\mu}_{an}$ (cm^{-1}) is the GNR absorption coefficient, $\hat{\mu}_{sn}$ (cm^{-1}) is the GNR scattering coefficient, $\hat{\mu}_{at}$ (cm^{-1}) is the tissue absorption coefficient, $\hat{\mu}_{st}$, (cm^{-1}) is the tissue scattering coefficient, $\hat{\sigma}_a$ (cm^2) is the absorption cross-section coefficient and $\hat{\sigma}_s$ (cm^2) is the scattering cross-section coefficient. We assume $\hat{\mu}_{at}$ and $\hat{\mu}_{st}$ are material constants, whereas $\hat{\mu}_{an}$ and $\hat{\mu}_{as}$ are functions of the local GNR concentration which are given by [31]

$$\hat{\mu}_{an} = \phi_n(\hat{r})\hat{\sigma}_a, \quad \hat{\mu}_{sn} = \phi_n(\hat{r})\hat{\sigma}_s, \quad \phi_n(\hat{r}) = \frac{\hat{C}_{tot}^{(j)}(\hat{r})}{\hat{\rho}_g}, \quad (j = T,\ N), \tag{4.16}$$

where ϕ_n is the GNR volume fraction and $\hat{\rho}_g$ is the density of the gold (constant). The total concentration of GNRs ($\hat{C}_{tot}^{(j)}$, $\mathrm{g/cm}^3$) (see Eqn. 3.31) is calculated from GNR transport model introduced in chapter 3 (Eq. 3.32).

The spatial distributions of the GNR volume fraction and the value of the laser source term across the tumor and the surrounding tissue are plotted in the Figs. 4.3 (A) and (B) for the case of no binding ligands conjugated to the GNRs, while the Figs. 4.3(C) and (D) are for the case of GNRs conjugated with binding ligands. The Figs. 4.3(A) and (C) show the profiles of the GNR volume fraction immediately prior the irradiation in the absence and the presence of binding ligands, respectively. The laser source value is constant at the tumor center within 0.1 cm from the tumor center according to the definition in Eq. (4.13), but it is three times larger in the absence of the binding ligands than in the presence of the binding ligands where binding ligands resist the GNRs from accessing the tumor center and accumulate at the tumor rim (Fig. 4.3(C)). As a result, the laser source term value peaks at the tumor rim (Fig. 4.3(D)) then decreases rapidly in the surrounding tissue. This laser source profile is a result of our assumption about that the laser irradiation can be represented as a point source at the tumor center in order to maintain the spherical symmetry of the model. We will address this approximation in the future work.

The GNR Volume Fraction in the Tumor

The volume fraction (ϕ_n) of GNRs in the tumor and healthy tissue is equivalent to the ratio of the GNR pointwise concentration to the gold density which can be derived using a control volume ($d\hat{V}$) in the physical domain contains GNRs with concentration $\hat{C}_{tot}^{(j)}(\hat{r}, \hat{t})$. The mass of gold ($d\hat{M}_n$) in the control volume can be estimated in two ways

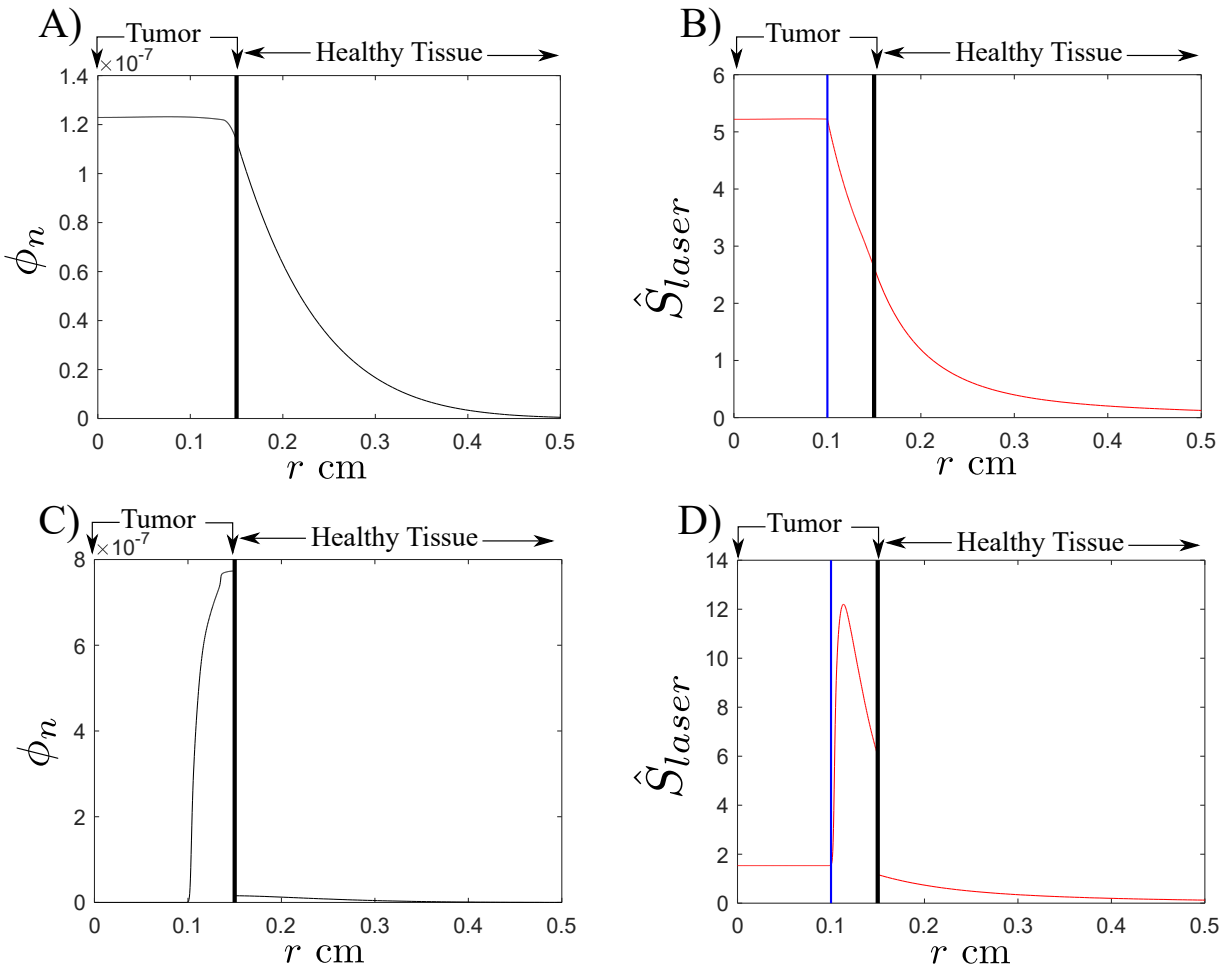

Figure 4.3: The laser source term (Eq. (4.13)) value and the GNR volume fraction across the tumor and the surrounding tissue are plotted using parameter values in Table 4.1. A)The spatial GNR volume fraction distribution in the absence of binding ligands. B)The spatial laser source term value in the absence of the binding ligands. C)The spatial GNR volume fraction distribution in the presence of binding ligands. D)The spatial laser source term value in the presence of the binding ligands.

$$d\hat{M}_n = \hat{C}_{tot}^{(j)} d\hat{V}, \qquad d\hat{M}_n = \hat{\rho}_g d\hat{V}_n, \tag{4.17}$$

where $d\hat{V}_n$ is the total volume of GNRs in the control volume. The volume fraction of GNRs ϕ_n in the control volume can be determined from

$$\phi_n = \frac{d\hat{V}_n}{d\hat{V}}. \tag{4.18}$$

Hence, we substitute (4.17) into (4.18) we get an expression for the pointwise GNR volume fraction that we can use in our model (4.16) as follows

$$\phi_n = \frac{\hat{C}_{tot}^{(j)}}{\hat{\rho}_g}. \tag{4.19}$$

The Absorption (Scattering) Cross-Section for GNRs

The absorption (scattering) cross-sections for GNRs determine the amount of energy absorbed (scattered) by the irradiated GNRs and can be calculated either experimentally or analytically [81]. Jain et al. [2006] [50] reported that $\hat{\sigma}_a$ and $\hat{\sigma}_s$ depend on the effective GNR radius ($\hat{r}_{eff}$, cm, the radius of the corresponding sphere which has the same volume ($\hat{V}_n$) of the GNR) which can be calculated from

$$\hat{r}_{eff} = \left(\frac{3\hat{V}_n}{4\pi}\right)^{\frac{1}{3}} = \left(\frac{3}{16}\hat{d}_n^2\hat{L}_n\right)^{\frac{1}{3}}, \tag{4.20}$$

where, $\hat{d}_n$ (cm) is the GNR diameter and $\hat{L}_n$ (cm) is the GNR length. Jain et al. [2006] [50] numerically calculated $\hat{\sigma}_a$, $\hat{\sigma}_s$ and the extinction cross-section ($\hat{\sigma}_{ext}$, cm^2, $\hat{\sigma}_{ext} = \hat{\sigma}_a + \hat{\sigma}_s$) for variety of GNRs with $7 \leq \hat{r}_{eff} \leq 23$. So, we extract from these data the values of both parameters $\hat{\sigma}_a$ and $\hat{\sigma}_s$ according to the GNR physical properties ($\hat{r}_{eff}$, cm) we use in this study, see Table 4.1.

4.2.3 Initial and Boundary Conditions For the Bioheat Equation

At the center of the tumor we apply the spherical symmetry condition, while at the outer edge of the healthy tissue the heat flux is proportional to the thermodynamic driving force (the temperature difference across the boundary) which is typically a Robin-type boundary condition. Also, we apply continuity of temperature and continuity of heat flux at the tumor/tissue boundary interface

$$\hat{u}^{(T)}\hat{T}^{(T)} - \frac{\hat{K}_t^{(T)}}{\hat{\rho}_t\hat{\gamma}_t}\frac{\partial\hat{T}^{(T)}}{\partial\hat{r}} = 0, \qquad (\hat{r} = 0), \tag{4.21}$$

$$\hat{u}^{(T)}\hat{T}^{(T)} - \frac{\hat{K}_t^{(T)}}{\hat{\rho}_t\hat{\gamma}_t}\frac{\partial\hat{T}^{(T)}}{\partial\hat{r}} = \hat{u}^{(N)}\hat{T}^{(N)} - \frac{\hat{K}_t^{(N)}}{\hat{\rho}_t\hat{\gamma}_t}\frac{\partial\hat{T}^{(N)}}{\partial\hat{r}}, \quad \hat{T}^{(T)} = \hat{T}^{(N)}, \qquad (\hat{r} = \hat{R}), \tag{4.22}$$

$$\hat{u}^{(N)}\hat{T}^{(N)} - \frac{\hat{K}_t^{(N)}}{\hat{\rho}_t\hat{\gamma}_t}\frac{\partial\hat{T}^{(N)}}{\partial\hat{r}} = \frac{\hat{h}}{\hat{\rho}_t\hat{\gamma}_t}(\hat{T}^{(N)} - \hat{T}_b), \qquad (\hat{r} = \hat{R}_\infty), \tag{4.23}$$

where ($\hat{h}$, J s^{-1} m^{-2} K^{-1}) is an experimental heat transfer coefficient. In this study we use a large domain so that the value of $\hat{h}$ have a negligible influence on the results. The

Table of parameters				
parameter	value	units	description	Ref.
ΔT	20	s	temperature rise at the tumor center due to laser	[25]
T_b	310.15	K	blood temperature	[94]
ρ_t	$1109 \times 10^{(-3)}$	g cm^{-3}	the tissue density (skin)	Database (IT'IS)
γ_t	$3390 \times 10^{(-3)}$	J g^{-1} K^{-1}	the specific heat capacity of the tissue (skin)	Database (IT'IS)
$K_t^{(T)}$	0.0037	J s^{-1} cm^{-1} K^{-1}	the thermal conductivity	Database (IT'IS)
$K_t^{(N)}$	0.0037	J s^{-1} cm^{-1} K^{-1}	the thermal conductivity	Database (IT'IS)
$\rho_b \omega_b$	$3.328 \times 10^{(-3)}$	g cm^{-3}	the blood density times blood perfusion rate	[103]
γ_b	$3617 \times 10^{(-3)}$	J g^{-1} K^{-1}	is the specific heat capacity of the blood	
μ_{at}	0.2625	cm^{-1}	medium absorbance coefficient	
μ_{st}	14.74	cm^{-1}	medium scattering coefficient	[31]
h	$2 \times 10^{(-3)}$	J s^{-1} cm^{-2} K^{-1}	is the heat transfer coefficient	[78]
σ_{ext}	5.376×10^{-11}	cm^2	extinction cross-section	[50]
σ_a	5.084×10^{-11}	cm^2	absorption cross-section	[50]
σ_s	0.292×10^{-11}	cm^2	scattering cross-section	[50]
g	0.8	-	is the anisotropy factor (human skin)	[82]
r_0	0.1	cm	a constant	[118]
ρ_g	19.3	g/cm^3	gold density	[69]
n	4.13		GNR shape factor	[25]
N_A	$6.022140758 \times 10^{23}$	mol^{-1}	Avogadro constant	
K_s	3.1	W cm^{-1} K^{-1}	gold thermal conductivity	
γ_s	0.129	J/g.K	gold specific heat capacity	
P	1.7	W/cm^{-2}	laser density	[25]
d_p	0.6	cm	laser beam diameter	[25]
A	6×10^{29}	s^{-1}	a scaling factor	[44]
E_a	200×10^3	J mol^{-1}	the activation energy	[44]
$\breve{R}$	8.3144598	J mol^{-1}K^{-1}	Gas constant	

Table 4.1: Dimensional parameters in the thermal and cell injury models. IT'IS is an abbreviation for the Foundation for Research on Information Technologies in Society.

initial temperature is the normal body temperature ($\hat{T}_b$)

$$\hat{T}(\hat{r}, t) = \hat{T}_b, \qquad (0 \leq \hat{r} \leq \hat{R}_\infty). \tag{4.24}$$

4.2.4 Dimensionless transformations

We use the normal body temperature as a baseline temperature and scale the temperature difference to baseline by the expected temperature rise ($\Delta\hat{T}$) at the tumor center. The timescale of the thermal model is different to the GNR transport timescale, we scale time using a timescale based on the tissue thermal conductivity. Hence, we write the

dimensionless transformations in the form

$$\hat{T} = \hat{T}_b + \Delta\hat{T}T, \quad \hat{t} = \frac{\hat{\rho}_t\hat{\gamma}_t\hat{R}^2}{\hat{K}_t^{(T)}}t, \quad \hat{u}^{(j)} = \frac{\hat{K}_t^{(T)}}{\hat{\rho}_t\hat{\gamma}_t\hat{R}}u^{(j)}, \quad \hat{P}_i^{(N)} = \hat{P}_{ss}^{(N)} + \hat{P}_e^{(N)}P_i^{(N)},$$
$$\hat{K}_t^{(j)} = \hat{K}_t^{(T)}K_t^{(j)}, \quad \hat{P}_l^{(N)} = \hat{P}_{ss}^{(N)} + \hat{P}_e^{(N)}P_l^{(N)}, \quad \hat{S}_{laser} = \frac{\hat{K}_t^{(T)}\Delta\hat{T}}{\hat{R}^2}S_{laser}, \quad \hat{T}_b = \Delta\hat{T}T_b. \tag{4.25}$$

Applying the nondimensional transformations (4.25) to Eqns. (4.11) and (4.12), we obtain the following two dimensionless PDEs

$$\frac{\partial T^{(T)}}{\partial t} = -\frac{1}{r^2}\frac{\partial}{\partial r}(r^2u^{(T)}(T_b + T^{(T)})) + \frac{1}{r^2}\frac{\partial}{\partial r}\left(r^2K_t^{(T)}\frac{\partial T^{(T)}}{\partial r}\right)$$
$$- H(r - r_n)\beta_T T^{(T)} + S_{laser}(r), \qquad (0 \le r \le 1) \tag{4.26}$$

$$\frac{\partial T^{(N)}}{\partial t} = -\frac{1}{r^2}\frac{\partial}{\partial r}(r^2u^{(N)}(T_b + T^{(N)})) + \frac{1}{r^2}\frac{\partial}{\partial r}\left(r^2K_t^{(N)}\frac{\partial T^{(N)}}{\partial r}\right)$$
$$- \beta_T T^{(N)} - \beta_l(P_i^{(N)} - P_l^{(N)})T^{(N)} + S_{laser}(r), \qquad (1 \le r \le R_\infty) \tag{4.27}$$

where

$$K_t = \frac{\hat{K}_t^{(N)}}{\hat{K}_t^{(T)}}, \quad \beta_T = \frac{\hat{\rho}_b\hat{\gamma}_b\hat{\omega}_b\hat{R}^2}{\hat{K}_t^{(T)}}, \quad \beta_l = \frac{\hat{\rho}_t\hat{\gamma}_t\hat{L}_{pl}\hat{S}_l^{(N)}\hat{P}_e^{(N)}\hat{R}^2}{\hat{K}_t^{(T)}\hat{V}^{(N)}}. \tag{4.28}$$

Applying the nondimensional transformations (4.25) on the boundary conditions (4.21-4.23) we get the corresponding dimensionless boundary and initial conditions in the form

$$u^{(T)}(T_b + T^{(T)}) - K_t^{(T)}\frac{\partial T^{(T)}}{\partial r} = 0, \quad (r = 0), \tag{4.29}$$
$$u^{(T)}(T_b + T^{(T)}) - K_t^{(T)}\frac{\partial T^{(T)}}{\partial r} = u^{(N)}(T_b + T^{(N)}) - K_t^{(N)}\frac{\partial T^{(N)}}{\partial r}, \quad T^{(T)} = T^{(N)}, \quad (r = 1), \tag{4.30}$$
$$u^{(N)}(T_b + T^{(N)}) - K_t^{(N)}\frac{\partial T^{(N)}}{\partial r} = \beta_h T^{(N)}, \quad (r = R_\infty), \tag{4.31}$$
$$T(0, r) = 0, \quad (0 \le r \le R_\infty), \tag{4.32}$$

where $K_t^{(T)}$ is the dimensionless thermal conductivity of the tumor, $K_t^{(N)}$ the dimensionless thermal conductivity of the tissue, β_T the ratio of the blood perfusion rate and the tumor thermal conductivity, β_l the ratio of the lymphatic volumetric flow to the tumor thermal conductivity and β_h the dimensionless heat transfer coefficient at the tissue edge which is

defined in the form

$$\beta_h = \frac{\hat{h}\hat{R}}{\hat{K}_t^{(T)}}. \tag{4.33}$$

4.3 The Cell Injury Model

Experiments indicate that the induced thermal damage in tissue is (approximately) exponentially dependent on tissue temperature and linearly dependent on duration of tissue exposure to heat [88]. Henriques [1947] [41] proposed a damage prediction model based on the Arrhenius equation, where he studied thermal damage induced in pig skin. Henriques [1947] [41] assumed that cell death occurs as a result of protein denaturation which requires a minimum amount of energy $\hat{E}_a$ (known as the activation energy) to trigger the process of programmed cell death. Therefore, the rate of cell death equals the fraction of cells which acquire energy greater than or equal to the activation energy $\hat{E}_a$. In addition the cell death rate induced in tissue increases with heating which is essential to break the activation energy threshold. This cell fraction can be estimated by Maxwell-Boltzmann energy distribution law in the form [117].

$$\frac{d\Omega}{d\hat{t}}(\hat{r}) = \hat{A}e^{-\hat{E}_a/\breve{R}\hat{T}(\hat{r},\hat{t})}, \tag{4.34}$$

where Ω is the damage index, $\hat{T}$ is the tissue temperature (K), $\hat{\tau}_1$ is the time period of laser irradiation (s), $\breve{R}$ is the universal gas constant (J mol^{-1}K^{-1}) and $\hat{A}$ is an empirical parameter (s^{-1}). The parameters $\hat{A}$ and $\hat{E}$ depend on the type of tissue and can be estimated by fitting to experimental measurements. Hence, the induced cell death as a result of heating prolonged for $\hat{\tau}_1$ seconds is defined as

$$\Omega(\hat{r},\hat{\tau}_1) = \hat{A}\int_0^{\hat{\tau}_1} e^{-\hat{E}_a/\breve{R}\hat{T}(\hat{r},\hat{t})}d\hat{t}. \tag{4.35}$$

Weinberg et al. [1984] [116] provided a correlation function which relates the damage fraction F_D to the damage index Ω in the form

$$F_D(\hat{r},\hat{\tau}_1) = \frac{\hat{C}_d(\hat{t}=\hat{\tau}_1)}{\hat{C}_0(\hat{t}=0)} = 1 - e^{-\Omega}, \tag{4.36}$$

where $\hat{C}_d$ is the concentration of the damaged cells, $\hat{C}_0$ is the initial concentration of the living cells and $F_D = 0$ for undamaged tissue.

4.4 Model Validation Against Experiments

We perform model validation against two sets of experiments. The experiments of El-Sayed et al. [2013] [28] successfully inhibited the growth of tumors *in vivo* by a laser irradiation of GNRs administrated either intravenously or intratumorally into either mice or rats. The GNRs were administrated every three weeks; the laser irradiation was conducted at one week post GNR administration while tumor growth was monitored over seven weeks. At each irradiation they used a laser with power density 50 W/cm^2 for 2 minutes, which elevated the temperature up to approximately 352 K (79°C) at the tumor center. This high temperature at the tumor center decayed monotonically to approximately 314 K (41°C) at edge of the tumor. They demonstrated that both intravenous and intratumoral administrations result in a similar GNR distribution across the tumor and are equipotent for tumor ablation.

In a similar study Dickerson et al. [2008] [25] studied photothermal therapy *in vivo* through implanted human squamous carcinoma cells (a type of skin cancer) into female mice. They administrated GNRs either intravenously or intratumorally in one of two different dose concentrations. They found that the GNRs administrated intravenously needed approximately one day to accumulate across the tumor. Following this, they exposed the tumors to 10 minutes of laser irradiation (1.7-1.9 W/cm^2) 24 hours after GNR intravenous administration or 2 minutes after GNR intratumoral administration. Both administration methods significantly reduced the tumor growth. They found that the maximum temperature at the center of the tumor was within the first three minutes of the ten minute irradiation. However, between 10 to 15 minutes of laser irradiation is needed for optimal tumor damage and minimal surrounding healthy tissue damage.

4.5 Model Validation Using Dickerson et al. [2008] [25] Experiment

In order to validate our model, we simulate the *in vivo* study provided by Dickerson et al. [2008] [25] following the protocol used in this experiment. Therefore, in our model we prescribe the tumor radius recorded in the experiment before the GNR administration. Then, we calculate the initial GNR concentration according to the dose injected into the rodent. In addition, we use the same time interval between GNR delivery and laser irradiation. Finally, we use the same laser irradiation time chosen in the experiment. Hence, we compare the thermal model predictions against the temperature profile measured in this *in vivo* study as shown in Figs. 4.4(A). In this figure we plot the model predictions for the temperature elevation at the tumor center during the time of laser irradiation and the predictions for temperature relaxation during the 5 minutes after irradiation against the experimental

data published by Dickerson et al. [2008] [25]. In simulations we loosely fit the model results to the data by choosing a suitable tumor vasculature density ($\hat{S}^{(T)}/\hat{V}^{(T)} = 250$ cm^{-1}), blood perfusion rate ($\hat{\rho}_b\hat{\omega}_b = 3.328 \times 10^{-3}$ g/s.cm^3) and suitable tumor and healthy tissue absorption coefficients ($\hat{\mu}_{at}$=0.4875 cm^{-1}). These three parameter values lie in the range of parameter values measured in the literature [20, 31, 55, 58]. Note we fitted the data (temperature at the tumor center) manually by inspection, but we will make this much more rigorous in future. In particular, we tested different values for laser spot size and blood perfusion rates because we observed (by inspection) that the temperature profile across the tumor during irradiation is highly sensitive to the laser spot size, and the temperature decay in the absence of the laser is dominated by the blood perfusion rate. Both of these parameters (used in data fitting) were not measured in the corresponding experiments, so we estimated their values to be within the range reported in the literature. Following this loose fitting the model exhibits good agreement with the data during the laser irradiation and heat relaxation after the laser irradiation (see Fig. 4.4).

4.6 Model Validation Using El-Sayed et al. [2013] [28] Experiment

In Fig. 4.4(B) we plot the spatial temperature profile (across the tumor and the surrounding tissue) predicted by the model, and the data measured by El-Sayed et al. [2013] [28] immediately after switching off the laser. We fit the model predictions of the temperature at the tumor center to the experimental data through estimating an adequate GNR blood half life ($\hat{\tau} = 1$ week), tumor vasculature density ($\hat{S}^{(T)}/\hat{V}^{(T)} = 100$ cm^{-1}), blood perfusion rate ($\hat{\rho}_b\hat{\omega}_b = 3.328 \times 10^{-3}$ g/s.cm^3) and the laser spot size ($\hat{d}_b = 0.174$ cm). These three parameters were not measured in the experiment [28], so we choose their values from the literature to fit the temperature at the tumor center (one point fit at $r = 0$) and then the model predict the temperature across the rest of the tumor and the surrounding tissue. The fitted values for the tumor vasculature, GNR diffusion coefficient and the laser spot size are consistent with other experiments in the literature [20, 45, 55].

However, the blood half life needed to fit the data is very long compared to experiments, which is thought to be less than one day [46]. Although El-Sayed et al. [2013] [28] reported that the GNRs disappeared from the blood after less than 3 hours of injection, their data showed that the maximum GNR concentrations in the tumor, liver, spleen or kidney were achieved after 72 hours of injection. We could not find a proper explanation for the elevation of GNR concentrations in these organs (including the tumor) for 72 hours without available GNRs in the blood after 3 hours of injection. Therefore, in order to fit our model to this experiment we have to prolong the presence of GNRs in the blood ($\hat{\tau} = 1$ week) to achieve the maximum GNR concentration in the tumor after 72 hours of injection

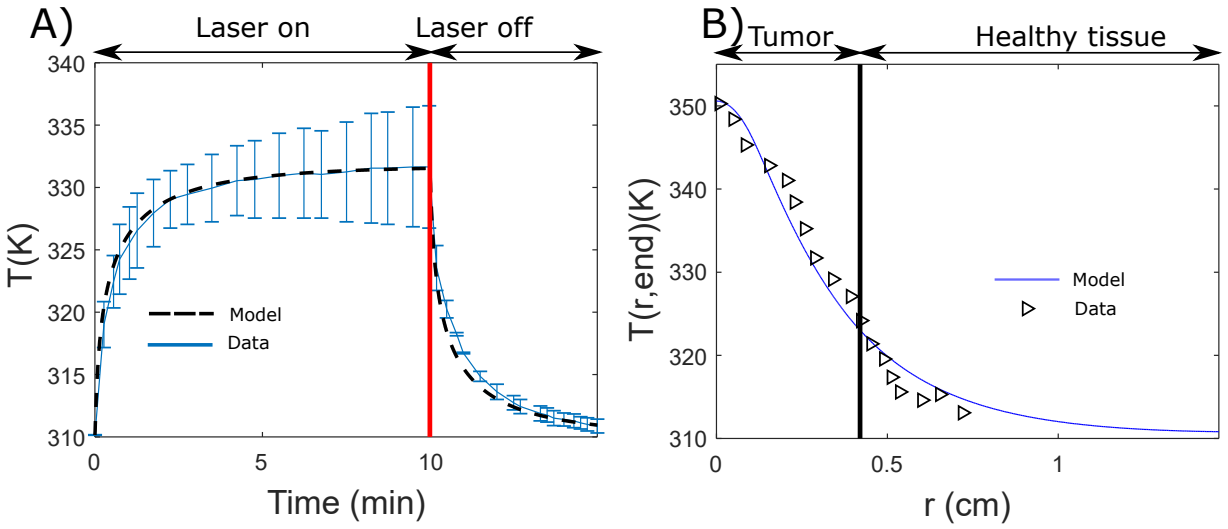

Figure 4.4: A) The model predictions for temperature ($\hat{S}^{(T)}/\hat{V}^{(T)} = 250$ cm^{-1}, $\hat{\rho}_b\hat{\omega}_b = 3.328 \times 10^{-3}$ g/s.cm^3 and $\hat{\mu}_{at}$=0.4875 cm^{-1}) against data published by Dickerson et al. [2008] [25], for the rest of model parameter values see Table 4.1. B)The model predictions for temperature ($\hat{\tau} = 1$ week, $\hat{S}^{(T)}/\hat{V}^{(T)} = 100$ cm^{-1}, $\hat{D}^{(T)} = 2.8 \times 10^{-7}$ cm^2/s and $\hat{d}_b = 0.16$ cm) against data published by El-Sayed et al. [2013] [28]

.

as observed in the experiment. In this simulation we chose the tumor and healthy tissue absorption coefficients as same as the value we fitted to the data from [25]. We estimated the laser spot size (by inspection) to fit the tumor temperature at the tumor center. It is clear from Fig. 4.4(B) that the model predictions for temperature across the tumor show good agreement with the data through one point fitting (at the tumor center).

4.7 Results in the Presence of Heating

We simulate the laser heating for a spherical tumor surrounded by healthy tissue (Fig. 3.1), using the mathematical model described in Sec. 4.2.4 coupled to GNR distribution obtained by solving the model in chapter 3. The laser power, the tissue-GNR thermal properties and the model parameters, listed in Table 4.1, are chosen to simulate the *in vivo* experiment conducted by Dickerson et al. [2008] [25]. The results of simulations of laser heating and tissue damage across the tumor and the surrounding tissue are presented in Fig. 4.5. The computational domain in this figure (tumor surrounded by a shell of tissue) is the same as the computational domain in Fig. 3.3 (which shows the GNR distribution) to easily relate the temperature profile to the GNR distribution.

The GNR distribution across the tumor and the surrounding tissue, which is calculated by the GNR transport model described in Sec. 3.2, is used as an input to the thermal model. Although the tumor tissue is loaded with GNRs, the GNR volume fraction (ϕ_n) is very small and has a negligible influence on the thermal properties of the tumor tissue

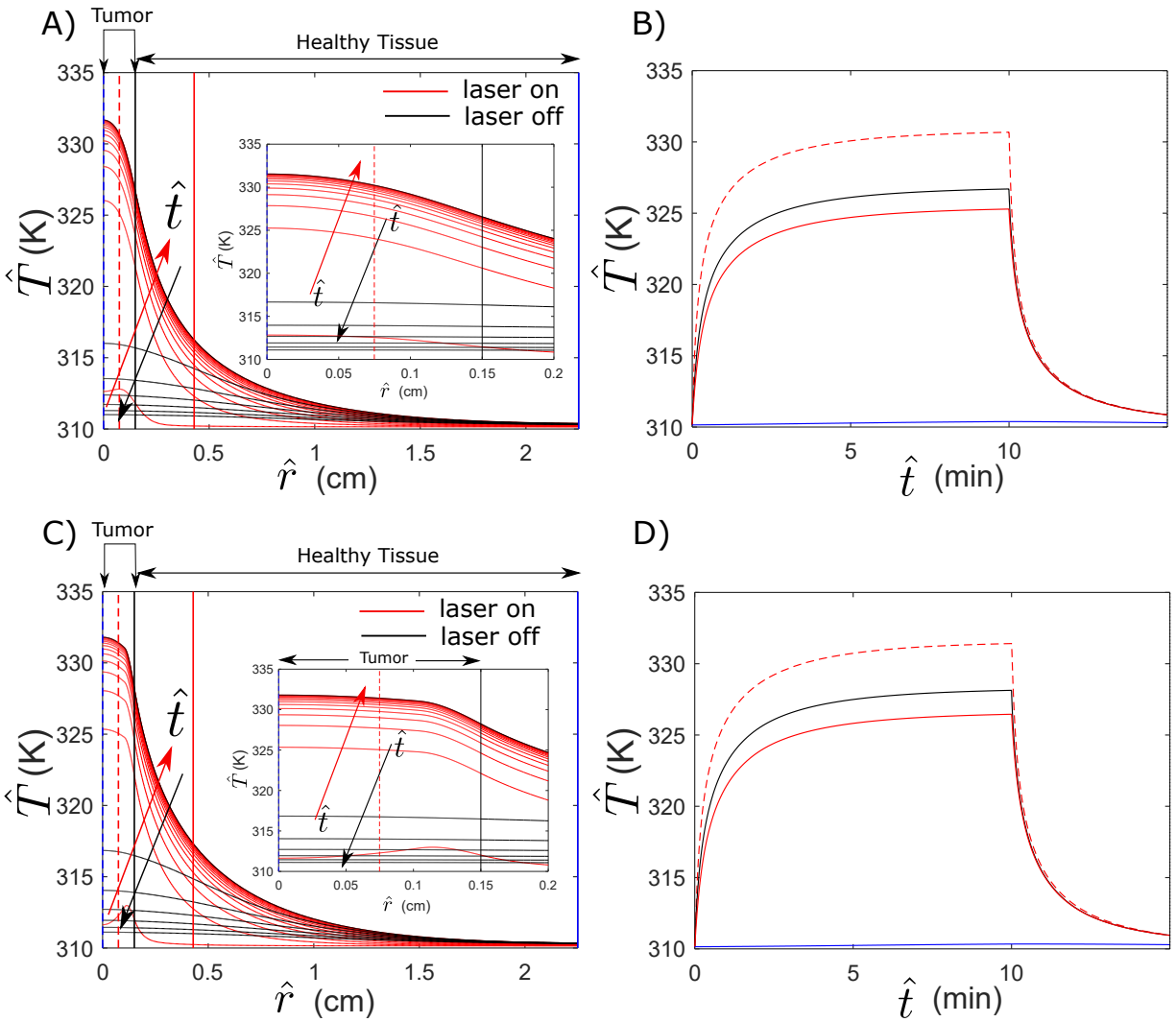

Figure 4.5: The temperature predictions across the tumor and the surrounding tissue during 10 minutes of laser irradiation and 5 minutes post laser irradiation (simulation of the *in vivo* experiment conducted by Dickerson et al. [2008] [25]), for the rest of model parameter values see Table 4.1. A) The spatial temperature distribution in the absence of binding ligands. B) The temporal temperature profile where the curve styles refer to the corresponding vertical lines with the same styles in (A). C) The spatial temperature distribution in the presence of binding ligands. D) The temporal temperature profile where the curve styles refer to the corresponding vertical lines with the same styles in (C).

such as tumor thermal conductivity and density. So, the GNRs have no contribution to heat transfer by conduction across tissue. In other words, the thermal properties of the tissue with embedded GNRs ($\hat{K}_t^{(j)},\ \hat{\rho}_t,\ \hat{\gamma}_t,\ j = N,\ T$) are constants and independent of the GNR distribution across the tumor.

On the other hand, the presence of the GNRs significantly increases the tissue absorption coefficient $\hat{\mu}_a$ which increases the amount of heat ($\hat{S}_{laser}$) generated across the tissue in the presence of GNRs, see Figs. 4.5(A)-(D). In these four figures we show the temperature elevation across the tumor and the surrounding tissue during laser irradiation (for 10

minutes, red colour curves) and after switching off the laser (for 5 minutes, black colour curves) in the absence of binding ligands (Figs. 4.5(A) and (B)) and in the presence of the binding ligands (Figs. 4.5(C) and (D)). These figures reveal that in both cases the laser irradiation induces a transient maximum in the temperature at the tumor center (where the laser spot is concentrated) and these maximal temperatures decrease across the tumor and the surrounding tissue (strongly heterogeneous temperature profile). The maximum temperature at the tumor center during the laser irradiation is a result of our assumption about the laser source term (Eq. (4.13)) which is maximal at the tumor center and decays exponentially away from the tumor center. This assumption is necessary to maintain the spherical symmetry of the model and it needs to be addressed in the future work because in practice laser irradiates the tumor starting from its surface towards its center which requires solving the Pennes' equation in 2D or 3D.

However, when the laser is switched off, the temperature profile across the whole tissue drops rapidly and quickly equilibrates to normal body temperature, which suggests that the heat transfer by conduction quickly spreads the heat to the surrounding tissue. This heat loss across the tumor is more clear in the temporal temperature profile (Fig. 4.5(B)). Though the laser irradiation lasts for 10 minutes, approximately 90% of the temperature elevation at the tumor center happens within the first three minutes, then the heat transfer by conduction dominates leaving a gradual temperature increase across the tumor until the laser is switched off. The temperature acquired at the tumor center beyond 10 minutes of laser irradiation reaches 330 K, but drops to 312 K within two minutes of switching off the laser.

Introducing binding ligands slightly enhances the temperature profile across the tumor periphery as revealed in the Figs. 4.5(C) and (D). Although there is no GNRs at the tumor center, the temperature increases at the tumor center due to the assumed mathematical definition of the laser source term (Eq. (4.13)) across the tumor. However, temperatures at the tumor periphery (Fig. 4.5(C)) are slightly larger than the corresponding temperatures in the absence of the binding ligands (Figs. 4.5(A)) due to the accumulation of the majority of the GNRs within the tumor rim in the presence of the binding ligands.

4.8 Results in the Absence of Binding Ligands

Exposure to heat induces the tissue damage due to protein denaturation [70], which can be estimated using the Arrhenius injury model described in Sec. 4.3 based on the temporal profile of the temperature at each spatial location. The results for the cell injury model are shown in Fig. 4.6. In Fig. 4.6(A) we plot the predicted spatial-temporal profile of damage across the tumor and the surrounding tissue. This profile depicts heterogeneous damage, where (as might be expected) the tumor core has more severe damage compared

to the tumor rim and the surrounding tissue.

In Fig. 4.6(B) we estimate the total induced damage across the tumor and the surrounding tissue during 10 minutes irradiation and 5 minutes post irradiation. This figure reveals that 99% of the tumor was damaged during the irradiation time, then no more damage is induced when the laser is switched off. Conversely, only 10% of the surrounding tissue is damaged during irradiation, but this damage has not saturated within the 5 minutes after irradiation.

In Fig. 4.6(C) we investigate how to maximize the tumor damage and minimize the healthy tissue damage by simulating the same experiment [25], but for different GNR delivery timescales (the period of time between the GNR injection and application of the laser) and fixing the other parameters in the model. So, we solve the GNR transport model described in chapter 3 over a period of $\hat{t}_{max}$ seconds, and then use the resulting GNR distribution across the tumor and tissue as an input to the thermal model to predict the temperature across the tumor and the surrounding tissue. Following this we then estimate the induced damage using the cell injury model [94]. We repeat this process ten times considering $\hat{t}_{max} = 0.5, \cdots, 3$ hours and show the tumor and tissue damage percentage in Fig. 4.6(C). This figure shows that the GNR delivery timescale has a significant influence on the tumor damage profile, but only a relatively minor influence on the surrounding tissue. This heterogeneous effect of the GNR delivery timescale can be attributed to the observation that the GNR concentration across the tumor is much larger than the GNR concentration in the surrounding tissue. In addition the laser irradiation is localized at the tumor center which makes the tumor damage much more sensitive to any change at the GNR distribution.

The damage induced in the tumor increases with the increase of the GNR delivery timescale, as shown at Fig. 4.6(D). However, when the GNR blood half life exceeds approximately 26 hours, the tumor damage fraction eventually decreases as we see at Fig. 4.6(D). That means prolonging the laser irradiation post GNR administration by (approximately) more than one day (twice the GNR blood half life used in this optimization) gives time for GNRs in the tumor to diffuse into the surrounding tissue lowering the GNR concentration across the tumor. In other words, the GNR diffusion towards the outside of the tumor dominates the GNR extravasation into the tumor and hence reduces the effectiveness of the therapy.

Furthermore, the tumor and healthy tissue damage can be optimized by controlling the GNR blood half life by adjusting the GNR physical dimensions. Therefore, we simulate this experiment again for different GNR blood half life values fixing the other parameters in the model, see damage profiles in Fig. 4.6(E). For every GNR blood half life in these simulations we postponed the laser irradiation for a period of time equals to the chosen GNR blood half life and illustrate the damage profile at the Figs. 4.6(E), (F). Fig. 4.6(E)

shows that the GNR blood half life has a significant influence on the tumor damage profile, but only a minor influence on the surrounding tissue, similar to Fig. 4.6(D).

The damage induced in the tumor generally increases with increases in the GNR blood half life value saturating as the GNR blood half life reaches approximately 17 hours (Fig. 4.6(F)). However, the damage induced across the surrounding tissue continues to increase with higher values of GNR blood half life. Therefore according to this measure, the optimal GNR blood half life is approximately 17 hours which is sufficient to ablate the whole tumor but with only minor damage to the surrounding tissue.

4.8.1 GNRs Conjugated with Binding Ligands

In this section we conduct simulations of photothermal therapy for a tumor bearing mouse *in vivo* using GNRs conjugated with binding ligands. In these simulations we use the experimental protocol described by Dickerson et al. [2008] [25]. We investigate the effect of introducing binding ligands to the GNRs on the tumor/tissue damage. We test the two cases, the first where the tumor cells have no maximal capacity for internalizing GNRs, as proposed by Dickerson et al. [2008] [25], and a second where the tumor cells have a maximal capacity for internalizing GNRs, as observed experimentally by [39, 40] and discussed in chapter 3.

As shown in chapter 3, introducing the binding ligands slows down the GNR diffusion towards the tumor center (due to binding and internalizing mechanisms), generating a strongly heterogenous GNR distribution across the tumor. Simulation results for tumor/tissue temperature and induced damage in the case of introducing the binding ligands are shown in Fig. 4.7. The temporal profile of temperature in the case of the tumor has a maximal capacity for internalizing GNRs, as shown in Fig. 4.7(A), is similar to the case of no binding ligands conjugated to the GNRs, see Fig. 4.5(B). GNRs manage to diffuse towards the tumor center within 24 hours due to the GNR saturation threshold (for internalized GNRs) and at the cell surface (for bound GNRs) as shown in Fig. 3.7(A). Furthermore, the heat transfer by conduction is large enough to conduct heat across the core to the tumor region which comprises accumulated GNRs (Fig. 4.7(A)). On the other hand, in the case of unlimited GNR internalization into the tumor cells, the tumor/tissue temperature increases are lower than the previous case (Fig. 4.7(B)). We hypothesise that this is because GNRs accumulate within a thin layer at the tumor rim which is relatively far from the tumor center where the laser heating is applied, see Fig 4.7(B).

The corresponding tumor/tissue damage caused by heat elevation in the presence of binding ligands is shown in the figures 4.7(C)-(F). In Figs. 4.7(C), (D) we plot the spatial profile of the cell injury fraction and the temporal profile of tumor/tissue damage, respectively, in the case of saturated GNR internalization by the tumor cells. These predictions are similar to the predictions in the case of no binding ligands conjugated to GNRs, see

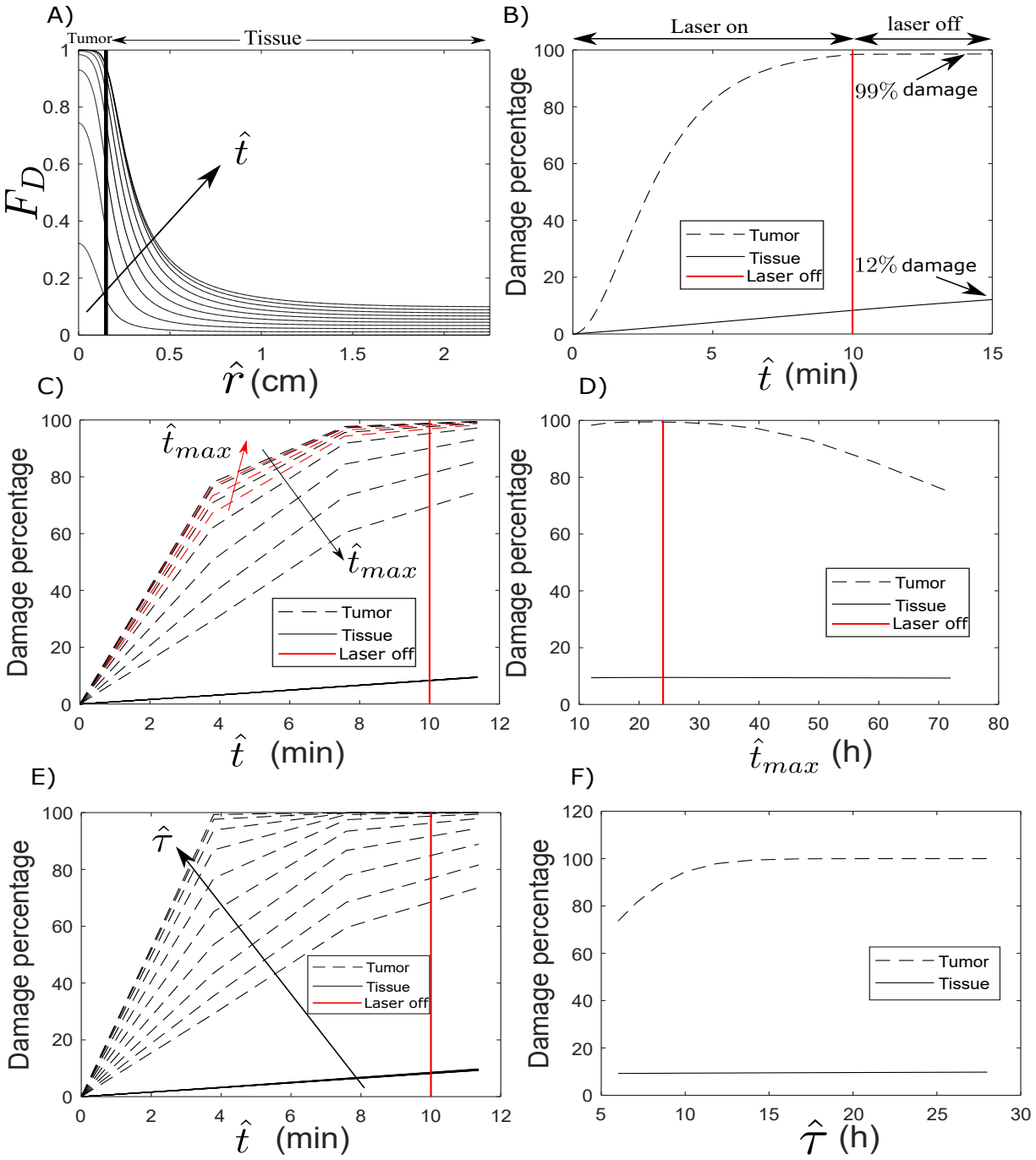

Figure 4.6: The cell death predictions across the tumor and the surrounding tissue during 10 minutes of laser irradiation and 5 minutes post laser irradiation (simulation of the *in vivo* experiment conducted by Dickerson et al. [2008] [25] where $\tau = 12.5$ h), for the rest of model parameter values see Table 4.1. A) The spatial profile of injury fraction distribution. B)The temporal damage percentage profile. C)The damage percentage in the case of different GNR delivery timescales (the period of time between GNR administration and conducting laser irradiation). D)The damage percentage against different GNR delivery timescales at 5 minutes post laser switch off time. E)The temporal damage percentage profile for different GNR blood half life values. F)The damage percentage against different GNR blood half life at 20 minutes post laser switch off time.

Sec. 4.8. This means that introducing binding ligands (at least with binding and internalization parameters used in this simulation) does not improve the efficiency of photothermal therapy. This observation is important since conjugating GNRs with binding ligands is expensive and requires special equipment and expertise [107], whereas GNRs themselves are very cheap (easy to synthesize and only a tiny mass of gold is needed for every patient).

On the other hand, in the case of tumor maximal capacity for GNR uptake by the tumor cells (Figs. 4.7(E), (F)) we found that the overall tumor damage profile after 10 minutes of laser irradiation is reduced by 6% in the tumor (reduced approximately from 99% to 93% of the overall tumor), but in the surrounding tissue the damage is almost identical to the case with no binding ligands conjugated to the GNRs. In this case GNRs can diffuse across the tumor surface towards the surrounding tissue, whereas in the tumor the GNRs distribution is limited within the tumor rim only which fails to elevate the tumor temperature to the same level as the case with no binding ligands, see Fig. 4.5(B).

4.9 Conclusion

We conclude from this chapter that the presence of GNRs within the tumor can magnify the thermal influence of laser irradiation across tissue comprising GNRs. So, the key step is to maximize GNR concentration within the tumor and minimize it in the surrounding tissue as we investigated in chapter 3. For the protocol of Dickerson et al. [2008] [25] and the parameter values used in this study, 99% of the tumor was damaged within 10 minutes of laser irradiation, whereas the corresponding damage in the surrounding tissue was only 12%.

We numerically investigated the optimal time for irradiating the tumor post injection and we found 24 hours gives the maximum damage in the tumor with a relatively minor damage in the surrounding tissue. However, this optimal time interval (24 hours) for GNR delivery is corresponding to the GNR-blood half life (which is 12.5 hours) used in this study, which means using GNRs with different blood half life will result in different optimal time interval for GNR delivery. We found the blood half life should be at least 17 hours to get the optimal tumor damage, so using GNRs with blood half life larger than 17 hours does not enhance the treatment efficacy, for the parameter value used in this study. Finally, conjugating GNRs with binding ligands decreases the effectiveness of the treatment where introducing binding ligands results in heterogeneous GNR distribution in the tumor which leads to heterogeneous tumor damage.

However, this model comprises some simplifying assumptions which need to be addressed in the future work. For instance, we assumed that blood perfusion is constant [19] which is typically a function of temperature. We need to study the heat exchange between the interstitial and the blood vessels at the microscale. So, in our model we approxi-

mated the thermal boundary layer at the vessel wall with the blood perfusion term $\hat{S}_{blood}$ (Eq. 4.9).

Another assumption was considering constant thermal and optical properties for the tumor tissue which are typically functions of temperature. Feng et al. [2009] [32] provided a model which addressed this assumption.

Finally, we assumed that the impact of the laser irradiation was at the tumor center to maintain the spherical symmetry of the problem. This is a significant simplifying assumption that should be addressed in future work, where laser irradiates tumors externally which requires a 2D or a 3D model.

To sum up, the thermal model introduced (in this chapter) coupled with the GNR transport model (in the preceding chapter) represent a step forward for establishing more sophisticated models to simulate the photothermal therapy to guide clinicians for the best treatment setup.

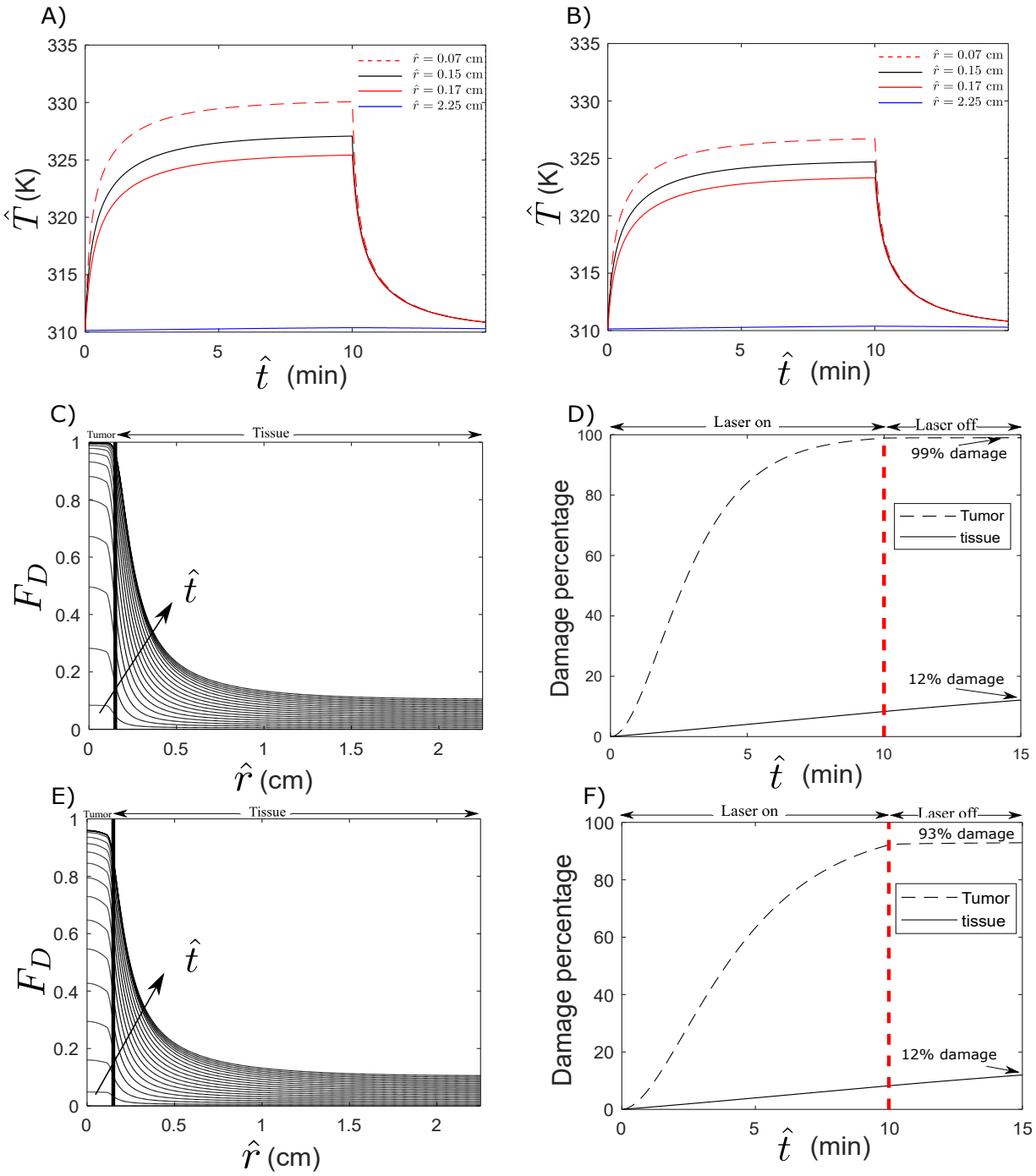

Figure 4.7: The temperature cell death predictions across the tumor and the surrounding tissue during 10 minutes of laser irradiation and 5 minutes post laser irradiation in the presence of binding ligands (where $\tau = 12.5$ h) using the parameter values in Table 4.1. A) The temporal temperature profile in the case of limited tumor cell capacity for internalizing GNRs. B) The temporal temperature profile in the case of unlimited tumor cell capacity for internalizing GNRs. C) The spatial profile of the injury fraction distribution in the case of limited tumor cell capacity for internalizing GNRs. D)The temporal damage percentage profile in the case of limited tumor cell capacity for internalizing GNRs. E)The spatial profile injury fraction distribution in the case of unlimited tumor cell capacity for internalizing GNRs. F)The temporal damage percentage profile in the case of unlimited tumor cell capacity for internalizing GNRs.

Chapter 5

Conclusion

5.1 Thesis Summary

In this thesis we modeled photothermal therapy of a spherical tumor surrounded by a shell of healthy tissue. The main object of this study was to investigate how to optimize this therapy, maximizing the tumor damage while minimizing side effects. In chapter 3 we studied the influence of tumor characteristics on the efficiency of the treatment and we found that tumor vasculature and porosity of tumor tissue play a vital role in delivering GNRs successfully (Fig. 3.11(B)). A large tumor vasculature density allows a large fraction of the GNR dose to access the tumor, while a large tumor tissue porosity allows GNRs to spread uniformly across the tumor. Hence, we can magnify photothermal therapy outputs by normalizing the tumor vasculature (eg. using bacterial collagenase enzymes [66]) or degrading the tumor interstitium (eg. using extracellular matrix degrading enzymes [34]).

We have compared the GNR distribution in the tumor in the presence or absence of binding ligands. In particular we found that introducing binding ligands results in an accumulation close to the vascularized region and so is more suitable for treating the tumor rim. We showed that the width of the tumor rim which is accessible for GNRs conjugated with binding ligands depends on the maximal tumor capacity for internalizing GNRs (where large maximal tumor capacity inhibit GNR penetration into deep tumor tissue). In the absence of binding ligands, the GNR distribution is more uniform across the tumor (but in smaller concentration values than in the case of using binding ligands). We also found that the GNR concentration across the tumor (in the presence or absence of binding ligands) can be increased by prolonging the GNR blood half life which prolongs GNR delivery time to the tumor.

When also including thermal effects in our model we found that heat generated in the tumor depends on laser power, laser spot size, blood perfusion rate and GNR distribution across the tumor. For example, our model predicted heterogeneous tissue damage between the tumor and the surrounding tissue, where 99% of the tumor was damaged while only

12% of the surrounding tissue was damaged (for the chosen parameter value in this study). We also investigated the influence of GNR delivery timescale (the time between GNR administration and laser irradiation) on the tumor damage percentage, finding that the most effective ablation occur when the GNR distribution (in the tumor) is approximately uniform and in a relatively large concentration value. We also compared ablation in the presence or absence of binding ligands and found that introducing binding ligands reduces the efficacy of the treatment by 6% and induce damage only at the tumor rim (for the parameter values considered). Overall, we concluded that using binding ligands reduces the treatment efficacy. Although using GNRs without binding ligands typically reduces the overall GNR concentration value, the GNR concentration in the tumor was still large enough to ablate 99% of the tumor efficiently (according to our damage model).

5.2 Model Limitations

Our model comprises various assumptions (in order to simplify the model and make it easier to analyze and explain the model outputs) which need to be addressed in the future work. For example, we assumed that the tumor is spherical and has uniform material properties. In practice, tumor tissue is strongly heterogeneous and has an irregular shape. Furthermore, we assumed that the tumor vasculature is homogeneous and continuously distributed over the vascularized region.

The model predictions depend strongly on the GNR extravasation flux which we compute in chapter 2, but we still need to validate the estimated value of blood perfusion rate ω_b (which is a key parameter in the bioheat equation) using similar asymptotic analysis through solving the heat transport equation in the thermal boundary layer across the vessel wall. We also need to incorporate the effects of metabolism which influences the temperature map across the tissue.

Furthermore, we still need to investigate the blood flow explicitly (blood flow in a realistic vasculature) and the variations of blood temperature. Finally, we need to study the direct influence of the laser beam on the tissue (not just the light scattering).

5.3 Model Contribution and Future Work

A commercial software package (NanoPlan) is available which simulates the hyperthermia using magnetic NPs [60]. Our model provides a preliminary platform for predicting the outputs of the photothermal therapy technique. The inputs of this model are the GNR physical and optical properties, the binding ligand association and dissociation rates, the tumor radius, the laser power, and the laser spot size. So, our model is the first model which simulates the whole process of the photothermal therapy including the GNR tumor

cell interaction, for the best of our knowledge.

However, our model comprises some simplifying assumptions which need to be addressed. For instance, we need to extend our model to 3D and estimate the blood perfusion rate as a function of temperature [112]. We also need to incorporate the changes of the optical and thermal properties of the tumor during laser irradiation [32]. Furthermore, we need to extend our GNR transport model to the case of heterogeneous GNR binding rate [63]. In addition, we can include the influence of GNR electric charge [63] and multivalent binding ligands [93] on the GNR delivery to the tumor.

Hence, by addressing these simplifying limitations we could provide a realistic software package to guide clinicians and predict the output of the photothermal therapy.

Appendix A

Properties of GNRs

Summary of properties of GNRs and experimentally fitted correlations

The mathematical correlation for the vessel wall permeability for spherical nanoparticles ($\breve{P}$), the vessel wall hydraulic conductivity ($L_{pv}^{(T)}$) and the osmotic reflection coefficient of spherical nanoparticles ($\breve{\sigma}$) are given by [20]

$$L_{pv}^{(T)} = \frac{\gamma_p r_0^2}{8\mu_b L},\ \breve{P} = \frac{\gamma_p H D_0^{(j)}}{L},\ \breve{\sigma}^{(j)} = 1 - W,\ (j = N, T), \tag{A.1}$$

where μ_b is the blood viscosity, L is the vessel wall thickness, r_0 is the vessel wall pore radius and γ_p is the fraction of the vessel wall surface area contains pores. The diffusive (H) and convective (W) hindrance factors are prescribed functions of (λ) the ratio of the GNR size to the vascular wall pore size in the form [24]

$$\begin{aligned} H(\lambda) = 1 + \frac{9}{8}\lambda \log \lambda - 1.56034\lambda + 0.528155\lambda^2 + 1.91521\lambda^3 - 2.81903\lambda^4 + 0.270788\lambda^5 \\ + 1.10115\lambda^6 - 0.435933\lambda^7, \end{aligned} \tag{A.2}$$

$$W(\lambda) = (1-\lambda)^2 \left(\frac{1 + 3.867\lambda - 1.907\lambda^2 - 0.834\lambda^3}{1 + 1.867\lambda - 0.741\lambda^2} \right), \tag{A.3}$$

The mathematical correlations for W and H are derived using Cross-Sectional Averaging for different values of λ, for more details see [24]. We used these correlations in our model as approximation for GNRs since there is no closed form mathematical expressions for W and H in the case of nonspherical particles in literature [4].

GNR Diffusion Coefficient

The macroscopic diffusion coefficient D for a GNR of length L and diameter d moving in a random direction is calculated in this study according to the following equation

$$D = \frac{K_B T}{3\pi\mu_t L}\left(\log\frac{L}{d} + 0.312 + 0.565\frac{d}{L} - 0.1\left(\frac{d}{L}\right)^2\right), \tag{A.4}$$

where K_B is Boltzmann constant (cm^2 g s^{-2} K^{-1}), T (K) is temperature and μ_t (g cm^{-1} s) is the interstitium viscosity. Tirado et al. [1984] [111] tested this correlation of diffusion coefficient for DNA fragments against experimental data and they found a good agreement.

Calculating the Optical Density for GNRs

The optical density (OD) of a sample of GNRs is calculated as [65]

$$OD = \varepsilon C^* l, \tag{A.5}$$

where ε ($M^{-1}cm^{-1}$) is the molar extinction coefficient, C^* (M) is the GNR molar concentration and l (cm) is the light path length (1 cm in a standard cuvette). The GNR molar concentration C^* is different from the gold molar concentration C_g^*, since one mole of gold has a mass of 196.9665 g mol^{-1} (gold molar mass) whereas one mole of GNRs has mass of the sum of 6.0221409×10^{23} (Avogadro's constant) GNRs mass (g mol^{-1}). So, we have to distinguish between the gold mass concentration (C_g, g/cm^3) and the GNR mass concentration (C, g/cm^3) which can be calculated using the molar concentration in the form

$$C_g^* = \frac{C_g \times 10^3}{196.9665}, \quad C^* = \frac{C \times 10^3}{N_A \rho_g V_{GNR}}. \tag{A.6}$$

where N_A (mol^{-1}) is the Avogadro constant (here it is the number of GNRs in one mole), ρ_g (g/cm^3) is the gold density and V_{GNR} (cm^3) is the volume of a single GNR (the factor 10^3 is to convert volume dimension from liter into cm^3).

The molar extinction coefficient ε ($M^{-1}cm^{-1}$) can be calculated from the following formula

$$\sigma_{ext} = 2.303\frac{\varepsilon \times 10^3}{N_A} = 3.82 \times 10^{-21}\varepsilon. \tag{A.7}$$

where σ_{ext} (cm^2) is the GNR extinction cross-section [50, 65, 86] (the factor 10^3 is to convert volume dimension from liter into cm^3). We can calculate the optical density using the number of GNRs presence in a cylinder (the dose container) of radius r_D (the same as the laser beam radius $d_n/2$) and length l_D (a part of the laser beam path) and volume V_D

using equation (A.5). The molar concentration of GNRs C^* in this cylinder is calculated as

$$C^* = \frac{n^* \times 10^3}{\pi r_D^2 l_D}, \quad n^* = \frac{n}{N_A} \tag{A.8}$$

$$\tag{A.9}$$

where n^* is the number of GNR moles in the cylinder and n is the number of GNRs (the factor 10^3 is to convert volume dimension from liter into cm^3). Thus, using Eqns. (A.5) and (A.8) we can write OD in the form

$$OD = \varepsilon \frac{n/N_A}{\pi r_D^2} \times 10^3, \tag{A.10}$$

$$OD = \frac{n\varepsilon \times 10^3}{\pi r_D^2 N_A}. \tag{A.11}$$

For a given dose volume V_D, optical density OD, GNR width d_n, GNR length L_n and laser beam radius r_D one can find the total mass of GNRs (M, g) in the dose using the following equation

$$M = \frac{\pi}{4} n \rho_g L_n d_n^2, \quad n = \frac{\pi r_D^2 N_A OD \times 10^{-3}}{\varepsilon}, \tag{A.12}$$

where d_n is the GNR diameter and L_n is the GNR length. There is another way of doing that using equations (A.5) and (A.6) as follows:

$$C = \frac{N_A \rho_g V_{GNR} \times 10^{-3}}{\varepsilon l_D} OD, \quad l_D = \frac{V_D}{\pi r_D^2} \tag{A.13}$$

$$M = CV_D = \frac{\pi r_D^2 N_A \rho_g V_{GNR} \times 10^{-3}}{\varepsilon} OD. \tag{A.14}$$

Appendix B

Deduction of Darcy's Model by Volume Averaging

In Fig. B.1, we have a homogenous porous medium of two phases, which are the fluid phase (f) and solid phase (s). The volume of the porous medium (V) is the sum of the volume of the fluid phase (V_f) and the solid phase (V_s), so we write:

$$V = V_f + V_s \tag{B.1}$$

The porosity (ε) of the porous medium is defined as the ratio of the fluid phase volume to the total volume of the porous medium, see Whitaker [2013] [119].

$$\varepsilon = \frac{V_f}{V_f + V_s} \tag{B.2}$$

The average velocity of the fluid in porous medium can be defined in terms of the fluid intrinsic average velocity $\langle \mathbf{v} \rangle^f$ which are defined as

$$\langle \mathbf{v} \rangle^f = \frac{1}{V_f} \int_{V_f} \mathbf{v} dV, \tag{B.3}$$

$$\langle \mathbf{v} \rangle = \frac{1}{V_f + V_s} \int_{V_f} \mathbf{v} dV. \tag{B.4}$$

From the definition of the porosity of the porous medium in Eq. B.2 we can write

$$\langle \mathbf{v} \rangle = \varepsilon \langle \mathbf{v} \rangle^f. \tag{B.5}$$

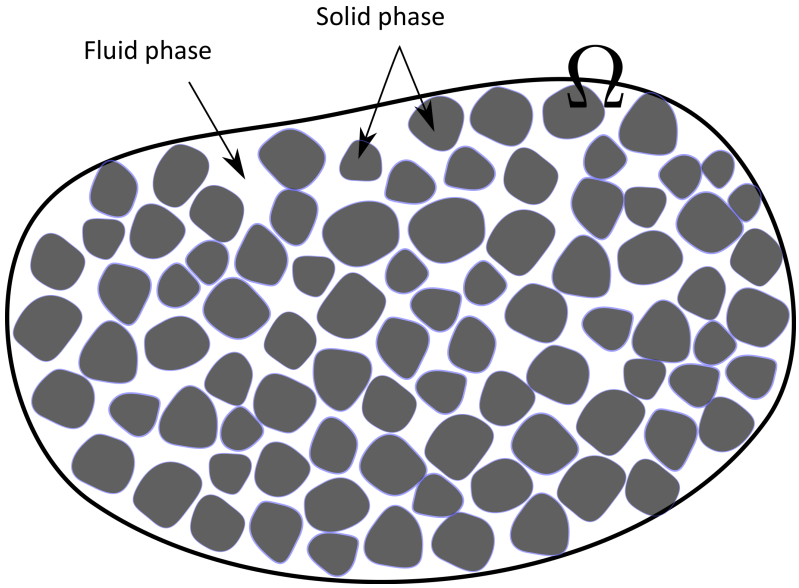

Figure B.1: Porous medium domain.

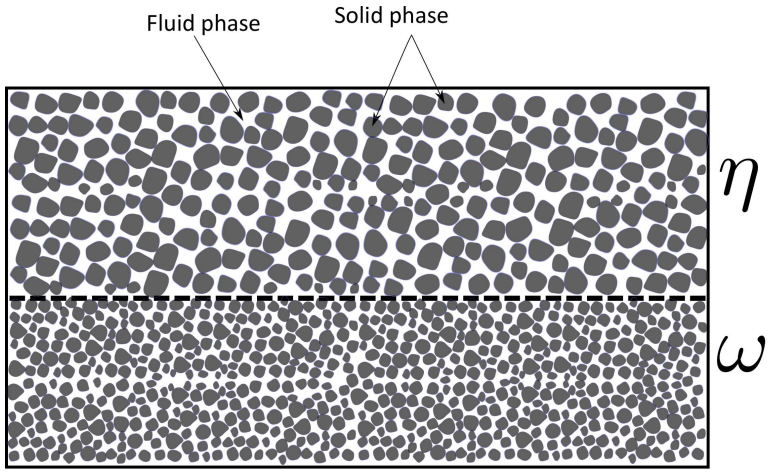

Figure B.2: Two adjacent porous medium domains.

So, we can write the fluid flow governing equations in a porous medium using Darcy's model in the form

$$\nabla \cdot \langle \mathbf{v} \rangle^f = 0, \tag{B.6}$$

$$\varepsilon \langle \mathbf{v} \rangle^f = -\frac{K}{\mu_f} \nabla \langle p \rangle^f. \tag{B.7}$$

The fluid flow in the two homogeneous porous mediums Ω_η and Ω_ω which are sketched

in Fig. B.2, can be modeled using the following system of equations

$$\nabla \cdot \langle \mathbf{v} \rangle_{\eta}^{f} = 0, \tag{B.8}$$

$$\varepsilon_{\eta} \langle \mathbf{v} \rangle_{\eta}^{f} = -\frac{K_{\eta}}{\mu_f} \nabla \langle p \rangle_{\eta}^{f}, \tag{B.9}$$

$$\nabla \cdot \langle \mathbf{v} \rangle_{\omega}^{f} = 0, \tag{B.10}$$

$$\varepsilon_{\omega} \langle \mathbf{v} \rangle_{\omega}^{f} = -\frac{K_{\omega}}{\mu_f} \nabla \langle p \rangle_{\omega}^{f}, \tag{B.11}$$

where the subscript η refers to variables in Ω_{η}; and ω refers to variables in Ω_{ω}. In order to solve the flow problem in Ω_{η} and Ω_{ω} we apply continuous pressure and continuous velocity at the interface between the two region as follows

$$\nabla \langle p \rangle_{\eta}^{f} = \nabla \langle p \rangle_{\omega}^{f}, \tag{B.12}$$

$$\varepsilon_{\eta} \langle \mathbf{v} \rangle_{\eta}^{f} = \varepsilon_{\omega} \langle \mathbf{v} \rangle_{\omega}^{f}. \tag{B.13}$$

Appendix C

Mesh Size Test

We solved the systems of PDEs in chapters (2)-(4) numerically using the method of lines using a built-in MATLAB solver. In particular, in chapter (2) we used 90 mesh points in each spatial direction, z and ξ. We tested different number of mesh points (70, 80, 90, 100, 110, 120) and calculated the corresponding relative error (RE) as shown in Fig. C.1(A). The relative error for an arbitrary objective function F is defined as:

$$RE = \frac{F_{N+1} - F_N}{F_{N+1}}, \tag{C.1}$$

where F_N is the value of the objective function F calculated using N mesh points and F_{N+1} is the value of the F for the case of using $N+1$ mesh points. The objective function here is the solute concentration at $\xi = 5.8 \times 10^{-4}$ cm, $z = 0$ and $t = 15.62$ hr. The relative error was of $O(10^{-4})$ (Fig. C.1(A)) which means that the results were independent of the mesh size.

Similarly, in the both chapters (3) and (4) we solved two systems of PDEs in 1D using 400 mesh points. We tested different mesh points sizes: 250, 300, 350, and 400. We used the concentration of the GNRs (Fig. C.1(B)) and the tissue temperature (Fig. C.1(C)) at the tumor/tissue surface interface as objective functions. The both relative errors were of $O(10^{-3})$ (Figs. C.1(B) and (C)) which means the results are independent of the mesh sizes.

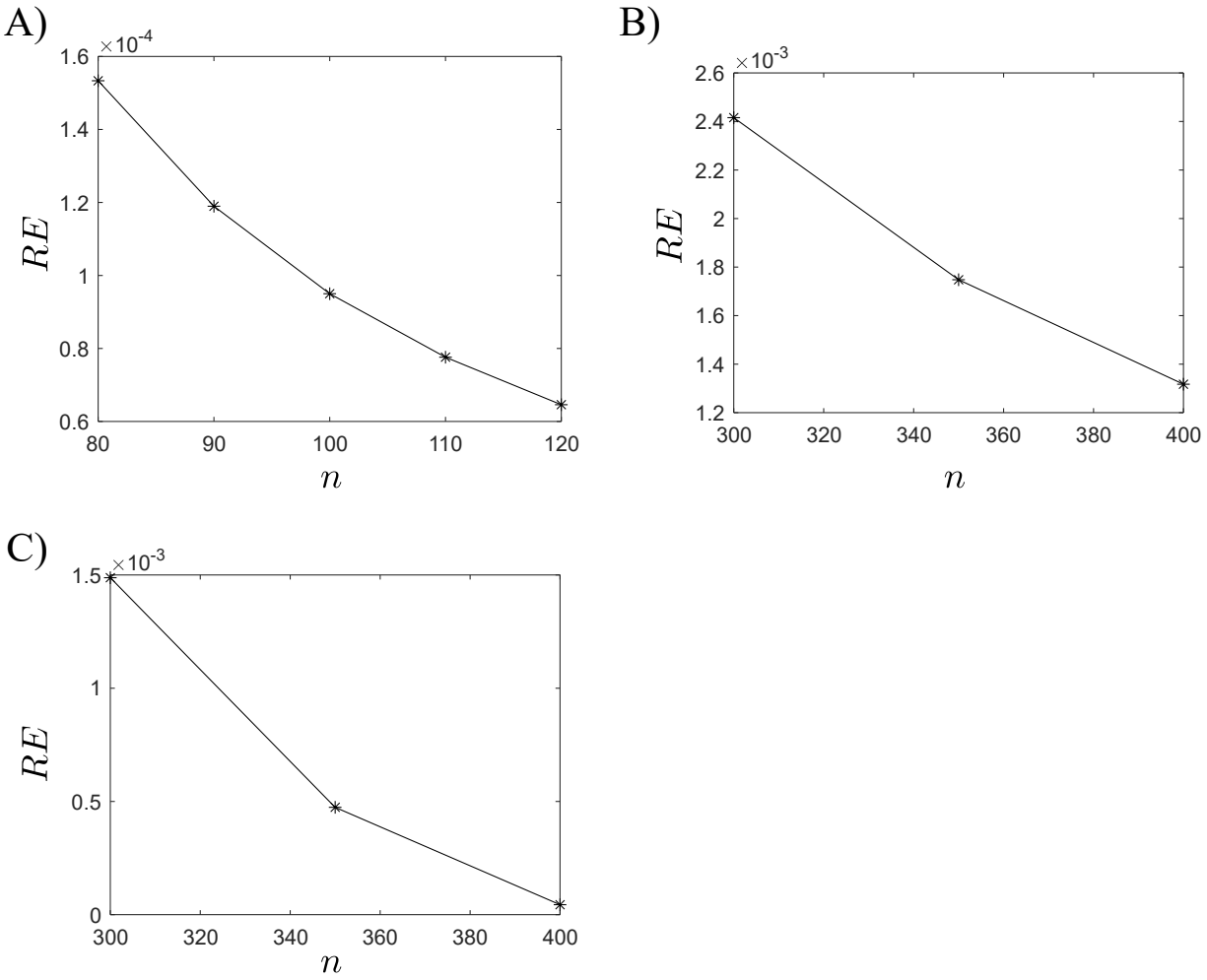

Figure C.1: The relative error for different mesh sizes. A) The relative error of solute concentration at $\xi = 5.8 \times 10^{-4}$ cm, $z = 0$ and $t = 15.62$ hr. B) The relative error of GNR concentration at the tumor/tissue surface interface. C) The relative error of tissue temperature at the tumor/tissue surface interface.

Bibliography

[1] David J Acheson. Elementary fluid dynamics, 1991.

[2] Yasuyuki Akiyama, Takeshi Mori, Yoshiki Katayama, and Takuro Niidome. The effects of PEG grafting level and injection dose on gold nanorod biodistribution in the tumor-bearing mice. *Journal of Controlled Release*, 139(1):81–84, 2009.

[3] Alexander R A Anderson, Mark A J Chaplain, and Stephen McDougall. A hybrid discrete-continuum model of tumour induced angiogenesis. In *Modeling Tumor Vasculature*, pages 105–133. Springer, 2012.

[4] John L Anderson. Configurational effect on the reflection coefficient for rigid solutes in capillary pores. *Journal of Theoretical Biology*, 90(3):405–426, 1981.

[5] Hamed Arami, Amit Khandhar, Denny Liggitt, and Kannan M Krishnan. In vivo delivery, pharmacokinetics, biodistribution and toxicity of iron oxide nanoparticles. *Chemical Society Reviews*, 44(23):8576–8607, 2015.

[6] Robyn P Araujo and Donald Leon Sean McElwain. A history of the study of solid tumour growth: the contribution of mathematical modelling. *Bulletin of Mathematical Biology*, 66(5):1039–1091, 2004.

[7] P Barvinschi and O M Bunoiu. A finite element method model to simulate the thermal response of vascularized tissue to laser irradiation. *Romanian Reports in Physics*, 69:610, 2017.

[8] Laurence T Baxter and Rakesh K Jain. Transport of fluid and macromolecules in tumors. I. Role of interstitial pressure and convection. *Microvascular Research*, 37(1):77–104, 1989.

[9] Laurence T Baxter and Rakesh K Jain. Transport of fluid and macromolecules in tumors. II. Role of heterogeneous perfusion and lymphatics. *Microvascular Research*, 40(2):246–263, 1990.

[10] Laurence T Baxter and Rakesh K Jain. Transport of fluid and macromolecules in tumors: III. Role of binding and metabolism. *Microvascular Research*, 41(1):5–23, 1991.

[11] Gordon S Beavers and Daniel D Joseph. Boundary conditions at a naturally permeable wall. *Journal of Fuid Mechanics*, 30(1):197–207, 1967.

[12] Carl M Bender and Steven A Orszag. *Advanced mathematical methods for scientists and engineers I: Asymptotic methods and perturbation theory*. Springer Science & Business Media, 2013.

[13] Lisa Brannon-Peppas and James O Blanchette. Nanoparticle and targeted systems for cancer therapy. *Advanced Drug Delivery Reviews*, 56(11):1649–1659, 2004.

[14] Irène Brigger, Catherine Dubernet, and Patrick Couvreur. Nanoparticles in cancer therapy and diagnosis. *Advanced Drug Delivery Reviews*, 64:24–36, 2012.

[15] Rita M Cabral and Pedro V Baptista. Anti-cancer precision theranostics: a focus on multifunctional gold nanoparticles. *Expert Review of Molecular Diagnostics*, 14(8):1041–1052, 2014.

[16] Colin Gerald Caro, T J Pedley, R C Schroter, and W A Seed. *The mechanics of the circulation*. Cambridge University Press, 2012.

[17] Antonio Cervadoro, Chiara Giverso, Rohit Pande, Subhasis Sarangi, Luigi Preziosi, Jarek Wosik, Audrius Brazdeikis, and Paolo Decuzzi. Design maps for the hyperthermic treatment of tumors with superparamagnetic nanoparticles. *PLoS One*, 8(2):e57332, 2013.

[18] M A J Chaplain. Avascular growth, angiogenesis and vascular growth in solid tumours: The mathematical modelling of the stages of tumour development. *Mathematical and Computer Modelling*, 23(6):47–87, 1996.

[19] Caleb K Charny. Mathematical models of bioheat transfer. In *Advances in Heat Transfer*, volume 22, pages 19–155. Elsevier, 1992.

[20] Vikash P Chauhan, Triantafyllos Stylianopoulos, John D Martin, Zoran Popović, Ou Chen, Walid S Kamoun, Moungi G Bawendi, Dai Fukumura, and Rakesh K Jain. Normalization of tumour blood vessels improves the delivery of nanomedicines in a size-dependent manner. *Nature Nanotechnology*, 7(6):383–388, 2012.

[21] Chenghan Chen and Han Qin. A Mathematical Modeling of the Reverse Osmosis Concentration Process of a Glucose Solution. *Processes*, 7(5):271, 2019.

[22] Paul Cherukuri, Evan S Glazer, and Steven A Curley. Targeted hyperthermia using metal nanoparticles. *Advanced Drug Delivery Reviews*, 62(3):339–345, 2010.

[23] Cheng-Ying Chou, Chih-Kang Huang, Kuo-Wei Lu, Tzyy-Leng Horng, and Win-Li Lin. Investigation of the spatiotemporal responses of nanoparticles in tumor tissues with a small-scale mathematical model. *PloS One*, 8(4):e59135, 2013.

[24] Panadda Dechadilok and William M Deen. Hindrance factors for diffusion and convection in pores. *Industrial & Engineering Chemistry Research*, 45(21):6953–6959, 2006.

[25] Erin B Dickerson, Erik C Dreaden, Xiaohua Huang, Ivan H El-Sayed, Hunghao Chu, Sujatha Pushpanketh, John F McDonald, and Mostafa A El-Sayed. Gold nanorod assisted near-infrared plasmonic photothermal therapy (PPTT) of squamous cell carcinoma in mice. *Cancer Letters*, 269(1):57–66, 2008.

[26] Amber L Doiron, Brendan Clark, and Kristina D Rinker. Endothelial nanoparticle binding kinetics are matrix and size dependent. *Biotechnology and Bioengineering*, 108(12):2988–2998, 2011.

[27] Erik C Dreaden, Lauren A Austin, Megan A Mackey, and Mostafa A El-Sayed. Size matters: gold nanoparticles in targeted cancer drug delivery. 2012.

[28] Mostafa A El-Sayed, Ali A Shabaka, Osama A El-Shabrawy, Nemat A Yassin, Sawsan S Mahmoud, Siham M El-Shenawy, Emad Al-Ashqar, Wael H Eisa, Niveen M Farag, and Marwa A El-Shaer. Tissue distribution and efficacy of gold nanorods coupled with laser induced photoplasmonic therapy in ehrlich carcinoma solid tumor model. *PloS One*, 8(10):e76207, 2013.

[29] Heiko Enderling, Mark A J Chaplain, Alexander R A Anderson, and Jayant S Vaidya. A mathematical model of breast cancer development, local treatment and recurrence. *Journal of Theoretical Biology*, 246(2):245–259, 2007.

[30] B.S. Everitt and A. Skrondal. *The cambridge dictionary of statistics*, volume 53. 2010.

[31] Y Feng, M N Rylander, J Bass, J T Oden, and K Diller. Optimal design of laser surgery for cancer treatment through nanoparticle-mediated hyperthermia therapy. In *NSTI-Nanotech*, volume 1, pages 39–42, 2005.

[32] Yusheng Feng, David Fuentes, Andrea Hawkins, Jon Bass, Marissa Nichole Rylander, Andrew Elliott, Anil Shetty, R Jason Stafford, and J Tinsley Oden. Nanoshell-mediated laser surgery simulation for prostate cancer treatment. *Engineering with Computers*, 25(1):3–13, 2009.

[33] Ronald L Fournier. *Basic transport phenomena in biomedical engineering*. CRC press, 2017.

[34] Thomas Goodman, Jingyang Chen, Konstantin Matveev, and Suzie Pun. Spatio-temporal modeling of nanoparticle delivery to multicellular tumor spheroids. *Biotechnology and Bioengineering*, 101(2):388–399, 2008.

[35] Christilyn P Graff and K Dane Wittrup. Theoretical analysis of antibody targeting of tumor spheroids importance of dosage for penetration, and affinity for retention. *Cancer Research*, 63(6):1288–1296, 2003.

[36] H P Greenspan. On the growth and stability of cell cultures and solid tumors. *Journal of Theoretical Biology*, 56(1):229–242, 1976.

[37] I M Griffiths, P D Howell, and R J Shipley. Control and optimization of solute transport in a thin porous tube. *Physics of Fluids*, 25(3):33101, 2013.

[38] Christian M Groh, Matthew E Hubbard, Pamela F Jones, Paul M Loadman, N Periasamy, Brain D Sleeman, Steven W Smye, Chris J Twelves, and Roger M Phillips. Mathematical and computational models of drug transport in tumours. *Journal of The Royal Society Interface*, 11(94):20131173, 2014.

[39] Daniela Guarnieri, Annarita Falanga, Ornella Muscetti, Rossella Tarallo, Sabato Fusco, Massimiliano Galdiero, Stefania Galdiero, and Paolo A Netti. Shuttle-mediated nanoparticle delivery to the blood–brain barrier. *Small*, 9(6):853–862, 2013.

[40] Daniela Guarnieri, Angela Guaccio, Sabato Fusco, and Paolo A Netti. Effect of serum proteins on polystyrene nanoparticle uptake and intracellular trafficking in endothelial cells. *Journal of Nanoparticle Research*, 13(9):4295, 2011.

[41] F C Henriques. Studies in Thermal Injuries V. The Predictability and the Significance of Thermally Induced Rate Processes Leading to Irreversible Epidermal Injury. *Archives of Pathology*, 43:489–502, 1947.

[42] Archibald Vivian Hill. The diffusion of oxygen and lactic acid through tissues. *Proceedings of the Royal Society of London. Series B, Containing Papers of a Biological Character*, 104(728):39–96, 1928.

[43] L R Hirsch, R J Stafford, J A Bankson, S R Sershen, B Rivera, R E Price, J D Hazle, Naomi J Halas, and J L West. Nanoshell-mediated near-infrared thermal therapy of tumors under magnetic resonance guidance. *Proceedings of the National Academy of Sciences*, 100(23):13549–13554, 2003.

[44] Huang-Chiao Huang, Kaushal Rege, and Jeffrey J Heys. Spatiotemporal temperature distribution and cancer cell death in response to extracellular hyperthermia induced by gold nanorods. *ACS Nano*, 4(5):2892–2900, 2010.

[45] Xiaohua Huang, Prashant K Jain, Ivan H El-Sayed, and Mostafa A El-Sayed. Determination of the minimum temperature required for selective photothermal destruction of cancer cells with the use of immunotargeted gold nanoparticles. *Photochemistry and Photobiology*, 82(2):412–417, 2006.

[46] Xiaohua Huang, Xianghong Peng, Yiqing Wang, Yuxiang Wang, Dong M Shin, Mostafa A El-Sayed, and Shuming Nie. A reexamination of active and passive tumor targeting by using rod-shaped gold nanocrystals and covalently conjugated peptide ligands. *ACS Nano*, 4(10):5887–5896, 2010.

[47] Sajid Hussain, Maria Rodriguez-Fernandez, Gary B Braun, Francis J Doyle, and Erkki Ruoslahti. Quantity and accessibility for specific targeting of receptors in tumours. *Scientific Reports*, 4:5232, 2014.

[48] Trachette L Jackson and Helen M Byrne. A mathematical model to study the effects of drug resistance and vasculature on the response of solid tumors to chemotherapy. *Mathematical Biosciences*, 164(1):17–38, 2000.

[49] Harsh Jain and Trachette Jackson. Mathematical modeling of cellular cross-talk between endothelial and tumor cells highlights counterintuitive effects of VEGF-targeted therapies, 2017.

[50] Prashant K Jain, Kyeong Seok Lee, Ivan H El-Sayed, and Mostafa A El-Sayed. Calculated absorption and scattering properties of gold nanoparticles of different size, shape, and composition: applications in biological imaging and biomedicine. *J. Phys. Chem. B*, 110(14):7238–7248, 2006.

[51] Rakesh K Jain. Transport of molecules across tumor vasculature. *Cancer and Metastasis Reviews*, 6(4):559–593, 1987.

[52] Rakesh K Jain. Delivery of novel therapeutic agents in tumors: physiological barriers and strategies. *JNCI: Journal of the National Cancer Institute*, 81(8):570–576, 1989.

[53] Rakesh K Jain. Normalization of tumor vasculature: an emerging concept in antiangiogenic therapy. *Science*, 307(5706):58–62, 2005.

[54] Rakesh K Jain and Triantafyllos Stylianopoulos. Delivering nanomedicine to solid tumors. *Nature Reviews Clinical Oncology*, 7(11):653–664, 2010.

[55] Rakesh K Jain, Ricky T Tong, and Lance L Munn. Effect of vascular normalization by antiangiogenic therapy on interstitial hypertension, peritumor edema, and lymphatic metastasis: insights from a mathematical model. *Cancer Research*, 67(6):2729–2735, 2007.

[56] Suneil Jain, David Hirst, and Joe O'Sullivan. Gold nanoparticles as novel agents for cancer therapy. *The British Journal of Radiology*, pages 101–113, 2014.

[57] Ahmedin Jemal, Freddie Bray, Melissa M Center, Jacques Ferlay, Elizabeth Ward, and David Forman. Global cancer statistics. *CA: A Cancer Journal for Clinicians*, 61(2):69–90, 2011.

[58] S C Jiang, N Ma, H J Li, and X X Zhang. Effects of thermal properties and geometrical dimensions on skin burn injuries. *Burns*, 28(8):713–717, 2002.

[59] Wu Jinghua, Guo Zhendong, and Chen Jian. Efficient cellular automata method for heat transfer in tumor. *Journal of Heat Transfer*, 136(7):71101, 2014.

[60] Chanchala D Kaddi, John H Phan, and May D Wang. Computational nanomedicine: modeling of nanoparticle-mediated hyperthermal cancer therapy. *Nanomedicine*, 8(8):1323–1333, 2013.

[61] Kwabena Kan-Dapaah, Bernard Asimeng, Samuel Kojo Kwofie, and Abu Yaya. A plasmonic photo-thermal probe for thermoablation of post-operative breast cancer cells. *Cogent Engineering*, (just-accepted):1331966, 2017.

[62] Punit Kaur, Maureen L Aliru, Awalpreet S Chadha, Alexzander Asea, and Sunil Krishnan. Hyperthermia using nanoparticles–Promises and pitfalls. *International Journal of Hyperthermia*, 32(1):76–88, 2016.

[63] Byoungjin Kim, Gang Han, Bhushan J Toley, Chae-kyu Kim, Vincent M Rotello, and Neil S Forbes. Tuning payload delivery in tumour cylindroids using gold nanoparticles. *Nature Nanotechnology*, 5(6):465–472, 2010.

[64] Sachiko Kodera, Jose Gomez-Tames, Akimasa Hirata, Hiroshi Masuda, Takuji Arima, and Soichi Watanabe. Multiphysics and thermal response models to improve accuracy of local temperature estimation in rat cortex under microwave exposure. *International journal of environmental research and public health*, 14(4):358, 2017.

[65] J R Lakowicz. *Principles of Fluorescence Spectroscopy*. Springer US, 2010.

[66] Lucas A Lane, Ximei Qian, Andrew M Smith, and Shuming Nie. Physical chemistry of nanomedicine: Understanding the complex behaviors of nanoparticles in vivo. *Annual Review of Physical Chemistry*, 66:521–547, 2015.

[67] Jens Lang, Bodo Erdmann, and Martin Seebass. Impact of nonlinear heat transfer on temperature control in regional hyperthermia. *IEEE Transactions on Biomedical Engineering*, 46(9):1129–1138, 1999.

[68] L Gary Leal. *Advanced transport phenomena: fluid mechanics and convective transport processes*, volume 7. Cambridge University Press, 2007.

[69] Harold Eugene LeMay, Bruce Edward Bursten, C J Murphy, T L Brown, and P Woodward. *Chemistry: The Central Science*. Prentice Hall, 1988.

[70] James R Lepock. Cellular effects of hyperthermia: relevance to the minimum dose for thermal damage. *International Journal of Hyperthermia*, 19(3):252–266, 2003.

[71] John H Lienhard. *A heat transfer textbook*. Courier Corporation, 2011.

[72] Megan A Mackey, Moustafa R K Ali, Lauren A Austin, Rachel D Near, and Mostafa A El-Sayed. The most effective gold nanorod size for plasmonic photothermal therapy: theory and in vitro experiments. *The Journal of Physical Chemistry B*, 118(5):1319–1326, 2014.

[73] Kristine M Mayle, Kathryn R Dern, Vincent K Wong, Shijun Sung, Ke Ding, April R Rodriguez, Zachary Taylor, Z Hong Zhou, Warren S Grundfest, and Timothy J Deming. Polypeptide-based gold nanoshells for photothermal therapy. *SLAS TECHNOLOGY: Translating Life Sciences Innovation*, 22(1):18–25, 2017.

[74] Sean McGinty and Giuseppe Pontrelli. A general model of coupled drug release and tissue absorption for drug delivery devices. *Journal of Controlled Release*, 217:327–336, 2015.

[75] Max D Morris. Factorial sampling plans for preliminary computational experiments. *Technometrics*, 33(2):161–174, 1991.

[76] Fotios Mpekris, Stelios Angeli, Athanassios P Pirentis, and Triantafyllos Stylianopoulos. Stress-mediated progression of solid tumors: effect of mechanical stress on tissue oxygenation, cancer cell proliferation, and drug delivery. *Biomechanics and Modeling in Mechanobiology*, 14(6):1391–1402, 2015.

[77] Karmani Murugan, Yahya E Choonara, Pradeep Kumar, Divya Bijukumar, Lisa C du Toit, and Viness Pillay. Parameters and characteristics governing cellular internalization and trans-barrier trafficking of nanostructures. *International Journal of Nanomedicine*, 10:2191, 2015.

[78] M Nabil, P Decuzzi, and P Zunino. Modelling mass and heat transfer in nano-based cancer hyperthermia. *Royal Society Open Science*, 2(10):150447, 2015.

[79] Mahdi Nabil and Paolo Zunino. A computational study of cancer hyperthermia based on vascular magnetic nanoconstructs. *Royal Society Open Science*, 3(9):160287, 2016.

[80] Janice A Nagy, Sung-Hee Chang, Shou-Ching Shih, Ann M Dvorak, and Harold F Dvorak. Heterogeneity of the tumor vasculature. In *Seminars in Thrombosis and Hemostasis*, volume 36, pages 321–331. © Thieme Medical Publishers, 2010.

[81] Weihai Ni, Xiaoshan Kou, Zhi Yang, and Jianfang Wang. Tailoring longitudinal surface plasmon wavelengths, scattering and absorption cross sections of gold nanorods. *Acs Nano*, 2(4):677–686, 2008.

[82] Stephan Nickell, Marcus Hermann, Matthias Essenpreis, Thomas J Farrell, Uwe Krämer, and Michael S Patterson. Anisotropy of light propagation in human skin. *Physics in Medicine & Biology*, 45(10):2873, 2000.

[83] Carl M Öberg and Bengt Rippe. A distributed two-pore model: theoretical implications and practical application to the glomerular sieving of Ficoll. *American Journal of Physiology-Renal Physiology*, 306(8):F844–F854, 2014.

[84] Hilary Ockendon and John R Ockendon. *Viscous flow*, volume 13. Cambridge University Press, 1995.

[85] Panagiotis Papageorgis, Christiana Polydorou, Fotios Mpekris, Chrysovalantis Voutouri, Eliana Agathokleous, Constantina P Kapnissi-Christodoulou, and Triantafyllos Stylianopoulos. Tranilast-induced stress alleviation in solid tumors improves the efficacy of chemo-and nanotherapeutics in a size-independent manner. *Scientific Reports*, 7, 2017.

[86] Kyoungweon Park, Sushmita Biswas, Sushil Kanel, Dhriti Nepal, and Richard A Vaia. Engineering the optical properties of gold nanorods: independent tuning of surface plasmon energy, extinction coefficient, and scattering cross section. *The Journal of Physical Chemistry C*, 118(11):5918–5926, 2014.

[87] C S Patlak, D A Goldstein, and J F Hoffman. The flow of solute and solvent across a two-membrane system. *Journal of Theoretical Biology*, 5(3):426–442, 1963.

[88] John Pearce and Sharon Thomsen. Rate process analysis of thermal damage. In *Optical-thermal Response of Laser-Irradiated Tissue*, pages 561–606. Springer, 1995.

[89] Chen Peng, Linfeng Zheng, Qian Chen, Mingwu Shen, Rui Guo, Han Wang, Xueyan Cao, Guixiang Zhang, and Xiangyang Shi. PEGylated dendrimer-entrapped gold nanoparticles for in vivo blood pool and tumor imaging by computed tomography. *Biomaterials*, 33(4):1107–1119, 2012.

[90] Francesca Pianosi, Fanny Sarrazin, and Thorsten Wagener. A Matlab toolbox for global sensitivity analysis. *Environmental Modelling & Software*, 70:80–85, 2015.

[91] Gregory L Pishko, Garrett W Astary, Thomas H Mareci, and Malisa Sarntinoranont. Sensitivity analysis of an image-based solid tumor computational model with heterogeneous vasculature and porosity. *Annals of Biomedical Engineering*, 39(9):2360, 2011.

[92] Zhenpeng Qin and John C Bischof. Thermophysical and biological responses of gold nanoparticle laser heating. *Chemical Society Reviews*, 41(3):1191–1217, 2012.

[93] Erkki Ruoslahti, Sangeeta N Bhatia, and Michael J Sailor. Targeting of drugs and nanoparticles to tumors. *The Journal of Cell Biology*, 188(6):759–768, 2010.

[94] Marissa Nichole Rylander, Yusheng Feng, Jon Bass, and Kenneth R Diller. Heat shock protein expression and injury optimization for laser therapy design. *Lasers in Surgery and Medicine*, 39(9):731–746, 2007.

[95] Marissa Nichole Rylander, Yusheng Feng, Yongjie Zhang, Jon Bass, Roger Jason Stafford, Andrei Volgin, John D Hazle, and Kenneth R Diller. Optimizing heat shock protein expression induced by prostate cancer laser therapy through predictive computational models. *Journal of Biomedical Optics*, 11(4):41113, 2006.

[96] Hemant Sarin. Physiologic upper limits of pore size of different blood capillary types and another perspective on the dual pore theory of microvascular permeability. *Journal of Angiogenesis Research*, 2(1):14, 2010.

[97] Mostafa Sefidgar, Madjid Soltani, Kaamran Raahemifar, Hossein Bazmara, Seyed Mojtaba Mousavi Nayinian, and Majid Bazargan. Effect of tumor shape, size, and tissue transport properties on drug delivery to solid tumors. *Journal of Biological Engineering*, 8(1):12, 2014.

[98] R J Shipley, S L Waters, and Marianne J Ellis. Definition and validation of operating equations for poly (vinyl alcohol)-poly (lactide-co-glycolide) microfiltration membrane-scaffold bioreactors. *Biotechnology and Bioengineering*, 107(2):382–392, 2010.

[99] Rebecca J Shipley and S Jonathan Chapman. Multiscale modelling of fluid and drug transport in vascular tumours. *Bulletin of Mathematical Biology*, 72(6):1464–1491, 2010.

[100] Rebecca L Siegel, Kimberly D Miller, and Ahmedin Jemal. Cancer statistics, 2019. *CA: A Cancer Journal for Clinicians*, 69(1):7–34, 2019.

[101] Matthew G Skinner, Megumi N Iizuka, Michael C Kolios, and Michael D Sherar. A theoretical comparison of energy sources-microwave, ultrasound and laser-for interstitial thermal therapy. *Physics in Medicine & Biology*, 43(12):3535, 1998.

[102] Sanjeev Soni, Himanshu Tyagi, Robert A Taylor, and Amod Kumar. Experimental and numerical investigation of heat confinement during nanoparticle-assisted thermal therapy. *International Communications in Heat and Mass Transfer*, 69:11–17, 2015.

[103] M Stańczyk and J J Telega. Modelling of heat transfer in biomechanics-a review. P. 1. Soft tissues. *Acta of Bioengineering and Biomechanics*, 4(1):31–61, 2002.

[104] Ernest H Starling. On the absorption of fluids from the connective tissue spaces. *The Journal of Physiology*, 19(4):312–326, 1896.

[105] Triantafyllos Stylianopoulos, Eva-Athena Economides, James W Baish, Dai Fukumura, and Rakesh K Jain. Towards optimal design of cancer nanomedicines: multistage nanoparticles for the treatment of solid tumors. *Annals of Biomedical Engineering*, 43(9):2291–2300, 2015.

[106] Di Su, Ronghui Ma, and Liang Zhu. Numerical study of nanofluid infusion in deformable tissues for hyperthermia cancer treatments. *Medical & Biological Engineering & Computing*, 49(11):1233–1240, 2011.

[107] Mohameedyaseen Syedbasha, Janina Linnik, Deanna Santer, Daire O'Shea, Khaled Barakat, Michael Joyce, Nina Khanna, D Lorne Tyrrell, Michael Houghton, and Adrian Egli. An ELISA based binding and competition method to rapidly determine ligand-receptor interactions. *JoVE (Journal of Visualized Experiments)*, (109):e53575, 2016.

[108] Li Tang, Xujuan Yang, Qian Yin, Kaimin Cai, Hua Wang, Isthier Chaudhury, Catherine Yao, Qin Zhou, Mincheol Kwon, and James A Hartman. Investigating the optimal size of anticancer nanomedicine. *Proceedings of the National Academy of Sciences*, 111(43):15344–15349, 2014.

[109] Carlos Tassa, Jay L Duffner, Timothy A Lewis, Ralph Weissleder, Stuart L Schreiber, Angela N Koehler, and Stanley Y Shaw. Binding affinity and kinetic analysis of targeted small molecule-modified nanoparticles. *Bioconjugate Chemistry*, 21(1):14–19, 2010.

[110] Georgii Sergeevich Terentyuk, Andrei Valentinovich Ivanov, Nina Ivanovna Polyanskaya, Irina Leonidovna Maksimova, A A Skaptsov, Daniil Sergeevich Chumakov, Boris Nikolaevich Khlebtsov, and Nikolai Grigor'evich Khlebtsov. Photothermal

effects induced by laser heating of gold nanorods in suspensions and inoculated tumours during in vivo experiments. *Quantum Electronics*, 42(5):380–389, 2012.

[111] M Mercedes Tirado, Carmen López Martínez, and José García de la Torre. Comparison of theories for the translational and rotational diffusion coefficients of rod-like macromolecules. Application to short DNA fragments. *The Journal of Chemical Physics*, 81(4):2047–2052, 1984.

[112] Geoffrey Von Maltzahn, Ji-Ho Park, Amit Agrawal, Nanda Kishor Bandaru, Sarit K Das, Michael J Sailor, and Sangeeta N Bhatia. Computationally guided photothermal tumor therapy using long-circulating gold nanorod antennas. *Cancer Research*, 69(9):3892–3900, 2009.

[113] J P Ward and J R King. Mathematical modelling of avascular-tumour growth II: modelling growth saturation. *Mathematical Medicine and Biology*, 16(2):171–211, 1999.

[114] John P Ward and J R King. Mathematical modelling of avascular-tumour growth. *Mathematical Medicine and Biology*, 14(1):39–69, 1997.

[115] John P Ward and John R King. Mathematical modelling of drug transport in tumour multicell spheroids and monolayer cultures. *Mathematical Biosciences*, 181(2):177–207, 2003.

[116] W Weinberg, R_ Birngruber, and B Lorenz. The change in light reflection of the retina during therapeutic laser photocoagulation. *IEEE Journal of Quantum Electronics*, 20(12):1481–1489, 1984.

[117] A J Welch. The thermal response of laser irradiated tissue. *IEEE Journal of Quantum Electronics*, 20(12):1471–1481, 1984.

[118] Ashley J Welch and Martin J C Van Gemert. *Optical-thermal response of laser-irradiated tissue*, volume 2. Springer, 2011.

[119] Stephen Whitaker. *The method of volume averaging*, volume 13. Springer Science & Business Media, 2013.

[120] Xiao Xu, Andrew Meade, and Yildiz Bayazitoglu. Numerical investigation of nanoparticle-assisted laser-induced interstitial thermotherapy toward tumor and cancer treatments. *Lasers in Medical Science*, 26(2):213–222, 2011.

[121] Chong T Ying, Juntian Wang, Robert J Lamm, and Daniel T Kamei. Mathematical modeling of vesicle drug delivery systems 2: targeted vesicle interactions with cells, tumors, and the body. *Journal of Laboratory Automation*, 18(1):46–62, 2013.

[122] Dan Zhu, Qingming Luo, Guangming Zhu, and Wei Liu. Kinetic thermal response and damage in laser coagulation of tissue. *Lasers in Surgery and Medicine*, 31(5):313–321, 2002.